Fabrication of metal-organic frameworks with application-specific properties for hydrogen storage application

By

Sonwabo Elvis Bambalaza (Student number 3699780)

A thesis submitted in fulfilment of the requirements for the degree of Doctor of Philosophy in the Department of Chemistry, Faculty of Natural Science, University of the Western Cape

Supervisor: Prof L. Khotseng

Co-supervisors: Prof H.W. Langmi and Dr N.M. Musyoka

November 2019

Declaration

I declare that Fabrication of metal-organic frameworks with application-specific properties for hydrogen storage application is my own work, that it has not been submitted for any degree or examination in any other university, and that all the sources I have used or quoted have been indicated and acknowledged by complete references.

Sonwabo Elvis Bambalaza

Signed: 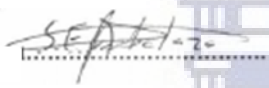 November 2019

Keywords

Hydrogen storage

Metal-organic frameworks

Nanocomposites

Pelletization

Coaxial electrospinning

Core-shell nanofibers

Gravimetric hydrogen capacity

Volumetric hydrogen capacity

Working capacity

Abstract

The application of porous materials into industrial hydrogen (H_2) storage systems is based on their use in combination with high-pressure cylinders. The processing of metal-organic frameworks (MOF) powders into shaped forms is therefore imperative in order to counteract the adverse effects of poor packing of powders in cylinders. The fabrication of shaped MOFs has, however, been shown to be accompanied by compromised properties such as surface areas, gravimetric and volumetric H_2 capacities, and also the working/deliverable H_2 capacities in comparison to MOF powders. The aim of the study was to fabricate MOF-based materials using pelletization and electrospun MOF/polymer nanofibers in order to impart improved shape-functionality, volumetric H_2 capacities, and H_2 working/deliverable capacities towards possibly reaching the US DOE system targets (H_2 working gravimetric capacity of 4.5 wt% and H_2 working volumetric capacity of 30 $g{\cdot}L^{-1}$).

The study reports on the use of high-pressure pelletization of the MOFs, MIL-101(Cr) and UiO-66, at an unprecedented applied pressure of ~700 MPa (100 000 psi) achieving greatly improved total volumetric hydrogen capacities by at least 150% in comparison to their powdered counterparts, but additionally, without compromising the total gravimetric H_2 capacity obtained in the powdered UiO-66 form, which is rare for MOFs. The pelletized MIL-101(Cr) showed a remarkable improvement in volumetric H_2 capacity of about 300% in comparison to powdered MIL-101(Cr). The MIL-101(Cr) also showed reasonable mechanical stability upon pelletization at 700 MPa, which has not been shown previously. The UiO-66 prepared in this study retained at least 90% of the original surface area and microporosity after pelletization at ~700 MPa, and the pelletized UiO-66 achieved a total gravimetric H_2 capacity between 4.2 and 5.1 wt% at 100 bar and 77 K in comparison to 4.6 and 5.0 wt% for the UiO-66 powder. The dynamic temperature-dependent behaviour of UiO-66 was experimentally demonstrated for the first time, and shown to be governed by a post-synthesis dehydroxylation process between 150 to 320 ^{o}C. The hydroxylated UiO-66 forms showed the greatest mechanical strength as it only exhibited a 9% reduction in gravimetric H_2 capacity whilst the pelletization of dehydroxylated UiO-66 forms resulted in reductions about 66% of their dehydroxylated UiO-66 powder counterparts. The pelletization of partially dehydroxylated UiO-66 powder samples, thermally treated at 200 and 290 ^{o}C, exhibited powder X-ray diffraction patterns indicative of an amorphous material, with low porosity (surface area reduced from between 700 and 1300 $m^{2}{\cdot}g^{-1}$ to *ca*. 200 $m^{2}{\cdot}g^{-1}$, and pore volume from between

0.4 and 0.6 $cm^{3}\cdot g^{-1}$ to 0.1 and 0.15 $cm^{3}\cdot g^{-1}$). The gravimetric H_2 capacities of pelletized dehydroxylated UiO-66 forms were between 0.7 - 0.9 wt% at 77 K and 100 bar, showing reductions of about 66% in comparison to their dehydroxylated UiO-66 powder counterparts. The observed activation temperature-induced dynamic behaviour of UiO-66 was unusual for MOFs and previously only been reported in computational studies. The results in this study showed that after pelletization at ~700 MPa, the structural properties and H_2 capacities for hydroxylated UiO-66 remained relatively unchanged, but were extremely compromised upon pelletization of dehydroxylated UiO-66 forms.

The fabrication of MOFs to improve their thermal conductivities and possibly attain gravimetric and volumetric H_2 working/deliverable capacities of about 4.5 wt% and 30 $g\cdot L^{-1}$ respectively, was proposed through the incorporation of graphene foam (GF) into UiO-66 powder, and through the co-pelletization of electrospun polymer-based binders with hydroxylated UiO-66 powder at ~700 MPa. The thermal conductivities of UiO-66 powder, GF/UiO-66 composite, and UiO-66 pellet were 0.077, 0.071, and 0.15 $W\cdot mK^{-1}$ respectively, with the incorporation of GF showing no improvements to the thermal conductivity of UiO-66 powder possibly owing to the extensive macropores present in the GF structure. The porosity of the materials was surprisingly found to have a more significant effect on the thermal conductivity than the chemical composition of the material. The UiO-66 pellet showed the highest thermal conductivity due to reduction in void volumes and possibly reduced grain sizes after pelletization at ~700 MPa. The UiO-66 pellets containing the polymer of intrinsic microporosity, PIM-1, nanofiber binders retained at least 86% of the porosity obtained in pristine UiO-66 pellets with a BET surface area of 1113 $m^{2}\cdot g^{-1}$ compared to 1300 $m^{2}\cdot g^{-1}$ and total pore volume of 0.59 $cm^{3}\cdot g^{-1}$ to 0.60 $cm^{3}\cdot g^{-1}$ in comparison to pristine UiO-66 pellet. This translated to respective total gravimetric H_2 capacities of 3.9 wt% compared to 4.2 wt% at 77 K and 100 bar, but crucially, the gravimetric H_2 working/deliverable capacity was 2.3 wt% in the pelletized UiO-66/PIM-1 composite compared to 1.9 wt% obtained in the pristine UiO-66 pellet. The improved H_2 working/deliverable capacity could be attributed to the introduction of mesopores only observable on the co-pelletized UiO-66/nanofiber composites and not on electrospun PIM-1 nor MOF/PAN (PAN = polyacrylonitrile) nanofibers prior to their co-pelletization. The observed mesopores could indicate a new method of co-pelletization of electrospun nanofiber and MOF alternating layers to possibly introduce hierarchical porosity into an initially highly microporous MOF such as UiO-66.

Outputs

Published manuscript(s)

- Sonwabo E. Bambalaza, Henrietta W. Langmi, Nicholas M. Musyoka, Jianwei Ren, Lindiwe E. Khotseng, *Incorporation of UiO-66 onto graphene foam for hydrogen storage applications*, Materials Today: Proceedings 5, **2018**, 10431–10439.

- Sonwabo E. Bambalaza, Henrietta W. Langmi, Robert Mokaya, Nicholas M. Musyoka, Jianwei Ren and Lindiwe E. Khotseng, *Compaction of a zirconium metal–organic framework (UiO-66) for high density hydrogen storage applications*, J. Mater. Chem. A, **2018**, 6, 23569-23577.

Submitted manuscript(s)

- Sonwabo E. Bambalaza, Robert Mokaya, Nicholas M. Musyoka, Lindiwe E. Khotseng, Henrietta W. Langmi. *Experimental demonstration of dynamic temperature-dependent behaviour of UiO-66 metal-organic-framework*: *Compaction of hydroxylated and deydroxylated forms of UiO-66 for high pressure hydrogen storage*. ACS Applied Materials & Interfaces.

- Sonwabo E. Bambalaza, Nicholas M. Musyoka, Lindiwe E. Khotseng, Henrietta W. Langmi. *Co-pelletization of a zirconium metal-organic framework (UiO-66) with polymer nanofibers for improved working capacity in hydrogen storage*.

Oral presentations

- S.E. Bambalaza, H.W. Langmi, N.M. Musyoka, L. Khotseng, *In-situ growth of zirconium-metal organic framework nanocrystals onto graphene foam and its `hydrogen storage properties*, Annual National Renewable and Sustainable Energy Postgraduate Symposium, Alice, South Africa, 5-6 September 2016.
- H.W. Langmi, N.M. Musyoka, S. Bambalaza, J. Ren, M. Mathe, D. Bessarabov, *Synthesis of MOF/Carbon Composite Materials for Enhanced Hydrogen Storage Properties*, European Materials Society (E-MRS) Fall Meeting, Warsaw, Poland, 19-22 September 2016.
- Sonwabo E. Bambalaza, Henrietta W. Langmi, Nicholas M. Musyoka, Jianwei Ren, Lindiwe Khotseng, *Incorporation of Zr-MOF into graphene foam for hydrogen storage applications*, 1st Africa Energy Materials Conference, Pretoria, South Africa, 28-31 March 2017.
- Sonwabo E. Bambalaza, Henrietta W. Langmi, Nicholas M. Musyoka, Lindiwe E. Khotseng, *Fabrication of application-specific properties onto MOFs for hydrogen storage applications*, Royal Society-Department of International Development (DFID) Africa capacity building initiative (ACBI) award holders' meeting, 1 – 3 April 2017, Dar Es Salaam, Tanzania.
- Sonwabo E. Bambalaza, Henrietta W. Langmi, Nicholas M. Musyoka, Lindiwe E. Khotseng, *Compaction of UiO-66(Zr) Metal-Organic Framework for High Density Hydrogen Storage*, Royal Society-DFID ACBI award holders' meeting, 1 – 6 December 2018, Saly M'bour, Senegal.
- Five oral presentations at RS-DFID ACBI Consortium meetings held at Kisumu (Kenya), Pretoria (South Africa), Nottingham (UK), and Yaoundé (Cameroon) between 2017 – 2019.

Poster presentations

- Sonwabo E. Bambalaza, Henrietta W. Langmi, Nicholas M. Musyoka, Robert Mokaya, Lindiwe E. Khotseng, *Compaction of UiO-66/MIL-101(Cr) Metal-Organic Framework composite material for high density hydrogen storage*, 7th European Chemistry Society (EuChemS) Congress, 26 – 30 August 2018, ACC Liverpool, UK.

Acknowledgements

I give all the praise to the Almighty God for giving me life and the most amazing parents, Nkosinathi Kenneth Bambalaza (father) and Tutuzelwa Evelyn Bambalaza (mother). I give thanks to my two wonderful families, the Macatshazas and the Bambalazas, I would not be where I am without their support and the values they taught me in getting to this point.

Friends:

Collin Bacela / Sir B / mentor – My first year Physics lecturer (Nelson Mandela Metropolitan University - NMMU). I was on one of my lowest points after being rejected direct entry into mainstream BSc, I had to do an extended program. You saw my pain and took me under your wing and showed me how setbacks could be handled without losing control and here I am on a PhD level. Thank you Sir B!

The Dimbaza family (Ntsika, Xolisa / Bawu Nkala, Akhona Zim, and Luyanda) – Always there with me through good and bad times, the first people to give me the title change (from Mr to Dr) by virtue of doing a PhD.

Xoliswa Dyosiba – I appreciate the person you are, you looked past my "no new friends" shield and became an integral part of my personal and professional life. I thank you for your friendship.

My supervisors:

Dr Nicholas Musyoka - I am grateful for the contribution you made in my research, you were very insightful and taught me a new level of thinking;

Prof Lindiwe Khotseng – As much as we never had the opportunity to meet properly, I appreciate your contribution towards my studies.

Prof Henrietta Langmi / Dr H – Thank you for your patience and understanding throughout my project. Thank you for allowing me creative control of my project, that meant a lot to me. Thank you for the immense time you spent on my project, for helping me with all the admin paperwork we had to submit for every trip. I one day wish to follow in your footsteps, you are an exemplary scientist.

Colleagues and collaborators:

HySA infrastructure colleagues – I thank you for the assistance with my work, the friendly and welcoming environment.

RS-DFID ACBI consortium (Strengthening African capacity in porous materials research) Prof. Robert Mokaya, Prof Crispin Kowenje, Prof Justin Kemmegne, Stephen Otieno, and Edwige Mouafo-Tchinda I was fortunate enough to get to know and work with you, for that I am forever grateful as I never thought I would go outside the boarders of my country. I wish to meet and work together in future endeavours. A special thank you to Prof Mokaya's group at the University Of Nottingham, for their hospitality and assistance throughout my visits to the university.

Funding: This study was funded by the Royal Society (RS)-Department of International Development (DFID) Africa Capacity Building Initiative (ACBI), and the Department of Science and Innovation (DSI) Hydrogen South Africa (HySA) Infrastructure Key Program 4. I was very fortunate to have received this funding as it placed me in a rare situation of travelling the world as a student, for that I am grateful.

To the future: Kaya (Kaizer), Lunje, Niyole (Asante), and Kusakhanya (Karibu): imiqathango yokuqala ndiyibekile, nakuze nani nenze kwande kwesisiqhamo sisantshulileyo. Niwasebenzise onke amathuba ayokuthi avele, niqhame ninganqandwa nasi sibhakabhaka, kwande kooMchumane, kwande kooNozulu, kwande kooMnguni. Ndiyanithanda kakhulu.

I DEDICATE THIS THESIS TO THE LATE GREAT ZAMUXOLO "BRA M" MALUSI WHO PASSED AWAY ON THE 25TH OCTOBER 2019.

NDITHI LALA NGOXOLO SHWEME, LIMAKHWE, ZILAMKHONTO, NDOHLALA NDIKUKHUMBULA.

Table of contents

List of figures

List of Tables

List of abbreviations

MOF – Metal-organic framework

PAN – Polyacrylonitrile

PMMA – Polymethylmethacryalate

PS – Polystyrene

NF – Nickel foam

GF – Graphene foam

ZTC – Zeolite templated carbon

PIM – Polymer of intrinsic microporosity

UiO - Universitetet i Oslo

MIL – M Institut Lavoisier

HKUST – Hong Kong University of Science and Technology

ZIF – Zeolite imidazole framework

IUPAC – International Union of Pure and Applied Chemistry

FTIR – Fourier Transform Infrared

TEM – Transmission electron microscopy

SEM – Scanning electron microscopy

PXRD – Powder X-ray diffraction

TGA – Thermogravimetric analysis

EDX – Energy-dispersive X-ray

MS – Mass spectroscopy

NLDFT – Non-localized density functional theory

DMF – Dimethylformamide

CVD – Chemical vapour deposition

Chapter 1

1. Introduction

This chapter firstly outlines aspects of hydrogen (H_2) storage that have been proposed in addressing the industrial implications for a sustainable H_2 economy. The chapter then gives a detailed description of the knowledge gap the study was aiming to address as it pertains to H_2 storage in solid-state porous materials, and the scope, motivation, delimitations and objectives of the study. Finally, the chapter gives an overview of the specific methods used to achieve the set objectives and also how the thesis chapters are structured.

1.1. Background

1.1.1. Renewable energy solutions and the environmental and socio-economic impact of climate change.

The global consumption of power is directly linked to the utilization of no less than 80% fossil fuels in energy production plants. The growing demand for energy supply together with an exponentially growing human population, the overdependence on fossil fuels raises major concerns for future energy demands. Even though the use of fossil fuels has been diversified to include a mixture of natural gas, crude oil, and coal as the major fuels, there exists environmental issues that are directly linked to fossil fuel-based power production, i.e. climate change and/or global warming. Climate change and/or global warming has had devastating environmental effects such as the increase in global temperatures, increasing ocean water levels, the spread of disease can be shown to be primarily linked to increasing atmospheric CO_2 levels, especially through industrial activity [3]. In order to ensure a sustainable future and reduce the environmental effects imparted by climate change and/or global warming, it is necessary to minimize the uses of fossil fuels in power production by developing alternative processes that are clean, able to meet global energy demands, and economically sustainable. This study proposes the concept of a H_2 economy where H_2 is proposed as an energy carrier in power generation, with particular interest in the use of H_2 fuel in mobile applications.

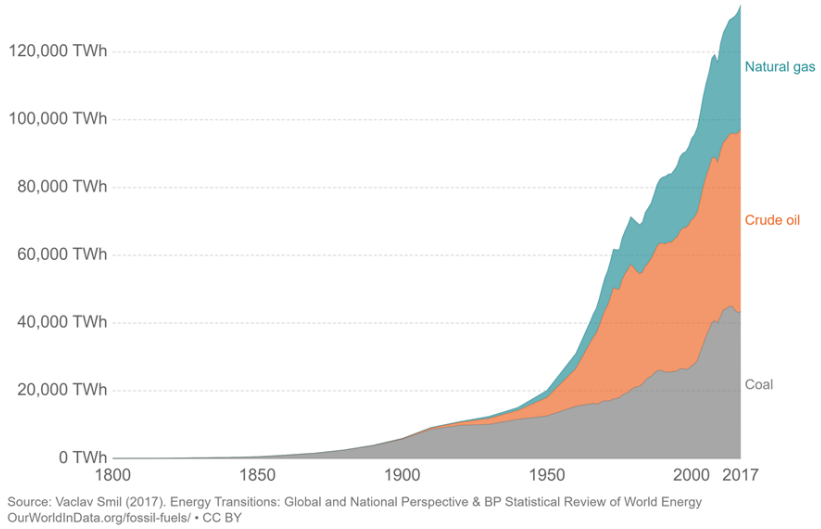

Figure 1.1: Recorded values showing the global consumption of the three major fossil fuels (natural gas, oil, and coal) per terawatt-hour from the 1800's to 2017 [1].

The H_2 energy economy is a concept aimed towards the development of energy supply systems based on the use of H_2 as an energy carrier. The energy density that can be harnessed from the complete combustion of H_2 far exceeds that of conventional fossil fuel-based fuels such as coal, natural gas, gasoline, and petroleum fuels [4]. The main aspect in a potential H_2-based economy lies on the production of H_2 from an abundant array of clean and renewable resources. A few examples can be made mention such as the electrolytic splitting of water producing H_2 and oxygen (O_2), but more importantly by harnessing solar energy through the use solar powered fuel cells in order to compensate for the large energy input required in the electrolysis process [5]. Not only does the electrolysis process produce high purity H_2, but also the use of solar power could possibly minimize the overdependence on fossil-fuel based H_2 production that produce large amounts of CO_2 that have been largely emitted into the atmosphere, such as steam/methane reform processes. Another alternative for producing H_2 through renewable resources includes the use of hydrocarbon-based biomass, e.g. gasification of cellulose or other naturally occurring crops, through a 'carbon-neutral' process. The term 'carbon-neutral' generally refers to a process whereby the CO_2 produced in one process, such as steam reform, can be balanced out through its use in another process so as to achieve a net zero carbon emission [6]. Production of biofuels from natural crops or waste carbonaceous products is one such carbon-neutral process as the CO_2 is emitted during burning of the biomass followed by its use in Fischer-Tropsch processes to produce hydrocarbons [7,8]. Furthermore, the use of H_2 fuel is a clean alternative as the major by-product in a fuel cell is water vapour.

There are currently challenges associated with the use of H_2 fuel in mobile applications, in particular automobiles. The density of H_2 gas under standard temperature and pressure (STP) conditions is about 0.090 $kg \cdot m^{-3}$, which means for a H_2-fuelled automobile to complete a 500 km journey, an estimated amount of about 5 – 13 kg of H_2 may be required before refilling, but the equivalent H_2 volume at STP is about 56 – 144 m^3 [9,10]. This means that at STP, the H_2 storage tank would possibly have a larger volume compared to the automobile. It is therefore imperative that the development of H_2 storage systems should have practical solutions applicable to automobile applications. The United States Department of Energy (US DOE) has compiled a set of H_2 storage system standards that state an operating temperature ranging from -40 ^oC to 60 ^oC, and pressure up to 100 atm (Parilla *et al.*, 2016; "US DOE targets" Cited from www.energy.gov, 2019). The US DOE targets therefore allow for the compression of H_2 gas at supercritical pressures and below ambient temperatures (298 K).

1.1.2. Material-based and conventional hydrogen storage methods

The current H_2 storage systems such as the use of liquid H_2 and H_2 stored in pressurized steel cylinders are not conducive for mobile applications. The use of liquid H_2 is an energy intensive process that involves cooling of H_2 down to its boiling point of 20.3 K and requirements associated with maintaining a constant temperature to keep the H_2 in its liquid form [13]. The use of pressurized H_2 gas in steel cylinders provides major setbacks in the size and weight of the storage system. Since the density of H_2 gas is 0.0076748 $g \cdot mL^{-1}$ [14], its pressurization in a cylinder typically requires the use of pressures in excess of 700 bar (70 MPa) in order to achieve the gravimetric and volumetric H_2 density/capacity targets set out by the US DOE under the specified temperature range. There are also major safety concerns associated with the use of pressures as high as 700 bar for on-board vehicle applications. For on-board hydrogen storage for light-duty fuel cell vehicles, the current system targets for the deliverable gravimetric H_2 capacity and volumetric H_2 capacity are 4.5 wt% and 30 $g \cdot L^{-1}$, respectively, with the ultimate targets being 6.5 wt% and 50 $g \cdot L^{-1}$, respectively. The system targets refer to the amount of H_2 gas deliverable to the fuel cell system in relation to the complete system, which would include the storage tank/cylinder, valves, regulators, piping, mounting brackets, insulation, and cooling system, and as such the storage material alone would have to show gravimetric and volumetric H_2 capacities that far exceed the aforementioned targets. The deliverable gravimetric H_2 capacity relates to the weight (in kilograms) of H_2 that can be

delivered to the fuel cell system divided by the total weight of the storage system components including stored H_2. The volumetric H_2 capacity refers to the weight of H_2 (in kilograms) deliverable to the fuel cell system divided by the volume of the system components including the volume of stored H_2[9,11,2,15]. The gravimetric and volumetric H_2 capacities referred to in this study were based on the weight of H_2 stored in the material divided by the weight of the material without H_2. An additional system requirement, amongst others, is a H_2 refilling time of 3 – 5 minutes and this requires that the proposed storage material of choice should exhibit fast kinetics in the uptake and release of H_2.

Studies conducted on solid-state material-based H_2 storage in combination with high-pressure cylinders have provided compelling evidence in potentially reducing the pressure requirements for on-board H_2 storage systems below 200 bar (20 MPa) using porous materials [16], and metal hydrides [17]. Metal hydrides are compounds consisting of single or multiple metal cations (M^+) and hydride (H^-) anions. The general concept of H_2 storage in metal hydrides is the pressure-induced absorption of H^- anions onto the metal cation centres to form stable metal hydrides, which is followed by the subsequent desorption of molecular H_2 via a chemical reaction such as disproportionation of the metal hydride complex, typically observed in complex hydrides [18]. Complex metal hydrides usually consist of more than one metal/metalloid, with the anion containing the hydride [19]. Other forms of metal hydride are known as intermediate hydrides which can exist in alloy-type forms [20]. Some metal hydrides have been shown to exhibit low-temperature H_2 desorption at temperatures ranging from -20 ^oC to about 120 ^oC with theoretical gravimetric and volumetric capacities, for these particular metal hydrides, ranging from 1 to 6 wt% and 40 to 100 $g{\cdot}L^{-1}$, respectively. It is important to note that the metal hydride types associated with volumetric H_2 capacities of about 100 $g{\cdot}L^{-1}$ also typically show low gravimetric H_2 capacities (*ca.* 1 wt%). The metal hydrides with gravimetric H_2 capacities in excess of 6 wt% tend to have desorption temperatures higher than 100 ^oC and as a result there is an energy penalty associated with H_2 release at high temperatures, and has shown limits to their use in a potential H_2 storage system [21].

Porous materials, on the other hand, are characterized by internal structures consisting of permanent pores which can be accessible to foreign or guest molecules that satisfy the dimensions of the pores. Some of the extensively studied porous materials for H_2 storage applications include, but not limited to, zeolites, activated carbons, zeolite-templated carbons (ZTCs), porous polymers, and metal-organic frameworks (MOFs) [22,23]. These materials can

be tailored to achieve surface areas in excess of 500 $m^2 \cdot g^{-1}$ with one of the highest experimentally measured surface area of 7000 $m^2 \cdot g^{-1}$ obtained in two MOFs, NU-100 and NU-110 (NU = Northwestern University) [24]. In porous materials, H_2 storage is achieved via the spontaneous physical adsorption (physisorption) of H_2 molecules onto energetically favourable sites, typically within the pores and surface, of the material. The conditions that provide the driving force for H_2 adsorption onto porous media are typically the applied pressure, heat of adsorption and temperature. The release or desorption of H_2 occurs by lowering the applied pressure, under the same conditions of temperature, since no chemical interactions are prevalent between the H_2 molecules and the surface of the porous medium [25,26]. This enables the uptake and release of H_2 molecules to occur with little to negligible energy inputs, meaning that the kinetics associated with physisorption-based H_2 storage are typically faster compared to other mechanisms such as absorption [27]. In physisorption, however, it is generally found that the highest H_2 adsorption capacities are obtained under cryogenic conditions (77 K), with H_2 adsorption capacities obtained at ambient temperature (298 K) very considerably lower relative to the capacities at cryogenic conditions. Since there are no chemical interactions, weak forces (such as van der Waals forces) govern the interactions between the surface of the material and the H_2 molecules as well as between H_2 molecules, and also due to the reduced mobility of the gas molecules at low temperature, these interactions become enhanced as the temperature is lowered [13].

1.1.3. Thermal management in physisorption-based H_2 storage

The material properties envisaged for material-based H_2 storage system are not only limited to the gravimetric and volumetric H_2 capacities achievable in a material, but also good thermal conductivity and mechanical stability of the material are key requirements in the preparation of highly efficient storage systems. The issue of heat management in physisorption-based H_2 storage can be addressed by considering two aspects, one at the material level of adsorbent-adsorbate interactions and the second at a system level which takes into account the physical properties of H_2 and its desorption/release from the storage device/tank. At the material level, the heat of adsorption (ΔH_{ad}) of H_2 is a measure of the interaction strength between the H_2 molecules and the adsorbent (in this case porous solids, MOFs and carbons) and generally determines the temperature and pressure conditions whereby adsorption would occur spontaneously [10,28]. In porous materials, it is typically found that ΔH_{ad} is highest at low adsorption pressures where the interaction is mainly between the H_2 molecules and the porous

surface, instead of H_2-H_2 interactions. However, the weak van der Waals interactions involved in the adsorption of H_2 typically mean that ΔH_{ad} generally does not exceed about 4-7 $kJ{\cdot}mol^{-1}$ for most experimental values reported in MOFs [10,29]. Higher ΔH_{ad} values are desired to improve the strength of H_2 adsorption onto MOFs, but as the ΔH_{ad} increases, so does the amount of heat generated during H_2 adsorption. In such cases, where it would be possible to attain ΔH_{ad} values much greater than 4-7 $kJ{\cdot}mol^{-1}$, it would become imperative that the thermal conductivity of MOFs, MOF monoliths, or MOF composites become improved for efficient dissipation of heat generated during adsorption. On the system-level H_2 storage applications where H_2 storage devices are expected to operate under high-pressure conditions, the issue of the physical properties of H_2 must be taken into consideration. For example, the critical pressure of H_2 is about 13 bar, meaning that at higher pressures H_2 becomes a supercritical fluid (SCF) where the H_2 gas and liquid phases become indistinguishable, thereby giving the SCF 'gas-like' and 'liquid-like' properties [14]. In this study the analysis of H_2 adsorption and desorption isotherms was investigated up to a pressure of 100 bar for measurements at 77 and 298 K, i.e. under supercritical conditions. In the general design of gas adsorption systems for CO_2, CH_4, and H_2, there are two common methods, namely, pressure-swing adsorption and temperature-swing adsorption [15,30–36]. Pressure-swing adsorption involves the uptake of gas from low to high pressure and its release from high to low pressure, under isothermal conditions. In the case of mobile H_2 storage applications, as set out by the US DOE, the minimum delivery pressure is set at 5 bar and a maximum storage pressure of 100 bar is generally reported in most high-pressure H_2 storage studies [37], although some studies have reported at 20 – 35 bar [38,39]. H_2 is in a gaseous phase at 5 bar and becomes a SCF phase at 20, 35, and 100 bar, meaning that for pressure-swing adsorption systems the release/desorption of H_2 occurs in the gaseous phase. Even though the desorption of H_2 down to 5 bar would involve a transition from SCF to gas phase, there would be minimal/negligible changes (if any) to the temperature of the gas since the temperature change is zero under isothermal conditions. This means the requirement for high thermally conductive adsorbent materials would not be a necessity given low to moderate ΔH_{ad} as is typical of most MOFs. Temperature-swing adsorption, however, involves the adsorption of H_2 at low temperature (e.g. 77 K) followed by desorption at a higher temperature (e.g. 298 K) under isobaric conditions. Temperature-swing adsorption provides an advantage for H_2 to be possibly stored (adsorbed) at cryogenic temperature and released (desorption) at a higher temperature at a considerably high working/deliverable capacity. This is because in physisorption, the amount of adsorbed H_2 increases with decreasing temperature, for example it is generally found that the gravimetric

H_2 capacity at 298 K typically is 1% to that obtained at 77 K at the same pressure [10,40]. The disadvantage is the existence of a physical phenomenon, known as 'pseudo boiling' that occurs under supercritical and isobaric conditions [41]. The study reported by Oschwald and Schik [42] showed that the drastic decrease in the density of a SCF as a function of temperature (under isobaric conditions above the critical pressure) may be accompanied by a significant increase (spike) in the specific heat capacity of the fluid. Although the spike in specific heat capacity exists only within a finite temperature range, it can be significant enough to raise the temperature of the fluid. In H_2 storage there could be significant implications during desorption of H_2 in temperature swing adsorption systems and thus could require improvement of the thermal conductivity of MOFs, MOF monoliths, or MOF composites that are candidate for H_2 storage system applications.

The proposed/candidate materials should exhibit efficient heat dissipation to counteract the heat generated during uptake of H_2 gas at high pressure [43,44]. It has also been shown that the use of solid-state storage materials in their powder form tends to show reduced performance with repeated cycles of H_2 uptake and release, owing to sintering effects upon repeated H_2 cycles on the powder particles, which is especially true for metal/complex hydrides. The sintering may be caused by repeated exposure of the powder particles to high pressure and heat fluxes and hence result in the agglomeration of powder particles introducing void spaces within the storage system. In order to counteract such effects, the performance of solid-state materials for H_2 storage may be used in compacted forms instead of pristine powders. The compaction ensures that the effects of sintering are minimized or negligible since the mobility of the solid particles become restricted in their compacted forms [21,45]. Some of the more successful strategies used for compaction of powdered H_2 storage materials include granulation, pelletization, or by embedding powders into a polymer matrix [34,46,47].

1.1.4. Development of immobilized and monolithic MOF structures for H_2 storage applications

Knowing that hydrogen storage materials are typically synthesized in powder form, which can contaminate the storage system pipelines, compaction of the powdered materials for improved handling is necessary. In addition to its use for improving material handling, compaction of powdered storage materials and particularly pelletization, may also be used to improve their inherently low bulk/packing densities through densification [38,48,49]. The density of porous

materials is a key property for H_2 storage applications as it relates to the volumetric H_2 capacity, with low density materials typically showing volumetric H_2 densities below the US DOE target of 30 $g{\cdot}L^{-1}$ [2,36,37]. Since solid-state porous materials also exist as crystalline (e.g. MOFs), semi-crystalline (e.g. porous polymers), and amorphous forms (e.g. activated carbons and ZTCs), it would be more practical to measure their densities and hence volumetric H_2 capacities of their bulk or powder forms. In MOFs, the consideration of crystal density alone may not be applicable for comparisons of volumetric H_2 capacities of MOFs to that of semi-crystalline polymers and amorphous carbons. Indeed the crystal density of MOFs has been shown to influence their volumetric H_2 capacity but it would also be practically challenging packing single crystals into high-pressure cylinders compared to the packing of their polycrystalline powder forms. The studies of Balderas-Xicohtèncatl and co-workers [50] report on the applicability of using packing densities for the determination of volumetric H_2 capacities in a wide range of powdered porous materials such as MOFs and activated carbons. In the latter studies, a predictive mathematical model that yielded theoretical volumetric H_2 capacities comparable to experimentally measured values and also taking into account some compacted forms of the materials, was developed. The model shows a strong correlation of the volumetric H_2 capacity to the packing density of the material. However, the problem associated with compaction strategies is that the compacted/shaped forms tend to show compromised gravimetric H_2 capacities compared to their powder counterparts [34,51,52]. In this study the focus was based on addressing the issues associated with shaping porous materials and how these could be minimized in order to achieve favourable properties for H_2 storage applications in shaped solid-state porous materials. This study was carried out under the Royal Society (RS)-Department of International Development (DFID) Africa Capacity Building Initiative, and the Department of Science and Innovation (DSI) Hydrogen South Africa (HySA) Infrastructure Key Program 4.

1.2. Problem statement

1.2.1. Challenges in fabrication of immobilized and monolithic MOF structures

Many fabrication approaches, such as pelletization, electrospinning, granulation, and sol-gel methods, have proven successful in obtaining shaped forms of MOFs, carbons and polymer materials [53,54]. In addition, the compositing of different types of carbons with MOFs has been reported to show improved thermal conductivities of the MOF/carbon composite

compared to the pristine MOF material [55,56]. The incorporation of MOFs and ZTCs into polymer nanofibers, via electrospinning, has also been shown to improve their handling compared to MOF and ZTC powders [57]. An almost inevitable challenge, however, which has been reported in many studies is that the composite and/or shaped forms of the porous materials tend to show compromised textural properties, such as surface areas and pore volumes, compared to their powder counterparts. The fact that H_2 adsorption onto porous materials occurs via physisorption means that any compromise or reduction to the binding sites (pores and adsorbent surface) would inevitably lead to a compromise of the H_2 storage capacities of the material [58,59]. Due to the US DOE current and ultimate system targets being set at 4.5 and 6.5 wt% gravimetric H_2 capacity, respectively, and 30 and 65 $g{\cdot}L^{-1}$ volumetric H_2 capacity, respectively, the compromised performance of shaped and/or composited porous materials is unfavourable to possibly meet the aforementioned industrial requirements for on-board storage. This is because at the material level, without considering the remaining components of the system i.e. the balance of plant (BOP), both the gravimetric and volumetric H_2 capacities should exceed the system targets. In order to maintain high-performance of candidate porous materials for H_2 storage, there is a need for the fabrication of porous materials to attain properties that would not show reductions in their H_2 capacities.

1.2.2. Recent advances in immobilized and monolithic MOF structures

There has, however, been significant development of MOF monoliths, which are shaped MOFs macrostructures such as granules, gels, and pellets. The properties of such monolithic forms may be tailored differently to the pristine MOF powders, for example, the study by Connolly et. al. [60] showed that the Zr-MOF, UiO-66, could form monolithic gels which could be tailored to consist of an increased degree of mesopores and macropores by adjusting the synthesis or process parameters of gelation. The creation of mesopres and macropores was shown not to change the permanent porosity of the UiO-66 unit cell, but the additional porosity was extrinsic, only observed in the monolithic gel structure. The study showed that for CO_2 and CH_4 storage, the UiO-66 gels could attain volumetric working capacities 11% greater in comparison to the volumetric working capacity of pristine UiO-66 powder. Other forms of MOF monoliths such as MIL-101(Cr) hexagonal pellets reported by Ardelean et al. [61] showed an improvement in volumetric H_2 capacity with increased envelope density of the MIL-101(Cr) pellets. This area of monolithic MOF structures has been shown to enable the fabrication of MOFs with application-specific properties for H_2 system applications

[53,54,62,63], which is being also addressed in the current study by pelletization of UiO-66 and MIL-101(Cr) at ~700 MPa, a sufficiently higher applied pressure than reported in other experimental studies [51,62,64,65]. This study focuses on the fabrication of solid-state porous materials, specifically MOFs-based materials using shaping techniques that can possibly tailor properties suitable for on-board H_2 storage applications.

1.3. Motivation and research questions

The ease of availability and proven track record of shaping techniques such as electrospinning and pelletization make it possible to carry out research based on the improvement of the shape-functionality of powdered porous materials in H_2 storage applications. The intrinsic properties of candidate porous materials such as MOFs have also been predicted through computational studies which may eliminate the need for numerous screening experiments from being carried out in laboratories [66–69]. The combination of the availability of robust shaping techniques and pre-existing theoretical knowledge of the behaviour of porous materials (specifically MOFs) can allow for an application-specific experimental study to be carried out. Indeed in this study, two of the porous materials of choice were zirconium- and chromium-based MOFs, UiO-66 and MIL-101(Cr). The UiO-66 MOF has been reported to have a high mechanical strength with a theoretical minimum shear modulus of 13.7 GPa [70]. Due to the high porosity of MOFs, they are typically found to be susceptible to applied pressure and as such their densities, through pelletization, are usually improved with significant negative effects on their structures and textural properties [71]. A mechanically robust MOF, such as UiO-66, could possibly be pelletized at high pressure with the possibility of achieving densities > 1 $g{\cdot}mL^{-1}$ and possibly maintain its structure. It is also noteworthy that the importance of post-synthesis thermal treatment temperature i.e. activation as it pertains to UiO-66 material properties has not always been given any consideration. Experimental investigations on the high-pressure pelletiztion of dehydroxylated UiO-66, especially as it pertains to H_2 storage applications, have not been documented in literature. This study attempted to show the first experimental proof for the pelletization of dehydroxylated forms of UiO-66, and potentially replicate the computational results reported by Chandival et al. [72] and Rogge et al. [73]. Their studies described the effect of the dehydroxylation of UiO-66 to possibly result in the compromise of its mechanical stability which highlight the shear modulus to be more compromised compared to the bulk modulus of UiO-66. The MIL-101(Cr) MOF has been shown to have surface areas in excess of 3000 $m^{2}{\cdot}g^{-1}$ and also a MIL-101@UiO-66 composite was successfully prepared by

Ren et al. [74] and found to have improved surface area, pore volume, and gravimetric H_2 capacity compared to the individual MOFs, UiO-66 and MIL-101(Cr). Another factor important for H_2 storage is the thermal conductivity of the material since the high-pressure adsorption of gases is an exothermic process and therefore generates heat onto the adsorbent material. Graphene is a material with one of the highest measured thermal conductivities ranging from 3000 to 5000 $W \cdot mK^{-1}$ and has further been shown to have H_2 adsorption properties [75–77]. In this study the use of graphene foam (GF) in combination with UiO-66 was proposed as the high thermal conductivity carbon source. Finally the incorporation of UiO-66 and MIL-101(Cr) into electrospun nanofibers from polymers with excellent electrical conductivities such as polyacrylonitrile (PAN), polymethylmethacrylate (PMMA), polystyrene (PS), and the polymer of intrinsic microporosity, PIM-1, was proposed. The electrical conductivity of the polymer is its key property in the electrospinning process. The ability of the polymer to form a 'Taylor cone' under an applied voltage, during the electrospinning process, is largely determined by the polymer's electrical conductivity (discussed in detail in Chater 2). The PAN, PMMA and PS polymers have been shown to be electrospinnable with powder materials such as MOFs, and their resultant MOF/polymer composites have been tested for H_2 storage [78–81].

The study, therefore, aimed to provide research answers to the following questions:

- Does pelletization of UiO-66 compromise its structure and textural properties?
- Does the mechanical strength of UiO-66 become compromised upon dehydroxylation of UiO-66 at ~300 ^oC?
- Can pelletization of UiO-66 improve its volumetric H_2 storage capacity without a significant reduction in its gravimetric H_2 storage capacity?
- Does the electrospinning of PAN-based and/or PIM-1 nanofibers with MOFs improve the H_2 capacity of the composite compared to the MOF powder?
- Does the incorporation of GF into UiO-66 show improved thermal conductivity compared to pristine UiO-66?

1.4. Aim and Objectives

The study aimed to fabricate a MOF-based material that could possibly attain tailored properties suitable for H_2 storage applications using predetermined synthesis and shaping techniques. Using the US DOE system targets for H_2 storage, the performance of the envisaged MOF-based material was set at possibly achieving gravimetric and volumetric H_2 capacities in excess of 4.5 wt% and 30 $g{\cdot}L^{-1}$ respectively.

The specific objectives of the study were as follows:

- To fabricate UiO-66 by pelletization at a possibly unprecedented applied pressure (> 500 MPa), which is much higher than previously reported for UiO-66, at which the UiO-66 crystals could be densified to achieve packing densities in excess of 1.0 $g{\cdot}mL^{-1}$ without significant compromise to their intrinsic textural properties (surface area and pore volume).
- To improve the volumetric H_2 capacity of UiO-66 using the pelletization method.
- To investigate the effect of high-pressure compaction on fully hydroxylated UiO-66 as well as partially dehydroxylated and fully dehydroxylated UiO-66 particularly as it relates to H_2 storage applications.
- To fabricate MIL-101 (Cr) by pelletization and elucidate the effects of compaction as it relates to its textural properties and hydrogen storage capacity
- To evaluate the gravimetric and volumetric hydrogen storage capacities of the fabricated UiO-66 and MIL-101 materials
- To fabricate core-shell MOF/polymer nanofiber composites using the coaxial electrospinning technique and possibly improve the MOF loading onto the nanofibers via selective removal of the polymeric material in the core region of the nanofiber composite.
- To compare the H_2 uptake of MOF/polymer nanofibers to that of the porous polymer PIM-1 nanofibers and select the best performing nanofibers to be used as possible polymer-based binders in the pelletization of UiO-66.
- To prepare GF using the chemical vapour deposition (CVD) method employing nickel foam (NF) as a template.
- To determine the degree of improvement of the thermal conductivity of a selected MOF (UiO-66 or MIL-101 (Cr)) through the addition of 10 wt% GF.

- To prepare a shaped MOF-based composite material with possibly improved gravimetric H_2 capacity, volumetric H_2 capacity, and thermal conductivity, compared to the pristine powder.

1.5. Hypotheses

- Theoretical studies have previously shown that UiO-66 has a minimum shear modulus of about 13.7 GPa, which is amongst the highest in MOFs (Wu, Yildirim and Zhou, 2013). This study hypothesized that the pelletization of UiO-66 powder at ~700 MPa (~100 000 psi) does not compromise the surface area and pore volume, and hence the gravimetric H_2 storage capacity and volumetric H_2 storage capacity.
- MOFs have been successfully incorporated into polymer nanofibers and also shown to be fully accessible to H_2 within the nanofibers [47,59,83]. This study further hypothesized that the preparation of core-shell MOF@ nanofiber composite could facilitate the improvement of the percentage MOF loading within the nanofiber via the selective removal of the core polymer. This could improve the H_2 adsorption of the MOF/polymer nanofiber composite.

1.6. Research Approach

The study was primarily conducted at the HySA Infrastructure laboratories within the Council for Scientific and Industrial Research (CSIR), Pretoria campus. Since the study was funded by the RS-DFID grant, it was also a requirement that part of the research be carried out in conjunction with the University of Nottingham in a series of student research visits to Nottingham.

The following sections give an overview of the experimental research approaches employed during the study as it pertained to the selected fabrication techniques, pelletization and electrospinning.

1.6.1. Synthesis of UiO-66 and MIL-101(Cr) under solvothermal conditions

The aims and objectives of this study were based on the use of predetermined MOFs, namely UiO-66 and MIL-101(Cr). These are well-defined MOFs that have been fully characterised according to their single crystal structures [84,85]. There have been various reported synthesis

approaches employed in their preparation, including solvent-free synthesis [86], using waste polyethylene terephthalate (PET) as a precursor [87–89], and the most common solvothermal synthesis method [90–94]. The successes of the solvent-free and PET-based synthesis methods have been well-documented, however, their use is mainly focused in studies concerning unconventional methods and approaches towards green synthesis chemistry of MOFs. The aim to achieve high-performance MOFs for H_2 storage applications has been mainly achieved through the use of solvothermal synthesis. The conditions in solvothermal synthesis have been shown to influence the achievable properties of the MOF such that the properties can be tailored according to the synthesis conditions employed [93,95–97]. For example in acid-modulated solvothermal synthesis of UiO-66, it was shown that the acid strength, molar equivalents of the acid relative to the Zr precursor, and the type of solvent, promoted the formation of UiO-66 crystals with surface areas ranging from 500 to ~1500 $m^{2}{\cdot}g^{-1}$ [98]. These observations were also shown in studies of MIL-101(Cr) whereby an increase in the molar equivalents of a monocarboxylic acid were found to improve the surface area by at least 15% (Ren *et al.*, 2014). This study, therefore, adopted the synthesis procedures previously reported by Ren et al. (Ren *et al.*, 2014) who demonstrated a possible optimization procedure for the synthesis of UiO-66 and MIL-101(Cr) using formic acid at 100 molar equivalents as a modulator and dimethylformamide (DMF) as the solvent.

1.6.2. Pelletization of pristine MOFs, UiO-66 and MIL-101(Cr)

In general, it is most common that the packing/bulk and crystal densities of MOF powders are lower than 1 $g{\cdot}mL^{-1}$, owing to their highly porous structures and high to ultrahigh surface areas [50,100]. The application of pressure onto MOF powders has also been shown to have negative effects on their textural properties due to the occurrence of possible pressure-induced structural changes such as pore widening, amorphisation, and solid-solid phase transitions [71,101–103]. In this study, the first part to the pelletization approach included a screening experiment whereby the effect of the applied pressure on the structure of the MOF was monitored by Powder X-ray Diffraction (PXRD) analysis. In nanostructured and polycrystalline materials, PXRD analysis can be used to determine the bulk properties of the material. The effects of pressure can be typically monitored through observing possible shifting in the diffraction patterns as these pressure-related shifts signify the introduction of stress or strain onto the crystals [104]. Also possible changes to peak intensities of the crystal phases can be monitored. The diminishing or reduction of relative peak intensities could show changes to individual

phases of the crystals. The diminishing of the peak intensities of the entire diffraction pattern generally signifies an onset of amorphisation process and in extreme cases the complete disappearance of peaks, such that they are indistinguishable from the background noise signal, signifies complete amorphisation of the material [86,105]. In the second part, the study investigated the pelletization of UiO-66 under different activation temperatures beginning from 80 to 320 ^{o}C, at 30 ^{o}C increasing intervals. This was aimed to address an important factor in the chemistry of UiO-66, which is the effect of pelletization on dehydroxylated UiO-66 forms. This is because, under solvothermal conditions, UiO-66 is typically synthesized in a hydroxylated form consisting of $Zr_6O_4(OH)_4$ inorganic nodes/clusters [84,98,106]. The thermal treatment of the hydroxylated form has been shown to yield a dehydroxylated form around 300 ^{o}C, which consists of Zr_6O_6 inorganic nodes. This "dehydroxylation" process has been shown to occur in simulation and experimental studies [107][108], but the influence of applied pressure on dehydroxylated UiO-66 has yet to be shown experimentally. This study investigated the effect of pressure on dehydroxylated UiO-66 by pelletizing hydroxylated and dehydroxylated forms of UiO-66 at ~700 MPa. The occurrence of the dehydroxylation process was investigated by thermogravimetric analysis (TGA) coupled to mass spectroscopy (MS) analysis and PXRD analysis was used to elucidate the effect of pelletization on the crystal structures of the hydroxylated and dehydroxylated UiO-66 forms.

1.6.3. Preparation of MOF/polymer nanofibers via electrospinning

The preparation of MOF/polymer nanofibers was based on continued work carried out at the HySA Infrastructure group where it was previously shown that a polyacrylonitrile (PAN) solution in DMF could be impregnated with MOF powders and successfully electrospun using a single-nozzle electrospinning setup [57]. The MOF/PAN nanofibers were shown to adsorb H_2 but could only achieve H_2 adsorption capacities no greater than 80% of the H_2 adsorption capacities achieved in the pristine MOF powder. The H_2 adsorption capacity of MOF/PAN nanofiber composites was shown to be directly influenced by the amount of MOF loaded onto the nanofibers, limited to about 20 wt%, and also it was shown that the PAN surface could be modified to have pores. In this study, the improvement of the MOF loading beyond 20 wt%, and possibly improvement of the H_2 adsorption capacities of MOF/PAN nanofibers, was proposed to be achievable through the use of a coaxial electrospinning setup, instead of the single-nozzle electrospinning used in the previous studies. This study investigated the electrospinning of other polymers such as polymethylmethacrylate (PMMA) and polystyrene

(PS) which shared similar properties to PAN suitable for electrospinning, such as high electrical conductivity and high solubility in DMF. The PMMA and PS could, therefore, be co-electrospun with PAN in order to produce core-shell X@PAN (X = PMMA or PS) nanofibers which could also be impregnated with the selected MOFs, UiO-66 and MIL-101(Cr). The polymers PAN, PMMA, and PS have different solubilities in acetone and chloroform. The PAN polymer tends to be virtually insoluble in acetone and chloroform under ambient conditions (25 ^{o}C and 1 bar) but PMMA and PS show rapid solubility in acetone and chloroform respectively, under the same conditions. This provided a method to possibly remove PMMA and PS selectively from a MOF/X@PAN nanofiber composite and possibly leave behind intact MOF/PAN nanofibers with improved MOF loading. For example a MOF/X@PAN composite consisting of 20 wt% MOF in X and 20 wt% in PAN could result in a 40 wt% MOF/PAN composite after removal of the core polymer, possibly improving the H_2 adsorption of the MOF/PAN composite to above 80% of the pristine MOF. An alternative to using PAN-based nanofibers explored in this study was the electrospinning of a porous polymer PIM-1 which consists of permanent micropores (2 Å ≤ pore size ≤ 20 Å) [15,109–112]. PIM-1 nanofibers have been mostly electrospun and used as precursors to produce porous carbon nanofibers through pyrolysis [113]. The electrospinning process of PIM-1 also uses a corrosive and toxic solvent, tetrachloroethane (TCE).

1.6.4. Co-pelletization of UiO-66 with polymeric nanofibers for H_2 storage applications

The method of co-pelletization was used to incorporate polymer-based binders into UiO-66 in order to form alternating layers of UiO-66 and polymer binders. This was a new method for incorporating polymer binders into MOFs and could potentially impart properties not observed on the pristine MOF and nanofibers. The UiO-66/nanofiber composites included the co-pelletization of UiO-66 with 5 wt% PIM-1 and core-shell MOF/X@PAN nanofibers (X = PMMA or PS) as polymeric binders. Another focal point was the attempt to improve the thermal conductivity of UiO-66 which was proposed through the incorporation of 10 wt% graphene foam (GF) as a potential high thermal conductivity carbon source. The surface area, pore volume, thermal conductivity, and gravimetric H_2 capacities of the co-pelletized UiO-66 composites were measured and compared to those of pristine UiO-66 powder and pellet forms.

1.7. Scope and delimitations of the study

The selected MOFs UiO-66 and MIL-101(Cr) were based on continued studies carried out by the HySA Infrastructure group as these were identified to show good moisture stability, limiting their storage under inert conditions, and high surface areas of ~2000 $m^2 \cdot g^{-1}$ in MIL-101(Cr) and ~3000 $m^2 \cdot g^{-1}$ in a MIL-101@UiO-66 composite. The theoretical robustness of UiO-66 towards pressure was envisaged as a property that would possibly show resistance to applied pelletization pressures above 500 MPa and result in packing densities greater than 1 $g \cdot mL^{-1}$. Additionally the use of Cr- and Zr-based MOFs also fitted the vision and strategy of the CSIR at large under the theme of using locally available metals and/or minerals for possible industrialisation in future. The electrospinning of PAN-based composite nanofibers was also based on continued work previously conducted by the HySA Infrastructure group. The optimization of the PAN electrospinning process was shown by Annamalai et al. [57] and the process parameters used in this study were largely based on the latter work with minor modifications. The experiments in this study were all done at laboratory-scale with product yields of as-synthesized UiO-66 not exceeding 5 g per batch and that of MIL-101(Cr) not exceeding 2 g per batch. The use of a multiple batch system was in part limited by the availability of a 150 mL high pressure reactor for the synthesis of MOFs. The analytical techniques available at the HySA Infrastructure labs (including the CSIR campus) and the University of Nottingham could be used to carry out crystallographic analysis, microstructural imaging, thermal analysis, and gas adsorption measurements. In particular, H_2 adsorption measurements could be obtained up to 100 bar at cryogenic (-196 ^oC) and ambient (25 ^oC) temperature, using a specialized Intelligent Hiden Isochema gravimetric analyser available at the University of Nottingham. The measurement of H_2 capacities at 100 bar was a key aspect of this study as it could allow for the comparison of the observed gravimetric and volumetric H_2 capacities of the selected MOFs to the US DOE targets and other benchmarks for MOFs investigated globally. It was acknowledged that MOFs also have been reported to show favourable gas adsorption properties suitable towards their application in carbon dioxide (CO_2) capture and methane (CH_4) storage. This study however, exclusively investigated the fabrication of MOF properties as they would be suited for H_2 storage and makes no mention of CO_2 and/or CH_4 storage.

1.8. Thesis chapter structure

This thesis opens with Chapter one which introduces the topic of the research and gives a brief description of currently available state-of-the-art used in H_2 storage. The chapter further highlights the rationale behind the study and the knowledge gap, motivation, objectives, and research questions the study aimed to answer. The study design is presented to briefly guide the reader to the experimental procedures used during the study. Lastly the scope of the study is presented together with the delimitations that it was carried out under for the given duration. Chapter two gives a detailed discussion of the previous work done on H_2 storage using porous solid-state materials such as ZTCs, MOFs, polymers, and carbons. In the chapter, a detailed description of the physisorption mechanism is also given to highlight the properties of adsorbent materials that influence the physical adsorption of gases such as H_2. The chapter also discusses the effect of the application of pressure through pelletization of nanostructured and porous materials as one of the main fabrication strategies in this study. Finally the chapter covers the electrospinning process as it specifically pertains to the incorporation of MOFs and the implication of the MOF/polymer nanofiber composites in gas adsorption studies. Chapter three gives details of the experimental procedures used to prepare materials and analytical methods used for the characterisation of the properties of the selected materials. Chapter four presents the first set of results on the pristine MOF materials, with emphasis on the effect of pelletization on their textural properties (surface area and pore volume) and H_2 adsorption capacities. Chapter five gives the results of the electrospun MOF/polymer nanofiber composites, mostly focusing on the imaging of the nanofibers prepared by single-nozzle electrospinning compared to those prepared by coaxial electrospinning. The imaging was an integral part of the electrospinning strategy especially to monitor the distribution of MOF crystals within the nanofibers. The chapter also gives a detailed discussion of the textural properties and H_2 adsorption capacities obtained for the different MOF/polymer nanofiber composites. Chapter six presents the thermal conductivity, textural properties, and H_2 adsorption capacity results of pristine UiO-66 in comparison a GF/UiO-66 composite. In addition, the chapter also reports on a new method involving the co-pelletization of UiO-66 with electrospun PIM-1 and core-shell MOF/X@PAN nanofibers (X = PMMA or PS) to produce UiO-66/nanofiber composites with alternating UiO-66 to nanofiber layers. The textural properties and H_2 adsorption behaviour of the co-pelletized UiO-66/nanofiber composites were compared to those observed for pristine UiO-66 pellets. Finally Chapter seven presents the conclusions that can be drawn from the study in comparison to previously reported

studies and makes recommendations based on the results obtained in this study that should be addressed in future research.

1.9. Chapter summary

This chapter briefly introduced the envisaged H_2 economy as one of the industrially viable renewable and sustainable alternatives towards the reduction of carbon emissions. The chapter discussed in detail how the use of solid-state porous materials could be used in conjunction with high-pressure cylinders to achieve industrial targets for H_2 storage in vehicular applications. The necessity to shape the loose powders of solid-state porous materials was highlighted as a key aspect in order to tailor properties suitable for application into storage systems. There are two strategies that were proposed for this study, namely pelletization and electrospinning, as these have been successfully employed in previous H_2 storage studies. The compromise of the textural properties in pelletized and/or electrospun porous materials was identified as a knowledge gap and provided a key motivation for the study. The chapter also highlighted how the volumetric H_2 capacity could be improved using the pelletization method through the improvement of the packing density. The chapter closes off with a brief description of the experimental procedures such as the use of PXRD analysis in establishing the highest applied pressure that would not compromise the structure of the MOF. The effect of the activation temperature on UiO-66 crystals was also described to gain information about the effect of pelletization on hydroxylated and dehydroxylated forms of UiO-66. The scope and limitations of the study are clearly described and importantly points out that the H_2 adsorption measurements would be conducted up to a pressure of 100 bar, both at -196 ^oC (77 K) and 25 ^oC (298 K), conditions that could be comparable to global standard in H_2 storage research.

Chapter 2

2. Literature review

2.1. Background

This study was conducted with the main focus on the shaping of solid-state porous materials such as metal-organic frameworks (MOFs), porous polymers, and carbons in order to impart application-specific properties for H_2 storage applications. This chapter, therefore, gives a detailed outline of the literature review as it pertains specifically to H_2 storage onto porous materials via physisorption and the principles involved in two shaping/fabrication techniques, namely pelletization and electrospinning, and their applications in shaping of porous materials envisaged for H_2 storage.

Both experimental and theoretical research has been undertaken to determine the hydrogen storage potential of many of these systems [36,114–116], though theoretical research has been limited due to the difficulty of modelling the dispersion interactions using first principle ab initio calculations. In some initial studies, as in the case of above mentioned work, experimental errors such as little amount of sample and/or the use of both non-purified samples and gas has led to a high dispersion and low reproducibility of storage values in some carbon systems [117]. Today, these issues are less prevalent and a greater understanding exists on the real potential of these carbon stores. The literature review presented in this thesis aims to provide detailed information on H_2 storage based on the concept of physisorption in order to support and substantiate the experimental results as presented in chapters 4 to 6. Due to the use of different types of materials ranging from polymers, carbons, and porous crystals known as metal-organic frameworks, the literature review begins with a general introduction of the concepts involved in gas adsorption onto different solid-state materials, with particular focus in H_2 gas adsorption.

The chemistry behind the storage of H_2 onto solid-state porous materials is governed by the mechanism of physical adsorption (physisorption). Molecules have the ability to attach to solid surfaces via weak interactions such as van der Waals forces, and/or London dispersion forces [118]. These forces occur via close-range attractions caused by permanent or induced dipole moments amongst the electron clouds of neutral molecules. The strength of the interactions is influenced by the electron density of the surface (adsorbent) and adsorbate molecules, meaning

the greater the electron densities, the stronger the interactions. The problem with H_2 is that it is the lightest molecule and contains the fewest amount of electrons amongst all molecules. Due to the low electron density it is typical that H_2 would adsorb weaker in comparison to a gas such as methane (CH_4) on a particular adsorbent material as demonstrated in Fig. 2.1. As a result, the isosteric H_2 enthalpy of adsorption on many non-porous surfaces do not exceed 4 $kJ{\cdot}mol^{-1}$, such as evidenced in graphitic carbons [76,117].

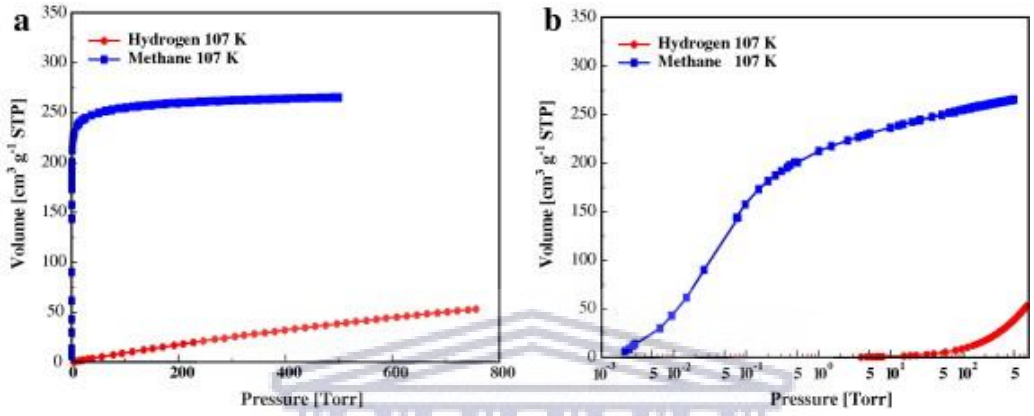

Figure 2.1: Comparison of the adsorption of methane and hydrogen at 107 K [119]. *(Image reused with permission from Elsevier).*

The effect of temperature generally plays a key role on the adsorption behaviour of gas molecules onto a solid surface. Although it has its limitations, the universal gas law provides a good estimation of the behaviour of gases under the influence of temperature, pressure, and quantity of gas in a system. For all gases, the gas law predicts the critical temperature-pressure conditions for which gas molecules may co-exist with their liquid/condensed phase. Beyond a critical temperature, the coexistence of vapour/liquid phases cannot be satisfied by the application of pressure alone. In relation to gas physisorption, the interactions of gas molecules with an adsorbent surface are further enhanced as the temperature is decreased, with the greater interactions enhanced towards the critical temperature of the gas [20,120]. At the critical temperature, there exist an opportunity for the adsorption of gas molecules in their liquid form, further improving the quantity of gas adsorbed and also representing equilibrium conditions for gas adsorption. The type of porosity in porous solid-state materials has also been shown to influence the adsorption behaviour of gas molecules. In order to better understand the influence of pores on gas adsorption, it is important to initially describe the basic components of a solid surface that promote physisorption of molecules.

2.1. Concept of physisorption of gases in porous materials

The surface of a solid particle can be made up of four basic regions to which an approaching adsorbate molecule or "probe" can make contact with the adsorbent surface (Fig. 2.2), namely: (1) **van der Waals surface** – represents the atomic scale region that is made up of the van der Waals spheres of the atoms on the surface; (2) **Connolly surface** – region just outside the van der Waals spheres of the of the adsorbent surface but accessible to the adsorbate molecules; (3) **Probe-accessible surface** – represents the region accessible to the probe sphere as it moves along the van der Waals surface; and (4) **r-distance surface** – represents the region that is positioned at a radius "r" from the Connolly surface [39]. These regions represent the fundamental areas of a solid material that govern the mechanism of physisorption. In porous materials there is additional considerations in that further divisions of the solid surface are applicable. In addition to the above-mentioned regions, a porous material also consists of an internal surface and an external surface. In general, the internal surface refers to the surface within all the pore walls and the external surface refers to the surface outside the pores. Highly porous materials are typically represented by low external surface areas, however, the accessibility of the internal surface area is dependent on the shape and size of the adsorbate molecules, and effectively the determination of the internal surface area and pore volume of the adsorbent is also dependent on the shape and size of its pores.

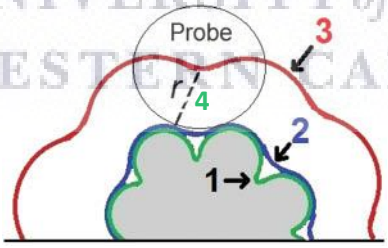

Figure 2.2: Schematic representation of a typical porous solid surface [39]. *(Image reused with permission from © IUPAC, De Gruyter, 2015).*

Based on the classification of the International Union of Pure and Applied Chemistry (IUPAC) [39], pores can divided into three basic types: (i) micropores (2 Å < pore diameter < 20 Å); (ii) mesopores (20 < pore diameter < 500 Å); and (iii) macropores (pore diameter > 500 Å). The type of pores within an adsorbent material can influence the gas adsorption behaviour giving rise to distinctive adsorption isotherms representative of the type of porosity present in a given

adsorbent. An adsorption isotherm can be described as the relationship between the amount of adsorbed gas, under isothermal conditions, and the equilibrium pressure of the gas. There are different types of adsorption isotherms under the IUPAC classification criteria [118](Groen, Peffer and Perez-Ramirez, 2003) and these are depicted in Fig. 2.3. The type of isotherm can reveal information about the pore structure of an adsorbent. The isotherms shown in Fig. 2.3 are a representation for a typical analysis carried out below the critical temperature of the gas, e.g. 77 K for N_2 adsorption/desorption isotherms, since the relative pressure (p/p_o) is used to compute the gas pressure. The relative pressure is the ratio of the equilibrium pressure (p) to the vapour pressure (p_o) of the gas. At temperatures below the critical temperature there exist the possibility for liquefaction, and hence pore filling or condensation, the isotherms obtained under such condition can fully describe the potential gas adsorption behaviour that can be exhibited by a solid-state porous material. There are six main adsorption/desorption isotherms defined under the IUPAC classification system. The Type I isotherms are characterized by a very high adsorption at very low relative pressure followed by a plateau up to $p/p_o = 1$. This type of gas behaviour is typical in highly microporous solids and distinction between Type I(a) and Type I(b) isotherms is that the former is mostly observed in microporous solids with pore sizes less than 10 Å, whereas the latter is normally depicted in microporous solids showing wider micropores or narrow mesopores (pore size ≈ 25 Å). The height of the plateau generally represents the monolayer capacity, which defines the amount of adsorbed gas molecules that covers the entire surface of the adsorbent with a single molecular layer. In Type II isotherms, the monolayer coverage (point "B") is generally small and followed by an increasing adsorption up to saturation. This is typical in non-porous or macroporous solids with the gradual increase in adsorption, at increasing p/p_o, promoted by an overlapping formation of mono- and multilayers of gas molecules. The Type III and Type V isotherms share a common feature in that both show no monolayer coverage, with the adsorption at high p/p_o resulting from adsorption onto favourable sites on the adsorbent. The absence of monolayer coverage shows very weak adsorbate-adsorbent interactions and such behaviour is most common in non-porous or macroporous solids. The difference of Type V to Type III isotherms is the possible condensation within the pores of the adsorbent which is represented by the presence of the hysteresis loop. The Type IV isotherms represent a two-step adsorption behaviour due to adsorbate-adsorbent interactions at low p/p_o, followed by interactions of the adsorbate with a condensed phase, leading to the formation of multilayers with increasing p/p_o. The difference to Type II isotherms is that the Type IV isotherms reach a limited adsorbed multilayer at the saturation pressure ($p/p_o = 1$). Type IV isotherms are typical in mesoporous solids and the

distinction between Type IV(a) and Type IV(b) isotherms is the size of the mesopores. Type IV(a) occurs when the mesopore size is larger than a certain critical pore size (~40 Å), leading to the appearance of the hysteresis loop. Type IV(b) isotherms are fully reversible and typically occur for mesoporous solids with narrower mesopores. Lastly, Type VI isotherms are characterized by a clear multi-step adsorption behaviour which signifies layer-by-layer formation between adsorbed adsorbate molecules. The height of a step is representative of its capacity and this type of adsorption/desorption behaviour is typical for highly uniform nonporous solids [39]. Gas adsorption isotherms may not be fully reversible due to the possibility of hysteresis occurring in the desorption isotherm.

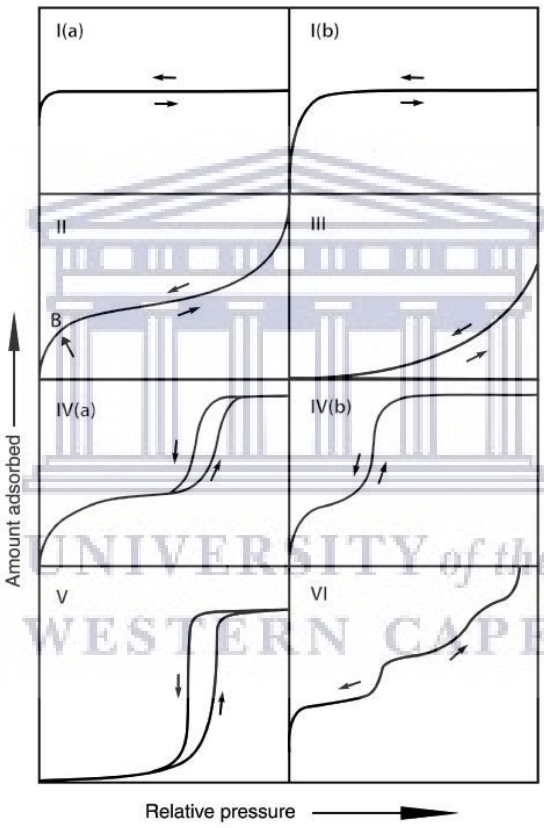

Figure 2.3: Schematic representation of the classification of the different types of adsorption isotherms [39]. *(Image reused with permission from © IUPAC, De Gruyter, 2015).*

Hysteresis can be described as the gap or delay between the equilibrium desorption and adsorption pressures due to molecules desorbing at lower pressures compared to adsorption pressures. Hysteresis is common for meso- and macroporous adsorbents, or adsorbents that promote multilayer adsorption where capillary condensation within pores is possible. Capillary

condensation results from strong interactions of molecules in multilayers within opposing pore walls. The interaction increases with the accumulation of the molecules to a point where the molecules may assume a lower thermodynamic energy state. This causes the desorption of these molecules from within the pores requiring larger pressure gradients in comparison to monolayer molecules, resulting in hysteresis. Hysteresis may also be affected by the temperature since temperatures above the critical temperature of the gas may not promote multilayer adsorption of molecules [39,66,94,118,122].

Hysteresis loops can be differentiated using the IUPAC classification system and give valuable information about the pore structure of an adsorbent. There are five main loop configurations, namely Type H1, H2, H3, H4 and H5. The near vertical Type H1 loops is normally observed for adsorbents with a very narrow and uniform mesopore size distribution. Type H2 loops are a common feature of highly disordered mesopore structures which contain mesopores of different shapes and sizes. The varying mesopores may form an interconnected network containing narrow connecting paths between neighbouring pores and to the bulk gas phase, known as ink-bottle pores. This means that in ink-bottle pores evaporation of molecules into the bulk gas phase may be delayed by the presence of condensate in a neighbouring pore and this pore blocking effect results in evaporation to occur at lower pressure giving rise to the characteristic Type H2 loop configuration. The difference between Type H2(a) and Type H2(b) is that in the latter, the evaporation originates from ink-bottle pores with much wider widths in comparison to those that cause Type H2(a) loops. Type H3 loops are similar to Type H2 loops as they also arise from an interconnected network pore structure, however, in this case the pore network may contain a large degree of macropores that are not completely filled with condensate. Type H4 loop is similar to Type H3 but distinguishable with the adsorption isotherm which shows a combination of Type I and Type II behaviour. Type H5 loops are very rare and may be associated with pore structures that exhibit partial pore-blocking effects together with open pore structures. Since this study focuses on the possible use of porous solid-state materials in H_2 storage applications, it is important to link the aforementioned properties of porous materials to the adsorption behaviour of H_2 via physisorption [118][39].

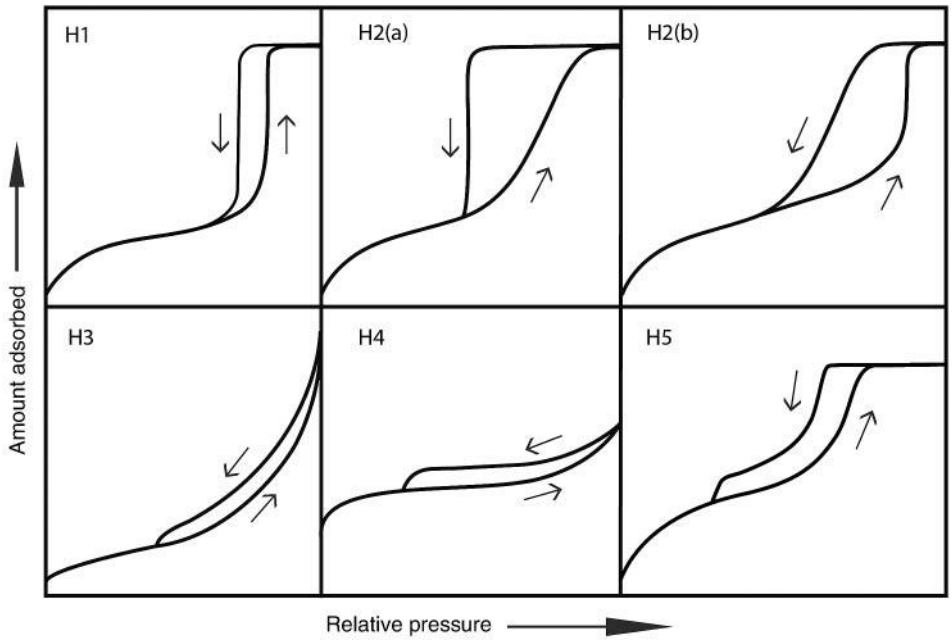

Figure 2.4: Schematic representation of the different types of hysteresis loops [39]. *(Image reused with permission from © IUPAC, De Gruyter, 2015).*

2.2. Factors that influence adsorption of H_2 in porous solids

2.2.1. Pore structure of adsorbent material

The surface properties of porous solid-state materials is important for H_2 storage applications. Studies [15,100] have shown that the amount of H_2 adsorbed in porous materials may be strongly influenced by the BET surface area and the pore structure of the material, which includes the pore volume, pore size distribution, as well as pore shape, regardless of other contributing factors such as polarisibility of the H_2 molecule. The influence of the BET surface area and micropore volume is reported to be more prevalent under cryogenic conditions such as at 77 K. In the experimental work conducted by Gogotsi et al. [123], it was shown through a series of porous carbons that were derived from carbide molecules, that at 77 K, the pores containing pore widths of 6 – 7 Å provided the highest gravimetric H_2 capacities per unit surface area both at standard pressure and elevated pressures. The general conclusion from the study was that pores larger than ~15 Å would contribute little to the gravimetric H_2 capacity. The study also highlighted that the effect of pore size was effectively more prominent in comparison to the effect of surface chemistry on the gravimetric H_2 capacity of the carbons.

Since H_2 storage systems are envisaged to operate at near ambient conditions as possible, the properties of porous materials at 298 K must be considered. The studies by Beneyto and co-workers [123] reported that at 298 K, the gravimetric H_2 capacity was dependent on both the micropore volume and the micropore size distribution. These findings highlighted the importance of the pore structure of a candidate adsorbent for H_2 storage applications. In moving towards system integration, it is however noted that highly microporous materials present an operational challenge. The proposed working pressure conditions for a H_2 system currently sits at working pressure of 5 bar (0.5 MPa), meaning that the working/deliverable H_2 capacity should be highest at pressures above 5 bar since H_2 stored below 5 bar would be inaccessible for utilization. The strong interaction of H_2 molecules and pore filling within very narrow pores (pore size < 7 Å) promotes very high H_2 adsorption at relatively low pressures and lead to Type I adsorption isotherms at cryogenic temperatures (77 K).

2.2.2. Isosteric heat of adsorption

The isosteric heat of adsorption represents the magnitude of the interaction strength between H_2 gas molecules and the surface of the adsorbent material. The isosteric heat of adsorption can be improved by the nanoconfinement of metal ions in porous solids and polymers [44,124], through the engineering of open/active metal sites and compositing with platinum (Pt) or palladium (Pd) to promote the dissociation of H_2 and adsorption of elemental hydrogen via the spill-over mechanism [15,16,28,40,97,115].

The type of porous solid materials that have shown great promise for H_2 storage applications through physisorption is a class of organometallic complexes known as metal-organic frameworks (MOFs). Their structures are highly tuneable, in comparison to other traditional porous inorganic solids such as zeolites, to attain high to ultra-high surface areas and large pore volumes that can range from highly microporous, mesoporous, or the creation of hierarchical porosities [63,125]. A detailed discussion of MOFs with particular focus on their application in H_2 storage is given in section 2.3.

2.3. Metal organic frameworks (MOFs)

Metal-organic frameworks (MOFs) form a relatively novel class of crystalline supramolecular porous materials that are typically made up of metal cations or clusters that are coordinated to organic anionic ligands (linkers) forming a 3-dimensional (3D) network structure with a permanently porous internal structure [63,125]. The 3D structure of MOFs typically contains polyhedrons via metal-ligand coordination that may consist of non-covalent interactions such as hydrogen bonds and π-π bridging interactions [126]. The development of MOFs can possibly be tracked back to the late 1950s to early 1960s from the synthesis of supramolecular crystals made up of metal-ligand coordination complexes. The internal pore structure of these types of complexes were found to act as 'hosts' for foreign or guest molecules that were small enough to fit into the internal volume and as a result could be used in sensor, separation, and storage applications [127–130]. There were challenges in the early developments of MOFs as MOF structures that were devoid of solvent molecules and stable after solvent removal were difficult to obtain, making them their industrial viability negligible in comparison to other porous solid such as zeolites. One of the first 'open' MOF structures to be prepared was reported by Li et al. [131] who successfully synthesized the zinc carboxylate MOF, MOF-5, that showed high stability after post-synthesis evacuation, as the internal pore structure was maintained after removal of solvent molecules from its pores. This breakthrough was key in the potential industrial application of MOFs in applications such as catalysis, gas separation and storage and increased the development of more stable MOFs with different crystal geometries and porosities. The key factor to the synthesis of a stable, degassed MOF-5 structure was proposed to be the choice of organic ligand, i.e. dicarboxylate linker, due to the high degree of rigidity offered by the linker. The properties of MOFs and their potential industrial applications in catalysis, gas storage, and sensor technologies can, therefore, be influenced by the type of metal ion and organic linker of choice used during their synthesis [92,132,133].

2.3.1. Synthesis of MOFs

The typical and most common synthesis technique used in the preparation of MOFs is epitaxial growth of MOF crystals under high pressure solvothermal conditions. This synthesis method generally involves heating a mixture of the metal ion precursor (typically a metal salt) and organic ligand dissolved in a solvent and heated in a tightly sealed reactor at temperatures above the boiling point of the solvent of choice [94,134–137].

2.3.1.1. Unconventional methods for MOFs synthesis

In recent times, however, solvent-free mechanochemical MOF synthesis methods have been successfully employed in the synthesis of MOFs such as zirconium-based MOFs, UiO-66 and UiO-66-NH_2 [138]. In addition, attempts have been made towards the synthesis of MOFs using relatively simple and inexpensive synthesis methods. Some of the more documented synthesis procedures include microwave-assisted methods [139,140], mechanochemical or solvent-free routes [141], and the use of organic linkers derived from waste materials, such as the extensively used MOF precursor, terephthalic acid (H_2BDC), that can be derived from waste polyethylene terephthalate (PET) to synthesise zirconium-based MOF (UiO-66) and chromium-MOFs (MIL-101 and MIL-53) [87–89,142].

2.3.1.2. Types of linkers in MOF synthesis

The organic ligands suited for MOF synthesis are typically organic acids that contain multiple functional groups. Some of the most commonly used organic linkers include carboxylates, phosphonates, imidazole, and sulfonates [143]. The carboxylate organic linkers have been reported to produce MOFs that are stable to moisture, high thermal stability, and mechanically stable zirconium-based MOFs [74,99,144–146]. One of the reasoning behind the choice of MIL-101(Cr) and UiO-66 in this study was based on the exceptional moisture stabilities and potential high mechanical strength of the two MOFs [9]. The chemistry of carboxylate organic linkers was therefore of particular interest in this study. For example,some metal carboxylate MOFs can share the same chemical composition but show different crystal geometries due to crystal-to-crystal solid-state transitions that may occur during epitaxial. For example in the synthesis of chromium (III) terephthalate MOF there exists two possible polymorphic forms (MIL-101(Cr) and MIL-53(Cr)) during the crystal growth under high pressure solvothermal conditions [90]. The MIL-101(Cr) product forms fast with typical octahedral crystals typically not exceeding 300 - 400 nm, however, under prolonged crystal growth, a more stable MIL-53(Cr) product may also form which is characterized by needle-like crystal morphology with multiple faces. Both the MIL-101(Cr) and MIL-53(Cr) have the same chemical composition and typically give rise to similar compositional spectra such as infrared (IR) and X-ray fluorescence (XRF), but they do have distinctly different surface areas and pore volumes The MIL-101(Cr) has a highly mesoporous structure and average surface areas around 3000 $m^{2}{\cdot}g^{-1}$ and MIL-53(Cr) is more microporous with average surface areas around 1000 $m^{2}{\cdot}g^{-1}$ [147].

The MIL-153(Cr) structure is also more flexible in comparison to MIL-101(Cr) as it has been reported to undergo adsorption-induced structural changes, particularly during CO_2 adsorption [71]. It is, therefore, important to control and optimize the process parameters, especially the synthesis time during MIL-101(Cr) synthesis and preferably prevent the formation of MIL-53(Cr) so as to obtain high surface areas as required for H_2 storage applications.

Another factor in carboxylate linkers is that the length of the organic linker plays a key role in controlling the pore diameters within a MOF. It is generally found that longer chain dicarboxylates, such as observed in isoreticular MOF (IRMOF) series shown in Fig. 2.5, can increase pore diameters which may impart differing gas adsorption isotherm behaviours.

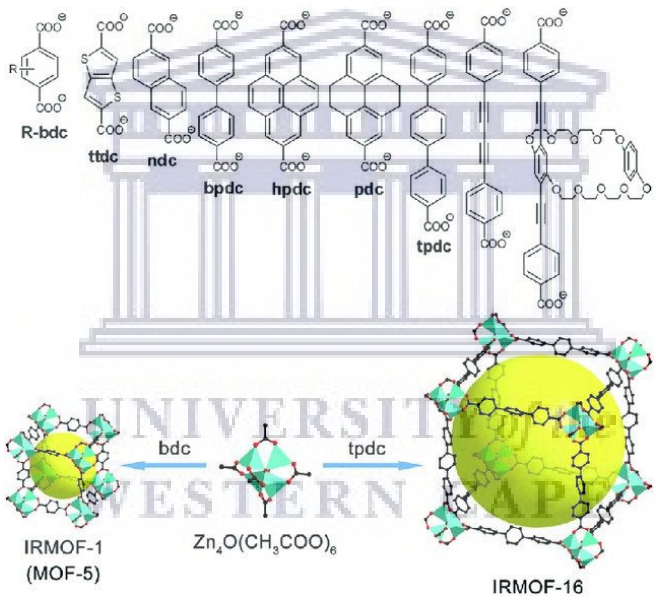

Figure 2.5: Representation of a series of dicarboxylate organic linkers and the effect of linker chain length on the pore size of the MOF. Colour scheme: Zn (turquoise polyhedral); O (red); C (black); free volume (yellow). (Image reused with permission from © The Royal Society of Chemistry 2014).

2.3.2. Post-synthesis activation of MOFs

In MOFs synthesized under solvothermal conditions, it is typically found that solvent molecules remain within the pores of the as-synthesized MOF product. In order to use the MOF for H_2 adsorption applications, it is necessary to remove the solvent molecules so as to obtain a stable MOF with fully accessible pores to facilitate the adsorption of the H_2 gas molecules.

The process of solvent removal from the MOF pores is known as 'activation'. This is an important step during MOF production as it has been observed in some instances that certain MOFs, such as may undergo incomplete solvent removal or the extreme case of pore collapse upon their activation [10,24,94,148]. The selection of an activation method that does not compromise the structure and accessibility of pores within the MOF is therefore an important step in post-synthesis treatment of MOFs since the fully activated MOF structure would reach its theoretical Brunauer-Emmett-Teller (BET) surface area. Poorly activated MOFs may be characterized by significantly low BET surface areas in comparison to their theoretical values [149]. There are two methods mainly used in the activation of MOFs: (1) heating at a specified temperature, based on the thermogravimetric behaviour of the as-synthesized MOF, under vacuum; (2) exchange of solvent molecules with a more volatile solvent, i.e. one that has a lower boiling point than the solvent used for MOF synthesis, followed by heat evacuation or drying at room temperature under vacuum. The type of exchange solvent may also play a key role in either obtaining a fully or partially evacuated MOF, for example, it has been shown that activation using supercritical CO_2 is more superior in removing solvent molecules in MOFs compared to the use of chloroform and/or heating. In addition, it is also possible that the selected exchange solvent may not activate different MOFs in the same manner. The work reported by Dodson et al. [148] showed for two different Zn-MOFs, SNU-70 (SNU = Seoul National University) and MOF-5, the use of tetrahydrofuran (THF) produced partially activated and amorphous crystals SNU-70, but fully activated and crystalline MOF-5 crystals.

2.4. H_2 storage in MOFs

The use of metal-organic frameworks (MOFs) in cryogenic hydrogen (H_2) adsorption has shown promise towards system integration due to the high surface areas and large micropore volumes reported, reproducibly, for benchmark MOFs such as MOF-5 and MOF-177 [150]. Also one of the highest measured total gravimetric H_2 capacities of 16.4 wt% H_2 was reported for the copper-based paddlewheel MOF NU-100 (NU = Northwestern university) at 77.3 K at a pressure of 70 bar [10] . The fast kinetics afforded by the physisorption mechanism means that the uptake and release (desorption) of H_2 molecules would require very minimal energy inputs, making MOFs close to ideal candidates for their use for mobile H_2 storage systems. Even though MOFs such as NU-100 have shown record gravimetric H_2 capacities, their application is not only limited to the gravimetric storage of H_2, especially for on-board vehicular applications. The United States department of energy (US DOE) has set universally

accepted standards towards the realisation of a potential H_2 storage system for on-board vehicle applications. The candidate solid-state storage materials are required to be used in combination with a high-pressure cylinder to potentially reach a minimum gravimetric H_2 capacity of 4.5 wt% and volumetric H_2 capacity of 30 $g{\cdot}L^{-1}$. Even though many MOFs have shown potential of gravimetric H_2 capacities in excess of 10 wt%, the problem is that their corresponding volumetric H_2 capacities are generally less than 30 $g{\cdot}L^{-1}$. Indeed, in a systematic study carried out by Goldsmith and co-worker [100] thousands of different types of MOFs were assessed in an effort to determine the proportion of MOF types with the potential of reaching the US DOE targets, the study explored the relationship between the total gravimetric H_2 capacities and total volumetric H_2 capacities of the selected MOFs. The study found that numerous MOFs showed relatively high gravimetric H_2 capacities but the bulk of those MOFs also showed low volumetric H_2 densities, and only a few were within the 2017 US DOE targets at the time (5.5 wt%; 40 $g{\cdot}L^{-1}$) within a single MOF material. On a plot of gravimetric H_2 capacity versus volumetric H_2 capacity, the study showed that a maximum volumetric H_2 capacity of ~55 $g{\cdot}L^{-1}$ was attainable in the selected MOFs, but crucially, it was shown that any further attempts to improve the textural properties and increase the total gravimetric H_2 uptake could consequently result in a reduction in the MOF's total volumetric H_2 capacity. This means that for the consideration and selection of candidate MOFs, their surface areas should ideally be limited to those that do not compromise the total volumetric H_2 capacity of the MOF. Their study concluded that future studies should attempt shifting focus towards a direction whereby both the total volumetric H_2 capacities *and* surface areas can be improved simultaneously without compromising the crystal structure of the MOF material. The combination of favourable surface areas and micropore volumes for physisorption-based H_2 storage, and potential green synthesis methods renders MOFs as being of high interest and promising for industrial applications.

In recent times, the emphasis for MOF application in potential industrial H_2 storage systems has also seen most studies shift their focus towards the improvement of the H_2 working/deliverable capacity. The H_2 working/deliverable capacity is the difference between the amount/quantity of H_2 adsorbed at 100 bar pressure to the amount/quantity of H_2 desorbed at 5 bar [22,151,152]. This means that not only is the adsorption behaviour of the adsorbent-H_2 system important, but it is also important to take into consideration the reversibility of the H_2 adsorption (i.e. the presence of absence of hysteresis). The recent study by Broom et al. [15] highlighted some of the concepts that have shown promise towards the improvement of

volumetric H_2 capacities and working/deliverable capacities, without necessarily improving the MOF textural properties. One such concept involves the co-crystallization of MOFs with similar crystal structures such that they form interpenetrated MOF composites. The interpenetration of MOF crystals was reported by Balderas-Xicohtèncatl et al. [50] to result in doubling of volumetric H_2 capacity of the interpenetrated MOF (CFA-7) in comparison to the non-interpenetrated MOF (MFU-4l). The study attributed this improvement to the improved density of the interpenetrated CFA-7, but its gravimetric H_2 capacity was found to be less in comparison to the non-interpenetrated MFU-4l due to the superior specific surface area of MFU-4l (MFU-4l_{SSA} ≈ 3000 $m^{2}{\cdot}g^{-1}$ and CFA-7_{SSA} ≈ 1700 $m^{2}{\cdot}g^{-1}$). This clearly showed a compromise in the textural properties due to the interpenetration. Other cobalt-based interpenetrated MOFs have been successfully synthesized and showed good properties for gas separation techniques [153]. The development of interpenetrated MOFs is a budding research area that shows promise in its application in gas storage and separation applications. A concept that can possibly improve the H_2 working/deliverable capacity in MOFs is the use of flexible MOFs that can undergo structural guest-induced transformations, the guest being H_2 molecules.

There are numerous attempts dedicated towards the development of new MOFs with tailored textural properties and stabilities that could possibly attain high gravimetric and volumetric H_2 capacities suitable for H_2 storage applications [15,35,63,97,100], however, there is still room to explore inexpensive and simple methods that can aid in improving the volumetric H_2 and working/deliverable capacities of pre-existing MOFs.

2.5. Pelletization of MOFs for H_2 storage applications

The system integration of MOFs in application-specific technologies is envisaged on shaped MOF materials compared to MOFs in their pristine powder form. The most common and successful shaping techniques used for shaping MOFs have been those that offer MOFs in the form of pellets, granules, membranes, or fibers [154–157]. There has, therefore, been interest in exploring the properties of MOFs in their shaped or fabricated forms. The shaping of MOFs is not only intended to improve the ease of handling MOF-based materials but may also play a role in enhancing some MOF material properties that are inherently diminished in the as-synthesized MOF powder form. The shaping of MOF powders through pelletization has been implemented successfully to improve the volumetric H_2 capacity and thermal conductivity of

MOFs. MOFs can show a wide range of flexibilities that afford them different responses to external pressures [38,51,52,61]. MOFs with rigid structures or high mechanical strength may undergo amorphisation at sufficiently high pressures. Some may show small but significant degrees of flexibility by going through structural changes, such as pore widening or other anisotropic topological changes. These structural changes can have a direct impact to gas adsorption properties of the MOF, and it is generally observed that pelletized MOF forms tend to show reduced surface area and diminished total gravimetric H_2 capacities in comparison to their powdered counterparts [102,158,159].

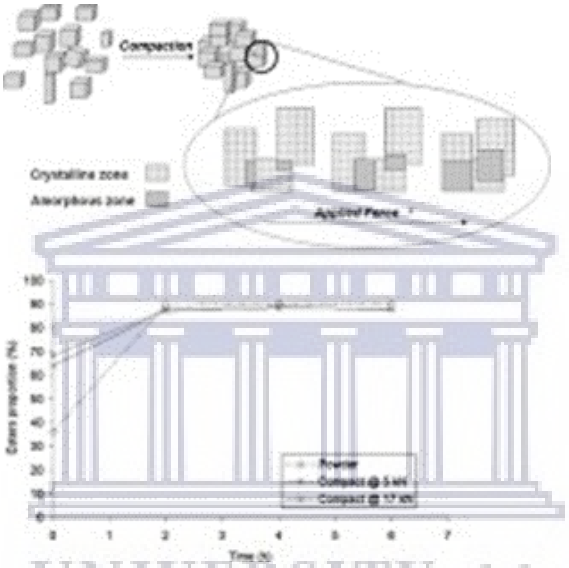

Figure 2.6: Schematic representation of the possible effects of pelletization on nanostructured crystalline materials [116] *(Image reused with permission from Elsevier).*

It is, however, important that the pelletization of MOFs be investigated on fully evacuated samples. The presence of solvent molecules within the MOF pores has been shown to make MOFs assume greater mechanical stabilities compared to their fully evacuated form. The effect of solvent molecules can be significantly high such that following the removal of the solvent molecules from the MOF pores, the MOF structure can collapse or become distorted [148]. Such observations are mostly common in MOFs containing flexible linkers but in MOFs considered to have high mechanical strength, such as observed in most zirconium-based MOFs, the effect of pelletization may be enhanced by pre-existing distortions in the MOF structure [70,160,161]. A study by Redfern et al. [162] compared the mechanical stabilities of MOFs belonging to the UiO series (Universitetet i Oslo) and NU-900 series (NU = Northwestern university) upon their pelletization at pressures below 500 MPa. The study found that MOFs

with distortions in their crystal structure were prone to significant reductions in their bulk modulus in comparison to MOFs with undistorted crystal structures (Fig. 2.7 and Fig. 2.8).

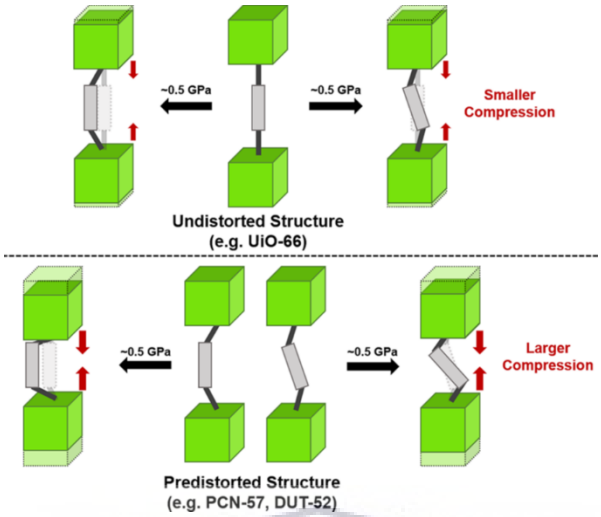

Figure 2.7: Schematic representation of the effect of applied pressure on undistorted and distorted crystals of UiO series [162]. *(Image reused with permission from © 2019, American Chemical Society).*

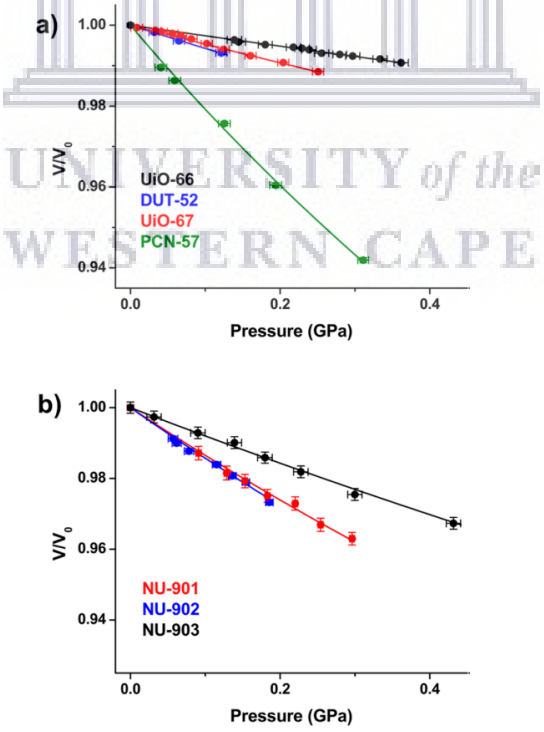

Figure 2.8: Comparison of the lattice compression in zirconium-based MOFs: (a) UiO series, and (b) NU-900 series [162]. *(Image reused with permission from © 2019, American Chemical Society).*

Other factors affecting the mechanical stability of zirconium-based MOFs have been reported on computational studies, with studies by Vandichel et al. [72] and Rogge et al. [73], showing that the presence of defects (i.e. missing linkers or missing nodes) in the UiO-66 structure would result in significant compromises to the shear modulus of the MOF. The bulk modulus was shown to be affected to a lesser extent. The implication of the structural deformations that may occur under applied pressures mean that both the textural properties and gas adsorption behaviour can be majorly affected by pelletization. Indeed it has been reported that in most cases where pelletization of MOF crystals is accompanied by structural changes, the surface area of the MOF becomes reduced and subsequently the gravimetric H_2 capacity of the MOF also becomes reduced [163].

Even though many studies have shown significant improvements of the volumetric H_2 capacity through pelletization of MOFs, it is important that attempts be undertaken in order to maintain the gravimetric H_2 capacity unaffected by the pelletization. The use of MOFs in their highly robust forms is, therefore, imperative in achieving high volumetric H_2 capacities with negligible effects on the gravimetric H_2 capacity. So far the most promising MOF is the zirconium-based UiO-66, which has been reported to have one of the highest minimum shear moduli amongst MOFs (*ca.* 13.7 GPa). It is, however, important to consider that UiO-66 has been shown to exist in two stable forms, namely hydroxylated UiO-66 made up of $Zr_6O_4(OH)_4$ inorganic clusters and dehydroxylated UiO-66 that is made up of Zr_6O_6 clusters. The deydroxylation process occurs to completion at ca. 300 ^oC as follows [72,84,96,160,164]

$$Zr_6O_4(OH)_2(s) \rightarrow Zr_6O_6(s) + 2H_2O(g) \qquad \text{Eqn. (2.1)}$$

This transition may be virtually undetectable by PXRD analysis as shown in previous studies [160][84]. The computational studies by Vandichel et al. [72] and others [73,161], further showed that, in addition to the presence of defects, the dehydroxylation process can also result in major reductions in the bulk and shear moduli of UiO-66, which become more enhanced in defective UiO-66. This means that dehydroxylated UiO-66 forms can possibly show lower mechanical stabilities in comparison to the hydroxylated UiO-66 analogue.

Important to the pelletization of MOF powders is the inevitable improvement in their packing densities. There have been numerous studies showing how densified MOFs translate to

improved MOF densities which in turn result in significant improvements of the volumetric H_2 capacity of the MOF. Of particular interest in this study was the study reported by Balderas-Xicohténcatl et al. [50] who showed over a large amount of MOFs that the volumetric H_2 capacity of a non-interpenetrated MOF would be directly proportional to its packing density via the MOF's volumetric surface area. The volumetric surface area can be described as the unit square area of the adsorbent occupying 1 mL of its volume. The higher the density of the adsorbent the higher the volumetric surface area, and this means that the increase in the packing density accompanying the pelletization of a MOF powder would also result in an increase in the volumetric surface area of the MOF. The study developed a mathematical model that illustrates the relationship between the volumetric surface area of a MOF and its volumetric H_2 capacity. Their calculations further reveal that this relationship yields the same "surface H_2 density" of 1.9 x 10^{-2} $mg.m^{-2}$ that is also obtained using the Chahine rule [165,166]. Most MOFs that were evaluated in the study showed experimental volumetric H_2 capacities that could be closely predicted using the model, except for interpenetrated MOF structures such as CFA-7 which showed the most significant deviation from the prediction model [50]. It is, however, key to note that the predictive model is applicable at volumetric H_2 capacities measured at 77 K and at pressure between 20 and 25 bar.

The shaping of MOFs can also be explored through their incorporation into polymers via the electrospinning method, forming MOF@nanofiber composite materials useful for gas storage applications. The incorporation of MOFs into electrospun nanofibers presents the opportunity for easy processing, handling, and up-scaling of fabricated MOF structures, and thus forms a key part towards the system-integration of MOFs for gas storage applications.

2.6. Principles of electrospinning

Electrospinning is the process of applying an electric voltage across an electrically conductive and viscous liquid solution [167]. The electrospinning setup is depicted in Fig. 2.9, and consists of an automated syringe pump that contains the conducting solution. At the needle-tip the voltage is applied and a collection screen (normally an aluminium screen) is situated on the opposite end of the needle-tip.

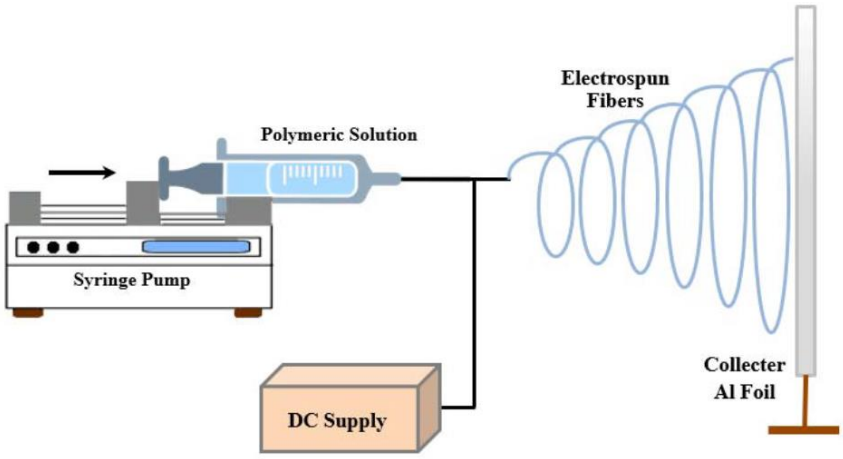

Figure 2.9: Schematic of a typical electrospinning setup [168].

The voltage is typically applied across charged steel needle and a charged collector, resulting in the migration of electrons and causes charge build up on the surface of the solution. The polarity of steel nozzle determines the charge build-up on the surface of the solution. If the needle is negatively charged, positive charges become attracted to the electrode, in the case of a positively charged needle, anions migrate to the electrode (Figure 2.10). The free surface of the liquid maintains an equipotential at all times, with the charges distributed in a way that maintains a zero electric field inside the liquid. When a voltage threshold is reached, Coulombic forces, resulting from the repulsion of similar charges on the solution surface overcome the surface tension that keeps the solution droplet intact. This results in the droplet becoming conical in shape, forming a Taylor cone that has a characteristic half angle of about 48.3º [169]. Although the size of the columbic force is correlated to the magnitude of the applied voltage, the density of ions and electrons in the overall neutral solution strongly influences the degree of charge build up.

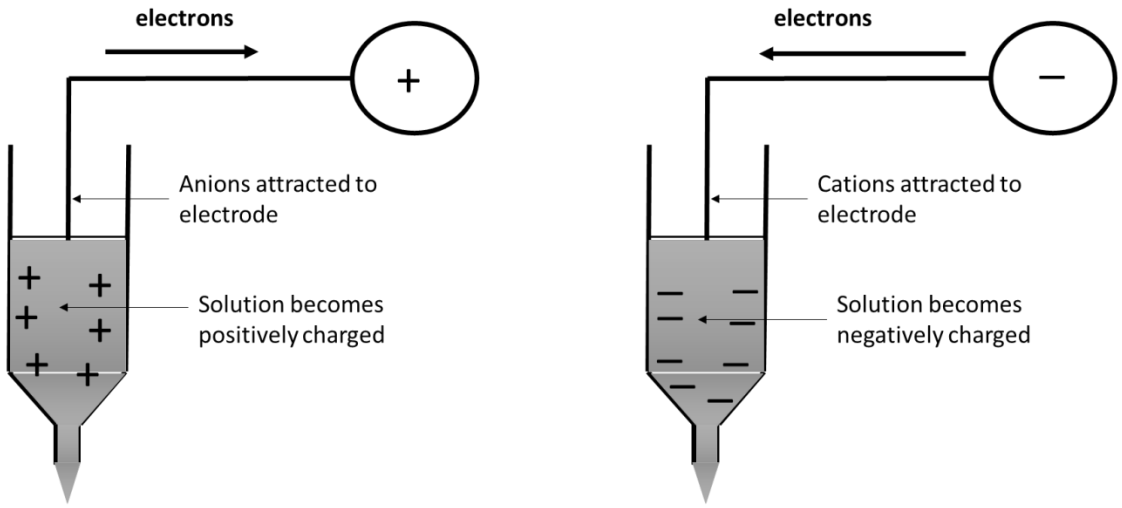

Figure 2.10: Schematic representation of electrospinning needle with positively charged and negatively charged electrodes showing charge build-up on the solution with respect to the polarity of electrode.

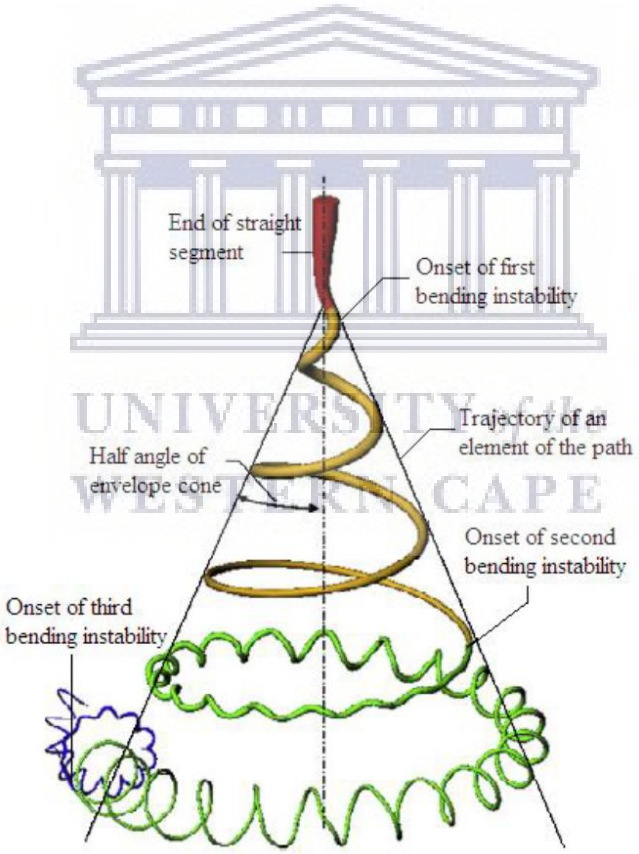

Figure 2.11: Schematic representation of solution at the needle-tip showing the different regions of the bending instability mechanism typical during electrospinning [169].

Once the Taylor cone is formed, it extends into an electrically charged fiber jet that is ejected from the tip of the cone and accelerated towards the collector screen. The fiber jet may undergo a series of stretching modes, as shown in Fig. 2.11. The inception regions of the jet form a

straight portion which is then followed by a radially spiralling conical region. This unstable region is caused by an asymmetric whipping mechanism. The whipping mechanism is caused by the coupled interaction of the coulombic forces on the jet with the electric field between the needle and the collector, thereby enabling a continuous stretching of the jet and resulting in the formation of a nanofiber network on the collector screen [167,170–172].

In this study, the process of electrospinning was based on the use of polymer solutions whereby MOF powders could possibly be co-electrospun and embedded on the polymer matrix. The selection of electrospinnable polymers was therefore crucial.

2.6.1. Types of polymers used in electrospinning

The parameters taken into consideration in choice of polymer include melting and glass transition temperatures, solubility or compatibility with other polymers-solvent systems when forming blends, chemical and biological compatibility (i.e. availability of specific functional groups) and/or suitability for post processing (e.g. whether it can be carbonised to make composite fibres). There are a wide variety of polymers that can be used for electrospinning and narrowing down the options available depends very much on the specific application, but for the purposes of fabricating MOF/polymer nanofibers, synthetic polymers are more suitable due to their durability, cost-effectiveness and tuneable properties (e.g. high tensile strength and viscoelasticity). Among some of the examples of synthetic polymers are: polymethylmethacrylate (PMMA); polystyrene (PS); polyacrylonitrile (PAN); polyvinyl alcohol (PVA); and polyvinylchloride (PVA) to name a few. Particular interest in this study was given to PAN, PS, and PMMA polymers as these have shown great promise in the production of MOF/polymer nanofibers [173–176]. In addition, due to the high thermal stability and thermal cross-linking of PAN, it is possible that PAN-based nanofibers can be converted into carbon nanofibers via thermal treatment under inert conditions, which is an added advantage for gas storage applications [57].

The chemical composition and electric conductivity only contribute to the electrospinnability of the polymer solution, but the properties of the fibers, particularly the fiber diameter, is mainly influenced by the process parameters or settings employed during the electrospinning.

2.6.2. Electrospinning parameters

The process parameters affecting the morphology of the resultant nanofibers can be divided into three groups as solution-based parameters, applied process parameters, and environmental parameters. The solution-based parameters refer to the intrinsic properties of the polymer solution such as the viscosity, polymer concentration, conductivity of the solution, the dielectric constant of the solvent, and polymer molecular weight. The applied process parameters refer to the applied voltage, the rate of pumping the solution through the needle-tip, diameter of the needle-tip, and the distance of the collector from the needle-tip. Finally, the environmental parameters include the humidity and temperature of the localized electrospinning setup, given an enclosed system/cabinet. In the electrospinning of PAN solutions, the electrospinnable concentration range can start from 8 wt% PAN dissolved in dimethylformamide (DMF) to about 12 wt% with an average molecular weight of 150 kDa [57,177]. The concentration and molecular weight alone are rather not sufficient to ensure successful electrospinning of PAN nanofibers, it is common that the combination of certain parameters be optimized in order to obtain desired morphologies.

2.6.3. Incorporation of MOFs into electrospun nanofibers

A variety of MOFs, ranging from zirconium-, iron-, chromium-, and copper-based MOFs, have been successfully electrospun with polymers such as polyacrylonitrile (PAN), polyvinylidene fluoride (PVDF), Poly-L-lactide (PLL), polystyrene (PS) to name a few [78,80,178]. The advantage of producting MOF/polymer composites is that they can be obtained as fibrous membranes with vast applications in gas separation, chemical sensors, water purification and used as polymer-based binders in shaping of powdered solid-state adsorbents [111,167,179–181]. The disadvantage to incorporating MOFs in nanofibers is that they tend to show compromised textural properties in comparison to the pristine MOF powders. In addition, due to the limitations of the electrospinning process, such as viscosity and polymer concentration, there are limits to the amount of MOF powder that can added onto a polymer solution that is electrospinnable. A challenge with incorporating MOF powders is also their effect on the morphology of the nanofiber properties such as nanofiber diameter and the absence of beaded fibers. It has generally been shown that loadings above 20 wt% of the powder with respect to

the polymer content may cause the polymer/powder mixture/emulsion to have a significantly higher viscosity compared to the polymer solution without powder material [57]. The increased viscosity would result in very slow flow rates upon electrospinning through a needle with a small inside diameter (typically < 1 mm in most electrospinning setups). The result of a restricted flow of the polymer solution/emulsion would lead to either a non-electrospinnable solution/emulsion or cause the formation of beaded nanofibers which would severely compromise the surface morphologies of the nanofibers [171,182]. In addition to electrospinning of MOF/polymer solutions, porous polymers such the polymers of intrinsic microporosity (PIMs) have also been shown to be electrospinnable. The advantage of PIMs is that they are made up of a permanently microporous structure that is not lost upon processing them into powders, nanofibers, or thin films. The H_2 storage capacities of polymer nanofibers, including MOF/polymer nanofibers, have not been shown to rival those obtained in pristine MOF powders. Due to the ease of fabricating nanofibers using electrospinning, it may be possible to develop nanofibers with hierarchical pore structures by incorporating MOFs of different nanoporosity [112,183,184]. The importance of porous solids with hierarchical porosity is that they can show combinations of gas adsorption behaviour. For example, micro-mesoporous material can show Type I adsorption at low pressure and also Type II adsorption at higher pressures [118]. This could improve the working capacity of the adsorbed gas, which has significant implications in H_2 storage applications.

The use of the proper analysis tools is important for accurately determining the amount of H_2 that can be stored in a porous material. It is important that H_2 capacities are measured based on the properties of the adsorbent materials.

2.7. Chapter summary

This chapter detailed some of the studies undertaken to investigate the mechanism of physisorption on porous materials, with particular focus on the physisorption of hydrogen gas (H_2). The chapter further discussed the fabrication of porous materials using the pelletization and electrospinning strategies. The benefits and limitations of each method were discussed and it was clear that the most concerning challenge in each method was that the shaped forms of MOFs, and their composites with polymers/binders, showed reduced textural properties (surface areas and porosity) in comparison to pristine MOF powders. It was, therefore, an underlying objective in this study that in the development of strategies to improve volumetric and usable H_2 capacities, much of the focus should be directed at reducing the negative effects of pelletization and electrospinning possibly to insignificant levels compared to previous reports.

Chapter 3

3. Methodology

This chapter gives a detailed discussion of the materials and methods used in this study. In figure 3.1 a summarized flow chart is given showing the top-down approach of the main materials and how the sample preparation methods linked during experimentation. The characterization techniques used in this study are given later in the chapter.

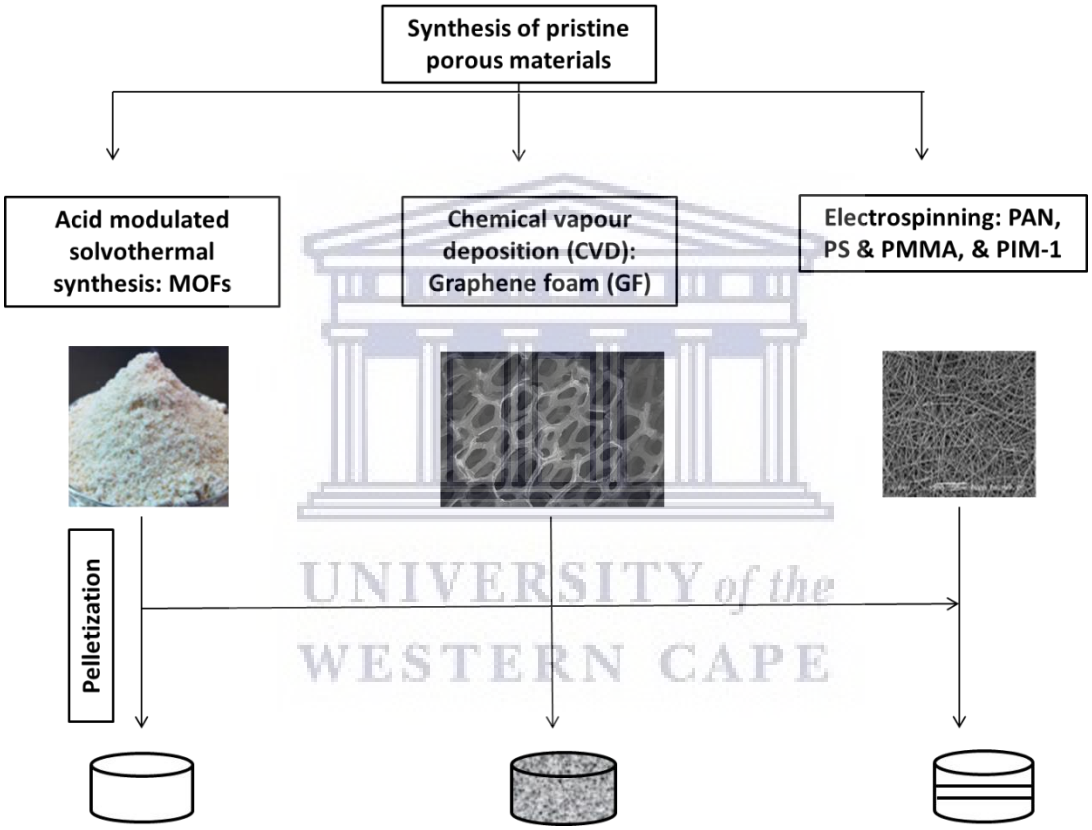

Figure 3.1: Flow diagram summarizing the sequence of material preparation towards obtaining a composite material with possibly optimized properties for H_2 storage applications.

Chemicals

The chemicals used in this study are listed in Table 3.1 and a brief description of their purpose in the study is also provided. All chemicals were used without further purification.

Table 3.1: List of all chemicals used during the study and a brief description of their role.

Chemical	**Chemical formula & supplier**	**Composition**	**Brief properties relevant to study**
Zirconium (IV) chloride	$ZrCl_4$ (Sigma Aldrich)	99.5%	Readily dissolves in DMF forming Zr^{4+} ions. Precursor for UiO-66.
1,4-Benzenedicarboxylic acid (BDC)	$C_8H_6O_2$ (Sigma Aldrich)	98%	Readily dissolves in DMF forming $[C_8H_4O_2]^{2-}$ anions. Precursor for UiO-66.
Chromium (III) chloride hexahydrate	$CrCl_3.6H_2O$ (Sigma Aldrich)		Readily dissolves in water forming Cr^{3+} ions. Precursor for MIL-101(Cr)
N,N-Dimethylformamide (DMF)	C_3H_7NO (Sigma Aldrich)	99.8%	Good solvent for $ZrCl_4$, BDC, PAN, PMMA and PS
Formic acid (FA)	CH_2O_2 (Sigma Aldrich)	95+%	Acid modulator for MOF synthesis
Dry acetone	C_3H_6O (Sigma Aldrich)		Drying agent
Deionized water	H_2O (HySA lab)	100%	Good solvent for $CrCl_3.6H_2O$
Polyacrylonitrile (PAN)	$[-C_3H_3N-]_n$ (Sigma Aldrich)	Avg. M_w = 150 kDa	Good electrical conductivity for electrospinning &readily dissolves in DMF
Poly(methyl methacrylate) (PMMA)	$[-C_5O_2H_8-]_n$ (Sigma Aldrich)	Avg. M_w = 120 kDa	Good electrical conductivity & readily dissolves in DMF & acetone
Polystyrene (PS)	$[-C_8H_8-]_n$ (Sigma Aldrich)	Avg. M_w = 50 kDa	Good electrical conductivity & readily dissolves in DMF
Nickel foam (NF)	Ni (Celmet, Japan)	1.6 mm thick, surface area = 7500 $m^2.m^{-3}$, cell size = 0.5 mm, 48-52 cells per inch	Readily absorbs carbon at ~1000 ºC & readily dissolves in hydrochloric acid (HCl)
Hydrochloric acid (HCl)	HCl (Sigma Aldrich)	36.8 – 38 % (~12 – 12.51 $mol.dm^{-3}$)	Strong acid which can dissolve metals
Polymer of intrinsic microporosity-1 (PIM-1)*	-	-	-
Tetrachloroethane (TCE)	C_2Cl_4 (Sigma Aldrich)	≥ 98 %	Organic solvent. Readily dissolves PIM-1 at room temperature
Tetrahydrofuran (THF)	C_4H_8O (Sigma Aldrich)	≥ 99 %	Organic solvent. Can dissolve PIM-1

3.1. Synthesis of pristine porous materials

3.1.1. Solvothermal synthesis of UiO-66

The synthesis of UiO-66 was based on a 1:1:100 $ZrCl_4$:H_2BDC:FA molar ratio for all experiments as the use of 100 molar equivalent of a monocaboxylic acid, such as FA, has been reported to promote fast nucleation of UiO-66 crystals [99]. The acid-modulated solvothermal method has also been shown to be relatively easy to control in order to obtain desired synthesis times and crystal sizes as well as the possibility of forming defects (missing linkers), and these variables may lead to tailoring desired textural properties in the as-prepared UiO-66 product. It is important in the current study that the surface area and pore volumes obtainable for UiO-66 are as a high as possible under such synthesis conditions in order to obtain high H_2 uptake capacities compared to those previously reported. Using the acid-modulated solvothermal synthesis, where the molar ratio of modulator to precursors can be as high as 100:1, it is possible to grow UiO-66 crystal sizes up to and/or above ~ 2 μm depending on the synthesis times [107,108]. The control over the UiO-66 crystal size is therefore important in this study as large crystals (~ 2 μm) tend to promote the formation of beaded nanofiber composites during electrospinning, which result in inconsistent fiber diameters caused by the "beads on a string" morphology.

In a typical synthesis procedure, $ZrCl_4$ and H_2BDC were ultrasonically dissolved in 50 mL DMF for about 15 minutes at room temperature. To the mixture, the 100 molar equivalent of FA was added and further sonicated for 5 minutes. The mixture was then transferred to a reflux setup, heated to 120 ^oC and kept at that temperature for a specified time (typically 4 to 48 hours) depending on the crystal size required. After the reaction was complete, the white product was collected in a centrifuge at about 10 000 rpm for at least 10 minutes. In order to remove unreacted reagents, the UiO-66 product was washed in 50 mL of pure DMF at 60 ^oC for 3 hours. After washing, the product was collected by centrifugation at 10 000 rpm for 10 minutes. As UiO-66 is a highly porous material, it was also important that solvent exchange be done in order to replace the DMF solvent molecules maintained within the pores with a more volatile solvent like acetone. This last step was done in a 100 mL conical flask and the UiO-66 product immersed in 50 mL acetone and stirred at room temperature for about 30 minutes, after which the final product was recollected by centrifugation at 10 000 rpm for 10 minutes. After re-collection, the UiO-66 product was dried in a vacuum oven at 25 ^oC under vacuum. The

selection of a specific degassing temperature within the aforementioned temperature range was found to play a significant part in the properties of UiO-66 and its effects are later discussed in chapter 4.

3.1.2. Solvothermal synthesis of MIL-101(Cr)

The synthesis of MIL-101(Cr) was also based on an acid-modulated procedure similar to that of UiO-66 where a 1:1:100 molar ratio of $CrCl_3.6H_2O$/BDC/FA was used throughout the study. In a typical procedure, 5 mmol $CrCl_3.6H_2O$, 5 mmol BDC, and 0.5 mol FA were ultrasonically dissolved in 50 mL deionised water for 30 minutes. The mixture was then heated and held at 210 ^oC for 8 hours, after which the resultant product was placed in a 100 mL conical flask and washed under stirring in 50 mL DMF at 60 ^oC for 3 hours. The washed product was recollected via centrifuge at 10 000 rpm for 10 minutes until no solid particles were observed in the supernatant liquid. The recollected solid was thentransferred to a clean 100 mL conical flask and washed under stirring in 50 mL acetone for 30 minutes, followed by re-collection at 10 000 rpm and finally the product was dried in a vacuum oven at 90 ^oC under vacuum for 12 – 24 hours.

The possible presence of MIL-53(Cr) cross-contamination can be detected using XRD and microscopy (SEM or TEM) due to the distinctly different structures that it exhibits from MIL-101(Cr) crystals.

3.1.3. Synthesis of graphene foam (GF) and GF/UiO-66 composite

The thermal conductivity of MOFs has been shown to be extremely low compared to other porous materials [15,43,55]. The need to improve MOF thermal conductivities is imperative for H_2 storage applications in order to ensure efficient heat dissipation during the adsorption of H_2 gas at high pressure. One of the most widely used methods is the addition of carbons to form MOF/carbon composites which tend to have much improved thermal conductivities compared to the pristine MOF, such as reported for MOF-5/ENG (expanded natural graphite) at ENG loadings as low as 5 wt% [51]. An ideal MOF/carbon composite would be one where the carbon shows extremely high thermal conductivity and also the possibility of itself adsorbing H_2 onto its surface. One such carbon material is graphene. The synthesis of graphene has for many years been achieved through chemical synthesis methods such as exfoliation of

graphite oxides [27,76,185–187], but recently direct synthesis of graphene was achieved using a hard templating technique where carbon atoms are deposited on a metal template, such as nickel (Ni) or copper (Cu), at high temperature, known as chemical vapour deposition (CVD). The technique has been shown to be an effective way of producing either single- or multi-layered graphene depending on the choice of metal template being used. A study by Chen and co-workers further showed that by using a nickel foam as a template, it was possible to produce 3-D graphene termed "graphene foams", which retained the initial structure of the Ni foam template [188].

In this study graphene foam (GF) was synthesized using the CVD method adopted from the works of Chen et al. [188]. The details of the procedure used for depositing carbon, in terms of the experimental gas flow rates and temperatures at the different stages of the CVD process, are shown in Fig. 3.2.

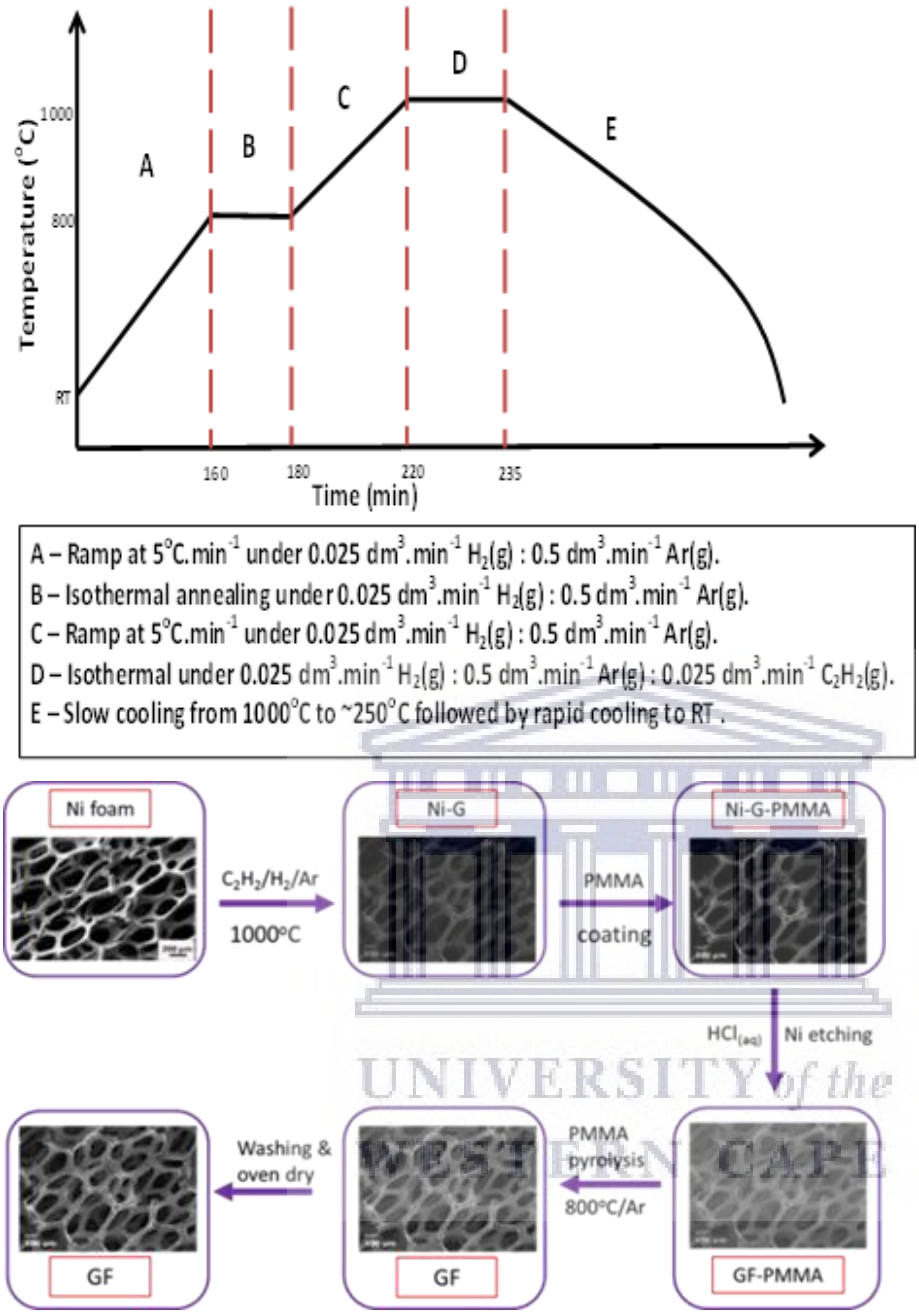

Figure 3.2: Schematic representation of the CVD process and the crystal growth of UiO-66 on the surface of GF: (top) Temperature control and gas purges during the carbon deposition step; (bottom) Carbon deposition and Ni template removal steps.

In the PMMA coating step, 0.5 g of PMMA granules were dissolved at 60 °C in 10 mL of DMF in a 50 mL beaker to obtain a 5 mg·mL^{-1} PMMA solution. After cooling the PMMA solution to room temperature, a 5 mL aliquot of the 5 mg·mL^{-1} PMMA solution was spread onto the surface of the Ni-G product using a syringe. The Ni etching was carried out with 3 M $HCl_{(aq)}$ solution over 3 days with fresh 10 mL aliquots of 3 M $HCl_{(aq)}$ added in each day to replace the previous etching solution. After the Ni etching, the PMMA coating was removed using two

methods, namely: (1) Acetone dissolution for 24 hours, to selectively dissolve the PMMA polymer without affecting the as-synthesized GF and (2) Pyrolysis of the GF/PMMA composite at 800 ^{o}C under a constant 0.025 mL·min^{-1} flow of argon gas (Ar). The pyrolysis method was found to be the more efficient at reducing the amount of contaminants on the surface of the as-synthesized GF (see Fig. 6.1 in chapter 6).

In Fig. 3.3 represents the in-situ growth of UiO-66 onto the surface of the graphene foam (GF) was conducted in a 50 mL round-bottom flask under static conditions.

Figure 3.3: Synthesis of UiO-66 onto CVD-grown GF using a single-step and two-step in-situ crystal growth method.

The GF was then used as a substrate to grow UiO-66 whereby an approximately 20 mg sample of GF was immersed in a solution containing a 1:1:100 molar ratio of a $ZrCl_4$:H_2BDC:FA mixture in 20 mL of DMF solvent. The experiment was divided into two approaches where the first approach involved the direct synthesis of UiO-66 on GF via a single step method. After the one-step synthesis, the GF/UiO-66 composite was soaked in hot DMF to remove any unreacted H_2BDC and importantly the washing step avoided the recollection of the product via centrifuging as that would have destroyed the structure of GF. This is because the manner in which the GF was prepared was such that no other mechanical reinforcing agents, such as silicone, were added to the as-synthesized GF in order to give it some degree of flexibility, meaning that the GF was prepared in a pristine but brittle state. The solvent exchange step with acetone was also done under static conditions in order to prevent physical damage to the GF/UiO-66 under mechanical stirring. In the second approach of in-situ UiO-66 crystal growth, a two-step method was utilized whereby a dried GF/UiO-66 product from the single-step or direct synthesis method was transferred to a 50 mL round-bottom flask containing a fresh solution of 1:1:100 molar ratio $ZrCl_4$:H_2BDC:FA in 20 mL DMF solvent. The mixture

was then heated to 120°C and maintained for 6 hours under static conditions. After the synthesis of UiO-66 onto the single-step GF/UiO-66 product, the final product was washed by immersing into DMF at 60 °C for 30 minutes. After decanting the supernatant liquid containing DMF and unreacted terephthalic acid, the GF/UiO-66 product was transferred to a clean petri dish, covered with perforated aluminium foil and allowed to dry in air for 12 – 24 hours.t. The overall percentage yield of UiO-66 that was grown on the 20 mg GF was approximately 85 – 95 wt% assuming an even distribution of the UiO-66 crystals onto the surface of GF.

3.2. Shaping of MOF materials and their composites

Metal-organic frameworks have shown great promise in applications such as gas storage, gas separation, water treatment, catalysis, and as support materials in batteries [189,190][191]. Their system integration in application-specific technologies has therefore found greater interest in shaped MOF materials compared to MOFs in their pristine powder form. The most common and successful shaping techniques used for shaping MOFs have been those that offer MOFs in the form of pellets, granules, membranes, or fibers. The interest of exploring the properties of MOFs in their shaped or fabricated forms has, therefore, become paramount in developing MOF or MOF composite materials that would have properties applicable to real-world technologies. The shaping of MOFs is not only intended to improve the ease of handling MOF-based materials but may also play a role in enhancing some MOF material properties that are inherently diminished in the as-synthesized MOF powder form. For example, there are well-documented studies on the pelletization of MOFs which have been shown to greatly improve the density of the MOF and subsequently showing significant improvements in the volumetric H_2 capacity of the MOF pellet compared to its powder counterpart [30,51]. In this section the two shaping techniques, namely, pelletization and electrospinning, employed in this work are presented.

3.2.1. Electrospinning of MOF/polymer composites for H_2 storage applications

In this study, the purpose of electrospinning was to incorporate UiO-66 and MIL-101(Cr) powders into nanofiber mats so as to produce MOF/polymer composites that were easy to handle compared to the loose MOF powders, but more importantly with surface areas that would not be significantly compromised when compared to the pristine MOF powders. The polymers of choice were the non-porous polymers PAN, PMMA, and PS, and one porous

polymer PIM-1. Two electrospinning techniques were employed in this study, namely the single-nozzle (Fig. 3.4) and the co-axial electrospinning methods (Fig. 3.5). The non-porous nature of PAN, PMMA, and PS poised a challenge as they typically show very small surface areas and their MOF/polymer composites would thus be expected to have significantly lower surface areas compared to the pristine MOFs. The potential to increase the MOF loading could, however, lead to improved surface areas and pore volumes in the MOF/polymer composites.

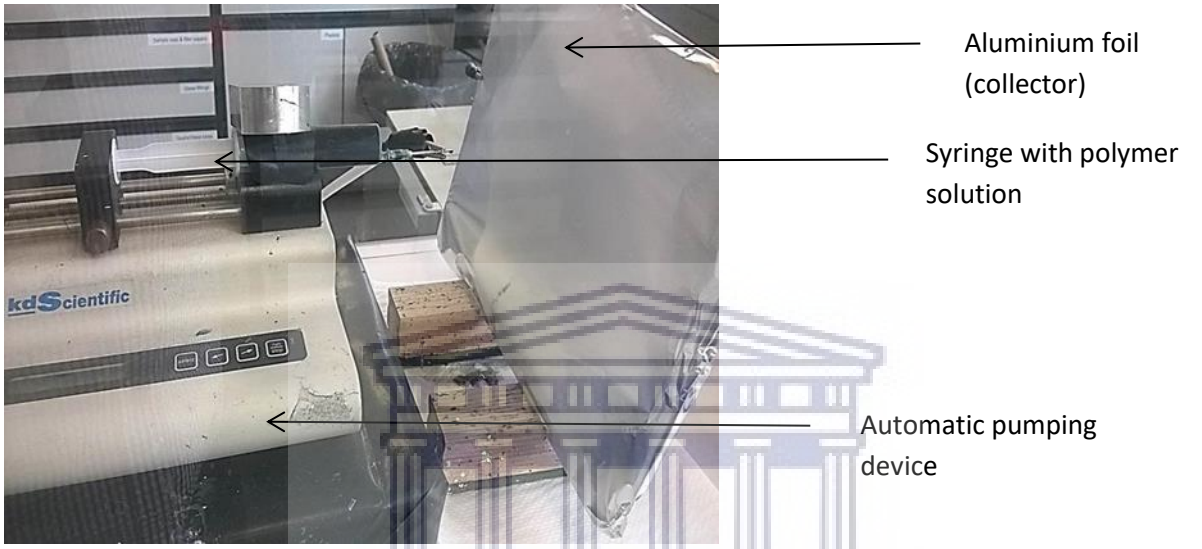

Figure 3.4: General experimental setup for the single-nozzle electrospinning method employed in the electrospinning of PAN, MOF/PAN, and PIM-1 polymer solutions.

Prior to the addition of MOFs onto each of the polymer solutions chosen in this study, the concentration(s) of the polymer (weight percentage of the polymer with respect to the solvent) which could give the most optimum nanofiber properties, showing little to no bead formation and consistent nanofiber diameters, had to be determined. The electrospinning of the non-porous polymers was based on previously reported literature and more specifically work that was previously done by Annamalai et al. [57] at the HySA Infrastructure group. The polymer concentrations used for PAN electrospinning were 8, 10, and 12 wt% in DMF and 20, 25, and 30 wt% for both PMMA and PS in DMF. In the preparation of MOF/polymer composites, 20 wt% of MOF powder, with respect to the mass of the polymer in solution (Table 3.2), was added in a conical flask together with the polymer granules. After addition of a 10 mL aliquot of DMF, the mixture was sealed and stirred at 250 rpm overnight at room temperature. It was found that mixtures stirred overnight (time > 8 hours) produced better dispersion of the MOF powder in comparison to mixtures stirred over shorter times.

The two other important process parameters during electrospinning were the distance (cm) of the collector from the needle tip and the applied voltage (kV). As previously discussed in chapter 2, the combination of polymer concentration, distance of the collector, and the applied voltage all have an effect on the morphology of polymer nanofibers during electrospinning [176,180,182,192,193]. A series of screening experiments were conducted in order to determine the best possible electrospinning conditions for each of the non-porous polymers which would give the desirable polymer nanofiber morphologies. It is important to note that this study did not focus on the use of statistical analysis tools, such as mixture designs, D-optimal designs or any form of statistical analysis software in order to elucidate the optimum electrospinning process parameters. Such analyses were done in previous studies [176] and in this study the aim was to select out of those proposed conditions the ones that would provide optimum conditions for both single-nozzle and coaxial electrospinning of MOF/polymer composites. The basis for the selection criteria was on the characterization of the resultant nanofibers after electrospinning at each of the aforementioned process parameters (see results in chapter 5). The optimal conditions that eventually gave the most desired nanofiber morphologies are given in Table 3.2.

In the single-nozzle method, only a single polymer solution producing a single solid nanofiber jet is obtained, whereas in the co-axial method the nanofiber jet is produced through a concentric needle and thus consists of a core and shell morphology (a detailed explanation of the two techniques is provided in chapter 2). This means that the single-nozzle technique could be used to optimize the electrospinning conditions for each polymer type before and after incorporation of the MOF powder.

The co-axial electrospinning setup used a concentric needle with two separate inlets bringing the two polymer solutions in the same direction as shown in Fig. 3.5 (insert). This required that a set of tubes be connected from the syringes to each inlet. In that case, the proper transfer tubes for the electrospinning procedures needed to be selected. The most commonly used tubing polymers such as polypropylene and polyethylene were found to dissolve, swell or rupture in DMF, THF and TCE solvents. The alternative tubing options available at our lab were Teflon and cross-linked polyethylene (XLPE) tubes. Both showed to be resistant to the solvents, with no swelling observed when immersed for 24 hours but the Teflon tubes were chosen for their flexibility compared to XLPE tubes and used for all the co-electrospinning

experiments. The electrospinning of PIM-1 was found to be the most difficult to electrospin compared to non-porous polymers. PIM-1 did not dissolve in common organic solvents such as DMF, acetone, or chloroform and thus required specialized, safe, and well ventilated conditions for its dissolution in the toxic tetrachloroethane (TCE) solvent.

Table 3.2: Experimental process parameters used in both single-nozzle and coaxial electrospinning. The solvent concentrations were obtained from screening experiments.

Polymer	**Vol. DMF or TCE/THF (mL)****	**Optimum [polymer] (wt% or g/g solvent)***	**Mass of polymer (g)**	**Mass of 20 wt% MOF loading (g)**	**Applied voltage (kV)**	**Solution flow rate ($mL.h^{-1}$)**
PAN	10	8	0.7552	0.1510	11	1.8
PMMA	10	25	2.36	0.4720	11	1.8
PS	10	25	2.36	0.4720	11	1.8
PIM-1	10	5	0.567	-	16	3.0
Distance from needle tip = 15 cm						

*optimum values determined from screening experiments done on pristine polymer solutions.

** A 7:3 v/v TCE:THF solvent mixture was used to electrospin PIM-1 and the mass of PIM-1 was with respect to the mass of TCE.

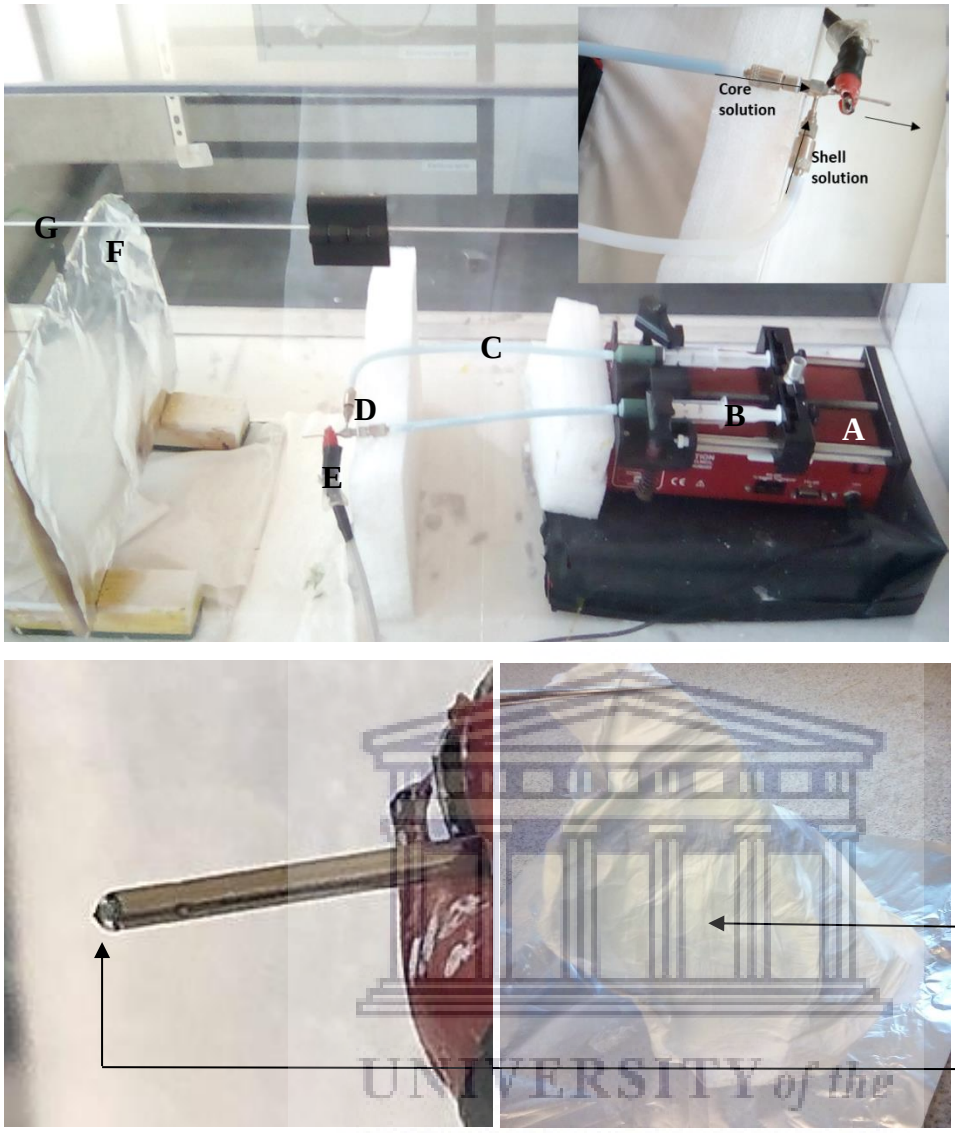

A – Automatic pump system

B – Syringe

C – Teflon tube

D – Concentric needle

E – Live wire (from voltage source)

F – Aluminium foil (collector)

G – Earth wire

Figure 3.5: Coaxial electrospinning setup used to prepare core-shell PMMA@PAN, MOF/X@PAN, and MOF/X@MOF/PAN nanofibers (X = PMMA or PS).

3.2.2. Pelletization of pristine MOFs and MOF/carbon composites

The fabrication of powdered materials into shaped bodies is important for industrial applications as it provides ease-of-handling and structural stability during processing. In porous materials, there is an added benefit to shaping powdered products into pellets or granules, and that is in improving the packing density of the material. The implications in H_2 storage is such that a high MOF packing density translates into a high volumetric H_2 capacity for the shaped MOF compared to its powdered counterpart. In this study the shaping of UiO-66 and MIL-101(Cr) powders by pelletization technique employed a Specac Manual Hydraulic

press and 13 mm diameter (surface area = 113 mm^2) stainless steel die as shown in Fig. 3.6. As it was shown earlier in Fig. 3.1, the pelletization method was done on various samples. Firstly the pristine MOFs were pelletized in order to investigate the effects of pelletizing pristine UiO-66 and MIL-101(Cr) powders without incorporating binders such as polymers, or using a solvent-assisted pelletisation method. The pelletization of pristine UiO-66 and MIL-101(Cr) was to show possible pressure-induced responses for each MOF and how the pelletization would affect the MOF textural properties compared to its powder counterpart.

In this study a series of screening experiments were performed on the pristine MOFs whereby a ~400 mg sample of MOF powder was pelletized at 2, 4, 6, 8, and 9 metric tonnes (150, 290, 440, 590, and 650 MPa respectively) for 15 minutes. In the initial experiments, the UiO-66 was first activated at 80 ^oC and pelletized according to the above-mentioned method. It was important to ensure that each sample was fully activated, i.e. they did not contain significant amounts of DMF solvent molecules as it has been shown that some MOFs may undergo a structural collapse after removal of solvent molecules [94,149]. The activation was therefore done firstly by solvent exchange of the as-synthesized MOF with 50 mL acetone in a 100 mL conical flask, as detailed in section 3.1.2. After drying the recollected product under vacuum and room temperature, a 500 mg sample of the UiO-66 powder was heated under vacuum (~10^{-7} bar) at 80 ^oC for 16 – 32 hours in a Micromeritics SmartVac degassing unit. The pelletization of UiO-66, activated at 80 ^oC, was done as an initial screening that would be used to establish the highest applied pressure where the packing density would ideally exceed 1 $g{\cdot}mL^{-1}$ but most importantly where the crystal structure of UiO-66 would not be greatly compromised, i.e. would not become amorphous (density measurements are described in section 3.5). The phase crystallinity of each sample was then monitored using Powder X-ray diffraction (PXRD) analysis after each pelletization step (section 3.4.2.1). Some MOFs can show a high degree of rigidity prior to their full activation [148], however, it was possible that after the complete removal of the solvent molecules (evacuation), the structure of the MOF could be compromised and in extreme cases even collapse into an amorphous powder. In other cases [15,101,194,195], MOFs, such as MIL-53, may show a high degree of flexibility such that upon removal of an applied external pressure the MOF would regain its original structure prior to the application of pressure. This shows two important aspects in MOF pelletization, full activation and flexibility of the MOF structure. In order to investigate such a possibilities in UiO-66 and MIL-101(Cr), each MOF sample was first pelletized at its specified pressure and then ground into a fine powder followed by PXRD analysis of the MOF sample in its densified/pellet and ground

forms. This would give information whether the application of pressure to UiO-66 and MIL-101(Cr) was a reversible or irreversible process. In the pelletization of MIL-101(Cr), all samples were first activated at 200 ^{o}C prior to their pelletization at 2, 4, 6, 8, and 9 metric tonnes and also followed by measurement of their packing densities and PXRD patterns to monitor any possible changes to the crystal structure.

The second part of the pelletization experiments involved pelletizing UiO-66 samples at 9 metric tonnes (665 MPa) that were activated at different temperatures beginning at 80 to 320 ^{o}C at intervals of 30 ^{o}C. As discussed in chapter 2, UiO-66 exists in two different forms that exhibit slightly but significant gas adsorption properties. It may exist in a hydroxylated form consisting of $Zr_6O_4(OH)_4$ inorganic nodes and also in a dehydroxylated form that is obtained by the dehydroxylation/dehydration of $Zr_6O_4(OH)_4$ nodes at ~300 ^{o}C to form Zr_6O_6 inorganic nodes [84]. In this study, the dehydroxylation process of UiO-66 was investigated using a Thermogravimetric analyser (TGA) coupled to a Mass spectrometer (MS) in order to determine the temperature range where hydroxylated UiO-66 became converted into dehydroxylated UiO-66 (details of the TGA-MS analysis are given in section 3.4.4.1). The UiO-66 samples were activated at 80, 110, 140, 170, 200, 230, 260, 290, and 320 ^{o}C followed by their pelletization at 9 metric tonnes (665 MPa) for 15 minutes. The crystal structure and textural properties were then measured as described in section 3.2.

The final part of the pelletization method was done on UiO-66 powder samples with the incorporation of MOF/nanofiber composites as binders and also pelletized with graphene foam (GF) in order to potentially improve the thermal conductivity. Only UiO-66 was used in the final pelletization method since higher yields could be obtained from a single batch instead of using MIL-101(Cr) which could only be obtained in small yields using a multi-batch synthesis method (described in section 3.1.1). Furthermore, only the MOF/nanofiber composite samples showing the highest surface areas were selected as binders. The pelletization of UiO-66 with MOF/nanofiber composites was done using ~400 mg UiO-66 powder to which ~10 mg of the MOF/nanofiber composite material was added as shown in Fig. 3.6. For these samples, only the textural properties and packing densities were measured. In the pelletization of UiO-66 and the UiO-66/GF composite material, about 400 mg of UiO-66 and 20 mg (5 wt%) of UiO-66/GF were mixed and ground into a fine powder using an agate mortar and pestle and the resultant mixture was pelletized at 9 metric tonnes (665 MPa) for 15 minutes.

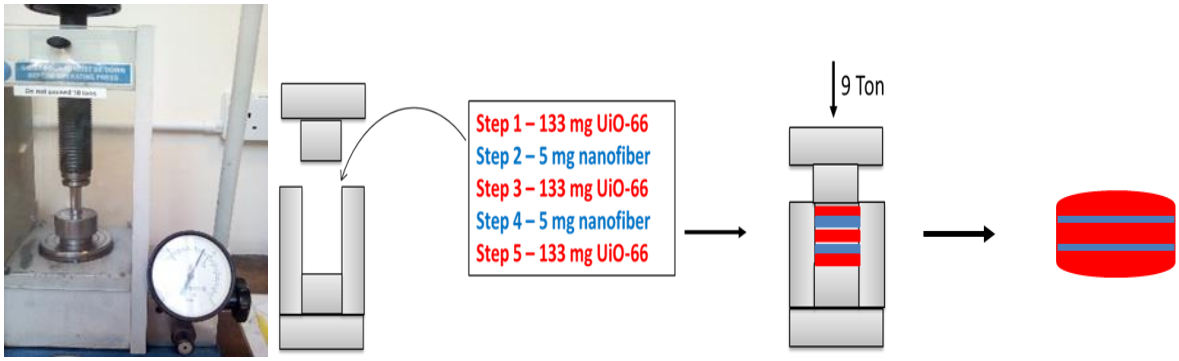

Figure 3.6: Image of the Specac hydraulic press used for the pelletization/compaction of pristine MOF powders (UiO-66 and MIL-101(Cr)) and the co-pelletization of UiO-66 with 5 wt% electrospun nanofibers as binders, forming layered UiO-66/nanofiber composites (schematic).

3.3. Characterization

This section reports on the characterization techniques employed in this study. Due to the use of crystalline, nanostructured and porous materials, the major characterisation techniques of interest were based on determining intrinsic material properties such as crystalline phases, crystal sizes, textural properties (surface area and pore volumes), chemical compositions, and thermal properties. The aim was therefore to analyze how these intrinsic properties influenced the hydrogen storage capacities that could be attainable using the aforementioned materials of choice. The characterisation was purely based on predetermined materials and no new materials are proposed in this study and hence some reference will be made to previous publications similar to this study for comparison purposes. The characterisation techniques are grouped into: (i) imaging; (ii) spectroscopy; (iii) crystallography (iv); gas adsorption; and (v) thermal analysis.

3.3.1. Imaging

The imaging of nanostructured materials plays an important role in elucidating the structure, in particular shapes and sizes, of pristine materials through the use of microscopic techniques. Imaging is particularly of interest in this study as it allowed for the determination of MOF crystal shapes and sizes, and also the MOF distribution onto the polymer nanofiber and carbon substrates.

3.3.1.1. Scanning electron microscopy (SEM)

SEM is a common technique used for imaging the microstructural features of a material's surface. A narrow beam of electrons of about 2 – 3 nm is focused through lenses onto a mounted sample which is used to scan the surface of the material. The resultant electron-electron interactions on the surface of the material may scatter some of the incident beam electrons or produce a secondary electron beam, or even produce X-rays. Depending on the type of detector being utilized, images from different depths of the material surface can be obtained. The secondary electrons can be collected to produce an image a few nanometers from the top of the material's surface. The scattered electrons on the other hand originate from deeper, about few hundred nanometers, and the image may give information about the distribution of contrasting elements on the surface of the material [196]. The X-rays are detected using a special kind of detector which uses the methods of energy-dispersive X-ray spectroscopy (EDX) and can produce images from a couple of micrometers into the material surface. The EDX coupled image produces not only distributions of contrasting chemical elements, but also their spectra. An important feature in SEM imaging is that the sample/material must be conductive in order to produce quality images. In semi- or non-conductive materials there becomes the problem known as the charging effect. Charging may be caused by the partial or complete restriction of electrons to penetrate the sample and thus resulting in the build-up of static electric charges on the surface of the sample. The most common problem associated with charging is poor contrast in the image produced, which would hugely affect the image quality of composites such as those used in this study. In order to overcome the effects of charging, the sample is pre-coated with a conductive material such as carbon or metals such as chromium or gold [196].

In this study, SEM imaging was done using a Carl Zeiss Auriga Cobra Focused Ion Beam Scanning Electron Microscope (FIB-SEM). The accelerating voltage was maintained at 30 kV and energy high tension (EHT) voltage at 3.00 kV with magnification up to 60 000X for all the imaged samples. In a typical procedure a sample was mounted onto carbon tape and placed on the sample stage. The samples were then coated with carbon for pristine MOF samples or chromium for polymers and MOF/nanofiber composites, for at least 15 minutes. After the coating, the samples were transferred into the FIB-SEM sample chamber which was maintained under vacuum for the duration of the analysis. A typical image of pristine MOF powder and pristine carbons included information about the shapes and sizes of the crystals, whereas that of the nanofiber material typically showed the fiber diameters and the presence or absence of

beads. In the composite materials, the FIB-SEM was coupled to an EDX detector in order to determine the distribution of MOFs on electrospun nanofibers and carbon substrates.

3.3.1.2. Transmission electron microscope (TEM)

The TEM technique works, in principle, similar to the SEM technique in that the imaging is produced from electron-electron interactions between the sample and the incident electron beam. In the TEM technique, the electron beam is higher in energy and allows for the imaging of materials down to the atomic scale. In TEM the interaction of the incident electron beam and the sample can result in either no scattering, single scattering or multiple scattering or a combination. The electron beam that experiences no scattering is captured on a fluorescent screen located beneath the sample and based on the electron density of the sample, a contrasting image consisting of bright and dark areas is produced. X-rays can also be scattered during the irradiation and using an EDX detector, elemental analysis such as mapping can be obtained from the sample [197]. In this study, TEM imaging was carried out on a 200 kV JEOL-Jem 2100 model. Each sample was dispersed in methanol and ultrasonicated for 30 minutes prior to transferring to the gold sample grid. After drying, the sample was then mounted onto the TEM stage and the analysis carried out under vacuum. The imaging was also coupled with EDX mapping and spectra to obtain the chemical composition of MOF/carbon composites and the distribution of MOF within the carbon substrates.

3.3.2. Spectroscopy

The intrinsic nature of MOFs is the crystallinity and permanent porosity of the MOF and as mentioned earlier, this study was based on predetermined materials with known structures. Spectroscopic techniques were used to confirm the chemical compositions of the selected MOFs and carbon-based materials. It is also widely reported that most MOFs, in particular UiO-66, can accommodate a large number of defects in their structure and that the post-synthesis treatment methods such as pelletization at high pressure and heat treatment may also result in structural and/or chemical changes to the MOF framework. The chemical composition of UiO-66 and its composites were monitored using Fourier Transform Infrared (FTIR) spectroscopy for both as-prepared and post-synthesis treated samples. Raman spectroscopy was further used to analyze the chemical composition of the GF obtained using the CVD method. Graphene can be obtained in different forms such as single layers or multilayers and

using Raman spectroscopy it is possible to distinguish between the different structures of graphene prepared using the CVD method [77,198,199].

3.3.2.1. Fourier transform infrared (FTIR) spectroscopy

Infrared (IR) spectroscopy involves the absorption of infrared light by molecular bonds. The technique involves exposing a molecule to a wavelength range in the infrared region, and due to the constant bond vibrations within a molecule, some of the light is absorbed at specific wavelengths that resonate with the specific bond vibrations in the molecule. There are, however, certain requirements for a molecule to be IR active and the most important is that the molecular bond must have a permanent or inducible dipole moment during bond vibration. In this study, an investigation was carried out on terephthalate-based MOFs UiO-66 and MIL-101(Cr), containing numerous polar bonds within their structures and thus expected to be IR active. The polymers used for electrospinning also have a high degree of polarity within their structures, e.g. the nitrile (-C≡N) and ester (-O-C=O-) functional groups in PAN and PMMA respectively [200]. The IR spectra of the MOF and MOF/polymer composites were measured on a benchtop Bruker FTIR spectrometer ALPHA II in a scanning range of 4000 to 400 cm^{-1} at a scan speed of 10 and 24 scans per run.

3.3.2.2. Raman spectroscopy

Raman spectroscopy is a subset of vibrational spectroscopy used to analyze symmetric vibrations in non-polar molecules. Raman spectroscopy differs to IR spectroscopy in that in Raman, the interaction of the molecule with light is not based on resonance effects, rather involves inelastic light scattering where a high-energy incident light beam loses some of its energy to the molecule and results in the scattering of low-energy light. The chemical composition of the non-polar molecule gives rise to a fingerprint frequency spectrum resulting from its Raman interaction with light. Raman spectroscopy has been shown to be very useful in the analysis of graphene and graphitic carbon forms [198,199,201]. In this study, Raman spectra of graphene foam (GF) were measured using a Jobin–Yvon T64000 Raman spectrograph with a 514.5 nm line Argon (Ar) ion laser.

3.3.3. Crystallography

The monitoring of the crystalline phases of the selected MOFs was a key factor in this study for the purposes of investigating the effect of pelletization on the stability of the MOFs and to elucidate the incorporation of MOFs within electrospun MOF/polymer nanofiber composites. As the study was based on predetermined MOFs, UiO-66 and MIL-101(Cr) it was most important to confirm the crystalline phases of as-synthesized MOFs to the those reported in literature and also monitor any deviations obtained experimentally that may be different to the structures and crystalline phases reported in literature for the respective MOFs. In this study, Powder X-ray Diffraction (PXRD) was specifically used since the aim was not to synthesize single crystals, rather to obtain polycrystalline MOF powders suitable for bulk pelletization into shaped pellets. The analysis of PXRD patterns was also important for the identification of MOFs upon their incorporation into electrospun MOF/nanofiber composites by monitoring the most prominent or characteristic crystalline phases (peaks) when embedded in the polymer nanofiber matrix. The use of PXRD was further key in monitoring possible changes in crystalline phases of UiO-66 upon its activation at different temperatures (80 – 320 ^{o}C) and also to monitor the subsequent effects of pelletization on the crystal structures of the different forms of UiO-66 (hydroxylated and dehydroxylated forms).

3.3.3.1. Powder X-ray Diffraction (PXRD)

Crystalline materials can be described as materials that are made up of an ordered array of atoms that form repeating units throughout the material's structure known as crystal planes, and these in turn constitute a crystal lattice. When an X-ray beam interacts with the crystalline phases, the X-rays are scattered/reflected in all directions, but at specific angles (Ɵ), some X-rays undergo constructive and destructive interference giving rise to a diffraction pattern as described by Bragg's Law (Fig. 3.7 and Eq. 3.1).

$n\lambda = 2dsin\theta$ ……(3.1)

n – an integer

λ – the wavelength of the X-ray

d – spacing between crystalline planes

θ – the angle created between the incident X-ray beam and the scatter plane.

The resultant diffraction pattern gives information about the atomic positions within the material's structure which in turn can be built up to determine the crystal structure of the material in terms of its unit cell [94,202]. PXRD was specifically used for analysis since the MOF synthesis conditions employed do not promote the formation of single crystals but rather the formation of a polycrystalline product with varying crystal sizes. The diffraction data was collected on a Rigaku Ultima IV diffractometer with CBO technology. The X-rays were generated using a Ni-filtered Cu-K_α radiation of 0.154 nm at a voltage and current of 40 kV and 30 mA respectively. The scanning speed was kept at $2^{o}{\cdot}s^{-1}$ and sampling width at 10 mm for all samples. The sample preparation of MOF powder samples involved finely grinding about 400 mg using an agate mortar and pestle, whereas the nanofiber samples were cut into sheets so as to fit into the well of the sample holder. The Rigaku Ultima IV diffractometer uses a fixed stage instead of a rotating stage allowing for the nanofibers to remain fixed on the sample holder for the duration of the analysis.

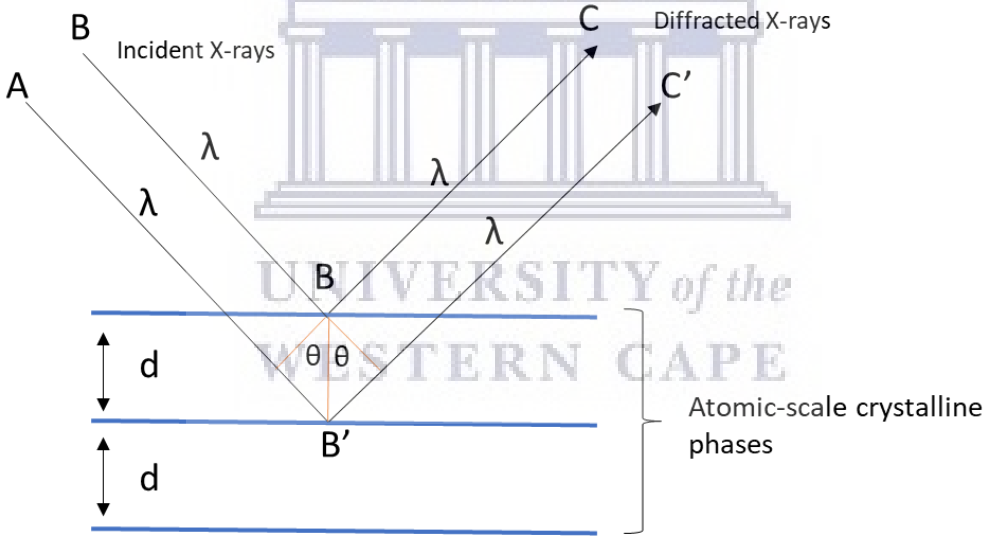

Figure 3.7: Schematic representation of constructive interference as described by Bragg's Law.

3.3.4. Thermal analysis

The response of MOFs to increasing temperature can be used as an indication of its thermal stability and more importantly in determining the thermal conductivity which is an important property for hydrogen storage applications. The physisorption process is exothermic, generating heat as gas molecules occupy the surface of the adsorbent. It is important that the

heat generated be sufficiently dissipated in order to maintain the structure of the MOF during adsorption. This would require the MOF material to have sufficiently high thermal stability and show good thermal conductivity. In this study, the thermal conductivities and thermal stabilities were compared between powder and pelletized forms of pristine MOFs to that of the MOF/carbon composites in order to obtain a possibly optimized sample that would be suitable for high pressure H_2 uptake up to 100 bar.

3.3.4.1. Thermogravimetric analysis (TGA)

The thermal stability of MOFs is an important property that determines the durability of the MOF upon exposure to increasing temperatures. The organic linkers in MOFs make them susceptible to thermal decomposition at rather lower temperatures compared to other porous solids such as zeolites [55]. Thermal stability is therefore an important property to consider MOFs for H_2 storage systems. The thermal stabilities of pristine and composite materials were measured with a thermogravimetric analyzer (TGA) (Mettler, Toledo, TGA/SDTA 851e) and the TGA-MS profiles obtained using a Discovery series Hi-resTM TGA-MS for the compositional analysis of gaseous by-products given off during decomposition of UiO-66 in air. In a typical procedure, a 10 mg sample was heated to 1000 ^oC at a ramp rate of 10 $^oC\ min^{-1}$ under 100 $mL.min^{-1}$ air flow. The analysis of the TG plots was done using TA Universal analysis software in order to extract derivative weight change and heat flow plots.

3.3.4.2. Thermal conductivity

The thermal conductivity of a material is a measure of the degree it can transfer heat through its structure. In materials with low thermal conductivity, heat transfer occurs at a slow rate while in materials with high thermal conductivity the rate of heat transfer is high [203]. The thermal conductivity measurements of pristine MOF, carbon and MOF/carbon composites were carried out using a C-therm thermal conductivity analyzer with a Modified Transient Plane Source (MTPS) sensor. The test was done under ambient conditions (~25 ^oC at atmospheric pressure) on ~ 2 g powder samples and 5 mm thick x 20 mm diameter pelletized samples. In a typical procedure, the instrument was first calibrated using a pyrex standard with a conductivity range of 1.085 to 1.200 W/m.K and effusivity between 1365.9 to 1509.7 $Ws^{1/2}/m^2.K$. An example of the sample placement for powder and pelletized samples is shown in Fig. 3.8.

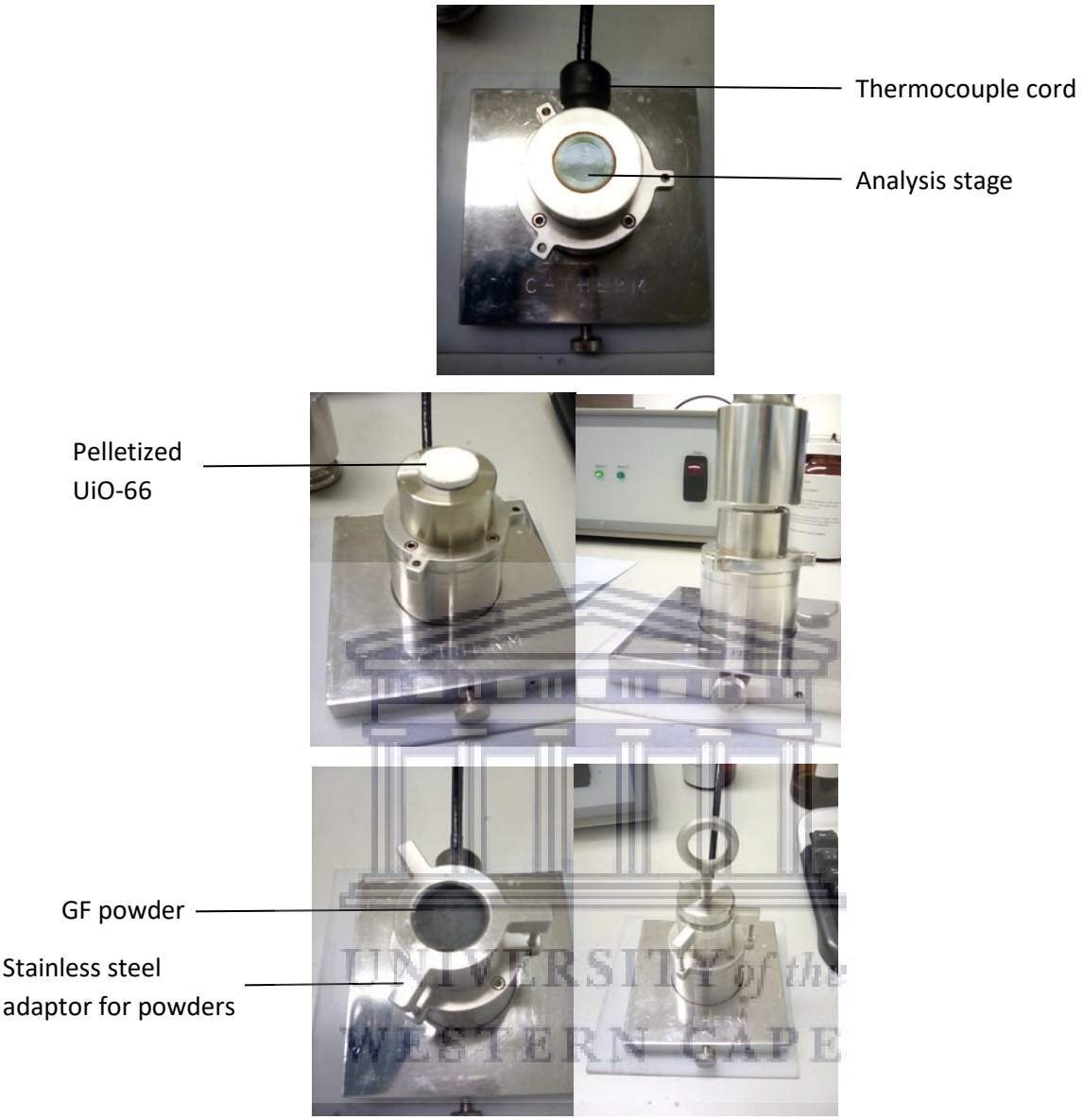

Figure 3.8: Images showing the setup of the C-therm thermal conductivity analyzer and the mounting of pelletized and powder samples onto the analysis stage.

3.3.5. Gas adsorption

Gas adsorption is an integral tool for the analysis of porous materials because it is widely accepted that the physisorption of gas molecules increases with decreasing temperature and increasing pressure. The permanent porosity of MOFs renders their gas adsorptive properties a key property in the storage of gases such as H_2 by the physisorption mechanism. It has been generally shown that the H_2 uptake in MOFs is proportional to the BET surface area via the

Chahine rule and also affected by the MOF density [39][13]. In this study, we employ gas adsorption methods such nitrogen (N_2) adsorption at 77 K and helium (He) pycnometry to measure the Brunauer-Emmett-Teller (BET) surface areas and densities respectively, for the pristine MOFs and composite samples.

3.3.5.1. Nitrogen (N_2) adsorption

The BET theory considers the adsorption of multilayers of gas molecules onto the adsorbent's surface and pore walls. The consideration of multi-layered gas adsorption is especially applicable where gas molecules may condense onto the adsorbent surface and/or within the pore walls due to increased intermolecular gas-gas interactions. These conditions are true for nitrogen gas adsorption at its boiling point (77 K) and increasing pressure. In a typical procedure, N_2 gas is incrementally dosed onto the adsorbent as the pressure increases from a partial pressure of $P/P_o = 0$ to $P/P_o = 1$, where P is the gas pressure of N_2 and P_o its vapour pressure at 77 K. The amount of adsorbed N_2 is calculated, using equation 3.2, as the volume of N_2 taken up or released (desorption) by the adsorbent at standard temperature and pressure (STP).

$$\frac{P}{V_a(P_o-P)} = \left(\frac{1}{CV_m}\right) + \frac{C-1}{V_m C}\left(\frac{P}{P_o}\right) \quad \text{.....(3.2)}$$

V_a – amount of N_2 adsorbed at a specified pressure P.
V_m – amount of N_2 adsorbed when the whole adsorbent surface is covered by a monolayer.
C – constant derived for multilayer adsorption.

The BET surface area is calculated in the linear region of the adsorption isotherm using the value of V_m and taking into consideration the area occupied by single, closely packed N_2 molecules on the adsorbent surface. The derivations and assumptions to the BET theory and equation are available in literature [118].

In this study, the BET surface area and porosity were measured on a 3-flex Micromeritics analyser using high purity N_2 gas (99.999 %). The BET surface area was calculated between $0 < P/P_o < 0.09$ and the pore volume calculated at $P/P_o \sim 0.99$ using the non-linear density functional theory (NLDFT) model. The activation/degassing of samples, prior to each analysis,

was done under vacuum using a Micromeritics SmartVac at 80, 110, 140, 170, 200, 230, 260, 290, and 320 ^{o}C for UiO-66 samples, 200 ^{o}C for MIL-101(Cr) and 80 ^{o}C for UiO-66@nanofiber and UiO-66/carbon composite samples.

3.3.5.2. Gravimetric hydrogen (H_2) adsorption

Hydrogen storage is the main focus area of this study and in order to determine the H_2 uptake capacities of the materials of choice, gravimetric H_2 adsorption isotherms were measured at cryogenic (77 K) and ambient temperatures (298 K) up to a H_2 pressure of 100 bar. Under the specified conditions, H_2 exists in gaseous form and as a supercritical fluid above 15 bar at 77 K [14,20] and its adsorption is via the physisorption mechanism. The gravimetric H_2 adsorption technique uses ultra-sensitive microbalances to monitor the change in weight of a sample as H_2 is incrementally added to the sample chamber. The measured data gives the excess H_2 adsorbed by the adsorbent which is then converted to total or absolute H_2 adsorbed using Eqn. 3.3.

$$\theta_T = \theta_{Exc} + \frac{d_{H2}\, x\, V_T}{(1+d_{H2}\, x\, V_T)} x\ 100\% \quad \text{.....(3.3)}$$

θ_T = total hydrogen uptake (wt%)
θ_{Exc} = excess hydrogen uptake (wt%)
d_{H2} = density (g·cm^{-3}) of compressed H_2 gas at the relevant temperature and pressure. The H_2 densities at 77 K in the 0 - 100 bar range were obtained from the National Institute of Standards and Technology (NIST) website (*Cited from: www.nist.gov*, 2019).
V_T = pore volume obtained from N_2 isotherm data.

Using the density of the MOF, the total/absolute gravimetric H_2 uptake can be converted in the total volumetric H_2 capacity using equation 3.4:

$$v\theta_T = \theta_T\, x\, d_{MOF} \quad \text{.....(3.4)}$$

$v\theta_T$= totalvolumetric uptake (g·L^{-1})
d_{MOF} = packing density of MOF material (g·L^{-1})

Equation 3.3 is described by the Langmuir model as the measurement conditions employed, 77 K or 298 K and 100 bar, are well above the critical point of H_2. It would, therefore, be expected that no possible condensation of H_2 would occur within the pore walls of the MOF and hence the maximum total or absolute H_2 capacity under these conditions would be expected to describe the amount of H_2 forming a monolayer surface coverage.

In this study, gravimetric H_2 uptake measurements were carried out using a Hiden Isochema XEMIS intelligent gravimetric analyser (Fig. 3.9). For each measurement, ultra-high purity 6.0 grade H_2 gas (99.9999 %) was used and buoyancy corrections were accounted for by using the skeletal density of each sample measured using He pycnometry. Prior to the analysis, each sample was degassed in-situ for at least 3 hours and up to 16 hours depending on the type of material. During the analysis, the hydrogen adsorbed was first equilibrated prior to recording the measured amount. The total time for each measurement was pre-set and fixed at ~13 hours including the desorption isotherm. As shown in Fig. 3.9, during the analysis at 77 K, liquid N_2 was added into a 5 litre canister and after 5-6 hours into the analysis, the canister was refilled in order to maintain the temperature at about 77 K to accommodate the desorption to occur to completion without a significant drop in the temperature.

Figure 3.9: Images of the Hiden Isochema XEMIS intelligent gravimetric analyzer, after analysis (left) and during liquid nitrogen refill (right), used to measure H_2 adsorption/desorption isotherms up to 100 bar at 77 K.

3.4. Density measurements

The highly porous nature of MOFs renders that they inherently have low densities in their pristine powder forms. In general the bulk/packing powder densities of MOFs do not exceed 1.0 g.mL^{-1} and the ultra-high surface area MOFs with pore volumes greater than 1 – 2 cm^3.g^{-1} tend to show even lower bulk/packing densities. As previously discussed in chapter 2, one of the strategies most commonly used for improving the packing density of MOFs has been the pelletization of MOF powders into pellets. It is also important to note that the use of the packing density alone for the calculation of the total volumetric H_2 capacity from gravimetric H_2 uptake data is not yet universally accepted as a standard format as some authors have reported the use of both skeletal and crystal densities of MOFs in their calculations. In this study, particular interest was on the work of Ahmed et al. [2] who developed an equation for the conversion of gravimetric H_2 uptake data into volumetric H_2 capacities which involves the use of the skeletal and crystal MOF density (Eqn. 3.5) [2].

$$n_v = p_{crys} n_{ex} + p_{gas}\left(1 - \frac{p_{crys}}{p_{sk}}\right) \quad \text{.....(3.5)}$$

n_v = total volumetric H_2 capacity (g·L^{-1})
p_{crys} = single crystal density for UiO-66 (1.24 g·cm^{-3} as reported by Goldsmith *et al.* [100]).
n_{ex} = measured excess H_2 adsorption (g·kg^{-1}).
p_{gas} = bulk density of H_2 gas at a given pressure (g·dm^{-3}) obtainable from the NIST website (*Cited from: www.nist.gov*, 2019).
p_{sk} = skeletal density of the MOF (g·cm^{-3})

The study, therefore, also compares the volumetric H_2 capacity values obtainable using Eqn. 3.4 and 3.5 and the results are given in chapter 4.

3.4.1. Packing density

In this study, the packing densities for powder samples was measured using finely ground samples packed (20 – 30 taps) into a container (pycnometer sample holder) with a fixed volume of 1 mL. The difference between the weight of the empty container and the packed container was recorded as the packing density of the powder. For the pelletized MOF samples, the

thickness of each pellet was measured using a digital calliper (Fig. 3.10) and the packing density calculated using the volume of the pellet (πr^2 x thickness). All packing density calculations were measured on activated/degassed samples and each measurement was repeated three times.

$$d_{MOF} = \frac{m}{\pi r^2 h} \quad \text{.....(3.6)}$$

d_{MOF} – Packing density of the MOF ($g \cdot mL^{-1}$)
m – mass of MOF pellet (g)
r – radius of the pellet (cm)
h – thickness of the pellet (cm)

Figure 3.10: Images showing the measurement of the thickness of pelletized UiO-66/GF (left) and UiO-66 (right) used to calculate their packing densities.

3.4.2. Helium pycnometry for density measurements

The density measurements were done to determine the skeletal densities for the pristine MOFs and MOF/carbon composites, an important property for MOFs in H_2 storage applications. The skeletal density has been shown to have a significant influence on gravimetric H_2 isotherms, especially at high pressure as low skeletal densities tend to give inflated excess H_2 uptake measurements [11]. The skeletal density has also been used to calculate the volumetric H_2 capacity from gravimetric H_2 uptake data [2]. It is therefore imperative that the skeletal density be measured as accurately as possible to its true value. In this study, helium (He) pycnometry was employed at standard temperature and pressure using an automated Micromeritics AccuPyc II 1340 model (Fig. 3.10). In a typical procedure, a sample of about ~0.3g was loaded onto a sample holder with fixed volume (1 cm^3) and 5 cycles of He gas introduced and vented

as described in the Micromeritics user guide to give 5 measurements of the sample volume, and the average volume used to calculate the skeletal density. According to the ASTM D3766 standard, the powder skeletal density is described as the ratio of the mass of the solid to the sum of the solid volume and volume of closed pores.

Figure 3.11: Image of the Micromeritics AccuPyc II 1340 helium pycnometer used to measure the skeletal densities of pristine MOFs and MOF composites.

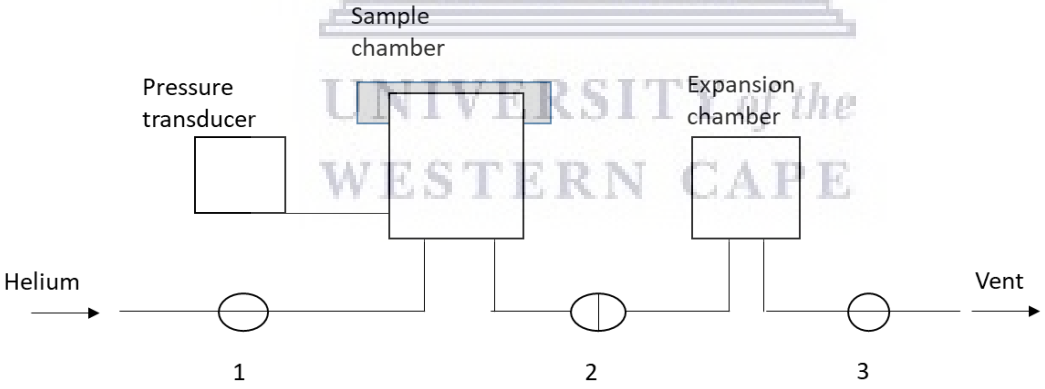

Figure 3.12: Schematic representation of the cross-section of a typical automatic helium pycnometer used for fixed sample cell sizes.

3.5. Chapter summary

This chapter demonstrated the various types of methods used for the synthesis of pristine UiO-66 and MIL-101(Cr) powders using predetermined synthesis conditions. The shaping of the MOF powders was done using two techniques, namely: electrospinning and pelletization. The electrospinning strategy involved single-nozzle electrospinning which allowed for the electrospinning of a single polymer solution/emulsion to obtain nanofibers, and a coaxial electrospinning strategy which allowed for the electrospinning of two different types of polymer solutions/emulsions in order to produce core-shell nanofibers. The single-nozzle electrospinning strategy was particularly used to optimize the electrospinning process parameters and establish conditions, such as the concentration of the polymer; magnitude of the voltage; and distance of the collector from the needle tip, which would also be applicable in the coaxial electrospinning strategy. The pelletization method was utilized on both pristine MOFs (UiO-66 and MIL-101(Cr), without the use of binders, and also UiO-66 with nanofibers as binders. The UiO-66 was more suitable for pelletization with binders compared to MIL-101(Cr) as it could be synthesized in bulk from a single batch, whereas only small yields of MIL-101(Cr) could be obtained from the multi-batch system used in this study. The characterization of the materials was mainly based on the analysis of the structure of the materials (crystallinity, morphology, chemical composition, and stability) and their gas adsorption properties (N_2, H_2, and He) giving information about the surface areas, pore volumes, H_2 capacities, and density of the selected materials.

Chapter 4

4. Synthesis and fabrication of powdered UiO-66 and MIL-101 into pellets for H_2 storage applications

This chapter covers the study of pre-existing synthesis conditions for UiO-66 and MIL-101(Cr) in which the textural properties (surface area and pore volume) could be tailored to achieve desired H_2 uptake capacities up to 100 bar. The BET surface areas of MOFs have been shown to be related to cryogenic H_2 adsorption (typically at 77 K) by the Chahine rule, which states that for every 500 $m^2 \cdot g^{-1}$, the excess H_2 uptake in MOFs increases by 1 wt% [204]. The chapter will first cover the solvothermal synthesis of the selected MOFs and the post-synthesis conditions that would give the highest possible BET surface areas and pore volumes. The study on the best performing MOF samples selected for high pressure H_2 uptake measurements will be presented. The chapter further reports on the effect of pelletization of best-performing MOF samples at ~700 MPa, sufficiently higher than most applied pressures reported for MOFs [48,105,155,205]. The pelletization strategy was proposed to improve handling and shape functionality of MOF materials and, most importantly, exploit the possible improvement of the intrinsically low packing densities typical of MOFs. The packing density of MOFs has been shown to have a strong correlation to the volumetric H_2 capacity of the MOF. Balderas-Xicohtèncatl and co-workers developed a mathematical model similar to the Chahine rule which relates the packing density of the MOF to its volumetric surface area via the "hydrogen surface density" (1.9×10^{-2} mg·mL^{-1}) and their findings were further shown to be applicable to pelletized MOFs [48,105,155,205]. From the results presented in this chapter, the effect of pelletization of hydroxylated UiO-66 at ~700 MPa was published and available online on 12 November 2018, which was followed by the publication of the first experimental demonstration of the dynamic temperature-dependent behaviour of UiO-66, which is currently under review.

This chapter is divided into four main sections discussing the optimization of the textural properties of MIL-101(Cr) powder (section 4.1), pelletization of MIL-101(Cr) and its gas (N_2 and H_2) adsorption behaviour at 77 K(section 4.2), optimization of the textural properties of UiO-66 (section 4.3), and pelletization of UiO-66 and its gas (N_2 and H_2) adsorption behaviour at 77 K (section 4.4.). In each section there are three sub-sections discussing the characterisation of the MOF samples according to their electron microscopy imaging, analysis of crystallographic, spectroscopic, and thermal properties.

4.1. Optimization of textural properties in MIL-101(Cr) powder samples.

MIL-101(Cr) crystal growth was achieved using the method described in Chapter 3 (section 3.2.2). Due to the low yields obtained in the 150 mL reactor (autoclave) that was available in the laboratory, a multiple batch procedure was used to obtain sufficient amounts for characterization and gas adsorption analyses. Three MIL-101(Cr) batches were synthesized successfully from screening experiments using the conditions described in section 3.2.2 and their properties are compared from section 4.1.1 to 4.1.4 (figures 4.1 to 4.5 and Table 4.1).

4.1.1. Electron microscopy of MIL-101(Cr) samples

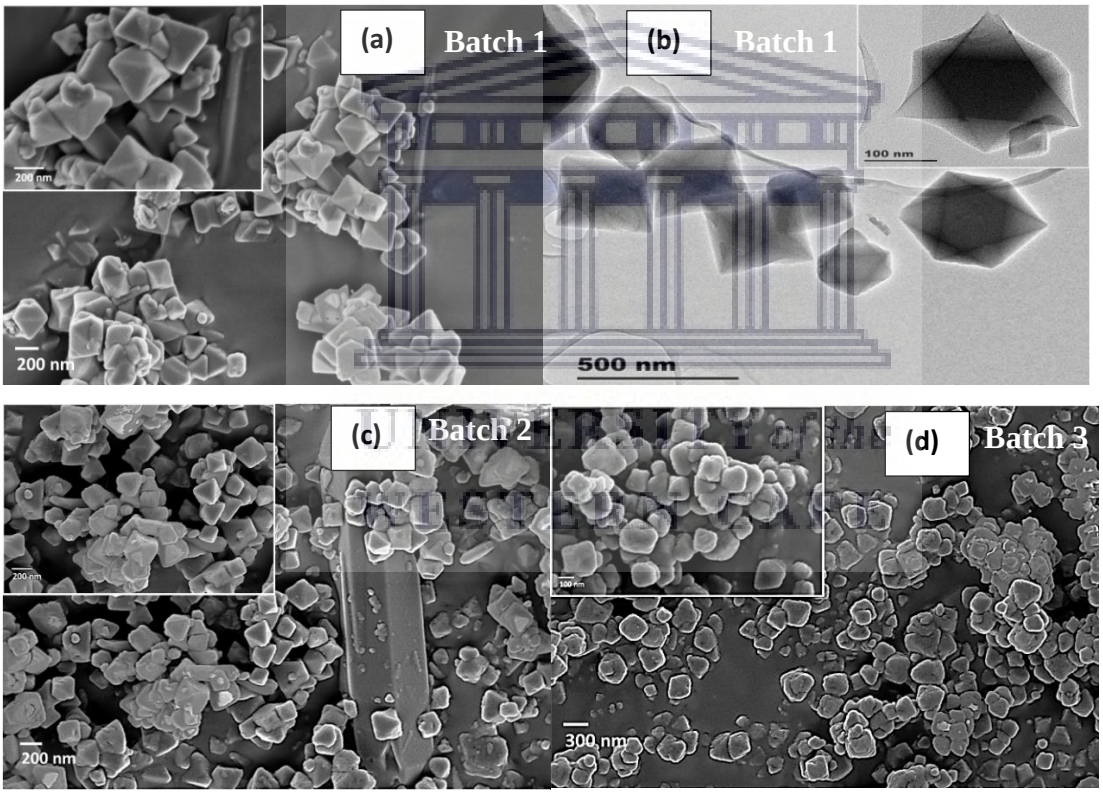

Figure 4.1: Morphology of MIL-101(Cr) samples: (a) SEM image of batch 1; (b) TEM image of batch 1; (c) SEM image of batch 2; and (d) SEM image of batch 3. All SEM insert images were obtained at 30 000 X magnification.

As it can be seen in SEM and TEM images (Fig. 4.1), the crystal sizes and shapes, amongst three batches successfully synthesized, showed the bulk polycrystalline material consisted of octahedral shapes with sizes ranging from 200 ~ 400 nm. To a lesser extent, elongated and

large multifaceted crystals could be observed particularly in batch 2, which may be due to unreacted terephthalic acid crystals or other impurities.

4.1.2. Thermal analysis of MIL-101(Cr) after post-synthesis treatment

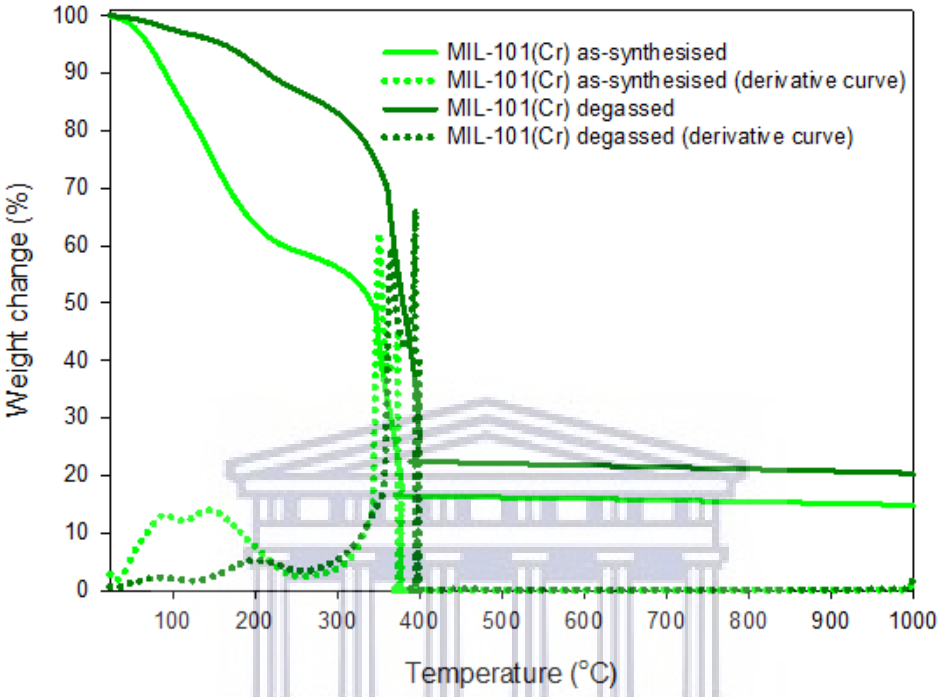

Figure 4.2: Thermal decomposition of a typical as-synthesized MIL-101(Cr) sample (batch 1) in comparison to a MIL-101(Cr) sample obtained after post-synthesis heat activation/degassing at 200 °C. The TG curves show the change in sample weight with increasing temperature under an air flow of 100 mL·min^{-1} and a heating rate of 10 °C·min^{-1}.

In Fig. 4.2, the derivative TG curve revealed decomposition steps at ~100 °C and 200 °C which could be attributed to adsorbed water and DMF or H_2O solvent molecules entrapped within the MIL-101(Cr) pores during the washing step. There are high chances of MOF pores to be occupied by guest molecules post-synthesis, and this is most likely to be solvent molecules used during the synthesis or washing stages [94,206]. The guest molecules can be evacuated by heating under vacuum (activation/degassing) or by the use of solvent exchange prior to degassing, or the use of supercritical CO_2 in extreme cases [94]. Due to the mesoporous and non-elastic pore structure of MIL-101(Cr), solvent exchange using acetone and subsequent degassing at 200 °C for 16 hours was found to significantly remove guest molecules. At temperatures higher than 200 °C, it was shown that MIL-101(Cr) was stable up to ~350 °C upon heating in air at 10 °C·min^{-1} and a solid residue remained at 1000 °C (~20 wt%). The peak

decomposition step at 350 ^{o}C could be attributed to framework collapse from the thermoxidation of terephthalate linkers into CO_2 and H_2O, assuming complete combustion, and leaving behind solid chromium (III) oxide (Cr_2O_3) which has a high melting point beyond 1000 ^{o}C.

4.1.3. Crystallography and spectroscopic analysis of MIL-101(Cr)

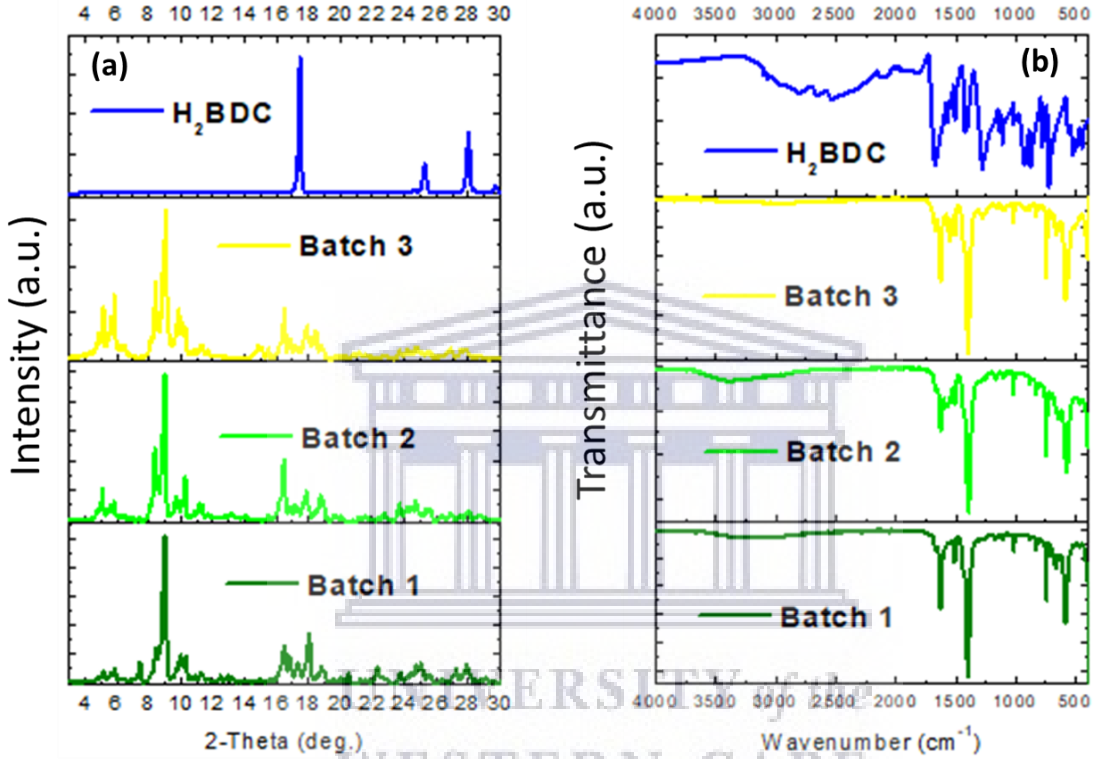

Figure 4.3: A comparison of the crystal structure and chemical composition of MIL-101(Cr) batches obtained under solvothermal conditions and post-synthesis heat activation/degassing at 200 ^{o}C: (a) PXRD patterns of finely ground MIL-101(Cr) powder and (b) FTIR spectra obtained in batch 1 (green), batch 2 (lime), and batch 3 (yellow).

The PXRD patterns and FTIR spectra in Fig. 4.3, showed little evidence of unreacted terephthalic acid (H_2BDC) as its characteristic high intensity Bragg peaks (2θ ≈17^{o}, 25^{o} and 27^{o}) and –OH stretch bands around 3300 cm^{-1} (H-bonded hydroxyls) were not prominent [88][89]. Both the PXRD and FTIR results in Fig. 4.3 showed consistent peak positions and vibrational band positions, respectively in each of the different batches, thereby suggesting the crystal geometry and chemical composition were consistent amongst the three batches. It was, however, noticeable that the relative peak intensities at Bragg peak ca. 5^{o}, 7^{o}, and 9^{o} became

reduced from batch 1-3. The observed changes could be caused by the possible appearance/disappearance of certain phases attributed to the aforementioned Bragg peaks via crystal-to-crystal transformations (e.g. metamorphism), which are typically observed during the synthesis of MOF crystals that can exist in different structural forms.

As the presence of unreacted terephthalic acid could not be justified based on the PXRD and FTIR data, another possibility for the appearance of needle-shaped crystals in the MIL-101(Cr) batches as shown in Fig 4.1 could have been the presence of MIL-53(Cr). It is well documented in literature that the chromium terephthalate MOF can exist in two polymorphs, MIL-101(Cr) as being the kinetic product, and MIL-53(Cr) as the thermodynamic product [90,207]. The synthesis time has been shown to be the major factor during the synthesis and as such, MIL-53(Cr) crystals are formed over longer synthesis times of about days to weeks compared to MIL-101(Cr) crystals which form over periods of hours from the start of the reaction. The acid modulator promotes a faster crystal growth rate, prompting the possibility that a small amount of MIL-53(Cr) crystals might form during an 8 hour acid-modulated synthesis [147]. Another possibility could be the formation of MIL-53(Cr) crystals via seeded crystal growth, given that MIL-101(Cr) crystals are present in solution at the start of the reaction. Indeed, due to the batch system utilized in this study, it was more likely that seeded growth might precede the growth of new crystals from solution since only one Teflon liner was used in the reactor for MIL-101(Cr) synthesis. The difficulty to remove solid MIL-101(Cr) from the walls of the Teflon liner could provide MIL-101(Cr) seed crystals for subsequent syntheses and could lead to seed-mediated crystal growth of MIL-53(Cr).

The consequence of having a mixture of MIL-101(Cr) and MIL-53(Cr) could have implications in the gas adsorption properties of the as-synthesised material. The two MOFs exhibit significantly different gas adsorption behaviour and textural properties (internal surface area and pore volume). The MIL-53(Cr) typically shows lower BET surface areas and pore volumes (~ 1000 $m^{2}{\cdot}g^{-1}$ and 0.5 $cm^{3}{\cdot}g^{-1}$, respectively), compared to MIL-101(Cr) (~ 2000 – 4000 $m^{2}{\cdot}g^{-1}$ and ~ 2 – 4 $cm^{3}{\cdot}g^{-1}$). MIL-53(Cr) N_2 adsorption isotherms are typically Type I isotherms representing a highly microporous crystal structure, whereas MIL-101(Cr) crystals exhibit more of Type IV N_2 adsorption isotherms which signifies a more mesoporous structure. In a mixture of the two, the presence of significant amounts of MIL-53(Cr) would reduce the BET surface area compared to pristine MIL-101(Cr), as it pertains to the law of mixtures [147,135].

4.1.4. Textural characterization of MIL-101(Cr) obtained from acid-modulated solvothermal synthesis conditions.

In Fig. 4.4, the adsorption isotherms for the MIL-101(Cr) samples prepared in this study showed full reversibility as both adsorption and desorption curves were observed to overlap. The shape of each of the isotherms was typical for Type IV adsorption curves showing monolayer capacities (saturation) at partial pressures (p/p_o) greater than 0.01, and also indicating the possible presence of a significant amount of mesopores within the adsorbent. There was also a near-vertical hysteresis loop observed for batch 1, extending from p/p_o 1.0 to 0.9 which typically represents a type H3 loop configuration in highly mesoporous materials, and the H3 configuration does not show any limiting adsorption at $p/p_o = 1.0$, as observed in Fig. 4.4 [118,121]. The higher N_2 adsorption observed for batch 1 compared to batches 2 and 3 could be a strong indication of a significant presence of MIL-53(Cr) co-crystals in batches 2 and 3 compared to batch 1, as a result of the possible seed-mediated crystal growth in batches 2 and 3. The absence of the H3 configured hysteresis loop in batches 2 and 3 could have further indicated their degree of mesoporosity was relatively small in comparison to batch 1.

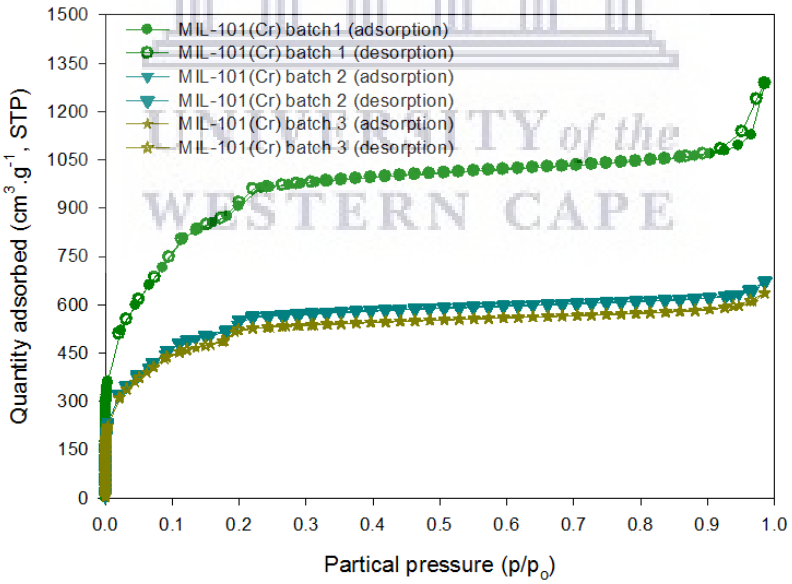

Figure 4.4: N_2 adsorption and desorption isotherms at 77 K for MIL-101(Cr) batches prepared under acid-modulated solvothermal conditions. The open symbols show the desopriton curve of the samples at 77 K.

It was further evident in Fig. 4.5 that the pore size distribution curves (fig. 4.5) showed a greater incremental pore volume in the mesopore region (20 Å ≤ pore ≤ 500 Å) for each sample. This

result was in support of the Type IV adsorption isotherms observed for the MIL-101(Cr) samples. There were significant pore sizes at ~6, 7.5, 12, 21, and 29 Å, which were consistent in all three batches of the prepared MIL-101(Cr) samples. The observed pore sizes compared well to those reported in literature, attributed to the free spaces inside the supertetrahedra (~8.6 Å), pentagonal windows (12 Å), hexagonal windows (14 Å by 16 Å), and two mesoporous cages at 29 Å and 34 Å. In literature, the optimum pore structure of MIL-101(Cr) typically consists of a cubic, zeolite-like super lattice crystal structure which can have Langmuir and BET surface areas around 6000 and 4000 $m^{2}{\cdot}g^{-}1$, respectively [85,208]. In Table 4.1, it can be seen that a BET surface area of 3300 $m^{2}{\cdot}g^{-1}$ was the highest obtained in this study, and BET surface areas of about 2000 $m^{2}{\cdot}g^{-1}$ were obtained for both batches 2 and 3. As it can be seen in Table 4.1, the micropore surface area and micropore volume of batch 1 made up ~15% and ~8% of the total BET surface area and total pore volume, respectively, and thus could be a clear indication that mesopores were the larger constituent of the MIL-101(Cr) internal structure. The micropore textural properties to the bulk textural properties, in batches 2 and 3, were higher at 20 and 30% micropore surface area, respectively (19 and 23% micropore volumes, respectively). The increased microporosity further could show evidence for the co-crystallization of the more microporous MIL-53(Cr) in batch 2 and 3 during the synthesis, as discussed earlier.

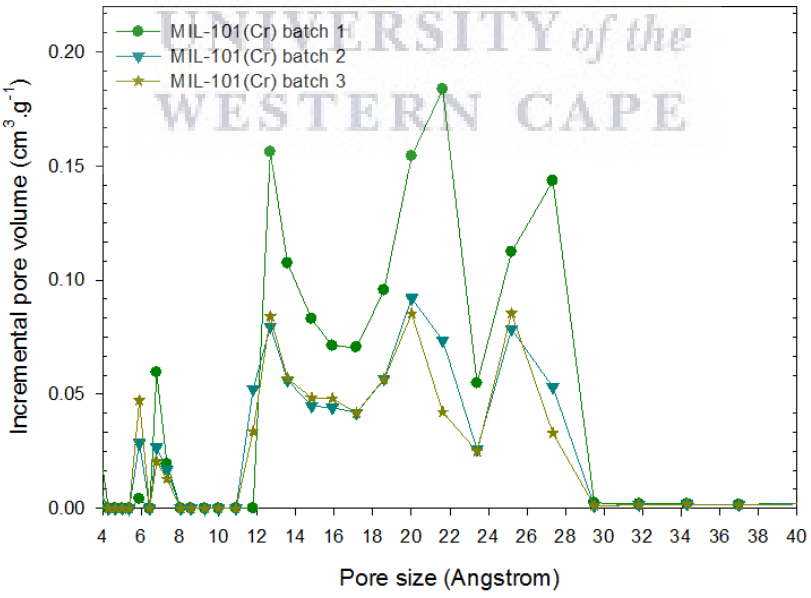

Figure 4.5: Pore size distribution (PSD) curves MIL-101(Cr) (batch 1 – 3) after post-synthesis activation/degassing at 200 °C for 8 hours. The PSD curves were deteremined from N_2 adsorption/desorption isotherms at 77 K using the NLDFT model.

Table 4.1: Summary of the BET report obtained for MIL-101(Cr) samples (batch 1 – 3).

Isotherm property	**MIL-101(Cr) sample**		
	Batch 1	**Batch 2**	**Batch 3**
BET surface area ($m^2 \cdot g^{-1}$)[a]	3343 (503, 15%)	2049 (610, 28%)	1974 (723, 37%)
NLDFT pore volume ($cm^3 \cdot g^{-1}$)[b]	2.00 (0.15, 8%)	1.04 (0.20, 19%)	0.99 (0.23, 23%)
Slope ($g \cdot cm^{-3}$, STP)	0.001280	0.0021	0.002172
Y-intercept ($g \cdot cm^{-3}$, STP)	0.000022	0.000034	0.000034
Q_m ($cm^3 \cdot g^{-1}$, STP)	768	471	453
Correlation coefficient	0.9997	0.9997	0.9996

[a]values in parentheses are given for the t-plot micropore surface area; [b]values in parentheses are given for the t-plot micropore volume.

The MIL-101(Cr) with the highest BET surface area and pore volume was clearly obtained in batch 1, however, it could not be assumed to be representative of the optimum crystal structure of MIL-101(Cr) as reported in literature. Due to the absence of the pore size at 34 Å and also the absence of crystalline phases expected at Bragg angles (2Ɵ) 3° and 4°, it could be assumed that the experimental synthesis procedure used in this study may not have prepared a MIL-101(Cr) product with an ideal MIL-101(Cr) unit cell as described in literature [208]. The BET surface area of 3300 $m^2 \cdot g^{-1}$, however, was sufficiently of high interest to analyze the H_2 uptake capacities in powder and pelletized MIL-101(Cr).

4.2. Pelletization of MIL-101(Cr) at ~700 MPa

In this section, the MIL-101(Cr) samples with the highest surface areas and pore volumes (batch 1) were selected for pelletization and high pressure hydrogen adsorption studies. The MOFs were subjected to a maximum applied pressure of 9 metric tonnes (equivalent to 665 MPa or ~700 MPa/100 000 psi in a 13 mm diameter die) in order to obtain highly densified MOF pellets with high packing densities. The effect of the pelletization on the structural stability of the MOFs was investigated by PXRD where the crystalline phases and peak positions were monitored for any significant changes upon compaction of the MOF powder samples.

4.2.1. Cryogenic N_2 adsorption/desorption isotherms for powdered and pelletized MIL-101(Cr)

In Fig. 4.6 the PXRD patterns comparing the MIL-101(Cr) powder sample to the pellet at 150 MPa showed that the peak positions shifted slightly towards lower 2Θ angles as indicated by the vertical lines. The peaks remained aligned between 150 and 440 MPa and more peak shifts could be observed at 590 and 665 MPa. The comparison between the peak positions observed at 665 MPa and the powder sample showed very significant shifting towards lower 2Θ angles for the pelletized samples. In the literature of nanostructured crystalline materials, the observations on PXRD peak shifting is typically encountered whenever there are stress and/or strain constraints introduced within a unit cell of the crystalline material [104]. Indeed it is reported in literature [61,135], that the MIL-101(Cr) crystals and topologies tend to show significant responsiveness towards applied pressure, such that anisotropic changes may occur in the unit cell upon application of sufficiently high pressures.

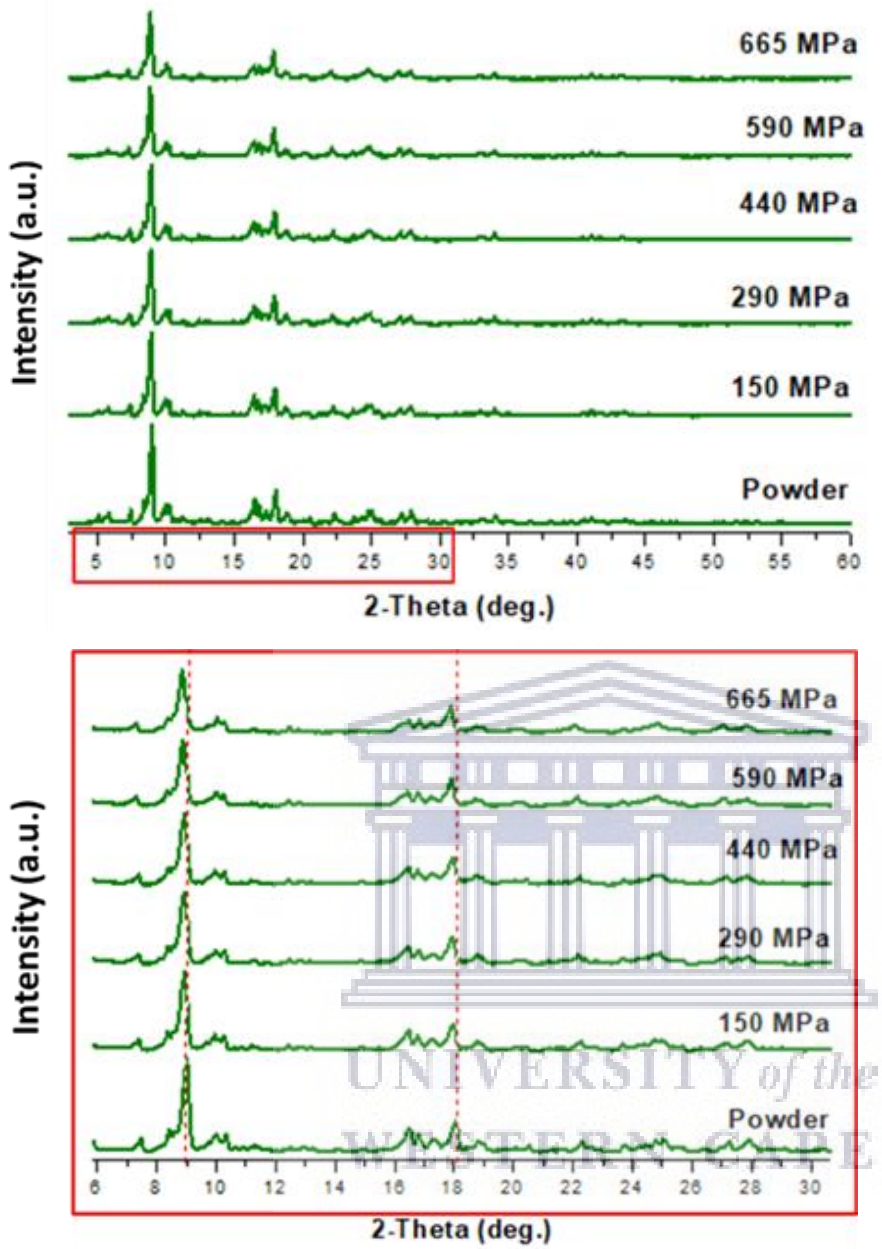

Figure 4.6: Crystallographic structural analysis of MIL-101 pelletized at increasing pressure: PXRD patterns for MIL-101(Cr) for powder and compacted samples (from batch 1). The plot on the right is an expansion of the region highlighted in the red box on the left plot.

The structural changes in MOFs under pressure have been reported at even lower pressures compared to the pressures applied in this study and include pore widening within the MIL-101(Cr) framework and at higher pressures, the framework may collapse resulting in a completely amorphous and non-porous powder [38]. It is therefore clear from previously reported literature that stress and strain introduced during the pelletization of MIL-101(Cr) could have a significant effect on the stability of its framework (unit cell) in terms of changing

the pore geometry or topology. The shifting of PXRD peak positions could be an indication of high stress and/or strain introduced into the MIL-101(Cr) framework upon pelletizing at pressures above 150 MPa. The majority of MOFs, with rigid and non-elastic pore structures, have been shown to exhibit mechanical strength with bulk moduli generally exceeding that of porous inorganic solids such as zeolites [70,161,204]. The shear modulus, on the other hand, compares significantly lower to the bulk modulus, making MOFs susceptible to shear deformations at sufficiently high pressures. A typical response and indication towards deformations in the pore structure of MIL-101(Cr) is typically signified in the measurement of reduced BET surface areas in MIL-101(Cr) pellets compared to their powder counterparts [135]. In Fig. 4.7 the N_2 adsorption/desorption isotherm for the MIL-101(Cr) pellet showed full reversibility and retained the Type IV isotherm as observed in the MIL-101(Cr) powder. The hysteresis loop, however, changed from Type H3 configuration to the Type H4 configuration which is generally characterized by a larger loop (p/p_o 1.0 to p/p_o 0.7). The BET monolayer capacity (Qm) was also lower for the MIL-101(Cr) pellet compared to the powder and evidently showed a reduction in the BET surface area (Table 4.1.2) upon pelletization of MIL-101(Cr) powder at ~700 MPa. The difference in hysteresis loops may have indicated a possible change in the pores of the MIL-101 structure as it was observed that the micropore volume of MIL-101(Cr) was significantly reduced upon pelletization at 700 MPa. Changes in pore structure could possibly introduce an ink-bottle effect between adjacent pores or, alternatively, the hysteresis may have been due to the restrictions in the diffusion of gas molecules during desorption from the highly densified or aggregated MIL-101(Cr) crystals in the pellet compared to MIL-101(Cr) crystals in the powder [51]. As described in the IUPAC technical report on adsorption of gases [39], both the ink-bottle effect and aggregated crystals are described to possibly result in Type H4 hysteresis loops, as observed in Fig. 4.7.

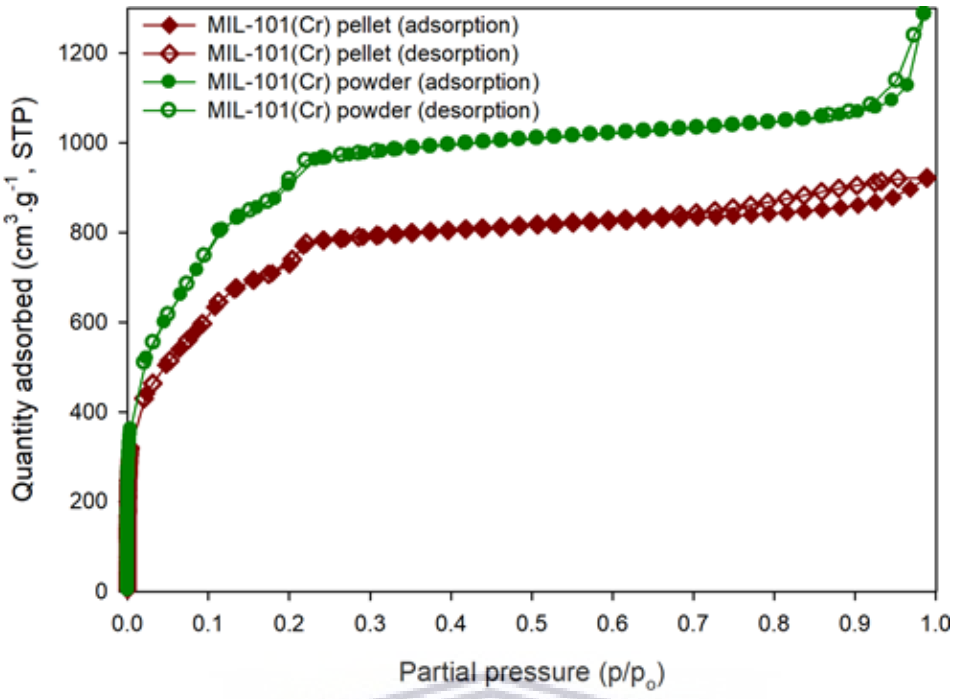

Figure 4.7: Cryogenic gas adsorption behaviour of MIL-101(Cr) before and after pelletization at 700 MPa: N_2 adsorption and desorption isotherms at 77 K for powdered and pelletized MIL-101(Cr) (batch 1). The MIL-101(Cr) samples were activated/degassed at 200 °C under vacuum for 16 hours prior to each measurement.

In Table 4.2, it was evident that the MIL-101(Cr) pellet showed a significant decrease in the micropore surface area being 8% of the total BET surface area (15% in MIL-101(Cr) powder) and a micropore volume 4% of the total pore volume (8% in MIL-101(Cr) powder). The results suggested a sensitive micropore structure in MIL-101(Cr) that may be compromised upon pelletization. As expected, the packing density of the MIL-101(Cr) pellet increased significantly compared to MIL-101(Cr) powder, from ~0.20 to ~1.10 $g \cdot cm^{-3}$. The H_2 uptake of powdered and pellet MIL-101(Cr) could be expected to resemble the trends in BET surface area, porosity and packing density as these properties have been shown to have a direct impact on the H_2 uptake via the Chahine rule and "H_2 surface density" [50].

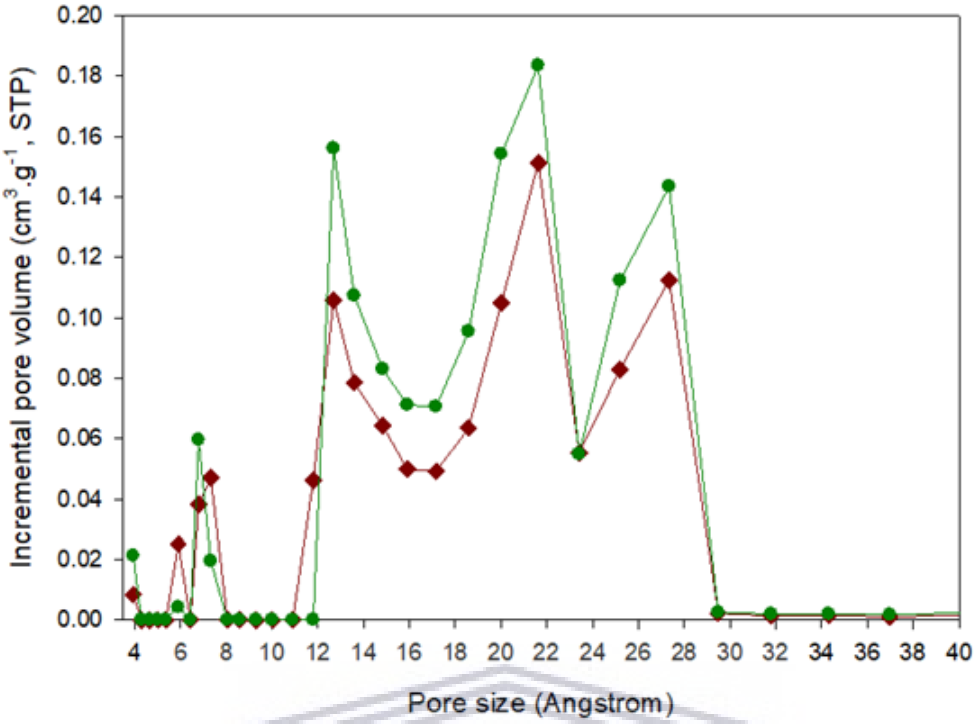

Figure 4.8: Pore size distribution curves for powdered and pelletized MIL-101(Cr).

Table 4.2: Summary of the BET report obtained for powdered and pelletized MIL-101(Cr).

Isotherm property	**MIL-101(Cr) sample**	
	Powder	**Pellet**
BET surface area ($m^2 \cdot g^{-1}$)[a]	3343 (503)	2661 (219)
NLDFT pore volume ($cm^3 \cdot g^{-1}$)[b]	2.00 (0.15)	1.43 (0.06)
Slope ($g \cdot cm^{-3}$, STP)	0.001280	0.001613
Y-intercept ($g \cdot cm^{-3}$, STP)	0.000022	0.000023
Q_m ($cm^3 \cdot g^{-1}$, STP)	768	611
Correlation coefficient	0.9997	0.9998
Packing density ($g \cdot cm^{-3}$)[c]	0.19 ±0.02	1.17 ±0.04
Volumetric surface area ($m^2 \cdot cm^{-3}$)[d]	635	3113

[a]values in parentheses are given for the t-plot micropore surface area; [b]values in parentheses are given for the t-plot micropore volume. [c]Calculated from experimental measurements using eqn. 3.6 in chapter 3 (section 3.5.1). [d]calculated by multiplying the packing density and the BET surface area [50].

4.2.2. H_2 adsorption/desorption isotherms for powdered and pelletized MIL-101(Cr) at 77 K up to 100 bar

This section reports on the gravimetric and volumetric H_2 capacities for powder and pelletized MIL-101(Cr). The H_2 isotherms were measured at 77 K and pressures up to 100 bar, correcting for buoyancy effects using skeletal density values from He pycnometry measurements. The working capacity, described as the difference between the amount of H_2 adsorbed at 100 bar (10 MPa) to that desorbed at 5 bar (0.5 MPa) [151], will be reported for both powder and pellet forms. Due to the measurements being conducted up to 100 bar, a prolonged period (> 10 hours) was required to conduct both adsorption and desorption in each measurement run. Therefore, it was possible that some plots did not show full reversibility in the desorption isotherms for H_2 adsorption measurements, though all samples would be expected to exhibit full reversibility. At times the temperature was well above 77 K at the end of the measurement run, as observed later in Fig. 4.24 for the UiO-66 powder sample, noting that the adsorption isotherm was conveniently recorded at 77 K, with the rise in temperature only occurring during the measurement of desorption as the sample was left to run overnight without sufficient levels of liquid nitrogen remaining in the canister. When the temperature was maintained at 77 K, the plots showed full reversibility for H_2 adsorption and desorption isotherms as it was observed in Fig. 4.9 and later in Fig. 4.19 and Fig. 4.28. The following results are based on the adsorption/desorption isotherms of powder and pelletized MIL-101(Cr).

4.2.2.1. Gravimetric H_2 capacity of powdered and pelletized MIL-101(Cr)

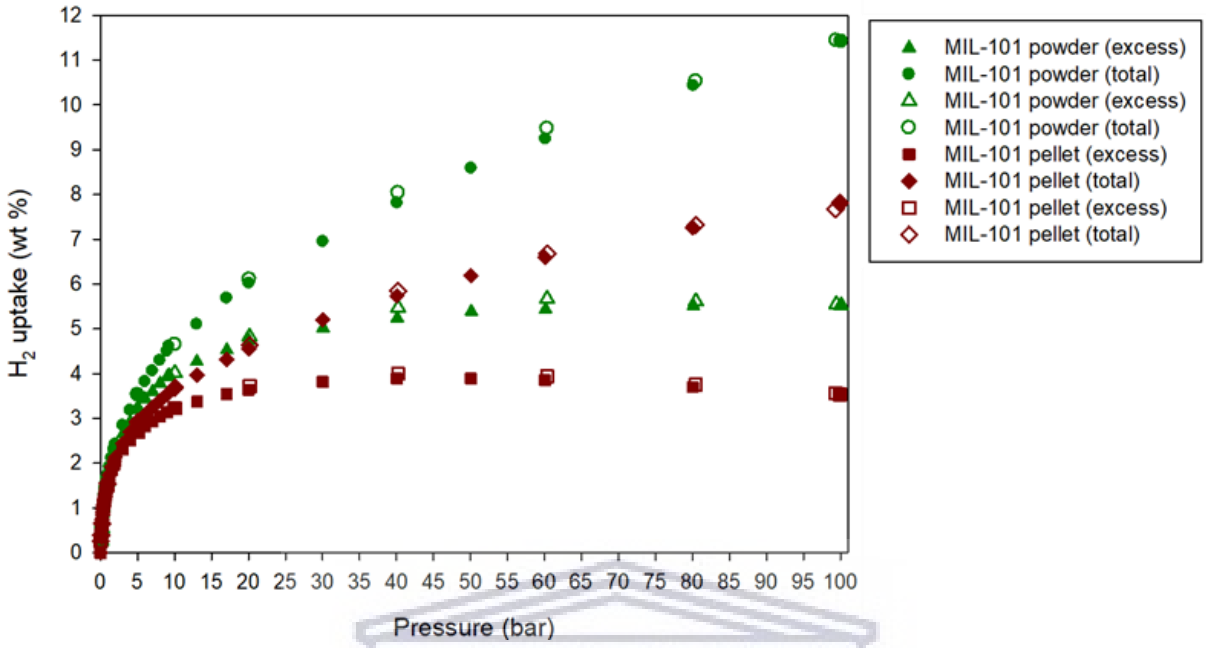

Figure 4.9: H_2 uptake for powder and pelletized MIL-101(Cr) measured at 77 K and pressures up to 100 bar. The closed symbols represent the adsorption H_2 isotherms and the open symbols represent the desorption H_2 isotherms.

It can be seen in Fig. 4.9 and Table 4.3 that the excess gravimetric H_2 uptake decreased by 29% after pelletization of MIL-101(Cr) at ~700 MPa. The results showed a strong correlation to the effect of pelletization on BET surface area and pore volume as shown in Fig. 4.7, Fig. 4.8 and Table 4.2. Based on the measured BET surface areas for both powder and pelletized MIL-101(Cr) (Table 4.3), the Chahine rule would estimate excess H_2 uptake values of ~6.7 and 5.4 wt% respectively.

The measured H_2 uptake in this study were about 18% (MIL-101(Cr) powder) and 28% (MIL-101(Cr) pellet) less than the estimated values. A contributing factor could be the synthesis of non-uniform polycrystallites of MIL-101(Cr) (Fig. 4.1) which could possibly show variations in the textural properties of individual crystals. Consequently the absence of the pore size at ~34 Å, as a result of pore blocking by strongly adsorbed solvent molecules, and the possible presence of MIL-53(Cr) crystals could result in excess H_2 uptake values that deviated from predicted values using the Chahine rule [209]. In Table 4.3, it can be seen that of the 11.4 and 7.8 wt% absolute/total gravimetric H_2 uptake, ~70% and 63% (for the powder and pellet,

respectively) was available as working capacity. This showed a further compromise of the H_2 adsorption properties of MIL-101(Cr) after pelletization.

Table 4.3: Summary of the excess and total/absolute gravimetric H_2 uptake obtained for powdered and pelletized MIL-101(Cr) at 5 and 100 bar at 77 K.

Sample	Maximum excess Uptake (wt%)		Total/absolute gravimetric H_2 uptake (wt%)[b]		Working capacity[c]
	Experimental	Estimate[a]	5 bar	100 bar	
MIL-101(Cr) powder	5.5	6.7	3.5	11.4	7.9
MIL-101(Cr) pellet	3.9	5.4	2.9	7.8	4.9

[a]Estimates based on the Chahine rule [209].[b]Calculated using eqn. 3.3 in chapter 3 (section 3.4.5.2). [c]Difference between the total H_2 uptake at 100 bar (adsorption) and 5 bar (desorption).

4.2.2.2. Volumetric H_2 capacity of powdered and pelletized MIL-101(Cr)

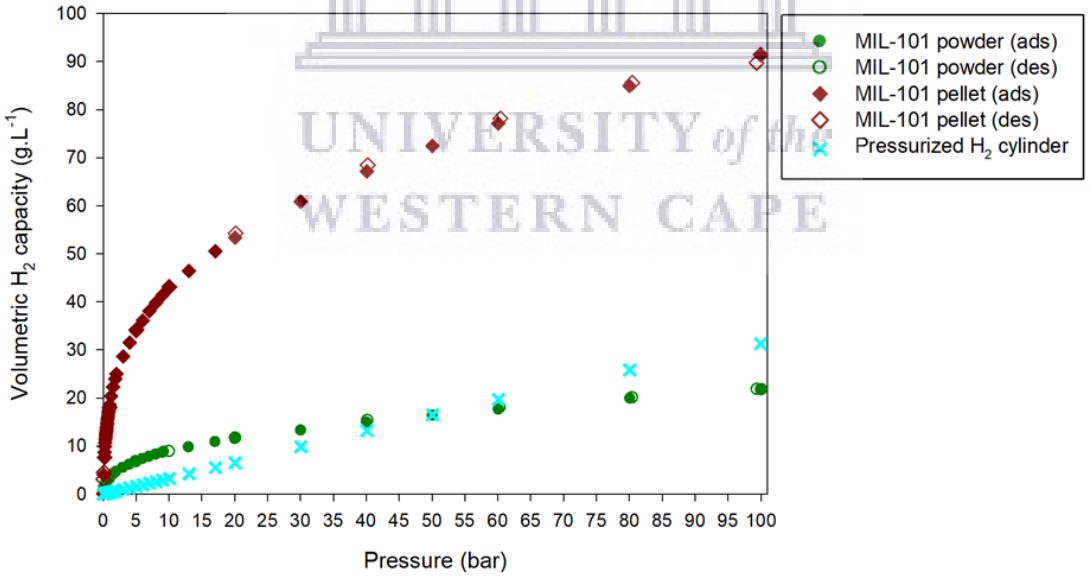

Figure 4.10: Total volumetric H_2 capacity for powdered and pelletized MIL-101(Cr) obtained at 77 K and pressures up to 100 bar. The closed symbols represent adsorption H_2 isotherms and open symbols represent the desorption H_2 isotherms.

There was a drastic increase in the volumetric H_2 capacity, as shown in Fig. 4.10, due to the improved packing density in pelletized MIL-101(Cr) compared to the powder. The volumetric

H_2 capacity of an "empty" H_2 cylinder (containing no adsorbent material) was shown to exceed that of the MIL-101(Cr) powder at pressures above 50 bar with almost double the working capacity between 100 bar and 5 bar (fig. 4.10). This observation could be a reflection on the inefficiency in packing powdered MOFs for H_2 storage compared to densified shaped forms. It is still a controversial topic on whether to use crystal density or packing densities of MOFs for volumetric H_2 capacity calculations but in this study, it was believed that due to the low practicality of packing single crystal MOF materials in cylinders, the powder packing/bulk density could possibly give more realistic and application-specific results. In Fig. 4.10 it was evident that the volumetric H_2 capacity of pelletized MIL-101(Cr) far exceeded that of the powder as well as that of a pressurized H_2 cylinder. The working capacity of the pellet was close to double that of a pressurized H_2 cylinder and almost four times compared to the powder, and remained 63% of the total volumetric H_2 capacity in the pellet. The results further substantiate the use of the pelletization fabrication strategy to improve volumetric H_2 capacities in MOFs, however, the observed reductions in BET surface area, pore volume, and gravimetric H_2 uptake may not be desirable for system applications. Indeed it is well-documented that the system application of MOF-based H_2 storage materials is preferred for stable MOFs under system conditions and with reasonably high gravimetric *and* volumetric H_2 capacities.

Table 4.4: Summary of the total volumetric H_2 capacity and working capacity for MIL-101(Cr) (powder and pellet) and within a pressurized H_2 cylinder.

Sample	Total volumetric H_2 capacity ($g.L^{-1}$)				Working capacity[c]
	5 bar	25 bar		100 bar	
		Experimental[a]	Estimate[b]		
MIL-101(Cr) powder	7	11	12	22	15
MIL-101(Cr) pellet	34	53	59	91	57
Empty H_2 cylinder	2	-	-	31	29

[a]Calculated using eqn. 3.4. [b]Calculated using the volumetric surface area (Table 4.2) and the "volumetric H_2 density" as recommended in ref [50].[c]Difference between the total H_2 uptake at 100 bar (adsorption) and 5 bar (desorption).

In the following section, the study investigates the effects of pelletization of the zirconium-based MOF, UiO-66, on its textural properties and H_2 uptake.

4.3. Optimization of textural properties in UiO-66 powder samples

In this section, the optimization of UiO-66 was slightly different to the optimization approach used for MIL-101(Cr). UiO-66 crystal growth does not necessarily require high pressure conditions to obtain well-defined crystal properties and can be synthesized using a reflux setup instead of an autoclave. This allowed the experiments to be carried out in relatively larger yields than MIL-101(Cr). The post-synthesis treatment of UiO-66 was a major interest as it has been shown that UiO-66 can exist in two forms, namely the hydroxylated and dehydroxylated forms. The hydroxylated and dehydroxylated forms have been reported to show different gas adsorption behaviour as shown in studies for CO_2 capture and H_2 storage. The dehydroxylated form generally shows reduced gas uptake capacities compared to the hydroxylated form and the conversion between the two forms is found to occur under thermal treatment conditions in the temperature range 100 – 300ºC [107,160]. In this study, the investigation of post-synthesis heat treatment is a key factor in obtaining UiO-66 crystals with optimum textural properties under the specified synthesis conditions.

4.3.1. Electron microscopy of UiO-66 powder

The morphology of the UiO-66 crystals obtained in this study show typical octahedral shapes as reported in literature (Fig. 4.11).

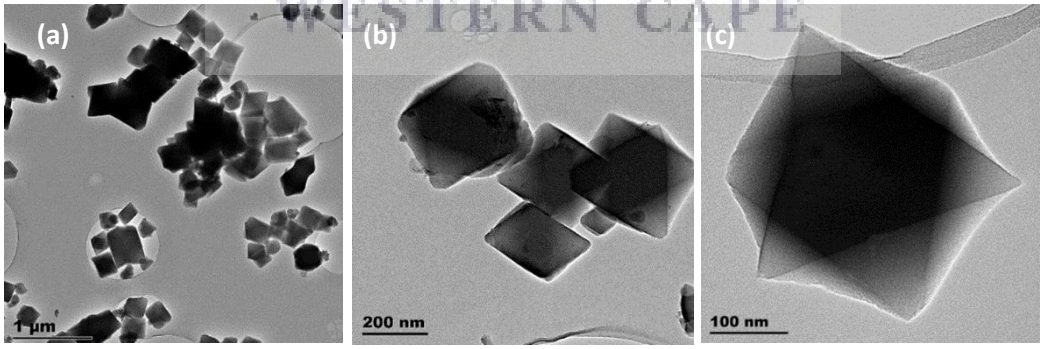

Figure 4.11: Morphological analysis of UiO-66 after post-synthesis activation at 80 ºC for 32 hours: TEM images showing the morphology of UiO-66 crystals at different magnification: (a) 10 000x; (b) 20 000x; and (c) 30 000x.

4.3.2. Crystallography of UiO-66 powder activated at low temperatures (80 ºC)

The crystal structure of UiO-66 has been well studied as having a cubic unit cell with typical major peak positions at 2θ angles of ~ 8, 9, and 25º. The PXRD patterns in Fig. 4.12 showed intense peaks at the theoretical peak positions of 6, 8, and 25º and the diffraction pattern from 2θ ~3 to 90º matched most of the proposed CIF structures for UiO-66 synthesized under solvothermal conditions. The presence of a peak at 2θ ~ 6º typically resembles crystals with a symmetry forbidden phase (1 1 0) which may result from defects in the crystals (Shearer *et al.*, 2016)[210]. Indeed UiO-66 is notorious for its extensively high level of tolerance towards structural defects with the crystal structure collapsing. Many studies have reported on stable UiO-66 defective structures with either missing terephthalate linkers or missing zirconia nodes as the defect sites in the structure [67,68,108,190].

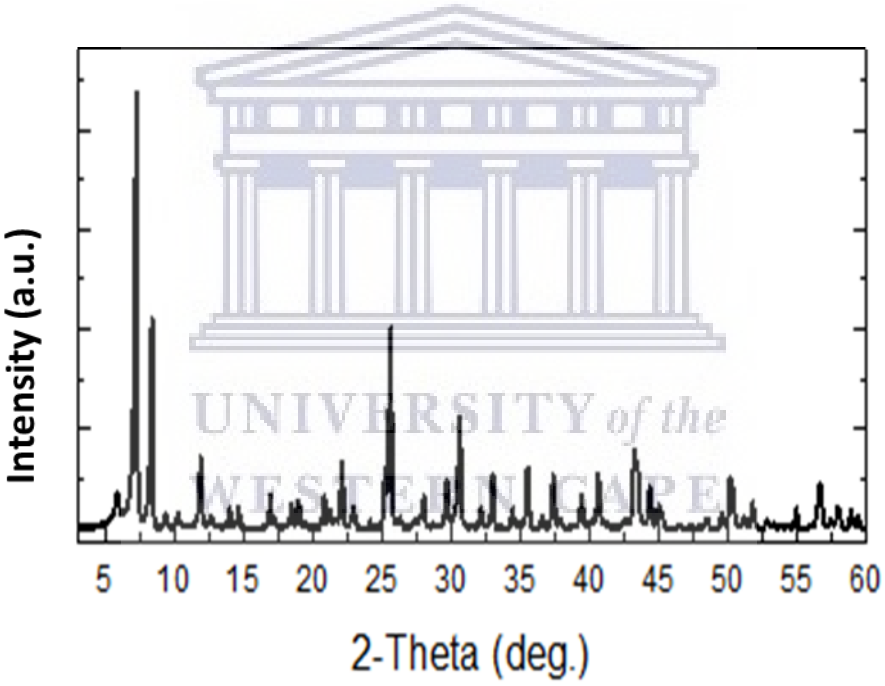

Figure 4.12: PXRD pattern of UiO-66 powder after solvent exchange with acetone followed by heat activation at 80 ºC for 32 hours.

The UiO-66 crystals have been generally shown to contain defects (missing linkers) under acid-modulated and solvothermal crystal growth conditions similar to this study [211].

4.3.2. Thermal decomposition and post-synthesis activation of UiO-66: Experimental demonstration of dynamic temperature-dependent behaviour

4.3.2.1. Thermal and chemical analysis of UiO-66 during post-synthesis activation

In Fig. 4.13 the thermal decomposition of UiO-66 was investigated by TG analysis, showing UiO-66 to be stable up to at least 500 ^{o}C. The remarkable thermal stability could be attributed to the high connectivity of the Zr-O bonding in UiO-66 nodes which can be made up of $Zr_6O_4(OH)_4$ in the hydroxylated form or Zr_6O_6 in the dehydroxylated form. The derivative curves in Fig. 4.13 showed the temperatures at which peak decomposition occurred as the temperature increased up to 1000 ^{o}C. There were three peaks observed at ~150, 250, and 500 ^{o}C for both the UiO-66 sample activated by solvent exchange with acetone and degassed at 80 ^{o}C prior to analysis. Upon degassing at higher temperatures, 200 and 290 ^{o}C, the two peaks at 150 and 250 ^{o}C were no longer observable, indicating the possibility for the removal of labile or weakly bound molecules from the UiO-66 structure. It is common in MOFs that guest molecules such as gases or solvent molecules can remain within the pores of the MOF after the synthesis.

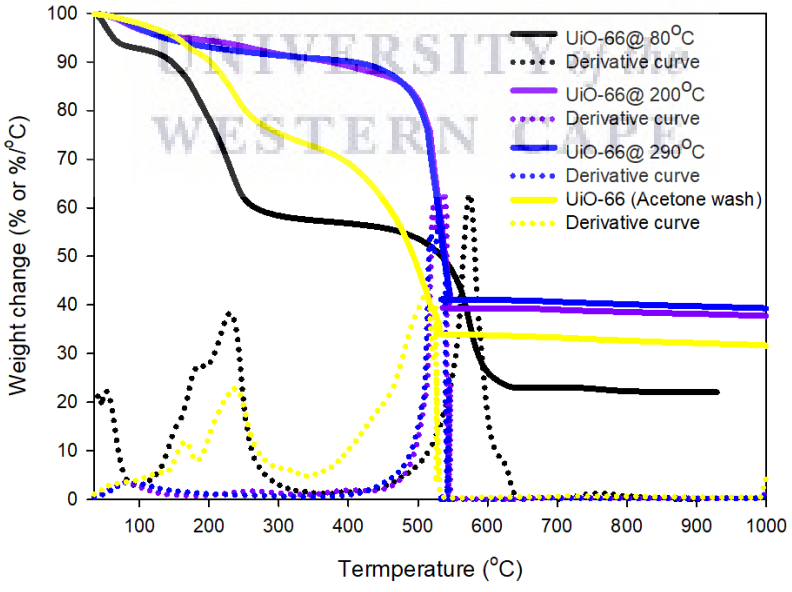

Figure 4.13: TGA curves showing the thermal decomposition of as-synthesised UiO-66 and after post-synthesis activation: degassed at 80^{o}C (black); degassed at 200^{o}C (purple); degassed at 290^{o}C (blue); and solvent exchange with acetone (yellow).

In Fig. 4.14, mass spectrometer (MS) signals were coupled to the TG curves in order to identify the composition of the gas by-products during the decomposition of UiO-66. The most prominent m/z signals were m/z = 18, indicative of H_2O, and m/z = 44 typical for the presence of CO_2. The m/z = 18 and m/z = 44 signals both peak at ~150 and 500 ^oC with the m/z = 18 signal showing a broad peak from ~150 to 300 ^oC and a small m/z = 44 peak at ~150 ^oC. The derivative weight loss peaks observed up to 100 ^oC were accompanied by a significant m/z = 18 peak and indicated the presence of moisture on the surface of the sample. The thermal events observed above 100 ^oC could be considered as resulting from the decomposition of the UiO-66 structure or due to other contaminants other than moisture.

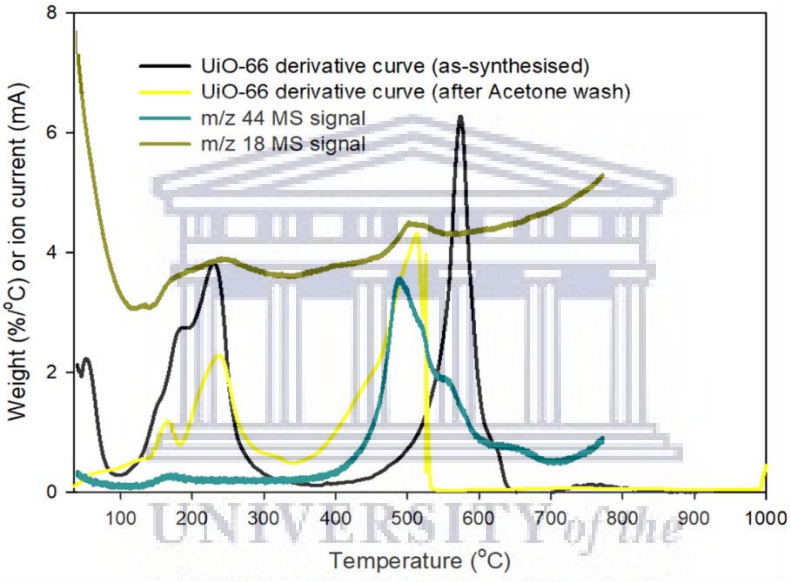

Figure 4.14: Thermal decomposition of as-synthesized UiO-66 in comparison to UiO-66 obtained after solvent exchange with acetone followed by heat treatment at 80 ^oC for 32 hours. The TG/DTG data was coupled with mass spectroscopic (MS) data as gaseous by-products were analysed by MS simultaneously with the thermal decomposition.

In Fig. 4.15 it can be seen from the FTIR spectra of as-synthesized UiO-66 that a significant amount of DMF was part of its structure. The solvent exchange with acetone was found to remove a significant amount of DMF molecules as the $–CH_3$ split band at 3000 cm^{-1}, -CN band at 1100 $cm^{-1}$and C=O stretch vibration at 1700 cm^{-1} are significantly reduced. The m/z = 44 signal can also indicate the presence of DMF molecules which can be ionised in the MS chamber to produce resonance-stabilised $[N(CH_3)]^+$ ions due to the lone electron pairs of the nitrogen atom [212]. The absence of other possible contaminants on the as-synthesized UiO-

66, therefore, means the decomposition of UiO-66 involved the removal of DMF and H_2O at ~ 150 ^oC, with the removal of H_2O continuing up to ~ 300 ^oC by dehydroxylation.

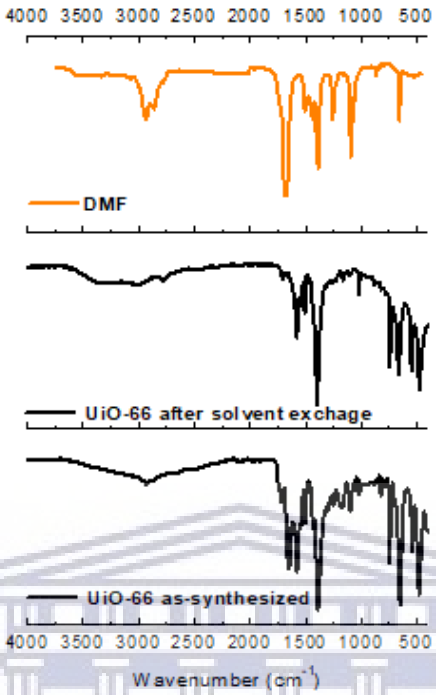

Figure 4.15: FTIR spectra for DMF, as-synthesized UiO-66, and UiO-66 after solvent exchange with acetone followed by heat activation at 80 ^oC for 32 hours.

The DMF molecules might have originated from the pores of the UiO-66 and H_2O molecules generated by the dehydration/dehydroxylation process reported to occur in UiO-66 crystals [72]. The m/z = 18 and m/z = 44 peaks at ~500 ^oC overlapped with the highest weight loss of the UiO-66 structure which is due to framework collapse resulting from the combustion of the terephthalate linkers into CO_2 and H_2O. At temperatures above 500 ^oC, the sample did not undergo complete decomposition as a residue of ~20 wt% of ZrO_2 remained for as-synthesized UiO-66 and ~36 wt% for the sample heated after solvent exchange with acetone. The increase in residue after solvent exchange could have indicated the removal of adsorbed molecules, most likely to be DMF solvent molecules as confirmed by FTIR in Fig. 4.15. The amount of ZrO_2 remaining has been used as an indication of UiO-66 structures with defects [84,106]. It is generally shown that a residue yield below 45 wt% would constitute at least one terephthalate linker deficiency per inorganic node/cluster in the UiO-66 structure, assuming an even distribution of defects. The highest residue yield obtained in this study was ~40 wt% for UiO-66 degassed/activated at 290 ^oC prior to TG analysis. The low yield may further substantiate the possibility of the UiO-66 structure having defects under the proposed synthesis conditions.

TG-MS and FTIR results, in this study, strongly suggested a dehydroxylation process occurring for UiO-66 between 150 and 300 ^{o}C. The observations prompted further analysis of the possible effect post-synthesis activation at high temperature would have on the UiO-66 textural properties.

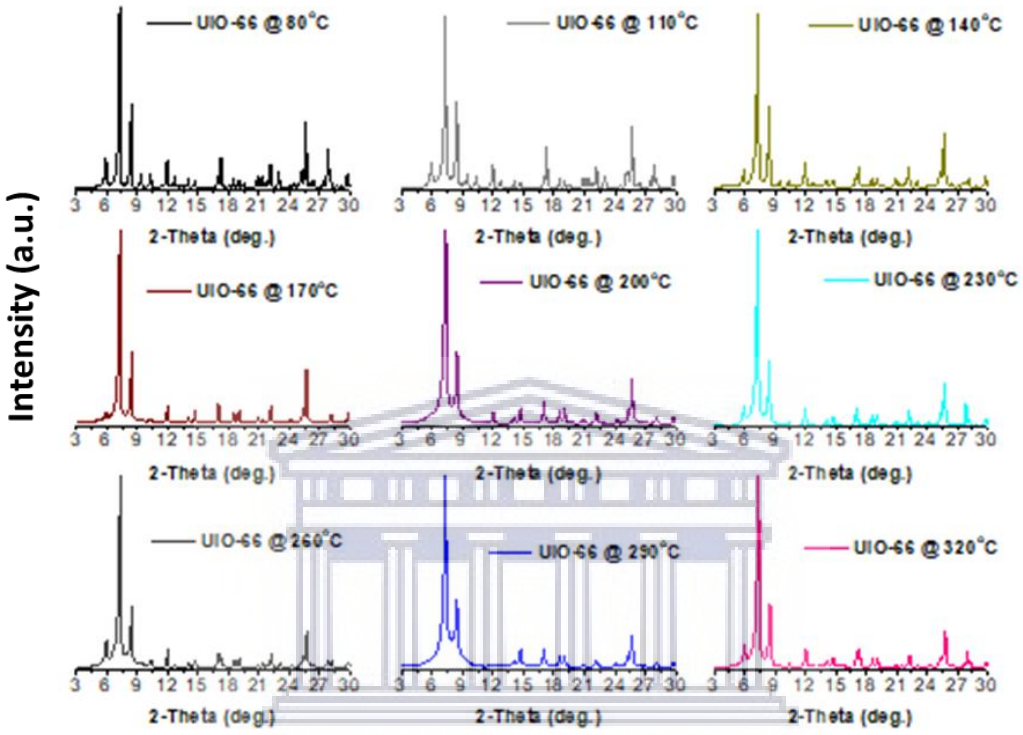

Figure 4.16: PXRD patterns for UiO-66 powder samples after activation/degassing at 80 – 320 ^{o}C (at 30 ^{o}C intervals). The samples were prepared by heating UiO-66 powder from room temperature to the target temperature at 10 ^{o}C·min^{-1} and maintained at the target temperature for 16 hours.

The results in Fig. 4.16 show the PXRD patterns for UiO-66 powder samples activated by heating for 16 hours under vacuum at the specified temperatures. It can be seen from the results that the main peaks at 2θ ~ 8, 9, and 25^{o} remained intact across all the activation temperatures which might indicate the bulk structure of UiO-66 remained unchanged upon heating to 320 ^{o}C, a result also confirmed by TG results in Fig. 4.13. There were noticeable differences at some peak positions which could have indicated possible changes to the crystal phases in the UiO-66 structure. In Fig. 4.17(a), the FTIR spectra of UiO-66 activated at 80, 200, 290, and 320 ^{o}C showed a trend where two vibrational bands at ~700 and 550 cm^{-1} diminished as the activation temperature was increased from 80 to 320 ^{o}C. In molecules containing Zr-O bonding,

the vibrational band at ~700 cm^{-1} typically represents Zr-O stretch vibrations which are present in the UiO-66 inorganic nodes. A study by Valenzano et al. [84] reported the detailed structure of defect-free UiO-66 to consist of $Zr_6O_4(OH)_4$ nodes coordinated to 12 terephthalate linkers, and in each node there are three bridging hydroxyl (–μOH-) groups and bridging oxo (μ-O-) groups giving rise to the typical 4m3m UiO-66 crystal structure. The presence of defects, however, may cause other molecules such as H_2O, monocarboxylates (e.g. formic acid), or other charge balancing molecules that may be present in the reaction mixture to coordinate in place of missing terephthalate linkers in the defective regions [97]. The possible presence of charge balancing molecules may contribute to extra phases in the UiO-66 crystal which would not be expected for a defect-free UiO-66 crystal lattice.

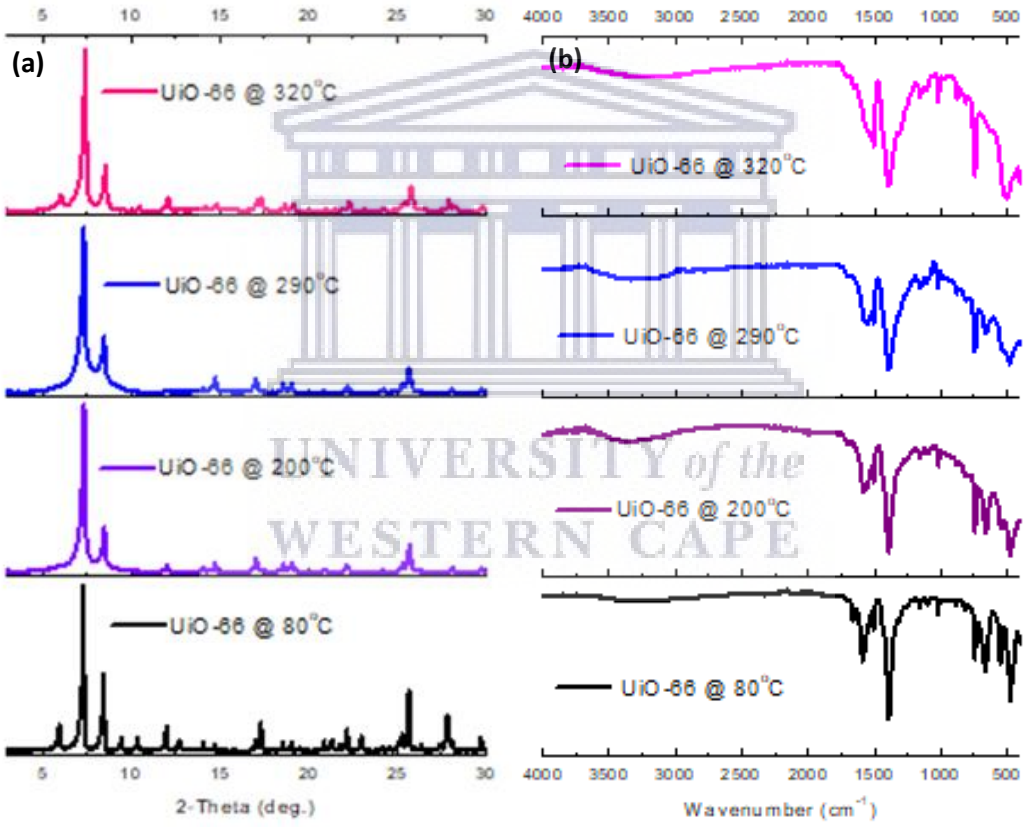

Figure 4.17: Effect of post-synthesis high temperature activation/degassing on the UiO-66 structure: (a) FTIR spectra for UiO-66 activated at 80, 200, 290, and 320 °C, (b) PXRD patterns for UiO-66 activated at 80, 200, 290, and 320 °C.

The results in Fig. 4.16 further showed that at 170 °C and 200 °C, the peak at 2θ ~ 6° and the two peaks between 9 and 12° were not observed. At higher activation temperatures of 230 and 260 °C, the peak at 2θ ~ 6° could be observed and the intensity of the peaks between 9 and 12°

remained significantly lower in comparison to UiO-66 activated at temperatures below 170 ^{o}C. The peak at 2θ ~ 6^{o} was not observed after activation at 290 ^{o}C and, furthermore, the peak at 2θ ~ 12^{o} was also not observed. Both peaks (2θ ~ 6 and 12^{o}) could, however, be observed after activation at 320 ^{o}C. It is important to consider that the activation of the UiO-66 was not done in-situ, rather on UiO-66 samples from the same batch that were activated under vacuum at a specified temperature, i.e. one sample for each temperature. The studies of Valenzano et al. [84] reported in-situ PXRD patterns with heating up to 1000 ^{o}C, but no evidence of the behaviour shown in Fig. 4.16 was noticeable in their results. In a recent study by Vandichel et al. [72], a computational analysis of the dehydroxylation process in UiO-66 showed that it was theoretically possible for structural changes to occur during the conversion of hydroxylated $Zr_6O_4(OH)_4$ nodes into dehydroxylated Zr_6O_6 nodes. The study showed the possibility of two transition states (TS) that may be formed prior to the full dehydroxylation process. It also proposed that the formation of the TS was heavily favoured in defective UiO-66 crystals and may influence the mechanical properties of the UiO-66 framework, with the shear modulus showing a more significant response to applied stress/strain compared to the bulk modulus. In this study, the effect of high temperature activation or dehydroxylation on the mechanical stability of UiO-66 was investigated by pelletizing UiO-66 samples activated at 80, 200, 290, and 320 ^{o}C and the results are discussed in section 4.2.2.

4.3.2.2. Cryogenic N_2 adsorption/desorption isotherms for UiO-66 powder activated at different temperatures (80, 200, 290, and 320 ^{o}C)

In order to obtain optimized UiO-66 structures giving the highest surface areas and pore volumes, N_2 adsorption/desorption isotherms were measured for UiO-66 powder samples activated at 80, 200, 290, and 320 ^{o}C. In Fig. 4.18 and Table 4.5 it can be seen that the N_2 adsorption/desorption of UiO-66 all showed typical Type I isotherms, owing to its highly microporous structure, as described according to the IUPAC isotherm classification (Groen, Peffer and Perez-Ramirez, 2003). The BET surface areas and total pore volumes were in the order of UiO-66$_{290^{o}C}$< UiO-66$_{320^{o}C}$< UiO-66$_{200^{o}C}$< UiO-66$_{80^{o}C}$.

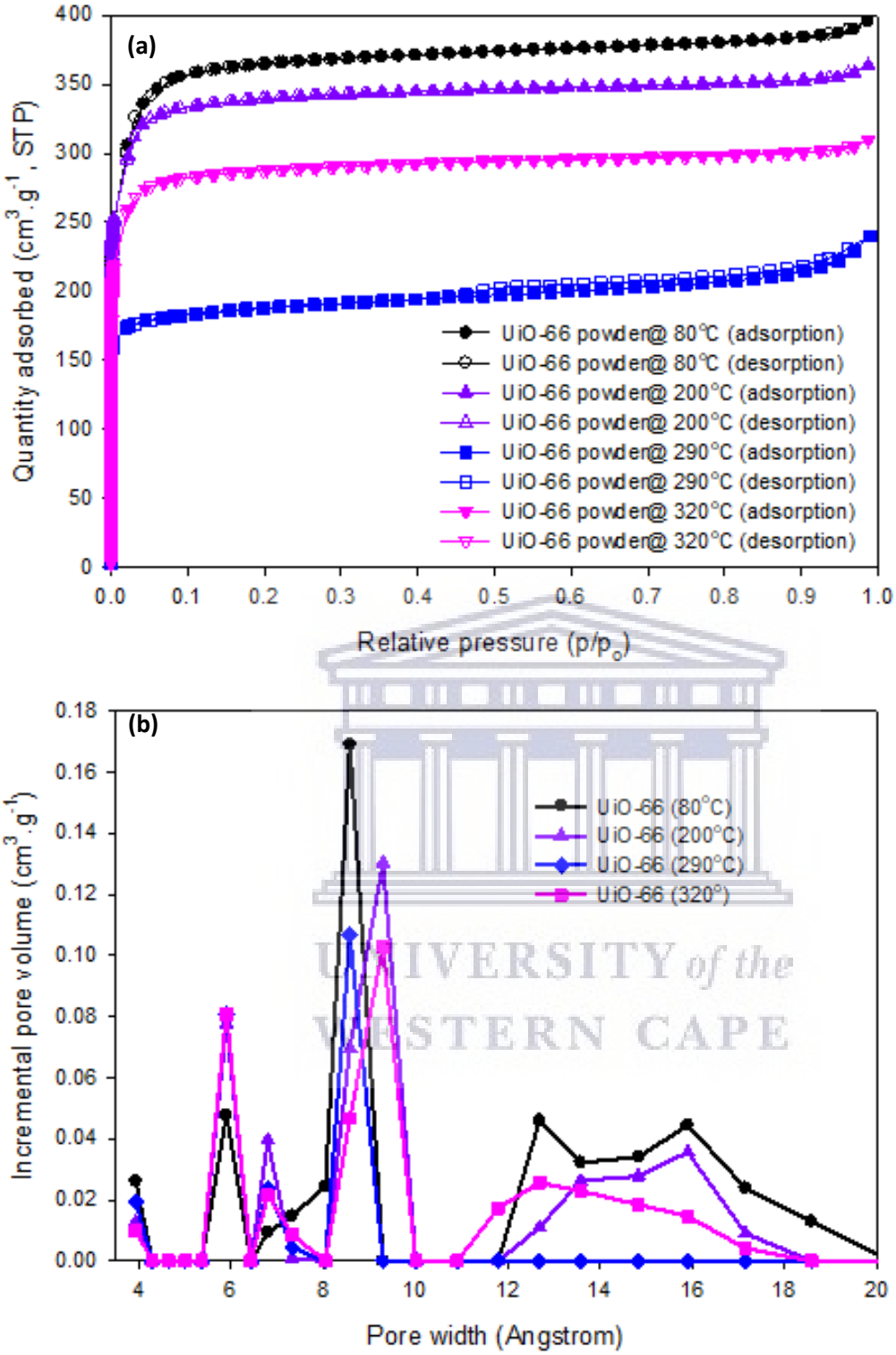

Figure 4.18: (a) Nitrogen adsorption isotherms at 77 K for UiO-66 heat treated at 80 (circle), 200 (triangle), 290 (square), and 320 °C (diamond). The open symbols represent desorption isotherms down to $p/p_o \approx 0.02$. (b) NLDFT pore size distribution, in the micropore region, for UiO-66 heat treated at 80, 200, 290, and 320 °C.

Table 4.5: Summary of the BET report for UiO-66 powder degassed at 80, 200, 290, and 320°C for 16 hours under vacuum.

Isotherm property	**UiO-66 powder sample (batch 1)**			
	80°C	**200°C**	**290°C**	**320°C**
BET surface area ($m^2 \cdot g^{-1}$)[a]	1413 (1260, 89%)	1307 (1194, 91%)	708 (610, 86%)	1100 (999, 91%)
NLDFT pore volume ($cm^3 \cdot g^{-1}$)[b]	0.61 (0.50, 82%)	0.56 (0.48, 86%)	0.37 (0.25, 68%)	0.48 (0.40, 83%)
Slope ($g \cdot cm^{-3}$, STP)	0.003079	0.003334	0.006161	0.003965
Y-intercept ($g \cdot cm^{-3}$, STP)	0.00001	-0.00004	-0.000015	-0.000007
Q_m ($cm^3 \cdot g^{-1}$, STP)	325	300	163	253
Correlation coefficient	0.99992	0.99991	0.99995	0.99994

[a]values in parentheses represent the micropore surface area and percentage of the total BET surface area. [b]values in parentheses represent the micropore volume and percentage of the total NLDFT pore volume.

The results indicated that low temperature activation/degassing at 80 °C prior to measuring gas adsorption was sufficient to remove guest/solvent molecules from the pores of UiO-66. In Fig. 4.18(b) the pore size distribution curves show that there were significant changes to the pore structure of UiO-66 with increasing activation temperatures. UiO-66 is a highly microporous MOF almost completely made up of pore diameters in the micropore range (2 Å to 20 Å).

The pore sizes of UiO-66 typically have diameters of ~6, 8, and 11 Å which represent the free spaces in tetrahedral cages, triangular windows, and octahedral cages respectively. The major pore sizes shown in fig. 4.18(b) were- at ~6, 7, 9, and 12 Å consistent with reported literature [70]. The appearance of larger pore diameters above 12 Å could also indicate the presence of open metal sites within a possibly defective UiO-66 structure. In the UiO-66 sample activated at 290 °C, the pore diameters at 6 and above 12 Å were not evident, an observation further showing some proof of possible phase/structural changes to UiO-66 as previously observed in the PXRD patterns in Fig. 4.16 and FTIR spectra in Fig. 4.17. The absence of the pore diameters at 6 and above 12 Å were also consistent with the lowest BET surface area and pore volume for the UiO-66 sample activated at 290 °C.

4.3.2.3. High-pressure H_2 adsorption/desorption of UiO-66 powder activated at different temperatures (80, 200, 290, 320 ºC).

The excess and total H_2 adsorption isotherms in Fig. 4.19 showed that most of the hydrogen uptake occurred at relatively low pressure (< 10 bar), an observation typical for a highly microporous adsorbent such as UiO-66. At pressures above 10 bar, it can be seen that the extent of H_2 adsorption was less steep compared to the low pressure adsorption, an indication of the UiO-66 reaching a saturated state where only small amount H_2 molecules could be adsorbed further. In the extreme case of saturation, the excess adsorption plot tends to slope down at high pressures, such as *ca.* 50 bar, where the rate of desorption of H_2 molecules may exceed the rate of adsorption. In Fig. 4.19(b), the excess H_2 adsorption isotherms can be observed to have reached saturation at pressures above 30 bar for UiO-66 activated at 80 and 200 ºC, whereas the UiO-66 activated at 290 ºC was found to possibly reach saturation at a higher pressure of 80 bar. The UiO-66 activated at 320 ºC was found to possibly reach saturation at the lowest pressure of about 10 bar. In Fig. 4.14, the dehydroxylation process was shown to have occurred between 150 and ~300 ºC, and in Fig. 4.18(b) the textural properties of UiO-66 was seen to vary with increasing activation temperature. The observed excess H_2 adsorption behaviour may therefore be affected by the changed chemical and structural environment at 290 and 320 ºC. The effect of saturation was not observable on the total H_2 adsorption isotherms as the total H_2 uptake takes into consideration the effects of pore filling which could be expected to accommodate a higher H_2 adsorption compared to excess H_2 adsorption isotherm which only considers the available excess surface near to the gas to outer adsorbent surface interface [66].

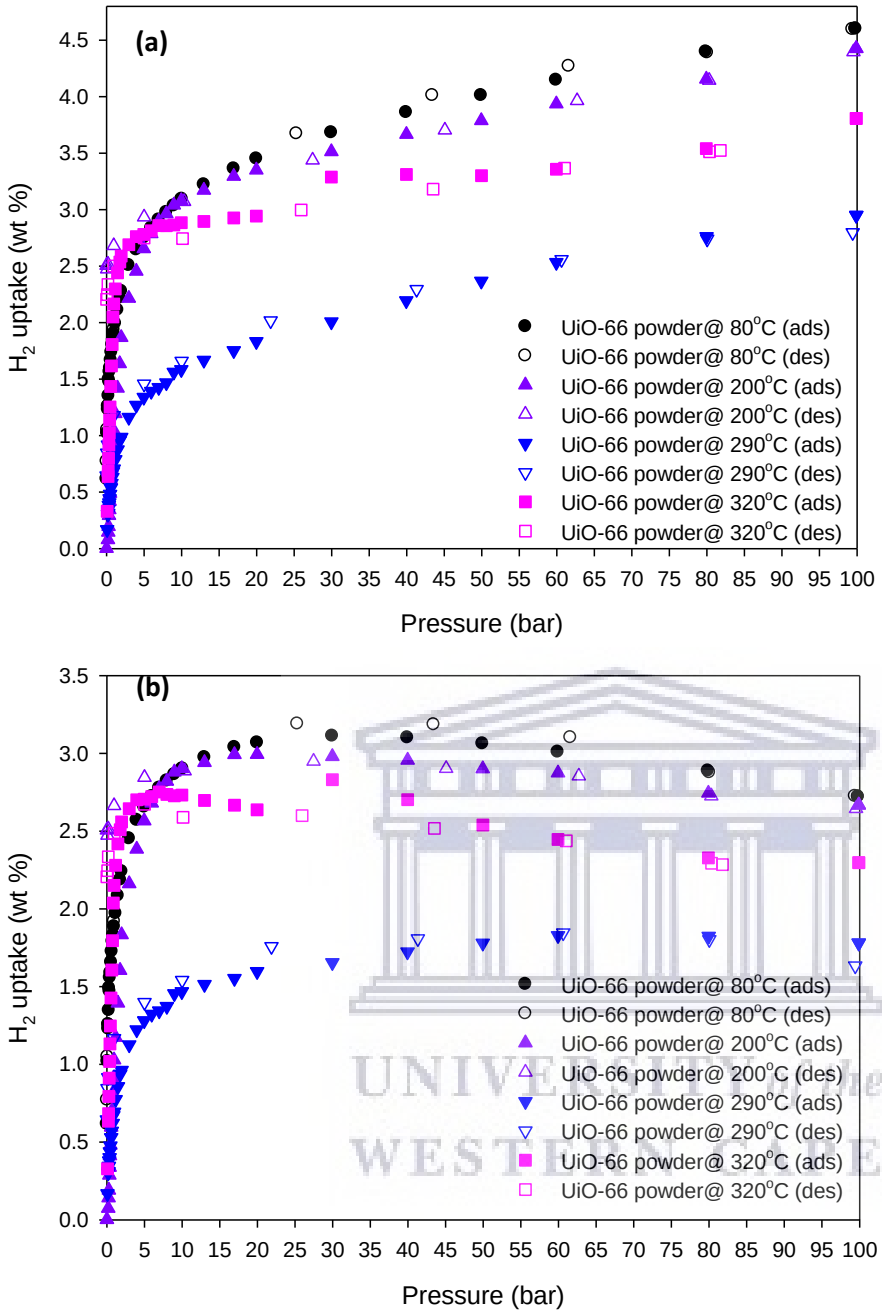

Figure 4.19: (a) H_2 adsorption isotherms at 77 K showing the total/absolute gravimetric H_2 uptake, and (b) excess H_2 uptake for UiO-66 powder (from batch 1) activated at 80, 200, 290, and 320 °C. The closed symbols represent the adsorption isotherms and open symbols represent the desorption isotherms.

Table 4.6: H_2 uptake at 77 K and 298 K (values in parenthesis) up to 100 bar obtained for UiO-66 powder samples activated at 80, 200, 290, and 320 ^oC.

Sample (batch 1)	Maximum excess Uptake (wt%)	Total/absolute gravimetric H_2 uptake (wt%)[a]		Working capacity (wt%)[b]
		5 bar	100 bar	
UiO-66 powder@ 80 ^oC	3.1	2.8	4.6	1.8
UiO-66 powder@ 200 ^oC	3.0	2.9	4.4	1.5
UiO-66 powder@ 290 ^oC	1.8	1.5	3.0	1.5
UiO-66 powder@ 320 ^oC	2.8	2.8	3.8	1.0

[a]Values calculated using eqn 3.3 in chapter 3 (section 3.4.5.2). [b]Values calculated from the difference between total H_2 uptake at 100 bar and 5 bar.

In Fig. 4.19 and Table 4.6, the gravimetric H_2 uptake of the samples could be seen to have correlated to their BET surface areas and pore volumes, with the UiO-66 activated at 80 ^oC showing the highest H_2 uptake at 77 K and 100 bar. Importantly the increase in activation temperature was not found to have a liner relationship with the BET surface area and pore volume, as it was found that the lowest values were obtained after activation of 290 ^oC instead of 320 ^oC (the highest activation temperature investigated in this study). The observed results were found to strongly suggest that UiO-66 could undergo a dynamic temperature-dependent behaviour as it pertains to gas adsorption. It was further mentioned in computational studies previously reported by Vandichel et al. [72] and Rogge et al. [73] that such a dynamic behaviour had an influence in the mechanical stability of UiO-66. In section

4.4. Pelletization of UiO-66 at 700 MPa

This section is divided into two parts where the study firstly investigates the pelletization of UiO-66 activated at low temperature and at high temperature. In the second part, the study investigates the comparative H_2 uptake properties of powdered UiO-66 and UiO-66 pellets. The experiments included the pelletization of UiO-66 at ~700 MPa after its activation at 80 to 320 ^oC (at 30 ^oC intervals) and the textural properties were measured for selected samples, namely those activated at 80, 200, 290, and 320 ^oC as these represented or closely resembled most reported activation temperatures.

4.4.1. Pelletization of UiO-66 after activation at different temperatures (80, 200, 290, and 320 ºC)

The results obtained in this section for low-temperature activation compared to those obtained for high-temperature activation would shed light on the effect of the dehydroxylation process on the textural and mechanical properties of UiO-66.

4.4.1.1. Crystallographic analysis of UiO-66 pelletization after activation at 80 to 320 ºC (30 ºC intervals)

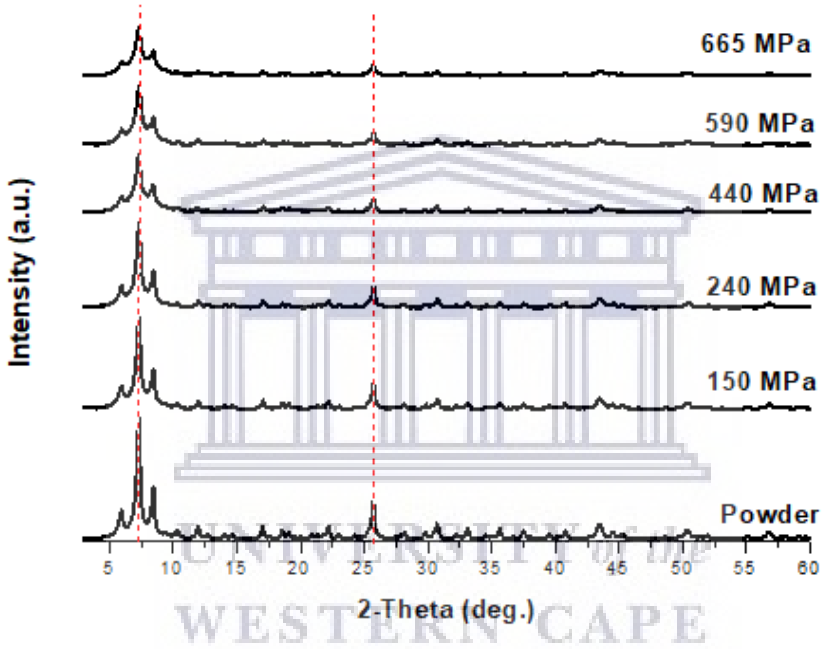

Figure 4.20: PXRD patterns for UiO-66 activated at 80 ºC (from batch 2) after pelletization up to ~700 MPa. The vertical dotted lines mark any possible peak shifting at the specified 2θ positions (~6º and 26º).

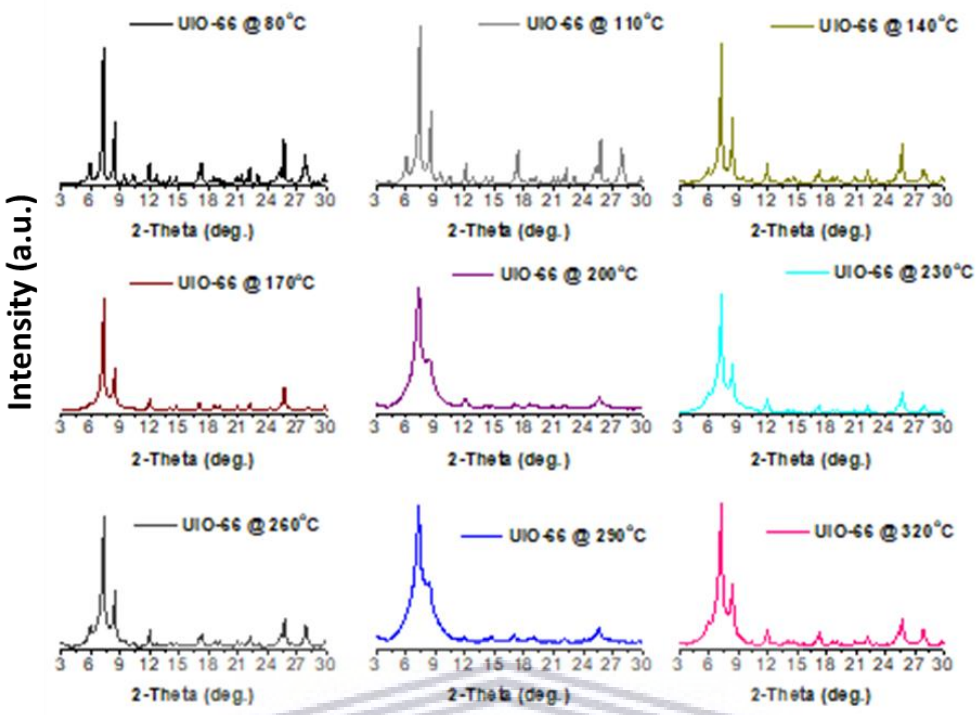

Figure 4.21: Structural analysis of pelletized UiO-66: PXRD patterns of pelletized UiO-66 (from batch 1) up to ~700 MPa after activation from 80 to 320 °C at 30 °C intervals.

The PXRD results in Fig. 4.20 showed no evidence of peak shifting upon pelletization of UiO-66 up to ~700 MPa of applied pressure regardless of the activation temperature prior to pelletization. This observation could suggest that the bulk UiO-66 framework experienced negligible strain or stress under the specified applied pressures. This could be expected because the reported value for the minimal shear modulus of UiO-66 is very high, around 13.7 GPa which is said to be attributed to the strong Zr-O bonding [45]. It is however very clear that the peaks became broader as the pressure was increased. The broadening of the peaks may have resulted from a process of amorphisation of the crystals which could be due to the reduction of grain boundaries between the powder particles [104]. In Fig. 4.21 it can be seen that the effect of peak broadening was, however, most significant on UiO-66 samples activated at high temperatures (200 – 320 °C). The PXRD patterns in particular for UiO-66 activated at 200 and 290 °C showed extreme peak broadening and as noted in the UiO-66 powder samples (Fig. 4.16), the symmetry forbidden phase at $2\theta \sim 6^{o}$ was clearly not observable at these temperatures even after the pelletization process. The effect of pelletization at ~700 MPa on the textural properties of UiO-66 activated at 80 °C are given in section 4.4.1.2.

4.4.1.2. Cryogenic N_2 adsorption/desorption isotherms for powdered and pelletized UiO-66 activated at 80 °C

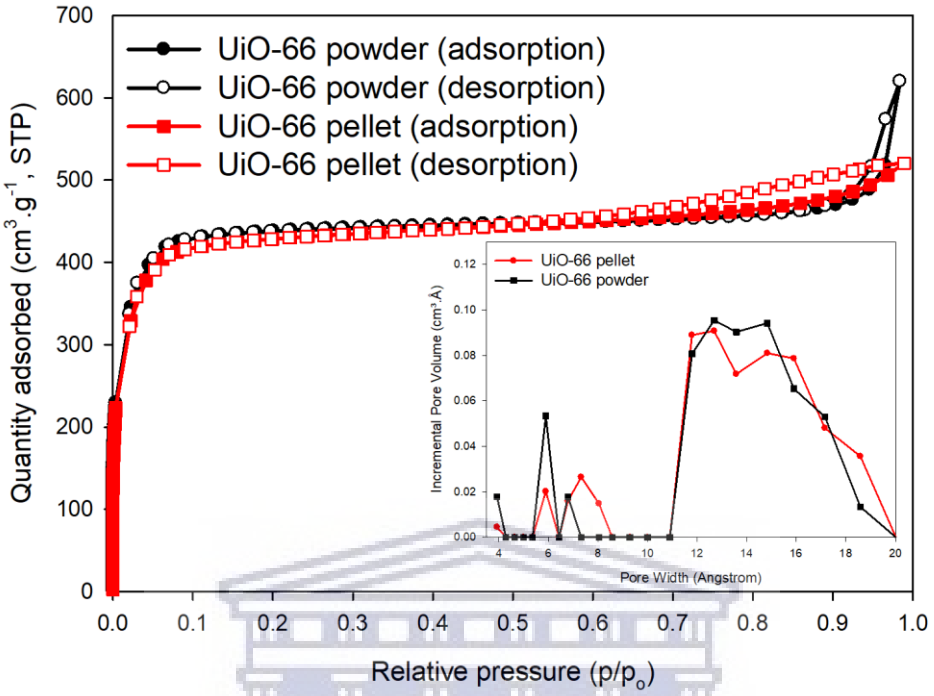

Figure 4.22: N_2 adsorption/desorption isotherms and pore size distributions (insert) obtained for powdered and pelletized UiO-66 activated at 80 °C for 32 hours (from batch 2).

Table 4.7: Summary of the textural properties obtained for powdered and pelletized UiO-66 activated at low temperatures (80 °C).

Isotherm property	UiO-66 sample (batch 2)	
	Powder	Pellet
BET surface area ($m^2 \cdot g^{-1}$)[a]	1737 (1559, 90%)	1707 (1484, 87%)
NLDFT pore volume ($cm^3 \cdot g^{-1}$)[b]	0.96 (0.60, 63%)	0.81 (0.57, 70%)
Slope ($g \cdot cm^{-3}$, STP)	0.002501	0.002542
Y-intercept ($g \cdot cm^{-3}$, STP)	0.000005	0.000008
Q_m ($cm^3 \cdot g^{-1}$, STP)	399	392
Correlation coefficient	0.9997	0.9997
Packing density ($g \cdot cm^{-3}$)[c]	0.57	1.45
Volumetric surface area ($m^2 \cdot cm^{-3}$)[d]	990	2475

[a]values in parentheses are given for the t-plot micropore surface area. [b]values in parentheses are given for the t-plot micropore volume. [c]Values are averaged from 5 experimental measurements.

In Fig. 4.22 it can be seen that both powdered and pelletized UiO-66 show typical Type I adsorption isotherms, but a near-vertical hysteresis loop of Type H3 configuration was observable for the UiO-66 powder. The hysteresis loop observed in the UiO-66 pellet extends over a wider partial pressure range and assumes a Type H4 configuration. The appearance of a hysteresis loop could have suggested a possibly extended pore structure in the UiO-66 sample. Indeed in Fig. 4.22 (insert) the pore sizes of both powdered and pelletized UiO-66 extend beyond 12 Å, with pore sizes up to ~18 Å, another indication of possible open metal sites or defects in the UiO-66 structure. In Table 4.7 it can be seen that the textural properties of the UiO-66 batch 2 were significantly higher compared to UiO-66 batch 1 in Fig. 4.18 and Table 4.5. The two batches were synthesized under exactly the same conditions, however, the post-synthesis heat treatment (activation) of batch 2 was done over 32 hours compared to 16 hours used in batch 1. The longer degassing/activation times could have played a significant role in the complete evacuation of guest molecules from highly microporous adsorbents such as UiO-66. Due to the narrow pores in the micropore region, guest molecules may remain tightly bound and would require much lower vacuum conditions (down to about ~10^{-7}) and long evacuation times to achieve possibly fully evacuated pores. Any presence of guest molecules, not completely removed from the UiO-66 framework, could possibly reduce the quantity of adsorbed N_2 than would be possible for a completely evacuated UiO-66 sample, and hence record lower BET surface areas and pore volumes than would be expected [94]. Another possibility would be the inherent statistical difference amongst batches synthesized separately at different times, a common feature of most ad-hoc synthesis experiments. The results in Table 4.7, however, do show that the UiO-66 pellet retained at least 98 % of the original BET surface area and 84% of the total pore volume observed in the UiO-66 powder. The difference of 16% in total pore volume could be attributed to the possible reduction of void or inter-particle macropores due to the more densified crystals in pelletized UiO-66.

4.4.1.3. Cryogenic N_2 adsorption/desorption isotherms for powdered and pelletized UiO-66 activated at 80, 200, 290, and 320 ºC

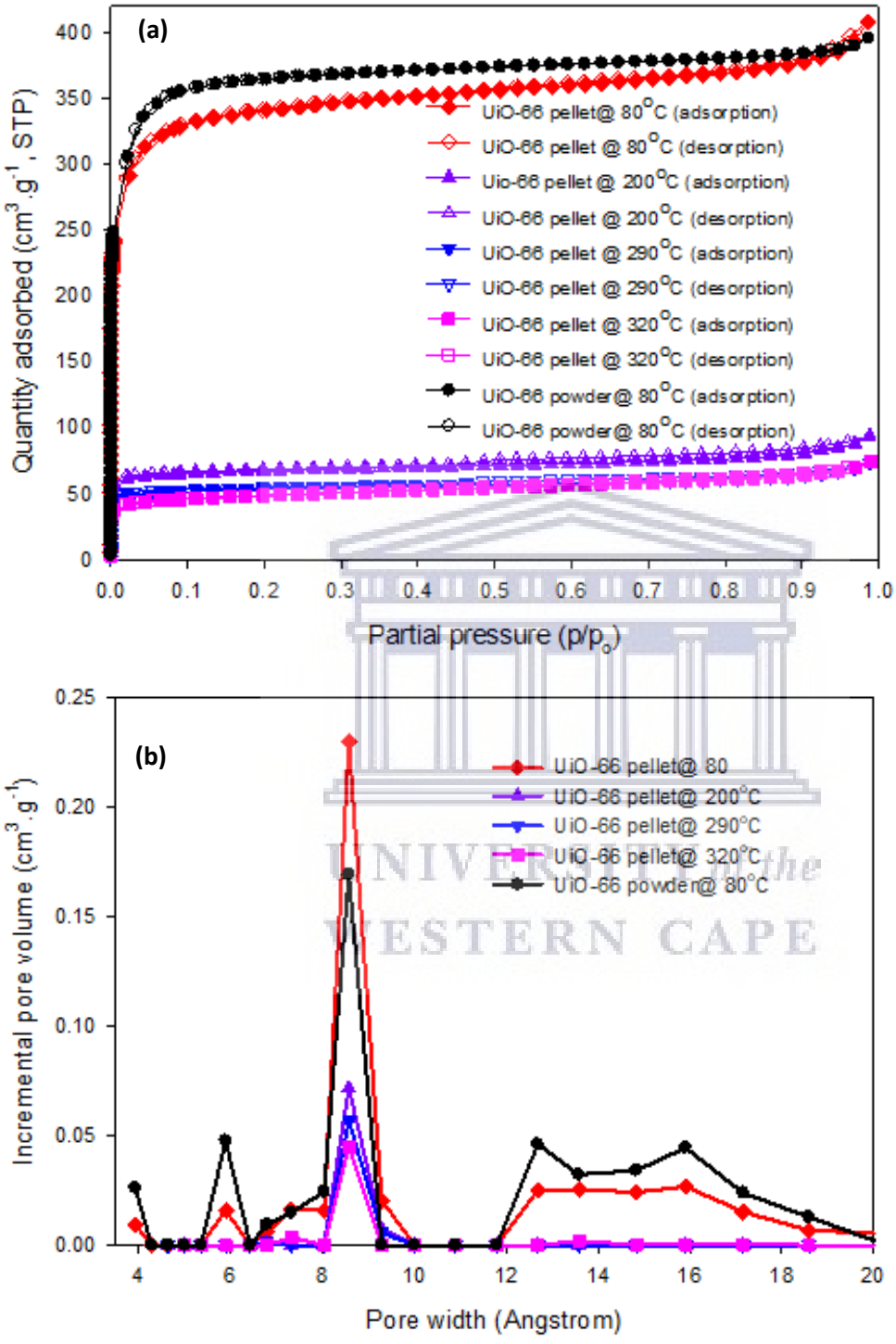

Figure 4.23: (a) N_2 adsorption/desorption isotherms and pore size distribution curves for UiO-66 pellets (from batch 1) activated at 80 to 320 ºC prior to pelletization. (b) Pore size distribution curves obtained for UiO-66 pellets (from batch 1).

In Fig. 4.23 and Table 4.8, similar results were obtained for powdered and pelletized UiO-66 activated at 80 ^{o}C (batch 1). The BET surface area of the UiO-66 pellet was 92% that of UiO-66 powder with the total pore volume retained being 98% that of the pellet. The UiO-66 pelletized after activation at 200 to 320 ^{o}C show significantly reduced BET surface areas of down to 13% retained for UiO-66 pellet activated at 320 ^{o}C and only 20% of the total pore volume retained. Since the pelletization of MOFs is typically accompanied by reduced textural properties, the observed result could be a strong indication of the compromised mechanical strength of UiO-66 upon activation at 200, 290, and 320 ^{o}C compared to UiO-66 activated at 80 ^{o}C. In Fig. 4.23(b) it can be seen that the pore diameters at 6 Å and above 12 Å were only observable for UiO-66 powder and pelletized UiO-66 activated at 80 ^{o}C and not for UiO-66 activated at 200, 290, and 320 ^{o}C. The reduction in total pore volume showed a significant collapse of the porous structure of UiO-66, indicating possible loss in mechanical strength after its activation at 200, 290, and 320 ^{o}C. The effect of pelletization on the H_2 uptake of UiO-66 is reported in section 4.5.

Table 4.8: Summary of the textural properties obtained for pelletized UiO-66 activated up to 320 ^{o}C compared to those obtained for UiO-66 powder (80 ^{o}C).

Parameter	**UiO-66 pellet sample (batch 1)**				
	Powder	**80 ^{o}C**	**200 ^{o}C**	**290 ^{o}C**	**320 ^{o}C**
BET surface area ($m^2 \cdot g^{-1}$)[a]	1413 (1260, 89%)	1300 (1091, 84%)	252 (208, 83%)	200 (163, 82%)	180 (123, 68%)
NLDFT pore volume ($cm^3 \cdot g^{-1}$)[b]	0.61 (0.50, 82%)	0.60 (0.44, 73%)	0.15 (0.09, 60%)	0.11 (0.07, 64%)	0.12 (0.05, 42%)
Slope ($g \cdot cm^{-3}$, STP)	0.003079	0.003347	0.017289	0.021851	0.02423
Y-intercept ($g \cdot cm^{-3}$, STP)	0.00001	0.00001	0.000035	0.000046	0.000016
Q_m ($cm^3 \cdot g^{-1}$, STP)	325	299	58	46	41
Correlation coefficient	0.99992	0.99996	0.99997	0.99997	0.99998
Packing density ($g \cdot cm^{-3}$)[c]	0.65	1.52	1.33	1.46	1.50
Volumetric surface area ($m^2 \cdot cm^{-3}$)[d]	919	1976	335	292	270

[a]values in parentheses are given for the t-plot micropore surface area; [b]values in parentheses are given for the t-plot micropore volume. [c]Calculated from experimental measurements using eqn. 3.6 in chapter 3 (section 3.5.1). [d]calculated by multiplying the packing density and the BET surface area.

4.5. Cryogenic H_2 adsorption/desorption isotherms for powdered and pelletized UiO-66 activated at 80 ºC

This section reports on the H_2 adsorption properties of UiO-66 with respect to gravimetric H_2 uptake and total volumetric H_2 capacities in powdered and pelletized UiO-66 (from batch 2). The results are reported for high pressure H_2 adsorption, with a maximum pressure of 100 bar at 77 K and 298 K. The working H_2 capacities are calculated from the difference between the H_2 adsorption curve at 100 bar (10 MPa) to the desorption curve at 5 bar (0.5 MPa) as described in literature [151]. Using the predictive model developed by Balderas-Xicohténcatl et al. [50], the theoretical volumetric H_2 capacity values will be compared to experimental results obtained in this study

4.5.1. Gravimetric H_2 capacity for powdered and pelletized UiO-66 activated at 80 ºC

In Fig. 4.24 and Table 4.9, it can be seen that the UiO-66 powder achieved a total gravimetric H_2 uptake of 5.0 wt% (1.0 wt% at 298 K) and the UiO-66 pellet obtained 5.1 wt% (0.9 wt% at 298 K). The observed H_2 uptake results strongly suggested that the crystal structure of UiO-66, activated at 80 ºC, did not change upon pelletization at ~700 MPa. A closer look at the shape of the isotherms revealed slight but significant differences in their H_2 uptake behaviour. It can be seen in Fig. 4.24 that at low to intermediate pressure (i.e. 0 ~ 30 bar), the excess and total H_2 uptake for UiO-66 powder were higher in comparison to the isotherms of pelletized UiO-66. This observation could be explainable by assuming the isotherms as following Langmuir adsorption model since the measurement conditions employed (77 K and to 100 bar) were above the critical point of H_2, i.e. under the specified conditions, H_2 could only exist in a gaseous and supercritical fluid state [28,213]. The measurements were also not obtained under equilibrium conditions as the duration of each experiment was pre-set using a timer as described in Chapter 3 (section 3.4.5.2). Based on the Langmuir adsorption model, the surface coverage of the adsorbent by gas molecules increases with increasing pressure and also depends on the availability of binding sites on the adsorbent.

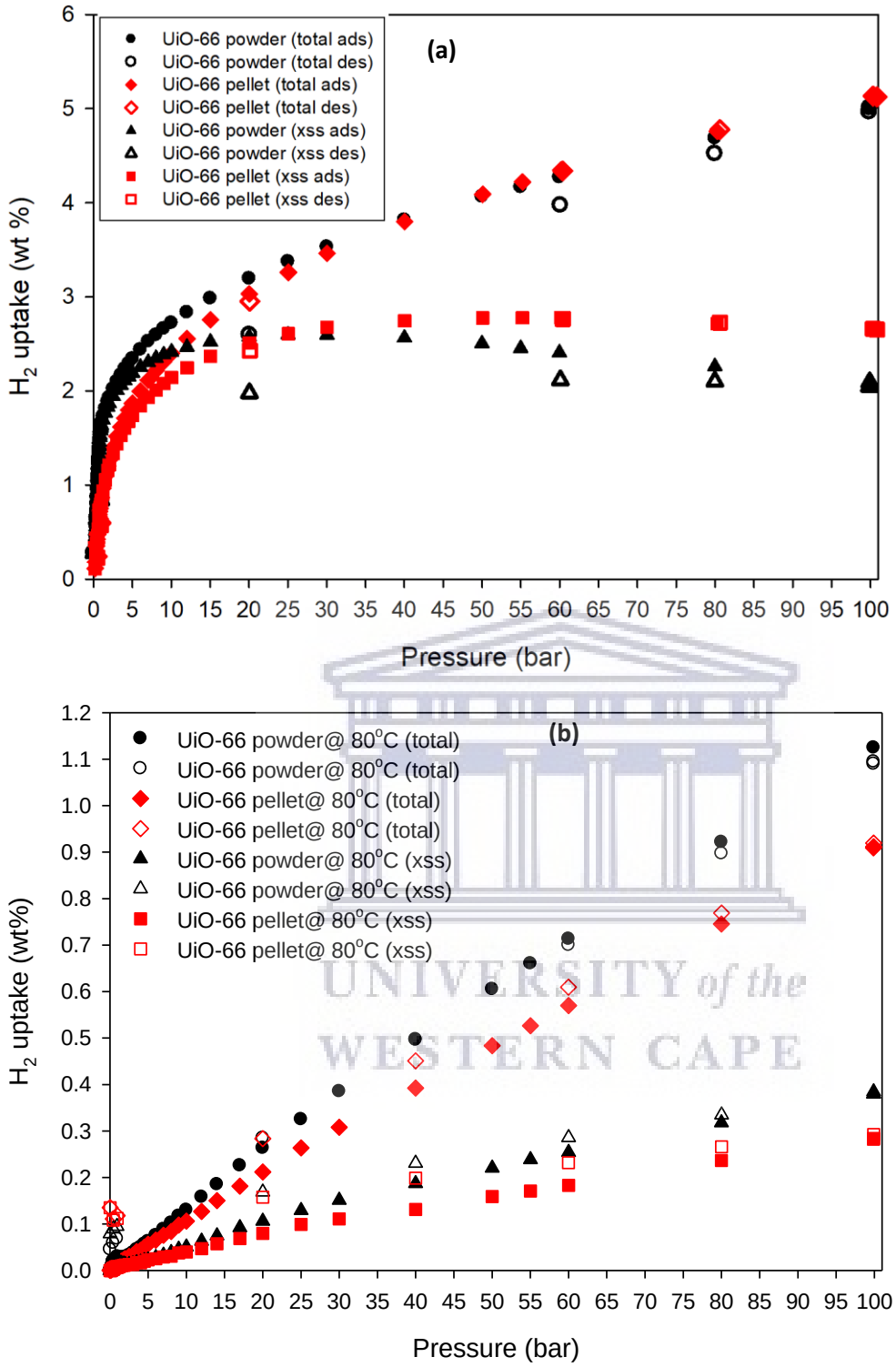

Figure 4.24: H_2 adsorption isotherms obtained for powdered and pelletized UiO-66 (from batch 2) from 0 to 100 bar at: (a) 77 K and (b) 298 K.

At high pressure, as the adsorbent surface becomes filled with gas molecules, the amount of gas adsorption would be exceeded by the amount of gas desorption since little adsorption sites are available at high surface coverage [39]. The loosely packed crystals in UiO-66 powder

would thus be expected to have more readily available adsorption sites (pores) accessible to the H_2 gas molecules at low to intermediate pressure. The resultant rapid surface coverage at low pressure, coupled with the highly microporous nature of UiO-66 would result in high H_2 adsorption at low pressure (< 30 bar) compared to higher pressure. In pelletized UiO-66, the crystals assumed a more densified and closely packed state, possibly with a reduced grain boundary compared to the powder. The result could be low accessibility for H_2 molecules to adsorption sites (pores) and higher pressures required to increase the surface coverage and pore filling. That also could mean the adsorbed H_2 gas molecules were more constrained within the pores due to the close packing of the densified UiO-66 crystals and therefore could readily desorb at high pressure. Indeed the results in Fig. 4.24 showed that the excess H_2 uptake for pelletized UiO-66 was higher than that of UiO-66 powder at high pressure (p > 30 bar) and hence the total H_2 uptake from about 40 to 100 bar matched that of UiO-66 powder. The observed shifting of adsorbed H_2 towards higher pressures could be considered to have an impact on the working capacity of UiO-66. The working capacity in pelletized UiO-66 (Table 4.9) increased by 0.5 wt%, meaning that the amount of adsorbed H_2 between 5 and 100 bar increased by ~10 % as a result of pelletizing UiO-66 at 700 MPa. It is very rare in MOFs that the MOF pellet not only retains the original surface areas and pore volumes of their powdered forms, but also retain the H_2 uptake with an improved gravimetric working capacity.

In Table 4.9, the maximum excess H_2 uptake in UiO-66 from batch 2 (2.6 wt% for UiO-66 powder activated at 80 ^oC) was lower compared to UiO-66 from batch 1 (3.1 wt% for UiO-66 powder activated at 80 ^oC) but their BET surface areas were found to be the opposite. The measurement of BET surface area uses a volumetric method where the volume of adsorbed N_2 is measured (Micromeritics report, cited from: www.micromeritics.com, 2016). In the volumetric method, the density of the adsorbent does not necessarily play a significant role in the measured volume of N_2 adsorbed. In the measurement of adsorbed H_2, on the other hand, the method used is a gravimetric method where there is a significant dependency of the amount of H_2 adsorbed on the skeletal density of the adsorbent, most especially for high pressure H_2 adsorption [197].

Table 4.9: Experimental gravimetric H_2 uptake results for powdered and pelletized UiO-66. The measurements were obtained at 77 K (and 298 K) up to 100 bar.

Sample (batch 2)	Maximum excess Uptake (wt%)		Total/absolute gravimetric H_2 uptake (wt%)[b]		Working capacity (wt%)[c]
	Experimental	Estimate[a]	5 bar	100 bar	
UiO-66 powder	2.6 (0.38)	3.5	2.3 (0.06)	5.0 (1.1)	2.7 (1.0)
UiO-66 pellet	2.8 (0.28)	3.4	1.9 (0.02)	5.1 (0.9)	3.2 (0.9)

[a]Estimated using the Chahine rule [209].[b]Calculated using Eqn. 3.3. [c]Difference between H_2 uptake at 100 bar (adsorption) and 5 bar (desorption). Values in parentheses represent H_2 uptake at 298 K.

In high pressure H_2 adsorption, it is generally found that at pressures above atmospheric pressure (*ca.* 1 bar) the density of H_2 increases linearly with increasing pressure and as such requires that the adsorbent must be corrected for buoyancy effects by using measured skeletal densities, typically using He pycnometry [11]. Any deviations between two samples, of the same material, in their measured skeletal densities may result in significant differences in the amount of adsorbed excess H_2 when comparing the two samples. As observed earlier in Fig. 4.18 and 4.22 the major difference between the two UiO-66 batches was in the pore size distributions; UiO-66 from batch 1 showed a higher degree of volume within the ~9 Å pore size whereas in batch 2 there was a higher degree in the pore size range 11 – 20 Å.

The significance of this difference was in the measurement of their skeletal densities using He pycnometry. As described in chapter 2, He pycnometry is done under ambient conditions and the diffusion of He gas into the adsorbent pores may be dependent on the pore sizes and narrow pores may be considered as "closed pores" under the ambient conditions [39]. This may result in an overestimation of the skeletal density under non-equilibrium adsorption conditions. In this study, the skeletal density was measured once for UiO-66 and utilized throughout without considering the difference in the significant pore sizes in the two UiO-66 batches.

4.5.2. Volumetric H_2 capacity for powdered and pelletized UiO-66 activated at 80 ^oC

The pelletization strategy was mainly used to improve the packing density of UiO-66 and possibly improve the volumetric H_2 capacity as reported by Balderas-Xicohténcatl et al. [50] and the results are shown in Fig. 4.25 and Table 4.10. The experimental results were also compared to the theoretical amount of H_2 gas stored in a pressurised H_2 cylinder with no adsorbent material. The comparison could show the effectiveness in using MOF-based storage compared to cylinders without MOFs. In order to substantiate the use of packing density for the calculation of the volumetric H_2 capacities from gravimetric H_2 uptake data, it can be seen from Table 4.10 that the experimental values obtained in this study (between 20 – 25 bar) were virtually the same as those estimated using the "hydrogen surface density" developed by Balderas-Xicohténcatl et al. [50]. This provided further correlation between the volumetric surface area of MOFs and their packing density.

In Fig. 4.25 it can be seen that the total volumetric H_2 capacity is 155 % higher in pelletized UiO-66 compared to UiO-66 powder at 77 K and 100 bar (86% higher at 298 K). This observation can be attributed to the increased volumetric surface area after pelletization, as shown in Table 4.8. In Fig. 4.25 it is observable that at pressures above 80 bar the volumetric H_2 capacity of UiO-66 powder is lower compared to the theoretical volumetric density of H_2 gas in a pressurised H_2 cylinder. As highlighted in many studies [2,15,37,215] it is key that for the possible application MOF-based H_2 storage systems, both the gravimetric and volumetric H_2 capacities must be balanced within material.

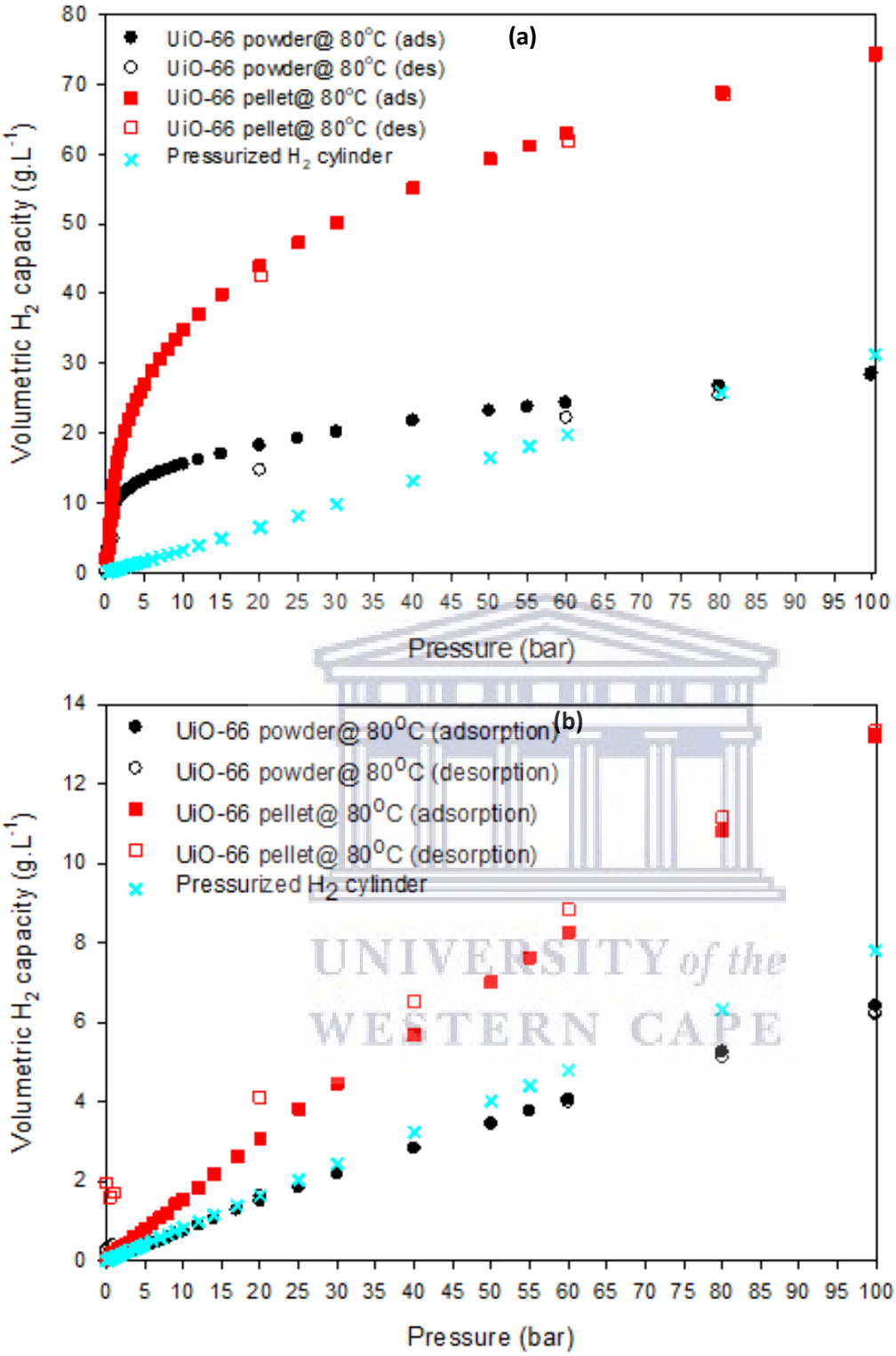

Figure 4.25: Volumetric H_2 capacities for pelletized and powdered UiO-66 compared to a pressurized H_2 cylinder without any MOFs: (a) at 77 K and (b) at 298 K from 0 – 100 bar pressure.

Table 4.10: Summary of volumetric H_2 capacities at 77 K and 298 K for powdered and pelletized UiO-66 activated at 80 ^oC.

Sample (batch 2)	**Total volumetric H_2 capacity ($g.L^{-1}$)**				**Working capacity[c]**
	5 bar	**25 bar**		**100 bar**	
		Experimental[a]	**Estimate[b]**		
UiO-66 powder	13 (0.4)	19 (2)	19	29 (7)	16 (7)
UiO-66 pellet	27 (0.9)	47 (4)	47	74 (14)	47 (13)
Pressurized H_2 cylinder	2 (0.4)	-	-	31 (8)	29 (8)

[a]Calculated using eqn. 3.4 in chapter 3 (section 3.4.5.2). [b]Calculated using the volumetric surface area (Table 4.8) and the "volumetric H_2 density" as recommended in ref [50]. [c]Difference between the total H_2 uptake at 100 bar (adsorption) and 5 bar (desorption).

The UiO-66 powder showed a high gravimetric H_2 uptake but fairly low volumetric H_2 capacity, whilst the UiO-66 pellet showed matching gravimetric H_2 uptake and a much higher volumetric H_2 capacity. Assuming the use of packing density to convert gravimetric H_2 isotherm data to volumetric data, and an accurate 'hydrogen surface density' model, the results showed remarkable and unprecedented H_2 adsorption properties of MOFs pelletized at ~700 MPa. In this study, the concept of compaction (or pelletization) of UiO-66 for enhancement of volumetric capacity without compromising gravimetric capacity was therefore proven, which is a rare case for MOFs (Tables 4.9 and 4.10). In addition, the applied pressure (~700 MPa) for pelletization was unprecedented for MOFs since most studies have reported a collapse of the MOF structure upon compaction at very high pressures.

In order to check the validity for the use of packing density to calculate the volumetric H_2 capacity, the study also investigated the use of a model proposed by Ahmed et al. [2] where both the MOF skeletal density and crystal density were employed to calculate the volumetric H_2 capacity from gravimetric data.

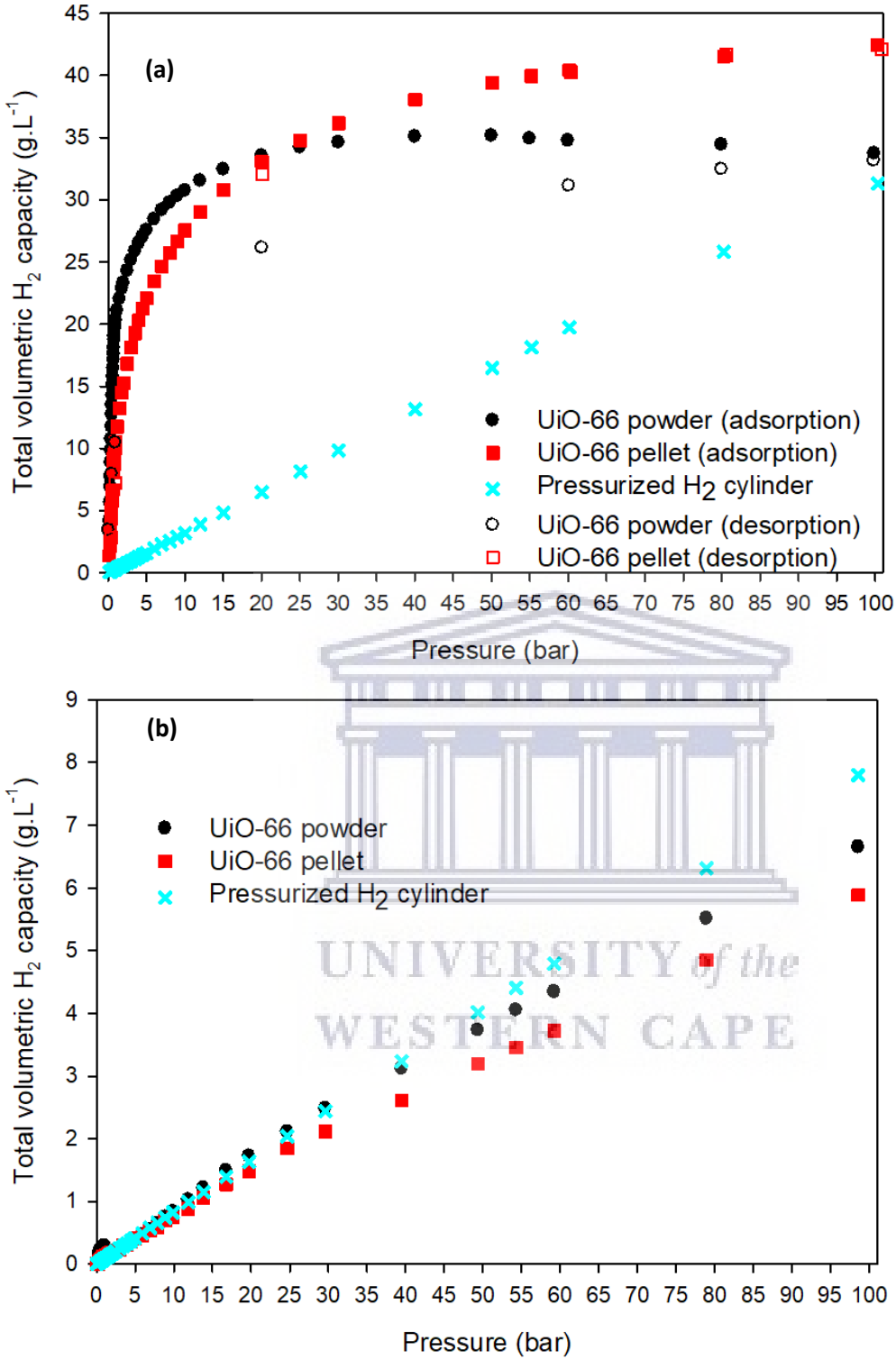

Figure 4.26: Total volumetric H_2 capacity isotherms for powdered and pelletized UiO-66 in comparison to a pressurized H_2 cylinder without MOFs: at (a) 77 K and (b) at 298 K. The volumetric H_2 capacity was calculated using the model developed by Ahmed et al. [2].

Table 4.11: Summary of volumetric H_2 capacities at 77 K and 298 K for powdered and pelletized UiO-66 activated at 80 ^oC. The values were calculated using the model developed by Ahmed et al. [2] (Eqn. 3.5 in chapter 3).

Sample	**Total volumetric H_2 capacity ($g.L^{-1}$)[a]**		**Working capacity[b]**
	5 bar	**100 bar**	
UiO-66 powder	28 (0.4)	34 (7)	6 (7)
UiO-66 pellet	22 (0.4)	43 (6)	21 (6)
Pressurized H_2 cylinder	2 (0.4)	31 (8)	29 (8)

[a]Calculated using eqn. 3.5 in chapter 3 (section 3.5). [b]Difference between the total H_2 uptake at 100 bar (adsorption) and 5 bar (desorption).

The results in Fig. 4.26 and Table 4.11 show that the volumetric H_2 capacity of pelletized UiO-66 was higher than UiO-66 powder at 77 K and 100 bar, however, at 298 K, the volumetric H_2 capacities for UiO-66 powder was higher than pelletized UiO-66 and furthermore both UiO-66 forms were found to have lower volumetric H_2 capacities in comparison to a pressurized H_2 cylinder without an adsorbent. The pelletization of MOFs has, however, been shown to generally improve the volumetric H_2 capacity as the densified MOF form would have an improved excess surface and thereby accommodate more H_2 compared to its powder form [213]. The densification also reduces the extent of void spaces/volume that may not necessarily contribute towards the adsorption of H_2 molecules. It would therefore be expected that the volumetric H_2 capacity of pelletized UiO-66 be higher than that of UiO-66 powder regardless of the temperature it is measured. The model proposed by Ahmed et al. [2] does not seem to be consistent with such an expectation whereas the use of packing density to calculate the volumetric H_2 capacity, as shown in Fig. 4.25 and Table 4.10, supports this expectation resulting from the pelletization of porous materials.

The ratio of the volume of H_2 adsorbed to the volume of H_2 in the gaseous/bulk phase (V_{ad}/V_{bulk}) could serve as an indication of the efficiency of H_2 storage in the MOF compared to that of an "empty" pressurized H_2 cylinder. Under the specified isotherm conditions (T = 77 K, 0 < P < 100 bar), the H_2 density ($g{\cdot}L^{-1}$) increased linearly with pressure and results in the ratio V_{ad}/V_{bulk} equal to 1 as calculated using the ideal gas equation (PV = nRT). This meant that, under ideal conditions, there would not be adsorption of H_2 molecules expected in a pressurized cylinder without adsorbents. In Fig. 4.27 it can be seen that in the presence of UiO-

66, however, the V_{ad}/V_{bulk} ratio could be seen to rapidly increase at pressures below 5 bar peaking at ~40 $cm^3.cm^{-3}$ for both powdered and pelletized UiO-66. This meant that at pressures below 5 bar, UiO-66 could store at least 40 times more H_2 by volume compared to the amount stored in an empty container/cylinder under the same conditions. As the pressure increased from ~5 bar up to 100 bar, the V_{ad}/V_{bulk} ratio decreased sharply initially and then steadily towards $V_{ad}/V_{bulk} \approx 1$. The rapid increase in adsorbed H_2 at low pressure could be attributed to the readily available adsorption sites (such as pores and pore walls). As these spaces/sites become filled with mono- and/or multilayers of H_2 molecules, the uptake of more H_2 could become restricted and possibly lead to an equilibrium state of adsorption being reached (i.e., saturation). Interestingly, from ~5 to 100 bar, V_{ad}/V_{bulk} for pelletized UiO-66 was greater than that of the powdered UiO-66, showing more uptake of H_2 at elevated pressures. This correlated with the excess adsorption isotherm obtained for pelletized UiO-66 in relation to the UiO-66 powder, i.e., the densified sample could take up more excess H_2 compared to UiO-66 powder. Clearly, the significant increase in the UiO-66 density after compaction at ~700 MPa translated to a rise in the calculated total volumetric H_2 capacity.

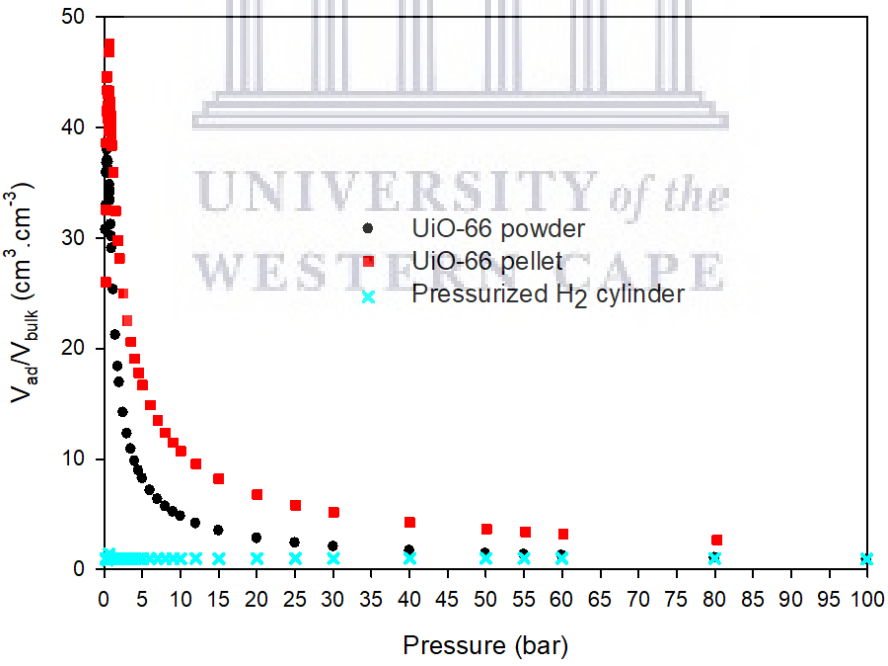

Figure 4.27: Volume of adsorbed H_2 per volume of H_2 in the bulk phase (V_{ad}/V_{bulk}) for pelletized UiO-66, UiO-66 powder and a pressurized H_2 cylinder without MOFs. The V_{ad}/V_{bulk} was calculated from the ideal gas law of H_2 gas (PV = nRT) using the volumetric H_2 capacity values obtained using the packing density.

4.6. Cryogenic H_2 adsorption/desorption isotherms for powdered and pelletized UiO-66 activated at 80, 200, 290, and 320 ^oC

The results in Fig. 4.28 and 4.29 and Table 4.13 showed the role of high-temperature activation of UiO-66 (from batch 1) and the H_2 adsorption isotherms (gravimetric and volumetric) for UiO-66 pellets (from batch 1) after activation at 80, 200, 290, and 320 ^oC. The results in section 4.2 showed that high-temperature activation of as-synthesised UiO-66 could undergo a dehydroxylation process up to ~300 ^oC. In the following discussions, the UiO-66 samples will be referred to as hydroxylated, partially dehydroxylated, and dehydroxylated for samples activated at 80, 200/290, and 320 ^oC respectively.

4.6.1. Gravimetric H2 capacity for powdered and pelletized UiO-66 activated at 80, 200, 290, and 320 ^oC.

In Fig. 4.28 and Table 4.12 it can be seen that the gravimetric H_2 uptake of pelletized UiO-66 differed with activation temperature relative to UiO-66 powder. The hydroxylated UiO-66 pellet was seen to have retained more than 90% of the gravimetric H_2 uptake obtained in UiO-66 powder and showed improved working capacity similar to the results in Table 4.9. The result showed some degree of reproducibility to the results presented in Fig. 4.24 even though the two isotherms did not exactly match up to 100 bar as shown in Fig. 4.24. The reason could be the slightly lower BET surface areas and pore volumes measured for pelletized UiO-66, and it was also noted during experimentation that longer activation times of up to 32 hours were required to completely evacuate the sample of guest molecules, especially in pelletized UiO-66 samples. The gravimetric H_2 uptake of partially dehydroxylated UiO-66 pellets, activated at 200 and 290 ^oC, was only about 20% of the H_2 uptake of powdered and pelletized hydroxylated UiO-66. The dehydroxylated UiO-66 pellet, activated at 320 ^oC, however, showed slightly higher H_2 uptake at 100 bar, with a retention of about 30% to that of hydroxylated UiO-66. The amount of H_2 adsorbed in partially dehydroxylated UiO-66 samples was lower at 100 bar compared to 5 bar and thus effectively resulted in a zero working capacity when considering the difference between H_2 adsorbed at 100 bar and desorbed at 5 bar. This reduction in gas uptake at high pressure is typical when adsorption sites (pores) become saturated with gas molecules and the rate of desorption far exceeds the rate of adsorption.

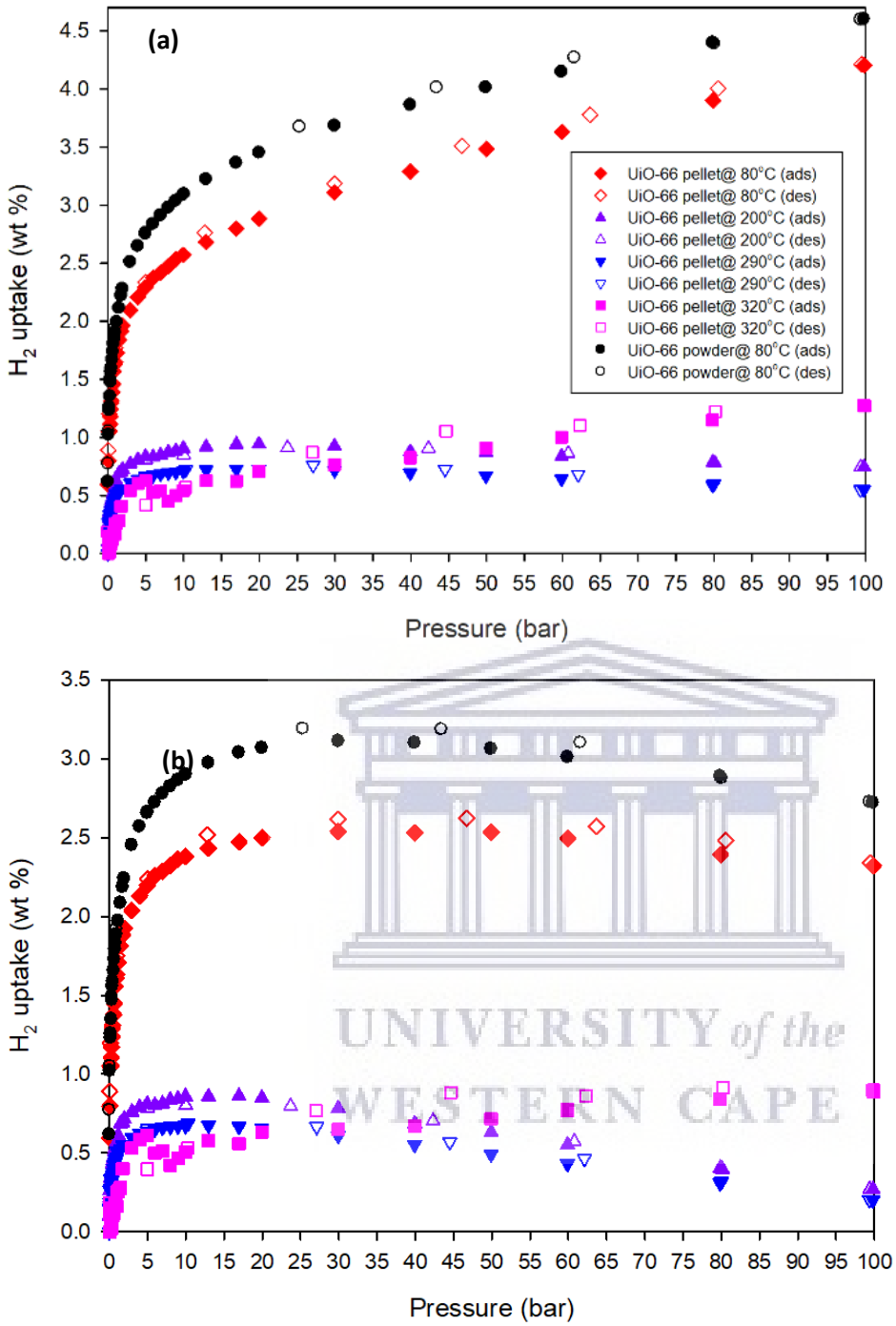

Figure 4.28: H_2 adsorption/desorption isotherms (77 K, 100 bar) for pelletized UiO-66 (from batch 1) after activation at 80, 200, 290, and 320 °C: (a) total H_2 uptake, and (b) excess H_2 uptake.

Remarkably the dehydroxylated UiO-66 pellet showed a positive working capacity of 0.9 wt% as its total H_2 uptake was at its highest at 100 bar. The excess H_2 isotherm for dehydroxylated UiO-66 activated at 320 °C was also found not to show signs of reaching saturation at 100 bar. This observation could be attributed to the restoration of crystalline phases in UiO-66 pelletized

after activation at 320 ^{o}C (Fig. 4.21) as it was observed that pelletized UiO-66 activated at 290 ^{o}C showed a high degree of amorphousness. The restoration of crystalline phases may have indicated a recombination of the UiO-66 structure and possibly its original H_2 adsorption behaviour as found in its hydroxylated form. In Fig. 4.28 it can be observed that pelletized hydroxylated UiO-66 activated at 80 ^{o}C also resulted in an excess H_2 adsorption isotherm showing little signs of saturation up to 100 bar. This observation was also seen in Fig. 4.24 and could possibly show that the pelletization of UiO-66 with a high degree of crystallinity (i.e. sharp peaks in their PXRD patterns) could have a tendency to reduce the rate of H_2 desorption at high pressure (>30 bar) and thereby retain a high amount of adsorbed H_2.

Table 4.12: Summary of the gravimetric H_2uptake at 77 K and 100 bar for UiO-66 powder (80 ^{o}C) compared to UiO-66 pellets activated at 80, 200, 290, and 320 ^{o}C.

Sample (batch 1)	**Maximum excess Uptake (wt%)**		**Total/absolute gravimetric H_2 uptake (wt%)[b]**		**Working capacity (wt%)[c]**
	Experimental	**Estimate[a]**	**5 bar**	**100 bar**	
UiO-66 powder@ 80 ^{o}C	3.1	2.8	2.8	4.6	1.8
UiO-66pellet@ 80 ^{o}C	2.5	2.6	2.3	4.2	1.9
UiO-66 pellet@ 200 ^{o}C	0.9	0.5	0.8	0.8	0
UiO-66 pellet@ 290 ^{o}C	0.7	0.4	0.7	0.6	0
UiO-66 pellet@ 320 ^{o}C	0.9	0.4	0.4	1.3	0.9

[a]Estimates based on the Chahine rule [209]. [b]Calculated using eqn. 3.3 in chapter 3 (section 3.4.5.2). [c]Difference between the total H_2 uptake at 100 bar (adsorption) and 5 bar (desorption).

4.6.2. Volumetric H_2 capacity for powdered and pelletized UiO-66 activated at 80, 200, 290, and 320 ^{o}C

In Fig. 4.29 it can be observed that the volumetric H_2 capacities between powdered and pelletized hydroxylated UiO-66 were consistent with results shown in Fig. 4.25. The UiO-66 pellet showed a volumetric H_2 capacity at least 100% higher in comparison to that of UiO-66 powder, and at pressures above 80 bar, the volumetric H_2 capacity of UiO-66 powder became less compared to the theoretical H_2 density in a pressurized cylinder.

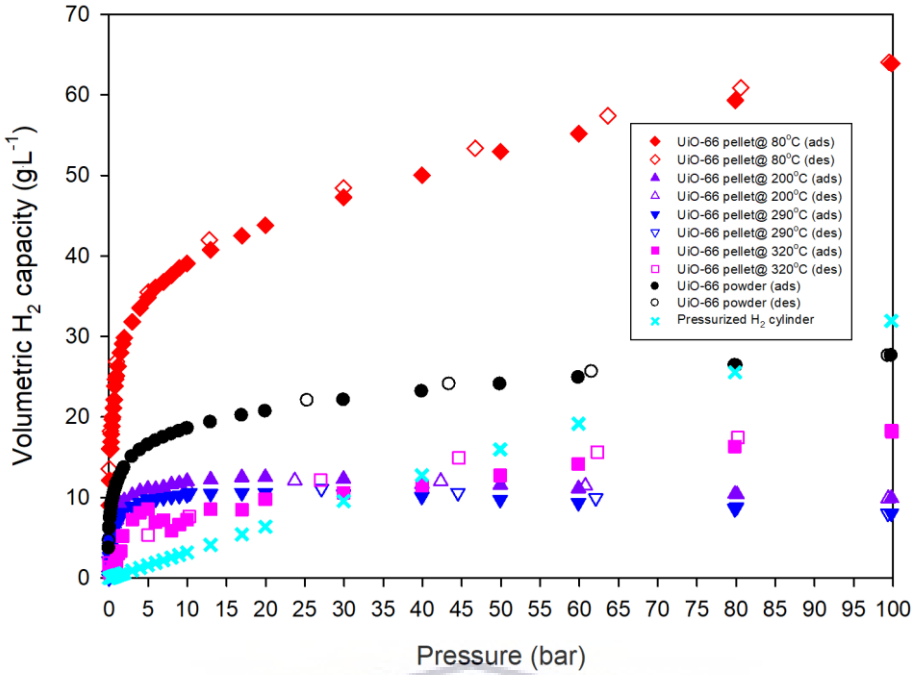

Figure 4.29: H_2 adsorption isotherms showing the volumetric H_2 capacity for hydroxylated and dehydroxylated UiO-66 pellets compared to hydroxylated UiO-66 powder.

In Table 4.13, the volumetric H_2 capacities of partially dehydroxylated UiO-66 pellets showed zero working capacity, whereas the dehydroxylated UiO-66 pellet showed a working capacity of 13 $g.L^{-1}$. The results could have suggested some degree of recovery in the mechanical stability of UiO-66 in its fully dehydroxylated form. Indeed the PXRD patterns shown earlier in Fig. 4.21 indicated crystalline peaks/phases not observed for UiO-66 pellets activated at 200/290ºC but present in UiO-66 pellets activated at 80 and 320 ºC. This is the first study to report experimental results showing such behaviour in UiO-66 gas uptake properties. This work demonstrated experimentally for the first time that UiO-66 responds in a dynamic fashion to changes in activation temperature within the range in which it has previously been considered stable. The results seemingly show strong agreement with the computational study reported by Vandichel et al. [72]. In this study, partially dehydroxylated UiO-66, at 200 and 290 ºC, were shown to exhibit crystalline phases with very high amorphous character (Fig. 4.21), extreme reductions in BET surface areas and pore volumes (Table 4.8) and extreme reductions in gravimetric and volumetric H_2 capacities upon pelletization at 700 MPa.

Table 4.13: Summary of the volumetric H_2 capacity at 77 K and 100 bar for UiO-66 powder (80 °C) compared to UiO-66 pellets activated at 80, 200, 290, and 320 °C.

Sample	**5 bar**	**Total volumetric H_2 capacity ($g \cdot L^{-1}$)**			**Working capacity[c]**
		25 bar		**100 bar**	
		Experimental[a]	**Estimate[b]**		
UiO-66 powder@ 80°C	17	22	18	28	11
UiO-66 pellet@ 80°C	36	46	38	64	28
UiO-66 pellet@ 200°C	11	12	6	10	0
UiO-66 pellet@ 290°C	10	11	6	8	0
UiO-66 pellet@ 320°C	6	11	5	19	13
Pressurized H_2 cylinder	2	-	-	31	29

[a]Calculated using eqn. 3.4 in chapter 3 (section 3.4.5.2). [b]Calculated using the volumetric surface area (Table 4.8) and the "volumetric H_2 density" as recommended in ref [50]. [c]Difference between the total H_2 uptake at 100 bar (adsorption) and 5 bar (desorption).

The study by Vandichel et al. [72] proposes that there could possibly exist two transition states during the dehydroxylation process of UiO-66, and the results obtained in this work could have suggested the presence of the said transition states around 200 and 290 °C. The fully dehydroxylated UiO-66 powder showed reduced BET surface areas, pore volumes, and H_2 capacities compared to hydroxylated UiO-66. It is noticeable in this study that the dehydroxylated UiO-66 pellet showed much inferior textural properties compared to hydroxylated UiO-66 pellets, thus suggesting some compromise to the mechanical strength of UiO-66 after dehydroxylation at 320 °C. Indeed Vandichel's computational study reports on reductions in mechanical strength for dehydroxylated UiO-66, that become enhanced in UiO-66 crystals with defects and with major effects on the shear modulus compared to the bulk modulus of UiO-66.

4.7. Determination of the heat of adsorption on powdered and pelletized UiO-66

Using the Clausius-Claperyon equation [29,204] the calculated values for the isosteric enthalpy (Table 4.10) of adsorption for powdered and pelletized UiO-66 activated at 80 °C 4.5 $kJ \cdot mol^{-1}$ and 3.9 $kJ \cdot mol^{-1}$ respectively, which were obtained at a coverage of 0.3; 0.5; 0.8; and 1.1 wt% total H_2 uptake. It can be seen in Table 4.14 that across the selected adsorbed amounts, the enthalpy of adsorption remained relatively constant for both powdered and pelletized UiO-66.

This observation generally represents a high level of homogeneity of an adsorbent surface, further proving the highly microporous nature of UiO-66.

Table 4.14: H_2 uptake experimental values used to calculate the isosteric enthalpy of adsorption (ΔH_{ad}) using the Clausius-Claperyon equation.

UiO-66 powder	**H_2 uptake (wt%)**	**T_1 (K)**	**P_1 (bar)**	**T_2 (K)**	**P_2 (bar)**	**ΔH_{ad} (J.mol^{-1})**	**ΔH_{ad} (kJ·mol^{-1})**
	0.3	77	0.2	298	25	4168	4.2
	0.5	77	0.25	298	40	4381	4.4
	0.8	77	0.39	298	70	4480	4.5
	1.1	77	0.56	298	100	4476	4.5
UiO-66 pellet	**Uptake (wt%)**	**T_1 (K)**	**P_1 (bar)**	**T_1 (K)**	**P_1 (bar)**	**ΔH_{ad} (J.mol^{-1})**	**ΔH_{ad} (kJ/mol^{-1})**
	0.3	77	0.3	298	30	3976	4.0
	0.5	77	0.56	298	55	3959	4.0
	0.8	77	0.91	298	80	3864	3.9
	0.9	77	1.2	298	100	3818	3.8

In the case of UiO-66, it is well-documented that UiO-66 is a highly microporous MOF and the results obtained in this study showed further proof with micropore surface areas as high as 91 % of the total BET surface area of UiO-66 activated at different temperatures (Table 4.5) and a constant enthalpy of adsorption.

4.3. Chapter summary

This chapter presented the analysis of MIL-101 and UiO-66 prepared via acid-modulated solvothermal synthesis, as highlighted in chapter 3. The results were obtained for both powder and pelletized MOF forms and included morphological characterizations, chemical and crystallographic compositions, and most importantly the gas adsorption properties of powdered MOFs compared to their pelletized counterparts. It was evident from the gas adsorption results that UiO-66 exhibited significantly different behaviour towards pelletization compared to MIL-101(Cr) with the former MOF being found to be the more robust compared to the latter. It was

also observed that the mechanical robustness of UiO-66 was dependent on the post-synthesis activation/degassing temperature employed to fully remove guest molecules from the as-synthesized crystals. It was demonstrated experimentally for the first time that UiO-66 responds in a dynamic manner to changes in activation temperature within the range in which it has up till now been considered stable. The concept of compaction (or pelletization) of UiO-66 to enhance volumetric capacity without compromising gravimetric uptake was also proven, which is a rare occurrence for MOFs. Furthermore, the applied pressure for pelletization (700 MPa) is also unprecedented for MOFs since most studies have reported a collapse of the MOF structure upon compaction at very high pressures. In closing, this chapter clearly demonstrated the pelletization strategy/method as a useful tool to improve the inherently low packing densities of MOFs and subsequently resulting in improved volumetric H_2 capacities of MOF pellets compared to their powder counterparts.

Chapter 5

5. Electrospinning of MOF/polymer composites for H_2 storage applications

This chapter covers the electrospinning of non-porous polymers polyacrylonitrile (PAN), polymethylmethacryalate (PMMA), and polystyrene (PS) and a porous polymer, PIM-1 (polymer of intrinsic microporosity-1), using two electrospinning techniques, namely single-nozzle and coaxial electrospinning. Initially, the results showed the optimization of the process parameters suitable to produce polymer nanofibers with uniform fiber diameters and negligible bead formation. The optimization results served to establish electrospinning conditions where the incorporation of the selected MOFs, UiO-66 and MIL-101(Cr), would be favourable for single-nozzle and coaxial electrospinning of MOF/polymer solutions/emulsions. The aim of the incorporation of MOFs into nanofibers was to embed the MOFs in a polymer matrix so as to improve their handling compared to their powdered, free-standing counterparts. The use of MOF/polymer nanofibers was proposed as a method that would facilitate easier system integration into a possible high-pressure cylinder compared to the use of MOFs as loose powders. In addition, the MOF/nanofiber nanofibers prepared in this study were also intended for use as polymer-based binders in the pelletization of UiO-66 that would possibly provide improved mechanical strength and structural integrity compared to UiO-66 pellets without binders (discussed in Chapter 6). The main challenge, however, was to overcome the inevitable reduction in the textural properties (surface areas and pore volumes) in the MOF/polymer nanofibers compared to the pristine MOF powders, due to the use of non-porous polymers and the PIM-1 polymer having a lower surface area and pore volume compared to UiO-66 and MIL-101(Cr). In order to counteract the challenge, the study proposed a post-electrospinning treatment of core-shell MOF/X@PAN nanofibers (X = PMMA or PS) prepared via the coaxial electrospinning method. The shell component of the nanofibers consisted of MOF/PAN and MOF/PMMA(PS) as a core material. The core polymer material was then selectively removed post-electrospinning by immersing in acetone (in the case of PMMA) or chloroform (in the case of PS), since both solvents do not dissolve PAN. This form of selective removal using solvents was demonstrated by Zander et al. [200] where PMMA/PAN core-shell nanofibers where soaked in a solvent to dissolve PMMA out of the composite, confirmed by FTIR and TGA, leaving behind PAN. In this study, the method of selective removal could possibly ensure that a core-shell MOF/PMMA@PAN nanofiber containing a 20 wt% MOF loading, with respect to the amount of PMMA, could be increased to about 60 wt% after the complete

removal of the PMMA core following treatment with a solvent such as acetone. This possible increase in the MOF loading could be further exploited in composites which contain 20 wt% MOF loadings in core *and* shell regions of the core-shell nanofiber composite. In the latter situation it would be possible to increase the MOF loading close to about 90 wt% with respect to the remaining PAN polymer after selective removal of the core polymer. The consistency of the proposed or possible improvements in MOF loadings would obviously be determined by the quality of the electrospun nanofiber composites using the specified electrospinning conditions as set out in this study. By improving the MOF loading, it could be possible to improve the surface areas, pore volume, and H_2 capacities of MOF/PAN nanofibers to resemble those of the pristine MOF powders.

5.1. Single-nozzle electrospinning of PAN and PIM-1 nanofibers

The electrospinnable polymers such as PAN are sensitive to process parameters as non-optimal conditions e.g. low polymer concentration, high voltage, impurities, high flow rates, may lead to severe bead formation and hence non-uniform fiber diameters that are not desirable.

5.1.1. Electron microscopy of electrospun PAN and PIM-1 via single-nozzle electrospinning

In Fig. 5.1 and 5.2, it can be seen that the morphologies of PAN and PIM-1 nanofibers were strongly affected by the process parameters employed during electrospinning. In Fig. 5.1a, it can be seen that for a PAN solution of 12 wt% in DMF, 3 $mL{\cdot}h^{-1}$ and applied voltage of 12 kV, the nanofibers were observed to consist of beads, but the degree of bead formation was found to be reduced upon simultaneously lowering the solution flow rate and applied voltage to 1.8 - 2 $mL{\cdot}h^{-1}$ and 11 kV respectively (Fig. 5.1b and Fig. 5.2a). In general, the main source of bead formation during polymer electrospinning is the viscosity of the solution and the influence of the applied voltage and flow rate become lessened upon reaching a critical viscosity that is ideal for electrospinning [171]. In cases whereby the concentration of the polymer solution does not represent a critical viscosity, the influence of the applied voltage and flow rate become enhanced [182]. It was, however, not in the scope of this study to include an in-depth investigation on the effect of the applied voltage and flow rate. The observation made in Fig. 5.1b and Fig. 5.2a was sufficient to maintain the applied voltage and flow rate at 11 kV and 1.8 $mL{\cdot}h^{-1}$ for the electrospinning of PAN-based polymer solutions/emulsions. The electrospinning

of PIM-1 was, however, more difficult as the formation of nanofibers was found to be influenced by the solution concentration *and* the solvent in which PIM-1 was dissolved. In Fig. 5.1c it can be seen that the electrospinning of a 10 wt% PIM-1 solution in TCE led to the formation of thin film, with no evident formation of nanofibers. The formation of film could be explained by considering that the solvent could have not evaporated under the specified electrospinning conditions, probably due to its high affinity for the polymer or the solvent having a high viscosity [113].

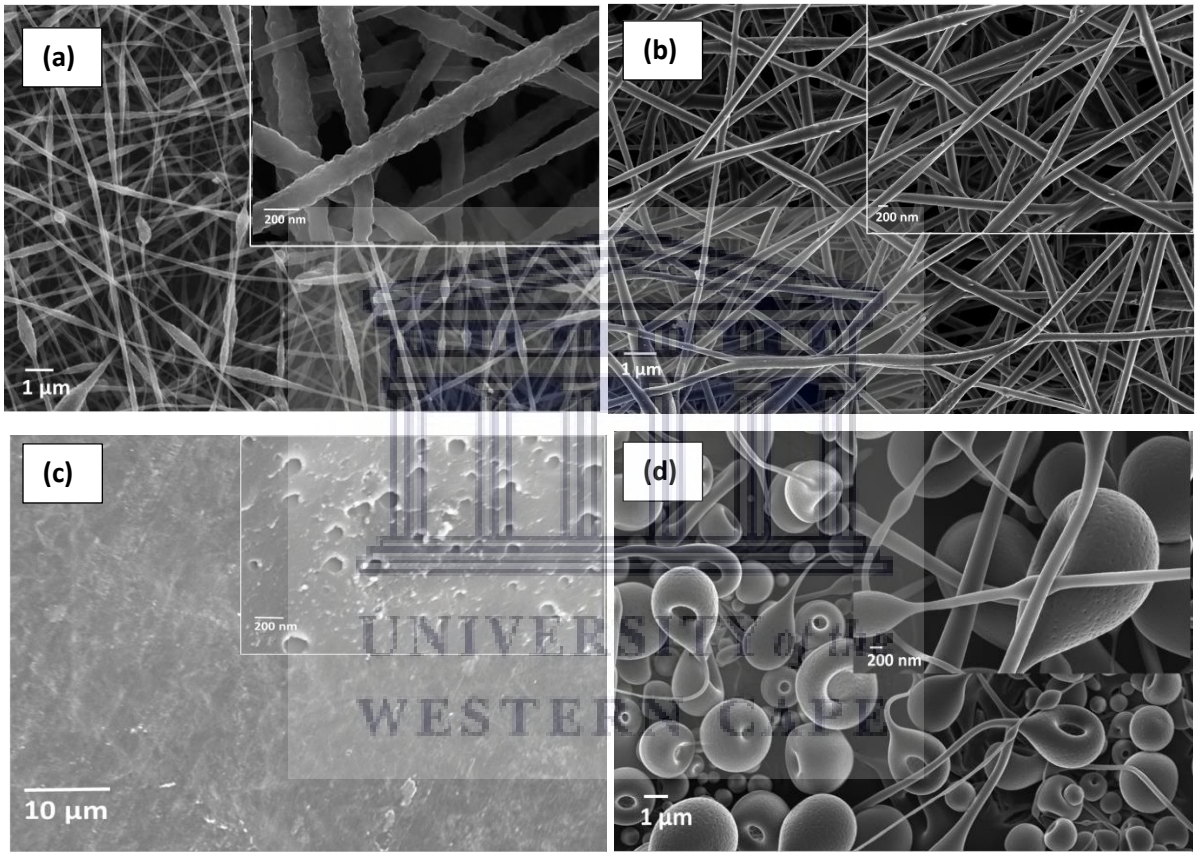

Figure 5.1: SEM images showing the microstructure of electrospun PAN and PIM-1: (a) PAN nanofibers obtained for a 12 wt% solution, 3 mL·h^{-1} flow rate, and at 12 kV applied voltage; (b) PAN nanofibers obtained for a 10 wt% solution, 2 mL·h^{-1} flow rate, and at 12 kV applied voltage; (c) PIM-1 thin film obtained post-electrospinning a 10 wt% (in TCE), at 3 mL·h^{-1} flow rate, and 16 kV applied voltage; and (d) PIM-1 nanofibers obtained for a 5 wt% solution (in TCE), 2 mL·h^{-1} flow rate, and at 12 kV applied voltage.

In Fig. 5.1d, the PIM-1 concentration was reduced to 5 wt% in TCE, but as can be seen, the electrospun PIM-1 contained a high content of beads and non-continuous fibers. The non-continuous nature of the fibers suggested that under the specified process parameters (12 kV,

2 mL·h^{-1}, and 5 wt% PIM-1 concentration) the deposition of PIM-1 on the collector could be considered as occurring via an electro-spraying mechanism.

It is common that the electrospinning and electro-spraying mechanisms may compete depending on the process parameters. Dilute polymer solutions, typically below 7 – 8 wt%, typically show low solution viscosities and experience jet breakdown during prolonged electrospinning procedures (time > 1 hour), therefore, leading to the formation of non-continuous or beaded nanofibers [216].

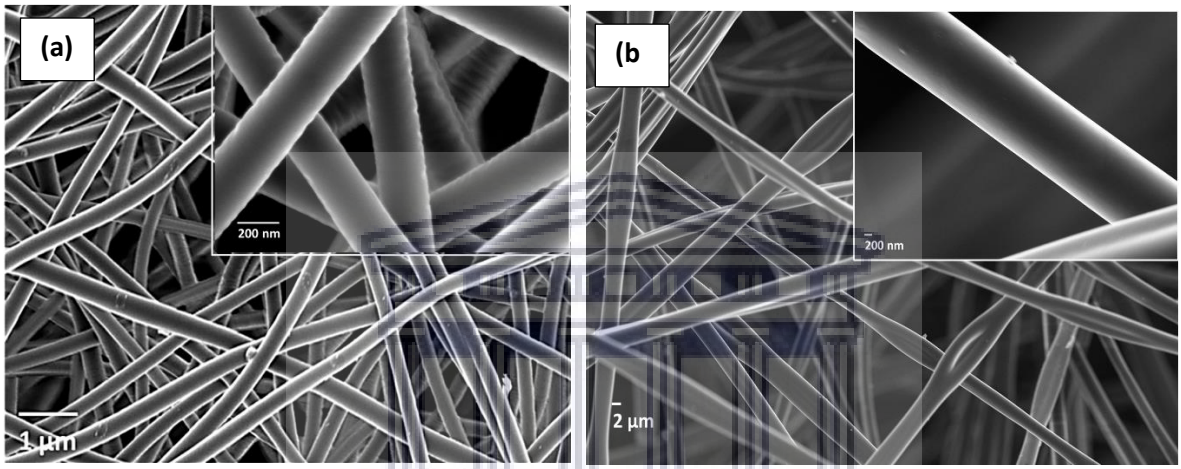

Figure 5.2: SEM images of PAN and PIM-1 nanofibers: (a) PAN nanofibers obtained for an 8 wt% solution, 1.8 mL·h^{-1} flow rate, and at 11 kV applied voltage; and (b) PIM-1 nanofibers obtained for a 5 wt% solution in a 7:3 v/v mixture of TCE:THF, 2-3 mL·h^{-1} flow rate and at 16 kV applied voltage.

In Fig. 5.2b it can be seen that the dissolution of PIM-1 in a solvent mixture containing 30 % v/v THF to TCE resulted in the formation of continuous PIM-1 nanofibers with little bead formation. The addition of THF was experimented based on the miscibility of THF and TCE [193,217].

5.1.2. Spectroscopy of electrospun PAN and PIM-1 via single-nozzle electrospinning

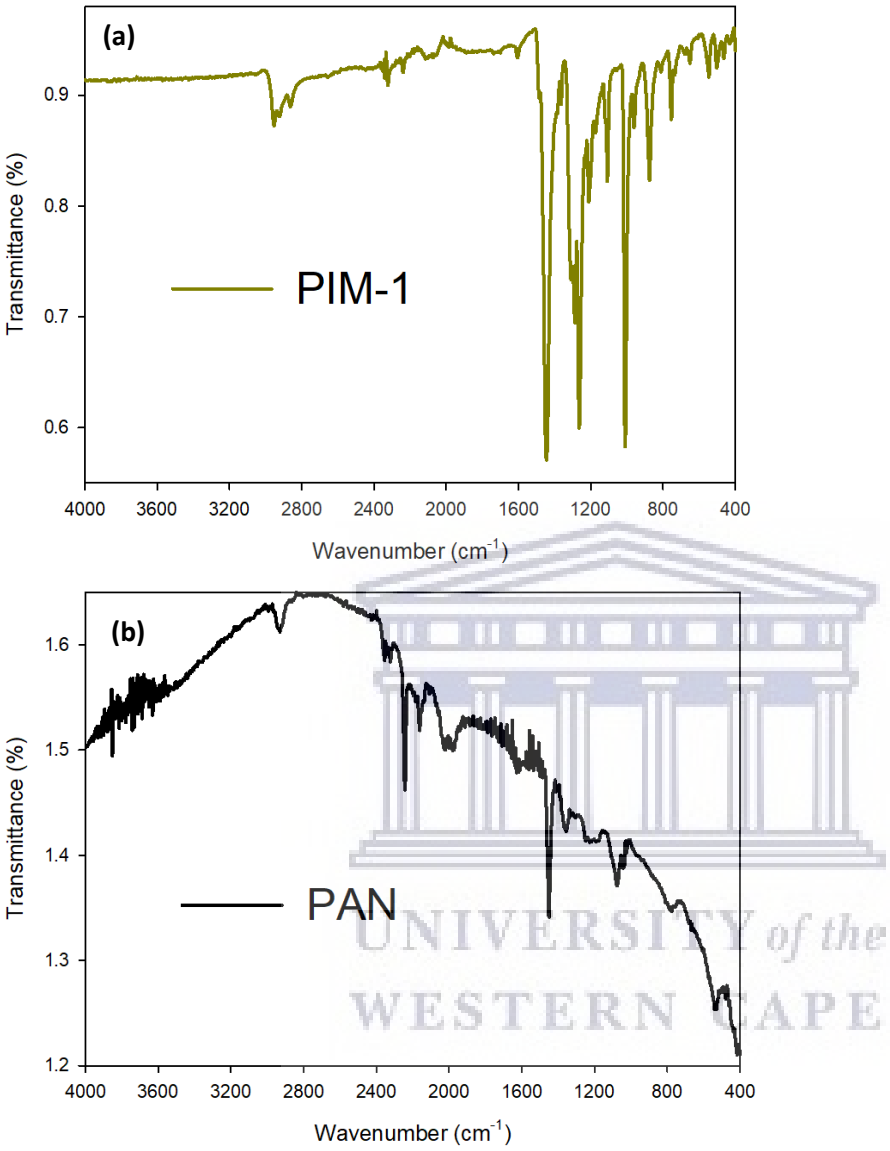

Figure 5.3: Chemical composition analysis of selected polymer nanofibers: FTIR spectra of electrospun polymer nanofibers collected between 4000 and 400 cm^{-1}, (a) PIM-1 nanofibers, and (b) PAN nanofibers obtained after activation at 200 ^{o}C for 16 hours. The PAN nanofibers were collected at 1.8 $mL{\cdot}h^{-1}$ flow rate, 11 kV voltage, and 15 cm needle-to-collector distance and PIM-1 nanofibers collected at 3 $mL{\cdot}h^{-1}$ flow rate, 16 kV voltage, and 16 cm needle-to-collector distance..

In Fig. 5.3, the major vibrational bands for PIM-1 were observed at wavenumbers of ~1400 cm^{-1} for methyl and ethyl groups present in the 5-membered rings of PIM-1 (CH stretch), ~1300 cm^{-1} for ester groups (C-O-C) and ~900 cm^{-1} for ethylenic groups present in the aromatic rings

of PIM-1 (-CH=CH_2) [218]. The FTIR spectrum of PAN also showed typical vibrational bands at wavenumbers ~1400 cm^{-1} and ~3000 cm^{-1} due to methyl deformation and stretch vibrations (-CH_3) respectively, in the polymer backbone. The vibrational bands at ~2300 cm^{-1} could be attributed to the presence of cyano groups (-C≡N) and –NH groups in the acrylic moieties. It was, therefore, observable that the chemical composition of both PIM-1 and PAN was maintained post-electrospinning as their FTIR spectra were consistent with those reported in literature.

In section 5.1.3, the textural properties (surface area and pore volume) of the electrospun PAN and PIM-1 nanofibers were determined from N_2 adsorption/desorption isotherms at 77 K.

5.1.3. Textural properties of electrospun PAN and PIM-1 nanofibers prepared via single-nozzle electrosptinning

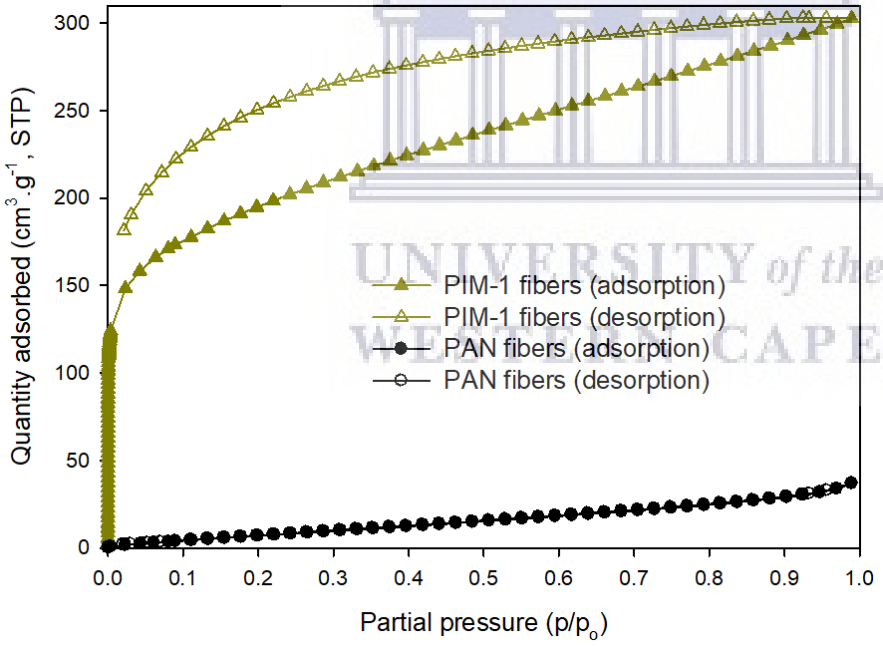

Figure 5.4: N_2 adsorption/desorption isotherms for electrospun PAN and PIM-1 nanofibers obtained under optimized process parameters (Chapter 3, Table 3.2). The PAN nanofibers were collected at 1.8 $mL{\cdot}h^{-1}$ flow rate, 11 kV voltage, and 15 cm needle-to-collector distance and PIM-1 nanofibers collected at 3 $mL{\cdot}h^{-1}$ flow rate, 16 kV voltage, and 16 cm needle-to-collector distance.

The results in Fig. 5.4 showed that the N_2 adsorption isotherm obtained for PAN nanofibers showed no adsorption at low relative pressure and gradually increased with increasing pressure. The type of isotherm is classified as Type III, as described by the IUPAC (International Union of Pure and Applied Chemistry) classification, which are typically observed on non-adsorbent or non-porous materials with the observed adsorption towards $p/p_o = 1$ resulting from macropores present in the material such as voids or interparticle spaces [39]. The desorption isotherm was found to coincide with adsorption isotherm, showing fully reversible behaviour with no evidence of hysteresis. The non-porous nature of PAN nanofibers was also observed on Fig. 5.5 as no peaks were observable in the micropore region (2 – 20 Å), but in the mesopore region (20 – 50 Å) some degree of porosity could be observed as the incremental pore volume at the pore widths of ~26 – 80 Å was ~0.005 $cm^3 \cdot g^{-1}$. In Fig. 5.2, it can be seen that the electrospun nanofibers formed a three-dimensional network consisting of void or inter-fiber spaces that were greater than 200 nm in diameter. The three-dimensional structure is an intrinsic property of electrospun nanofiber mats and may provide a permanent porosity present in the mat, but not on the surface of the nanofiber, with meso- to macro-sized openings, as nanofibers have been shown to have size exclusion properties when applied in filter technologies [167,219]. The N_2 adsorption isotherm obtained for PIM-1 showed a combination of two types of isotherms, a Type I(a) portion characterized by a steep adsorption at low relative pressure ($p/p_o << 0.1$) and a Type II portion from the point of inflection to $p/p_o = 1$.

Indeed the pore size distribution in Fig. 5.5 showed micropores with pore sizes at 6, 8, and 13 Å that are consistent with typical pore sizes reported in literature for PIM-1 [111,112,184,220]. In the mesopore region, the pore size distribution curve was found to show similar behaviour to that of the PAN nanofibers and this could be attributed to the nanofiber mat consisting of a three-dimensional structure with a permanent porosity formed by overlaying of the nanofibers.

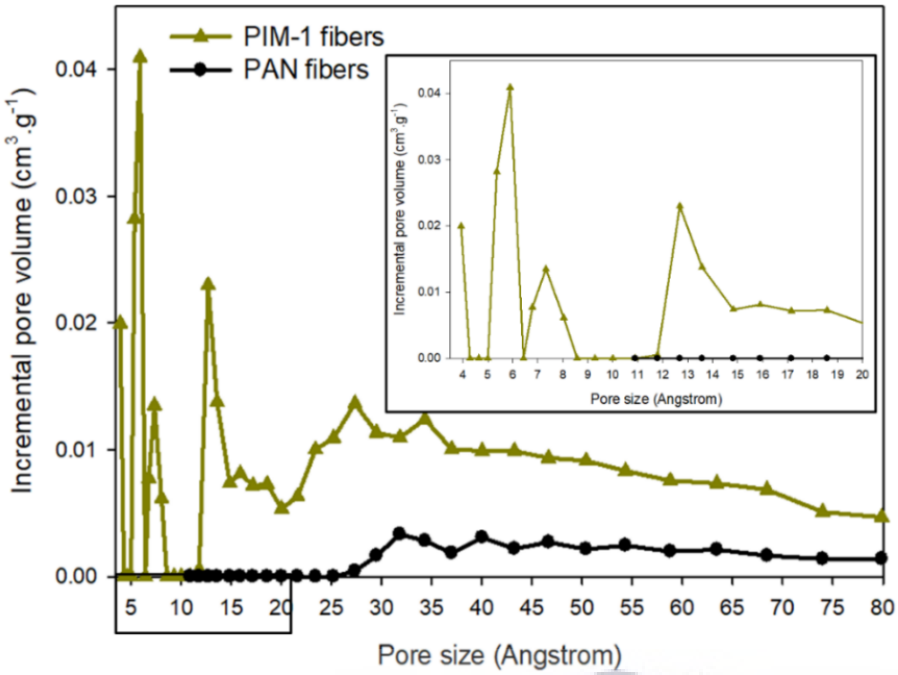

Figure 5.5: Pore size distribution curves for PAN and PIM-1 nanofibers obtained under optimum electrospinning parameters (Chapter 3, Table 3.2). The selected area (black) represents the micropre region ranging from 2 – 20 Å. The PAN nanofibers were collected at 1.8 mL·h^{-1} flow rate, 11 kV voltage, and 15 cm needle-to-collector distance and PIM-1 nanofibers collected at 3 mL·h^{-1} flow rate, 16 kV voltage, and 16 cm needle-to-collector distance.

The mesoporosity observed could be associated with the Type III portion of the PIM-1 N_2 adsorption isotherm. The N_2 desorption isotherm of PIM-1 (Fig. 5.3) was found not to overlap with the adsorption isotherm, showing a big hysteresis loop from $p/p_o = 1$ down to $p/p_o = 0$. The appearance of a hysteresis loop indicated a possible hierarchical and complex pore structure within PIM-1. The type of hysteresis loop could be identified as a Type H4 loop which is a common feature of micro-mesoporous carbon-based materials. It is also common that Type H4 loops occur in a combination of Type I and Type II adsorption isotherms and the broadness of the hysteresis loop signifies micropores and may be filled with condensed N_2 molecules as the PIM-1 pores may undergo adsorption-induced swelling [184,218,221].

5.3.1.2. Infrared spectroscopy of electrospun PMMA@PAN nanofibers

The chemical composition of the PMMA@PAN nanofibers was analysed using FTIR, and in Fig. 5.6 it can be seen that the vibrational bands corresponding to both PAN and PMMA were observable on the FTIR spectrum of the co-electrospun PMMA@PAN nanofibers.

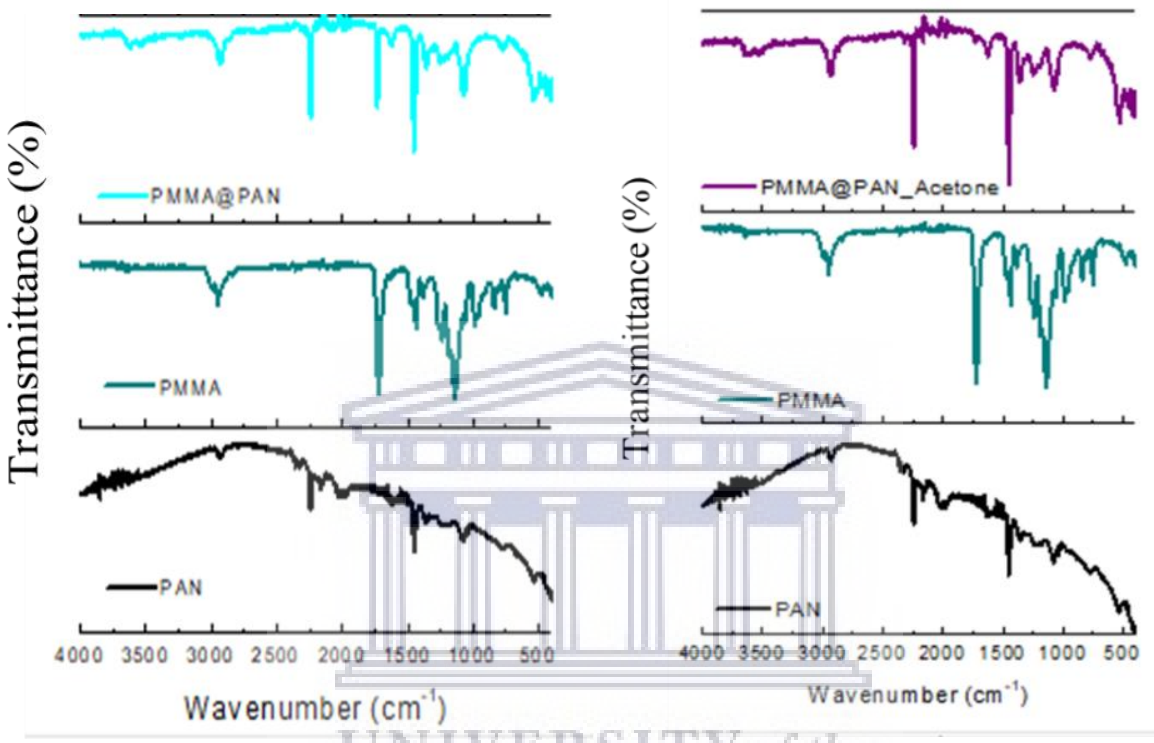

Figure 5.6: FTIR spectra obtained for pristine PAN and PMMA granules in comparison to co-electrospun PMMA@PAN nanofibers (1.8 mL·h^{-1} flow rate; 11 kV voltage; and 15 cm needle-to-collector distance): (a) as-spun nanofibers; and (b) nanofibers after treatment with acetone.

In Fig. 5.6, the treatment of co-electrospun PMMA@PAN nanofibers with 20 mL aliquots of acetone resultant in the disappearance of the main vibrational band at *ca.* 1700 cm^{-1}, characteristic of pristine PMMA. The remaining vibrational bands in the acetone-treated PMMA@PAN nanofibers showed increased intensities in the vibrational bands matching those of pristine PAN, i.e. at *ca.* 2800, 2300, 1500, and 1100 cm^{-1}. The FTIR results showed that the treatment of co-electrospun PMMA@PAN nanofibers with acetone was sufficient to remove PMMA without affecting the structure of the remaining PAN nanofibers and also with no changes to the chemical composition of PAN. The results confirm the incorporation of PMMA in the core region during co-electrospinning.

5.2. Preparation of MOF/PAN nanofibers by single-nozzle electrospinning

The preparation of MOF/PAN nanofibers was carried out for the incorporation of both UiO-66 and MIL-101(Cr) crystals into the PAN polymer matrix. The optimum electrospinning process parameters used for the electrospinning of PAN in section 5.1 were also applicable to the electrospinning of MOF/PAN nanofiber composites using the single-nozzle electrospinning technique. There were two MOF loadings prepared separately using 8 wt% PAN solution, a 20 and 40 wt% MOF loading. The selection of the two loadings was based on previous studies carried out in the HySA Infrastructure group and adopted in this study.

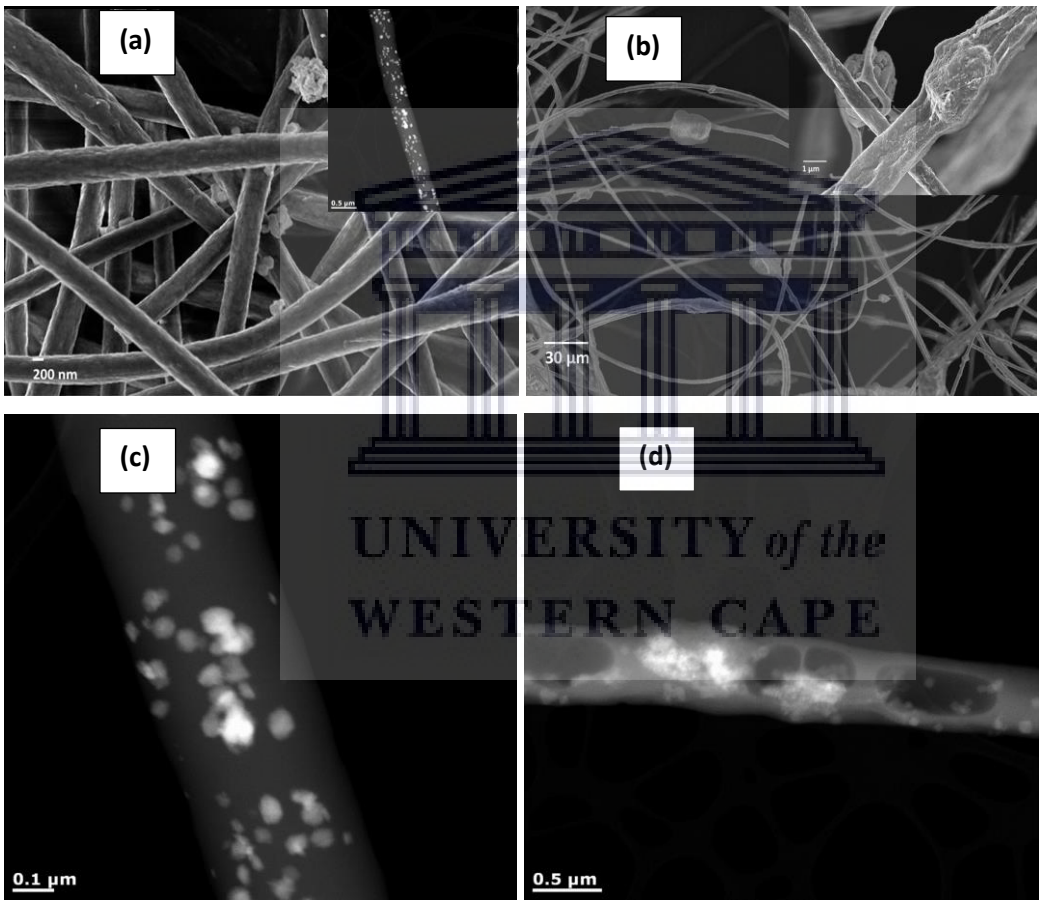

Figure 5.7: SEM images of UiO-66/PAN nanofibers prepared using single-nozzle electrospinning: (a) UiO-66/PAN nanofibers containing 20 wt% UiO-66 loading; (b) UiO-66/PAN nanofibers containing 40 wt% UiO-66 loading; (c) TEM image of UiO-66/PAN nanofiber containing 20 wt% UiO-66 loading; and (d) TEM image UiO-66/PAN nanofiber containing 40 wt% UiO-66 loading. The nanofibers were collected at 1.8 mL·h^{-1} flow rate, 11 kV voltage, and 15 cm needle-to-collector distance

In Fig. 5.7a and Fig. 5.7d, it can be seen that under the selected process parameters, the MOF/PAN nanofibers consisting of 20 wt% UiO-66 were found to have consistent distribution of MOF crystals mainly embedded within the PAN matrix with small amounts observed on the surface of the nanofibers. The nanofibers containing 40 wt% UiO-66 were observed to have inconsistent fiber diameters ranging from 1 up to about 15 µm due to the formation of aggregates within the PAN nanofiber, as shown in Fig. 5.6c. Based on the results, a MOF loading of 20 wt% was selected for further electrospinning experiments in the study.

In Fig. 5.8 the TEM image was marked (SOI 1 particle) for analysis of a section of the UiO-66/PAN nanofiber in order to qualitatively determine the chemical composition of the observed crystals using EDX analysis. The EDX spectrum showed that the selected region predominantly consisted of zirconium (Zr) metal and carbon as they exhibited the most intense peaks compared to other identified elements. The identification of copper (Cu) could be due to the sample grid background and a chromium (Cr) peak was found to overlap with oxygen (O). The possibility for the presence of Cr in the sample could have been significant and resulted from cross-contamination since the electrospinning experiments were also carried out on MIL-101(Cr)/PAN nanofibers. It is, however, evident that the major element consisted of Zr elements due to the presence of UiO-66 crystals within the PAN matrix.

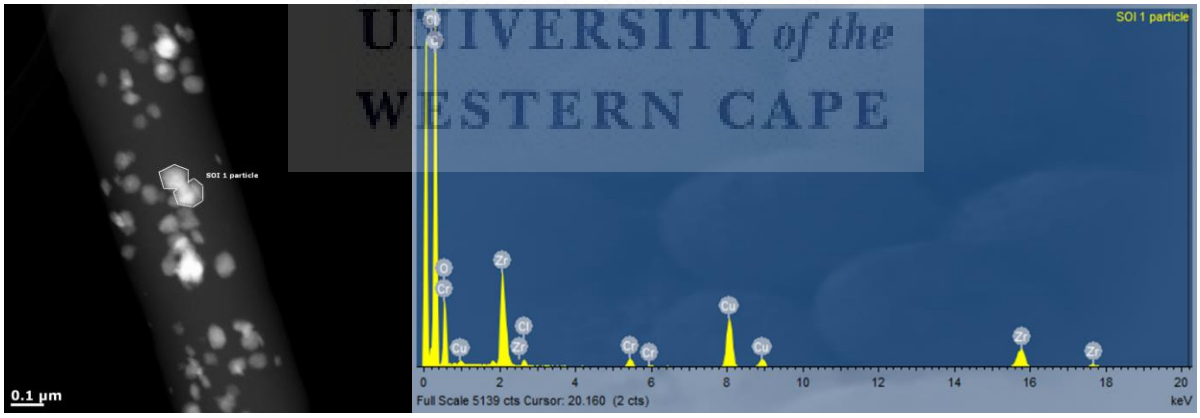

Figure 5.8: TEM image and EDX spectrum of UiO-66/PAN nanofiber containing 20 wt% UiO-66 loading. The spectrum refers to the particles marked as "SOI 1 particle" on the TEM image. The nanofibers were collected at 1.8 mL·h^{-1} flow rate, 11 kV voltage, and 15 cm needle-to-collector distance

In addition to imaging, the incorporation of UiO-66 and MIL-101(Cr) onto electrospun PAN nanofibers were further investigated by FTIR, PXRD and TG analysis by comparing the results obtained for the composite nanofibers to that of pristine MOF and polymer materials.

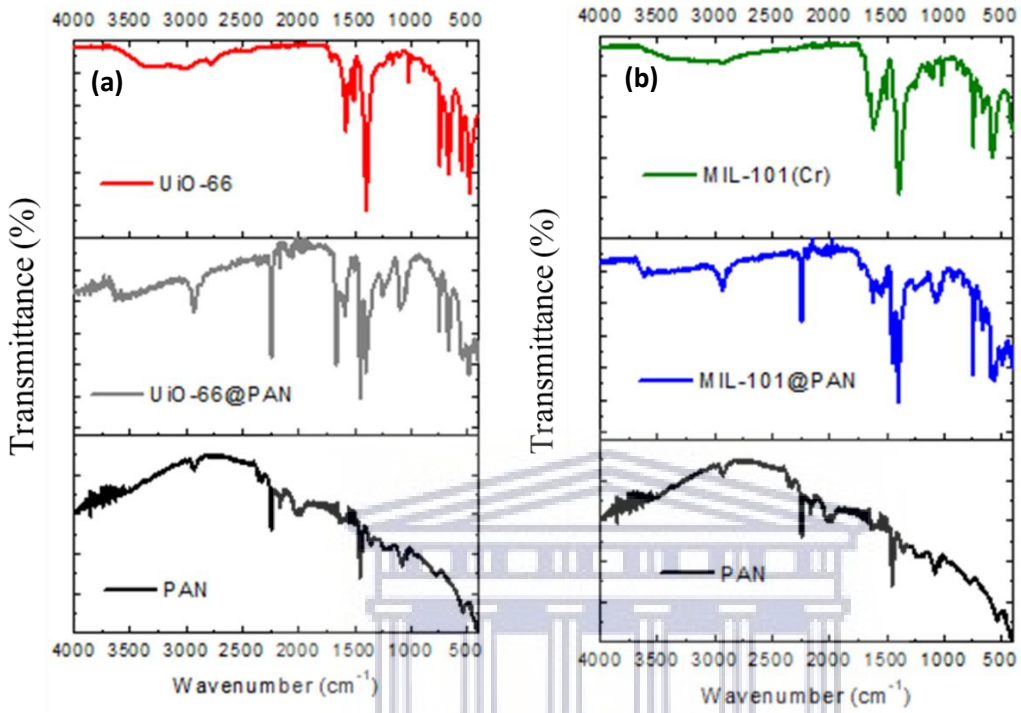

Figure 5.9: Comparison of FTIR spectra: (a) UiO-66 powder, PAN nanofiber, and UiO-66/PAN nanofiber composite; and (b) MIL-101(Cr) powder, PAN nanofiber, and MIL-101/PAN nanofiber composite. The nanofibers were collected at 1.8 mL·h^{-1} flow rate, 11 kV voltage, and 15 cm needle-to-collector distance

In Fig. 5.9, the FTIR spectra showed that both the UiO-66/PAN and MIL-101/PAN nanofiber composites consisted of overlapping vibrational bands with those of PAN, pristine UiO-66, and MIL-101(Cr) respectively. There were also no evident additional or absent vibrational bands in FTIR spectra of both MOF/PAN nanofiber composites, meaning there was no chemical bonding that was observable. It could, therefore, be proposed that the UiO-66 and MIL-101(Cr) crystals were embedded by physical attachment to the PAN matrix. The PXRD patterns in Fig. 5.10 also showed evidence of the incorporation of UiO-66 and MIL-101(Cr) into the PAN matrix as the XRD patterns of the MOF/PAN nanofibers contained the diffraction peaks of the constituent MOF and PAN. It was, however, observable that the PXRD patterns of the MOF/PAN composites contained a significant portion of amorphous character (hump)

that was consistent with PAN. Such an observation could provide additional evidence to the distribution of the MOFs within the PAN surface, as was observed in Fig. 5.8 and 5.9.

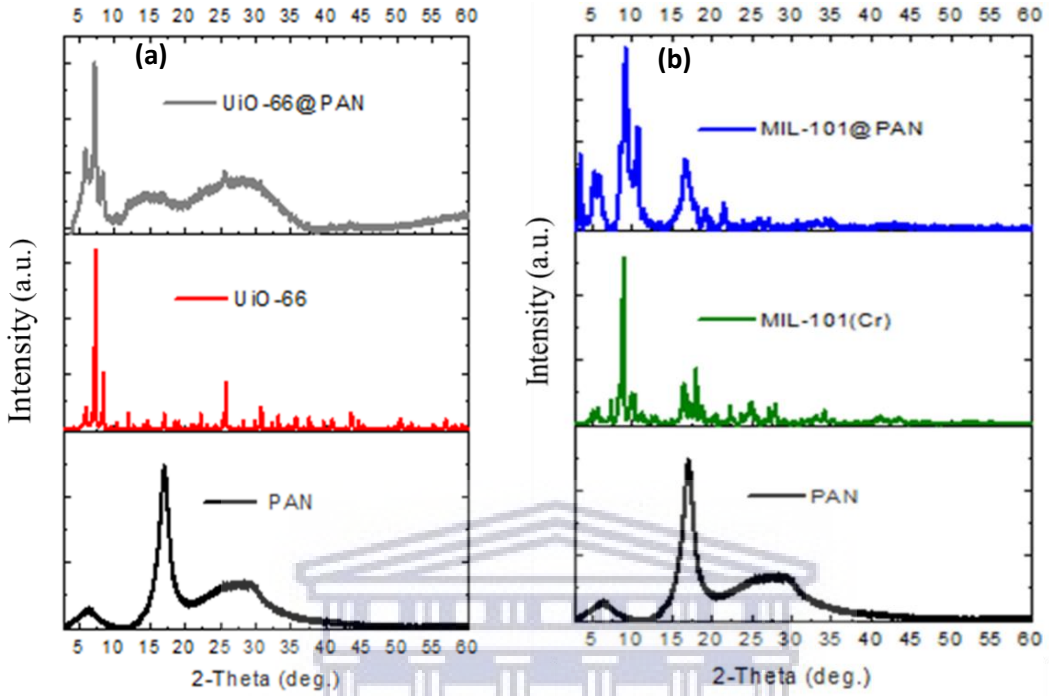

Figure 5.10: Comparison of the PXRD patterns for MOF/PAN nanofiber composites to that of the pristine materials: (a) PAN, UiO-66, and UiO-66/PAN, and (b) PAN, MIL-101(Cr), and MIL-101/PAN. The nanofibers were collected at 1.8 mL·h^{-1} flow rate, 11 kV voltage, and 15 cm needle-to-collector distance

The presence of cyano groups in PAN enable the polymer to undergo thermal cross-linking whereby bond breakages in -C≡N moeties result in the formation of –C=N- and hydrogen-bonding –N-H bonds between the polymer chains [222]. The cross-linking affords PAN a significantly higher thermal stability of about 600 ^{o}C compared to most hydrocarbon polymers [223–225]. Indeed the results in Fi g. 5.11 showed a two-step decomposition of PAN initially at ~300 ^{o}C and then followed by complete decomposition at 600 ^{o}C. The thermal stability of the UiO-66/PAN composite showed a slightly lower thermal stability of ~500 ^{o}C compared to pristine PAN. The thermal stability of the MIL-101/PAN composite was even lower at ~450 ^{o}C. In both composites, however, the initial decomposition step of PAN was unaffected as it was observed to occur at ~300 ^{o}C irrespective of the MOF.

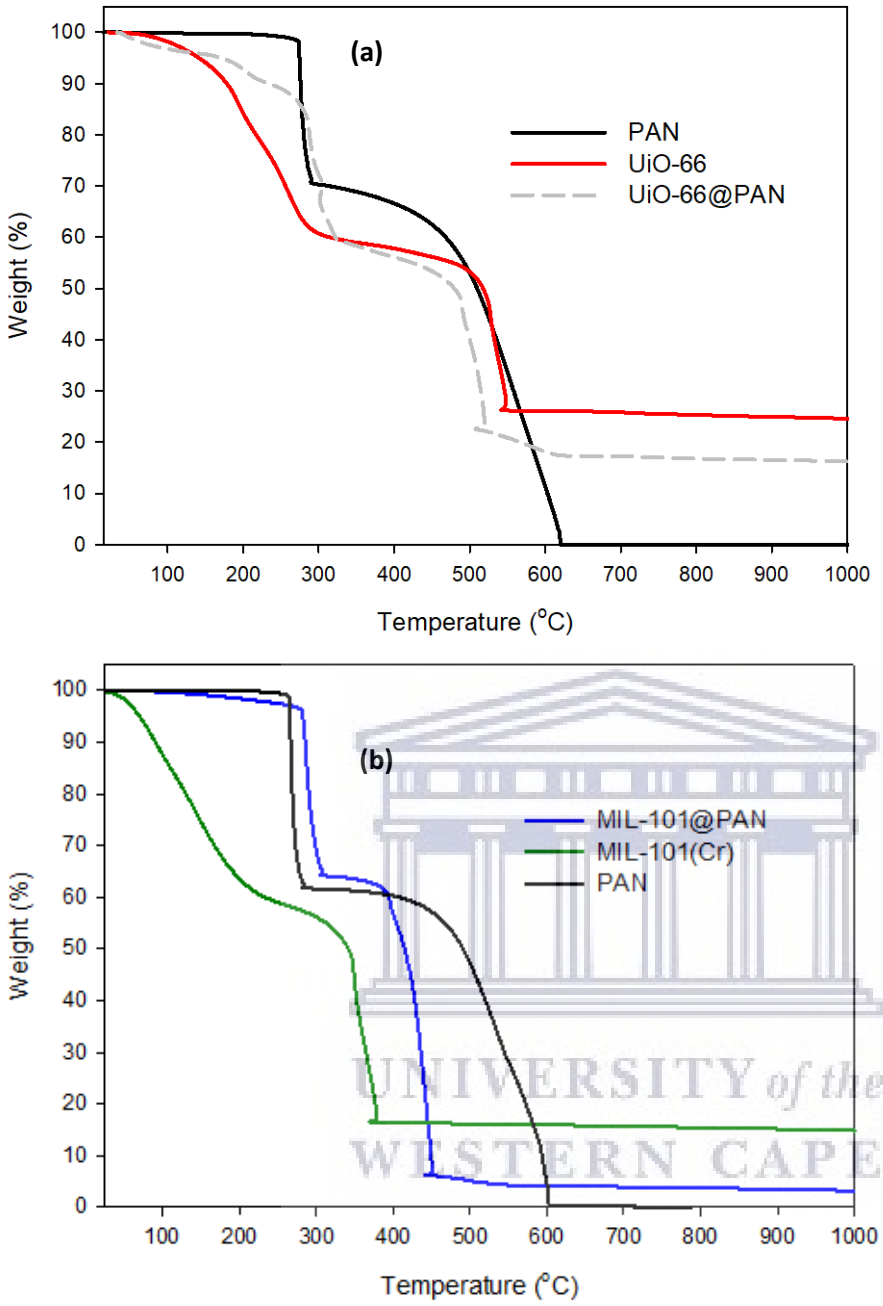

Figure 5.11: Comparison of the TGA curves for MOF/PAN composites to pristine MOFs and PAN nanofibers: (a) UiO-66/PAN, and (b) MIL-101/PAN. The analysis was carried up to 1000 °C in air. The nanofibers were collected at 1.8 mL·h^{-1} flow rate, 11 kV applied voltage and 15 cm needle-to-collector distance

The observed behaviour could mean that the cross-linking of PAN was not affected by the removal of DMF solvent molecules in MIL-101(Cr) and the removal of H_2O during dehydroxylation of UiO-66, as were both discussed in Chapter 4. The temperatures at which the MOF framework decomposed could be assumed to accelerate the decomposition of the PAN matrix.

In Fig. 5.12, 5.13, and Table 5.1, the textural properties of the MOF/PAN nanofibers were compared to that of the pristine MOFs. It was earlier proposed that the incorporation of MOF crystals into the PAN nanofibers was through physical adherence to the PAN matrix, as no evidence of chemical interactions were observable on FTIR spectra. This meant that the combined or effective physical properties of the MOF/PAN nanofibers could expectedly be governed by the law of mixtures. Taking this assumption into consideration would mean that the properties of MOF/PAN nanofibers were dependent on the proportion (%) of each constituent in the composite. In Fig. 5.12, it can be seen that both the N_2 isotherms obtained for UiO-66/PAN and MIL-101/PAN composites were consistent with the Type III isotherm obtained for PAN nanofibers (Fig. 5.4), which could signify a large proportion of the MOF/PAN nanofiber composites as non-porous. Indeed the MOF loading in each composite was limited at 20 wt% with respect to the polymer concentration.

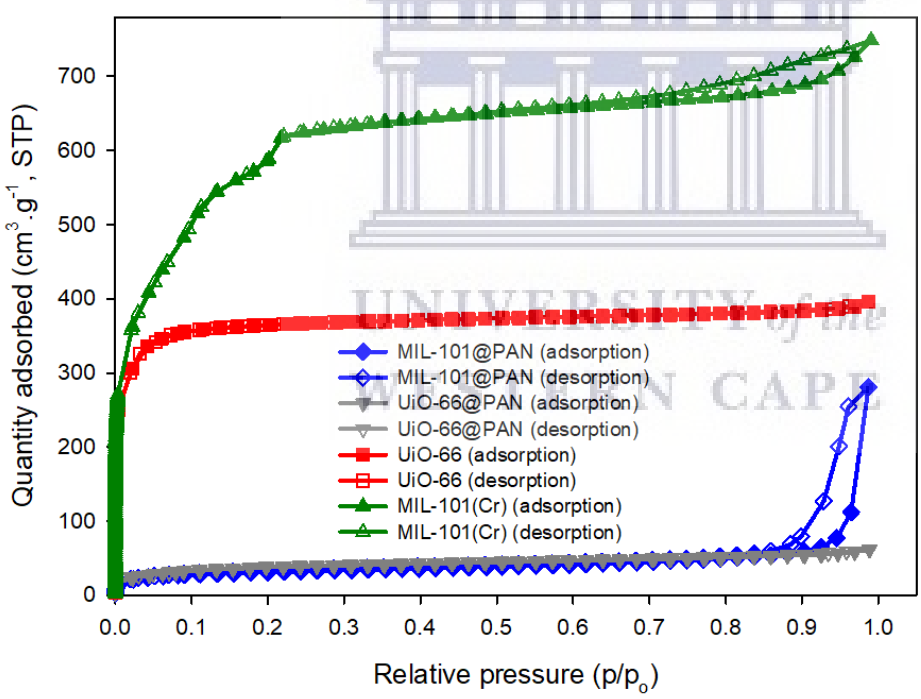

Figure 5.12: N_2 adsorption/desorption isotherms obtained for UiO-66/PAN and MIL-101/PAN in comparison to pristine UiO-66 and MIL-101(Cr). The nanofibers were collected at 1.8 mL·h^{-1} flow rate, 11 kV applied voltage and 15 cm needle-to-collector distance

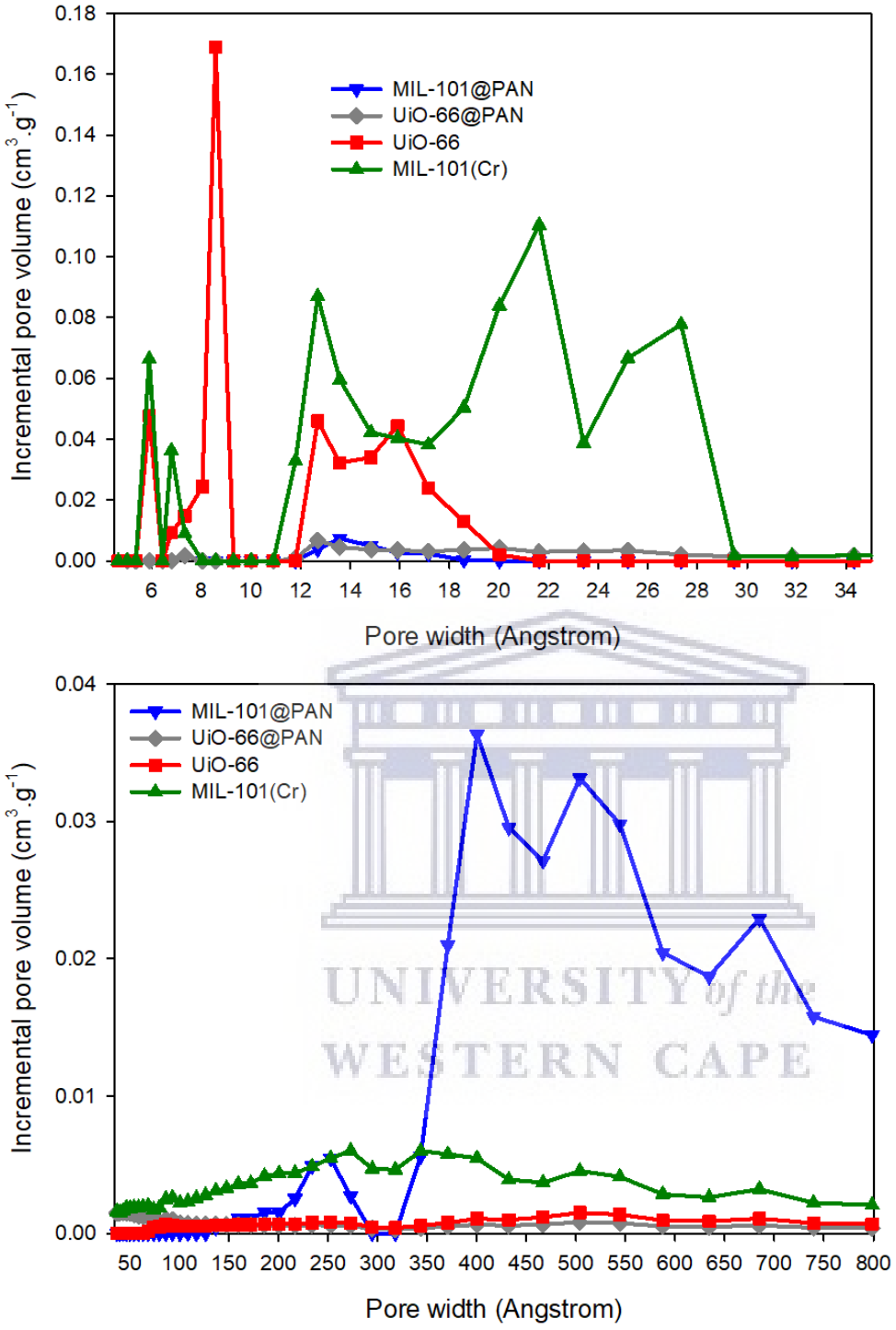

Figure 5.13: NLDFT pore size distribution curves for UiO-66/PAN and MIL-101/PAN in comparison to pristine UiO-66 and MIL-101(Cr). The nanofibers were collected at 1.8 mL·h^{-1} flow rate, 11 kV applied voltage and 15 cm needle-to-collector distance

In Table 5.1, the BET surface area of UiO-66/PAN was found to be 8% that of pristine UiO-66, and MIL-101/PAN only 6% that of pristine MIL-101(Cr). Studies conducted by Ren et al. [226], reported UiO-66/PAN and MIL-101/PAN nanofibers with about 60% the BET surface

areas of their respective pristine UiO-66 and MIL-101(Cr). The latter findings, however, were based on a combination of incorporating the MOFs followed by post-spinning heat-treatment under vacuum to induce the formation of pores on the surface of the PAN nanofibers. In that study, the heat-treatment was done at 280 ^{o}C, which was not ideal in the current study as it was shown in Chapter 4 that high-temperature activation of UiO-66 could significantly compromise its mechanical stability. The nanofibers prepared in this study were envisaged to be used as binders for the pelletization of UiO-66-based composites, and hence could not be activated at 280 ^{o}C. The MIL-101/PAN nanofibers were, however, observed to exhibit a Type H1 hysteresis loop which was also evident in pristine MIL-101(Cr) and a pore volume of 0.44 $cm^{3}{\cdot}g^{-1}$ compared to 0.096 $cm^{3}{\cdot}g^{-1}$ obtained for UiO-66/PAN nanofibers. It can be seen in Fig. 5.12 and Table 5.1 that the pore volume of MIL-101(Cr) was higher compared to that of UiO-66, and hence it could be expected that UiO-66/PAN would also show lower pore volumes compared to MIL-101/PAN.

Table 5.1: Summary of the BET report obtained for MOF@PAN nanofibers prepared via single-nozzle electrospinning in comparison to pristine UiO-66 and MIL-101 powders.

Isotherm property	**Sample**			
	MIL-101/PAN	**UiO-66/PAN**	**UiO-66**	**MIL-101(Cr)**
BET surface area ($m^{2}{\cdot}g^{-1}$)[a]	142 (43)	116 (42)	1413 (1260)	2151 (479)
NLDFT pore volume ($cm^{3}{\cdot}g^{-1}$)[b]	0.44 (0.016)	0.096 (0.014)	0.61 (0.50)	1.16 (0.18)
Slope ($g{\cdot}cm^{-3}$, STP)	0.03742	0.03031	0.003079	0.001998
Y-intercept ($g{\cdot}cm^{-3}$, STP)	0.000276	0.000381	0.000001	0.000026
Q_m ($cm^{3}{\cdot}g^{-1}$, STP)	33	27	325	494
Correlation coefficient	0.9999	0.9999	0.9999	0.9998

[a]values in parentheses are given for the t-plot micropore surface area; [b]values in parentheses are given for the t-plot micropore volume.

The results observed for the MOF/PAN nanofibers prepared by single-nozzle electrospinning showed that a low MOF loading of 20 wt% in the composite could result in textural properties much lower in comparison to the pristine MOF powders. A method to improve the MOF loading, without possibly compromising the morphology of the nanofibers, could be achieved through coaxial electrospinning of MOF/X@PAN (X = PS or PMMA) composites followed by selective removal of the core polymer (X). The results are discussed in section 5.3.

5.3. Preparation of core-shell MOF/polymer nanofibers by coaxial electrospinning

This section reports on the preparation of core-shell MOF/X@PAN nanofibers via coaxial electrospinning. The aim was to electrospin two solutions containing 20 wt% MOF simultaneously followed by selective removal of the core polymer (X) by immersing the nanofibers in acetone to remove PMMA, and chloroform to remove PS. Section 5.3.1 reports on the preparation of core-shell PMMA@PAN nanofibers without the addition of MOFs in order to validate whether the PMMA core could be completely removed through the PAN shell by immersing the PMMA@PAN composite in acetone. In section 5.3.2, UiO-66 was initially incorporated into the core polymer forming UiO-66/PMMA@PAN nanofibers and then incorporated into core and shell to form UiO-66/PMMA@UiO-66/PAN nanofibers. The textural properties of the two composites were measured before and after PMMA removal. In section 5.3.3, PS was used as an alternative core polymer to PMMA due to its cost-effectiveness and its comparatively good electrospinning properties. Based on the results obtained in section 5.3.2, MIL-101 was incorporated into the core and shell to form MIL-101/PS@MIL-101/PAN nanofibers.

5.3.1. Electrospinning of core-shell PMMA@PAN nanofibers

5.3.1.1. Electron microscopy of electrospun PMMA@PAN nanofibers

The TEM images in Fig. 5.14 showed a consistent contrast along the length of the nanofibers which consisted of a dark inner/core region. The diameter of the nanofibers were about 1 µm with the core region ranging between ~200 nm to 800 nm.

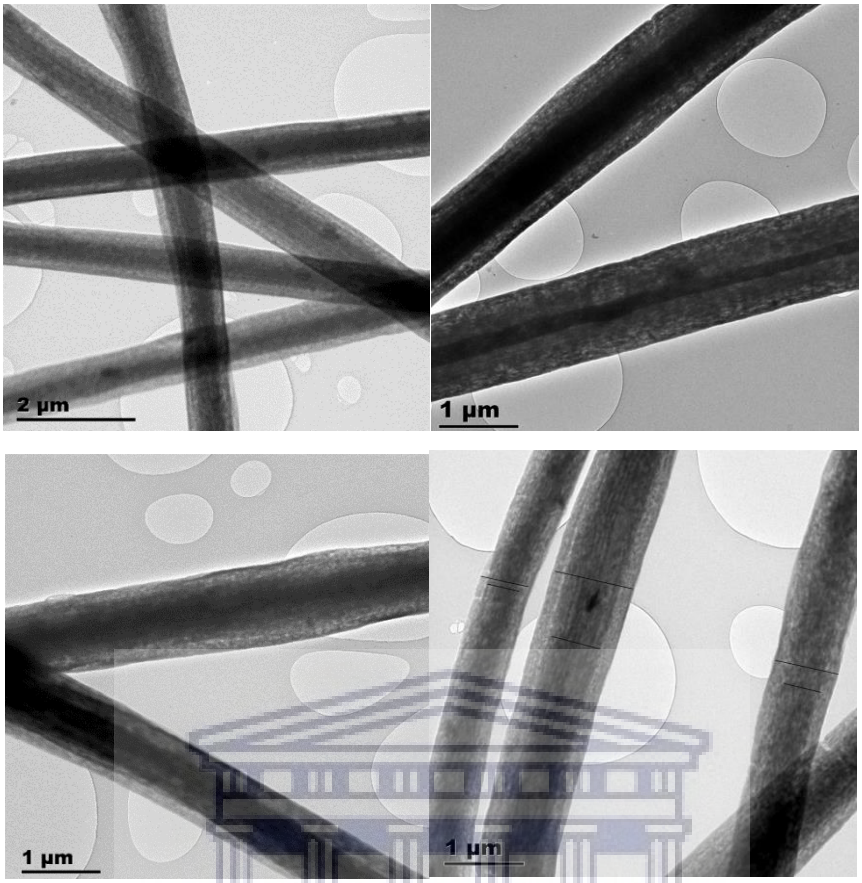

Figure 5.14: TEM images of co-electrospun PMMA@PAN nanofibers collected at a flow rate of 1.8 mL·h^{-1}at an applied voltage of 11 kV and 15 cm distance from the needle tip to the Al screen collector.

In Fig. 5.15 it can be seen that the treatment of PMMA@PAN nanofibers with 20 mL aliquots of acetone resulted in PAN nanofibers with reduced diameters of about 300 nm from the original ~1 µm initially observed in the as-spun core-shell PMMA@PAN nanofiber composites (Fig. 5.15). This could suggest a possible collapse of the core region during the dissolution of PMMA in acetone, which may be further enhanced by the evaporation of acetone from the nanofibers during drying. The resultant PAN nanofibers were also observed to be flattened after PMMA removal, which could further confirm the collapse of the core region. Also the core-shell structure was not evident in the acetone-treated nanofibers, which could be a strong indication for the removal of the core region. The results could be used to confirm that PMMA was incorporated in the core region during co-electrospinning by FTIR analysis to determine the chemical composition of the co-electrospun nanofibers after treatment with acetone

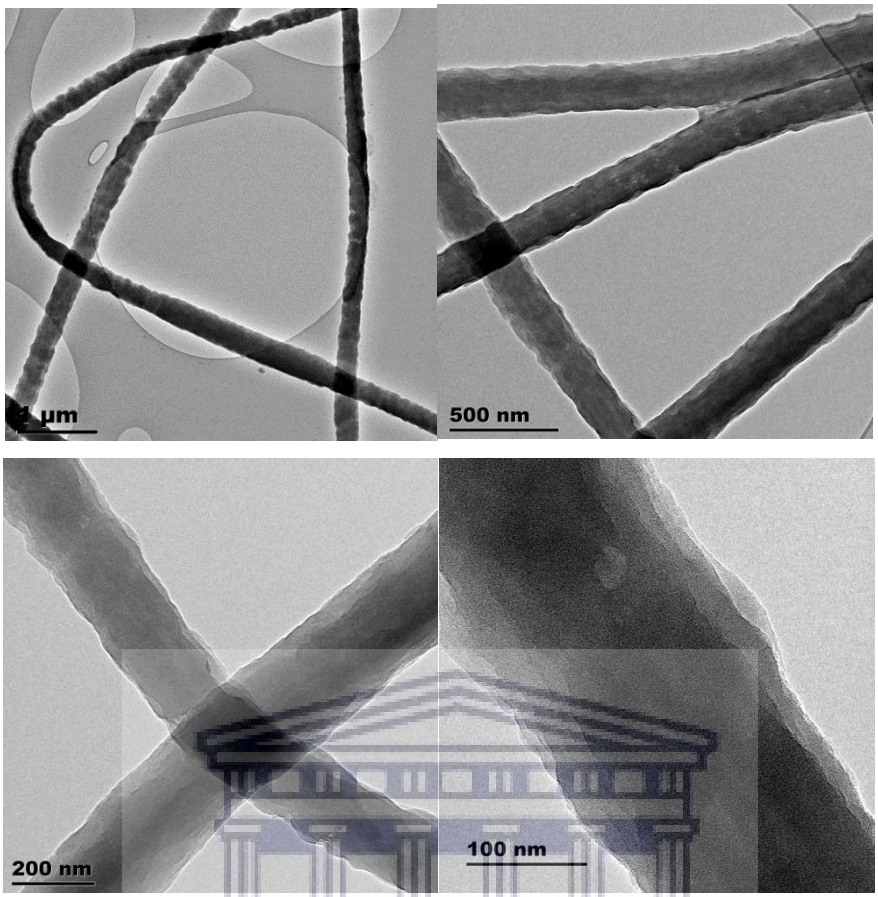

Figure 5.15: TEM images of co-electrospun PMMA@PAN nanofibers (collected at 1.8 mL·h^{-1} flow rate, 11 kV applied voltage and 15 cm needle-to-collector distance) after treatment with 20 mL aliquots of acetone.

5.3.1.3. Thermogravimetric analysis of electrospun PMMA@PAN nanofibers

In Fig. 5.16, the TGA profile of the PMMA@PAN nanofibers was also found to be a combination of the TGA profiles of the pristine PAN and PMMA granules, with the initial decomposition around 400 ^{o}C corresponding to the complete decomposition of PMMA, and the PAN component of the composite was found to decompose from 400 to about 620 ^{o}C. There was no residual material obtained beyond 620 ^{o}C for the co-electrospun PMMA@PAN, PAN, and PMMA, suggesting complete decomposition under the specified conditions.

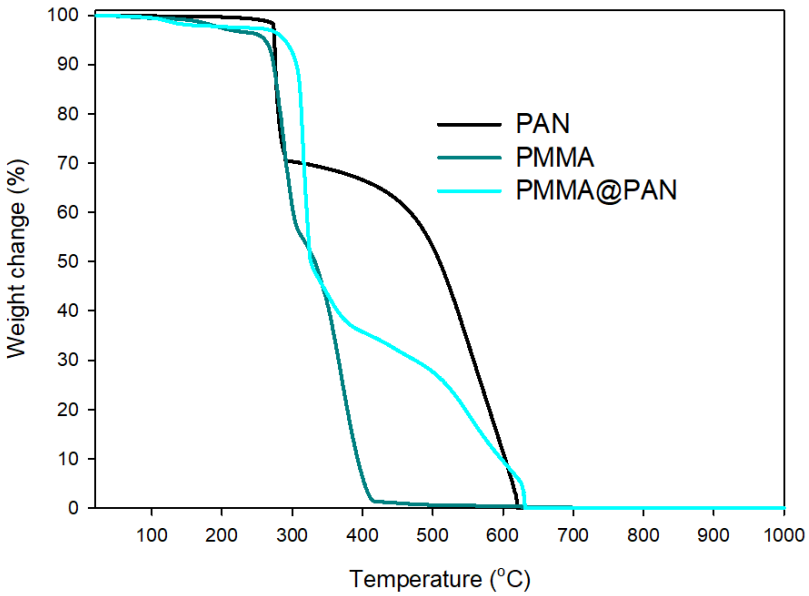

Figure 5.16: Thermal decomposition of core-shell PMMA@PAN in comparison to pristine PMMA and PAN nanofibers (1.8 mL·h^{-1} flow rate; 11 kV voltage; and 15 cm needle-to-collector distance). TGA profiles were obtained under 100 mL·min^{-1} air flow and 10 °C·min^{-1} ramp rate.

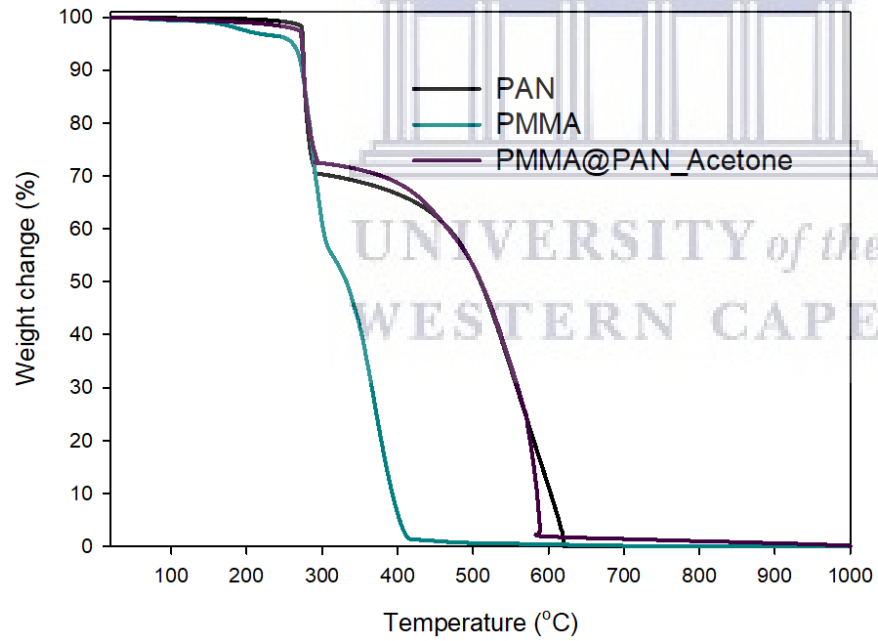

Figure 5.17: Thermal decomposition of core-shell PMMA@PAN after treatment with acetone in comparison to pristine PMMA and PAN nanofibers (1.8 mL·h^{-1} flow rate; 11 kV voltage; and 15 cm needle-to-collector distance). TGA profiles were obtained under 100 mL·min^{-1} air flow and 10 °C·min^{-1} ramp rate.

In Fig. 5.17 the TGA profile of the co-electospun nanofibers was observed to match the TGA profile of pristine PAN, showing little evidence of a combination of the PMMA profile. This showed that the acetone treatment possibly removed all the PMMA in the core region, assuming an uniform distribution and constant diameter of the PMMA core in all the co-electrospun PMMA@PAN nanofibers.

The results in provided in section 5.3.1 showed proof of the preparation of core-shell PMMA@PAN nanofibers whereby the PMMA core could be selectively removed using acetone. In section 5.3.2, the core-shell nanofibers were prepared with MOF loading of 20 wt% and analysed in a similar manner to the PMMA@PAN nanofibers.

5.3.2. Electrospinning of core-shell UiO-66/PMMA@PAN and UiO-66/PMMA@UiO-66/PAN nanofibers

This section initially reports on the electrospinning of UiO-66/PMMA@PAN nanofibers where 20 wt% UiO-66 was loaded in core PMMA solution and not in the PAN solution.

5.3.2.1. Electron microscopy of core-shell UiO-66/PMMA@PAN nanofibers

The SEM and TEM images in Fig. 5.18 showed the UiO-66/PMMA@PAN nanofibers were electrospun with negligible formation of beads using the optimum process parameters described in Chapter 2. In order to determine the location and distribution of the UiO-66 crystals within the nanofibers, during TEM analysis the sample grid was rotated 180^{o} and the positions of the MOF crystals monitored after rotation in relation to their original positions. In this particular case, the agglomerate/lump in Fig. 5.18d was used as reference throughout the rotation. In Fig. 5.19 the full rotation is shown in a series of images beginning at a position marked "-20" to "19" signifying the 180^{o} rotation.

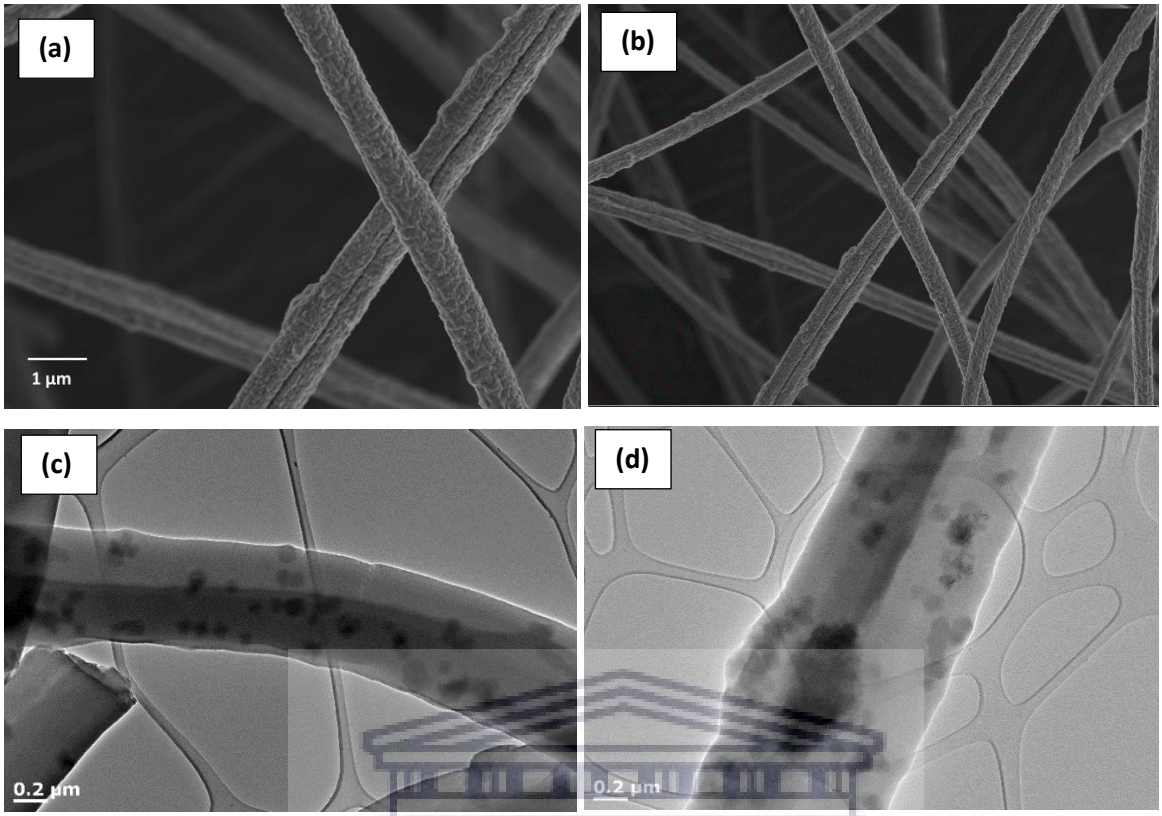

Figure 5.18: Microstructural images of core-shell UiO-66/PMMA@PAN nanofibers where the UiO-66 powder was only added to the PMMA solution prior to electrospinning: (a) – (b) SEM images, and (c) – (d) TEM images. The nanofibers were collected at 1.8 mL·h^{-1} flow rate, 11 kV voltage, and 15 cm needle-to-collector distance.

It can be seen in Fig. 5.19 that the core region was not evident at the "-20" starting position, however as the sample was rotated through 180^{o} ("19" position) there was a clearly observable darker region in the core of the nanofiber. By monitoring the position of UiO-66 lump it could be proposed that there were no positional changes that occurred during the rotation, and that the observation could be most likely possible given the lump was situated in the core region of the nanofiber. It is, however, acknowledge that there was no control over the distribution of the UiO-66 crystals prior and during the electrospinning process. It can, therefore, also be accepted that the UiO-66 crystals could have distributed randomly on the surface of the nanofiber. The fact that the UiO-66 crystals were intentionally included in the core PMMA solution prior to electrospinning may possibly provide a way to distribute the majority of the UiO-66 crystals in the core region, but the possibility of random distribution could not be ignored.

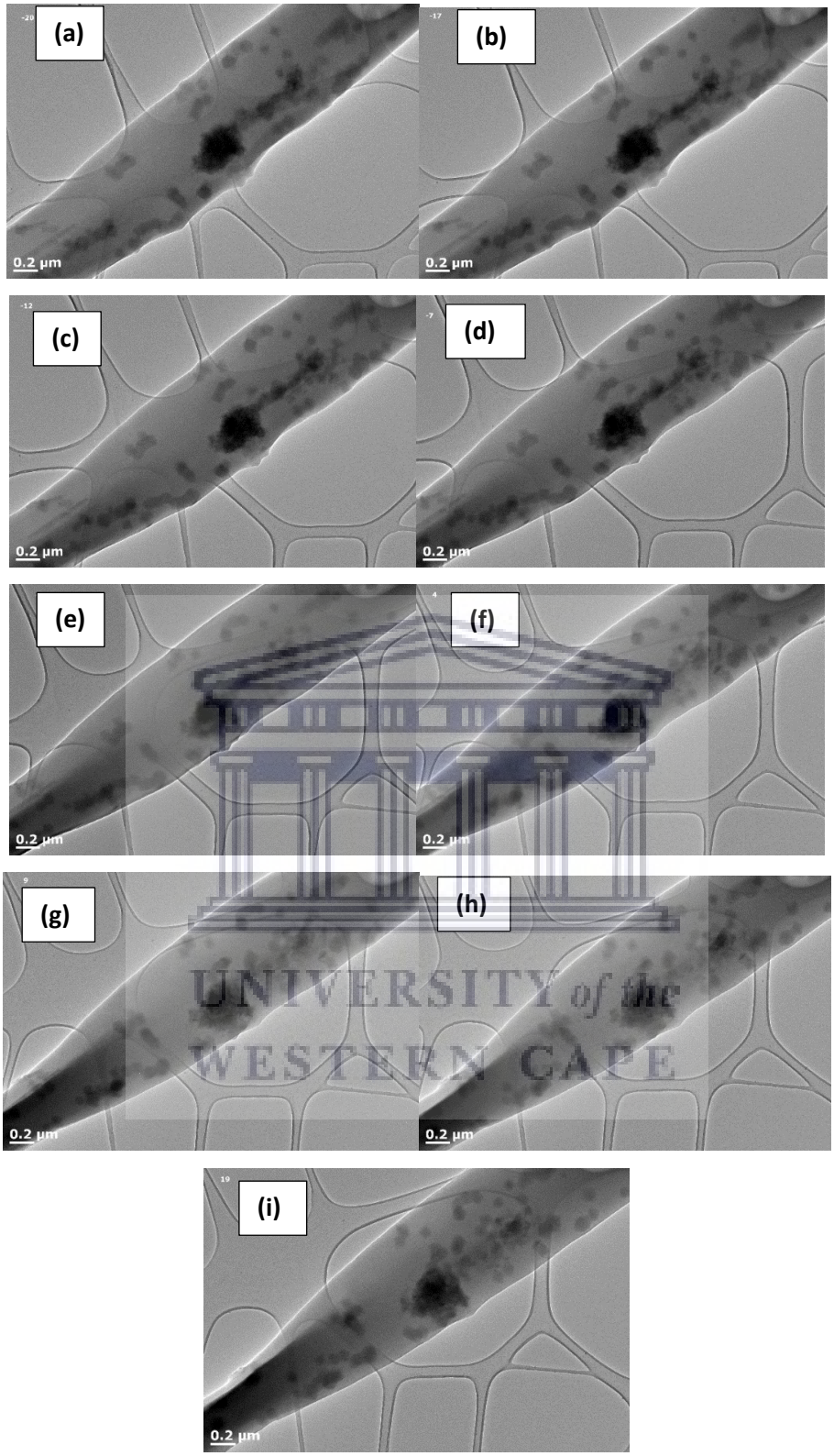

Figure 5.19: TEM images of as-spun UiO-66/PMMA@PAN nanofibers where UiO-66 was only added to the PMMA solution prior to electrospinning. The nanofibers were collected at 1.8 mL·h^{-1} flow rate, 11 kV voltage, and 15 cm needle-to-collector distance The sample was rotated by moving the sample grid at 180^{o} relative to the lenses starting at image (a) to (i).

The removal of PMMA from UiO-66/PMMA@PAN nanofibers was found to result in flattened UiO-66/PAN nanofibers (Fig. 5.20 and Fig. 5.21), consistent with the observations made on PMMA@PAN nanofibers. In addition, the TEM images in Fig. 5.21 showed that the uniform distribution of UiO-66 crystals, initially observed before acetone treatment, could not be observed after acetone treatment. The UiO-66 crystals were observed to form lumps/agglomerates within the resultant PAN nanofibers as seen in both Fig. 5.20 and Fig. 5.21. This could suggest that the UiO-66 crystals were shifted out of their initial positions during the dissolution of PMMA in acetone or alternatively the individual crystals observed in Fig. 5.19 could have been leached out of the PAN, leaving behind the UiO-66 lumps. Also noticeable were breakages across the diameter of the nanofibers (Fig. 5.21) that were not observable on the SEM images (Fig. 5.20). In TEM analysis, one of the prerequisite sample preparation methods is the dispersion of the sample in a solvent such as methanol followed by ultrasonication for at least 30 minutes. It is, therefore, more likely that the observed breakages resulted from the sample preparation rather than the effects of PMMA removal using acetone. The same analysis was then done for the incorporation of UiO-66 in the core *and* shell polymer solutions so as to prepare UiO-66/PMMA@UiO-66/PAN nanofiber composites. This would represent a higher loading of UiO-66 compared to the UiO-66/PMMA@PAN nanofibers.

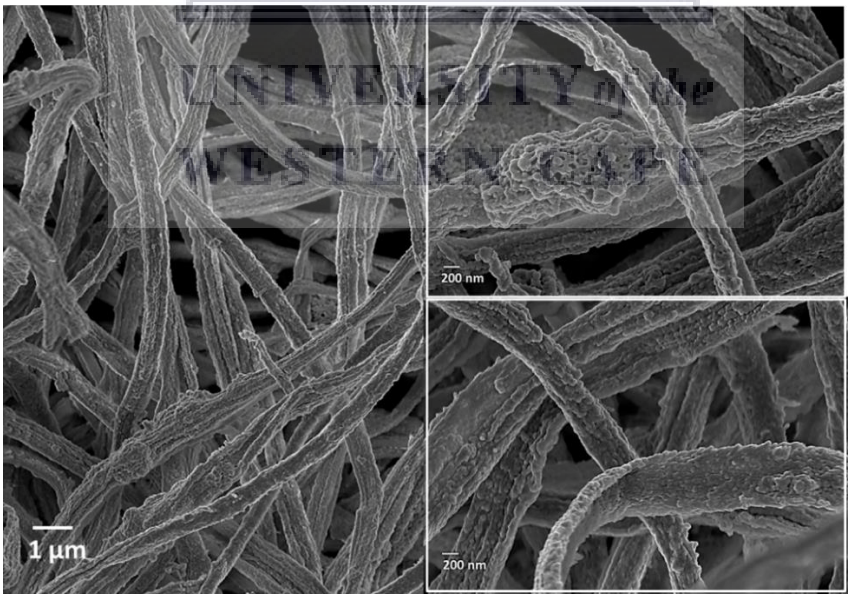

Figure 5.20: SEM image of UiO-66/PMMA@PAN nanofibers after treatment with acetone. The nanofibers were collected at 1.8 mL·h^{-1} flow rate, 11 kV voltage, and 15 cm needle-to-collector distance.

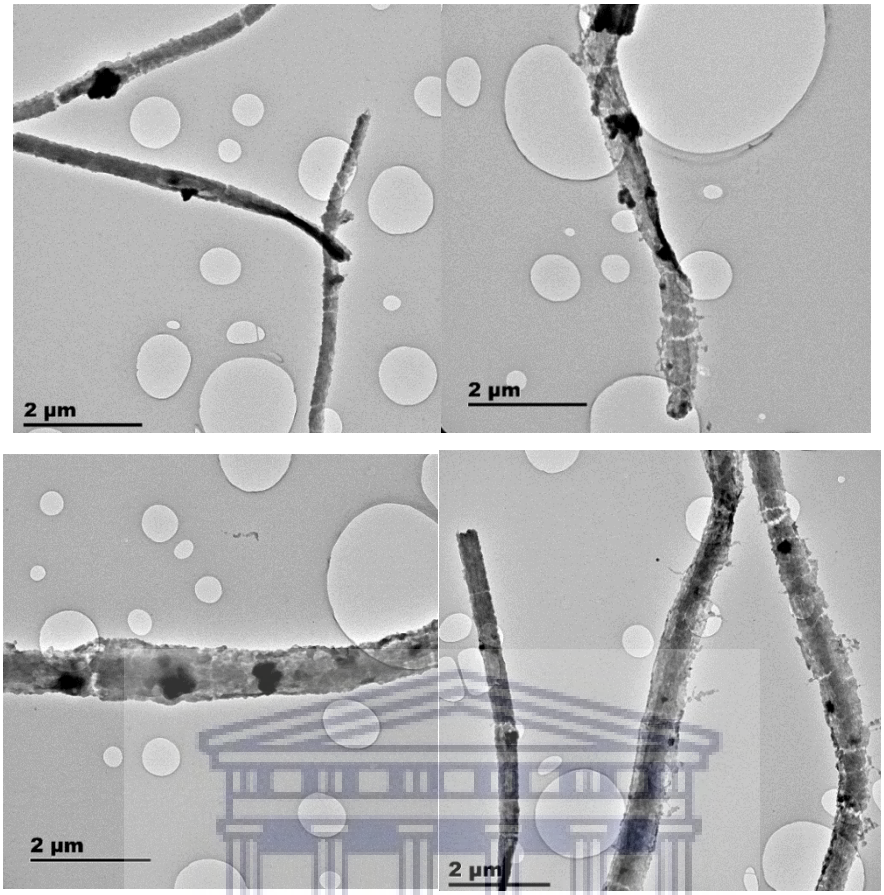

Figure 5.21: TEM images of UiO-66/PMMA@PAN nanofibers after treatment with acetone. The nanofibers were collected at 1.8 mL·h^{-1} flow rate, 11 kV voltage, and 15 cm needle-to-collector distance.

The SEM images in Fig. 5.22 and 5.23 showed that the increased UiO-66 loading not only caused significant agglomeration of the UiO-66 crystals within the nanofiber matrix (Fig. 5.22), but also after PMMA removal, the remaining PAN nanofiber exhibited significant physical damage along the length of the nanofibers (Fig. 5.23). The nanofibers in Fig. 5.23 also did not show evidence of a flattened morphology such as observed in PMMA@PAN and UiO-66/PMMA@PAN nanofibers. There was a clear indication of the leaching of UiO-66 crystals that were observable on the surface of the nanofibers after PMMA removal (Fig. 5.23), which were not observed before PMMA removal (Fig. 5.22).

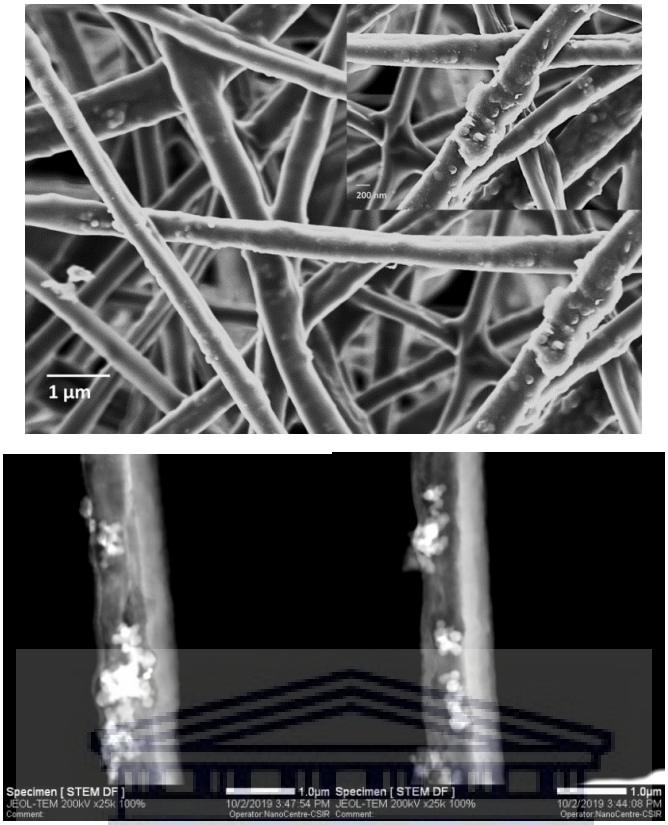

Figure 5.22: SEM and STEM images of as-spun core-shell UiO-66/PMMA@UiO-66/PAN nanofibers with 20 wt% UiO-66 loadings in each polymer. The nanofibers were collected at 1.8 mL·h^{-1} flow rate, 11 kV voltage, and 15 cm needle-to-collector distance

These observations could be explained by considering the results in Fig. 5.16 which showed that the removal of PMMA was accompanied by a significant collapse along the diameter of the remaining PAN nanofibers. The nanofibers were found to possibly collapse down to 30% of the original diameter of PMMA@PAN nanofibers. Given the increased UiO-66 loading in UiO-66/PMMA@UiO-66/PAN nanofibers, and the significant amount of UiO-66 agglomerates present within the nanofibers, it could be expected that collapsing of the remaining PAN nanofibers onto the mechanically robust UiO-66 crystals could result in rupturing of the nanofiber surface, as observed in Fig. 5.23. The leaching of UiO-66 crystals would make it difficult to determine the remaining UiO-66 loading after PMMA removal. A non-destructive method of selectively removing the core polymer would be required to ensure a measurable UiO-66 loading.

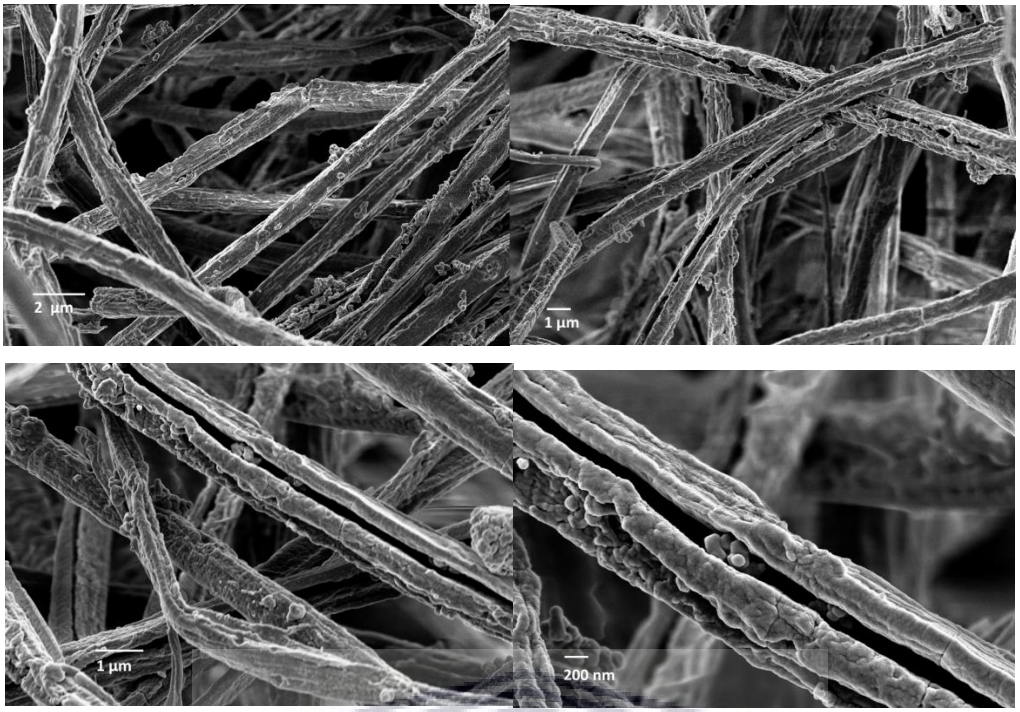

Figure 5.23: SEM images of UiO-66/PMMA@UiO-66/PAN after acetone treatment. The nanofibers were collected at 1.8 mL·h^{-1} flow rate, 11 kV voltage, and 15 cm needle-to-collector distance

In addition to imaging, the incorporation of UiO-66 in the core-shell nanofibers was also analysed by FTIR, PXRD, and TGA in order to confirm the presence of the UiO-66 crystals within the nanofibers.

5.3.2.2. Crystallography and spectroscopy of core-shell UiO-66/PMMA@PAN and UiO-66/PMMA@UiO-66/PAN nanofibers

In Fig. 5.24 the PXRD patterns and FTIR spectra (Fig. 5.25) for UiO-66/PMMA@UiO-66/PAN nanofibers were consistent with those of the constituent UiO-66, PMMA and PAN materials, showing successful incorporation of UiO-66 crystals in the nanofibers. In the single-nozzle electrospinning of UiO-66/PAN, it was shown in Fig. 5.10 that the PXRD pattern of the composite exhibited a high degree of amorphous character due to the UiO-66 crystals being embedded within the nanofiber matrix.

In Fig. 5.24 a similar result was observed on the UiO-66/PMMA@UiO-66/PAN nanofibers. After PMMA removal using acetone, the amorphous character of the PXRD pattern was found to diminish, and sharper peaks were prevalent in the PXRD pattern. The sharp peaks were also matching with those of pristine UiO-66. This could indicate the presence of UiO-66 crystals on the surface of the nanofibers after PMMA removal, an observation that was also evident in Fig. 5.24.

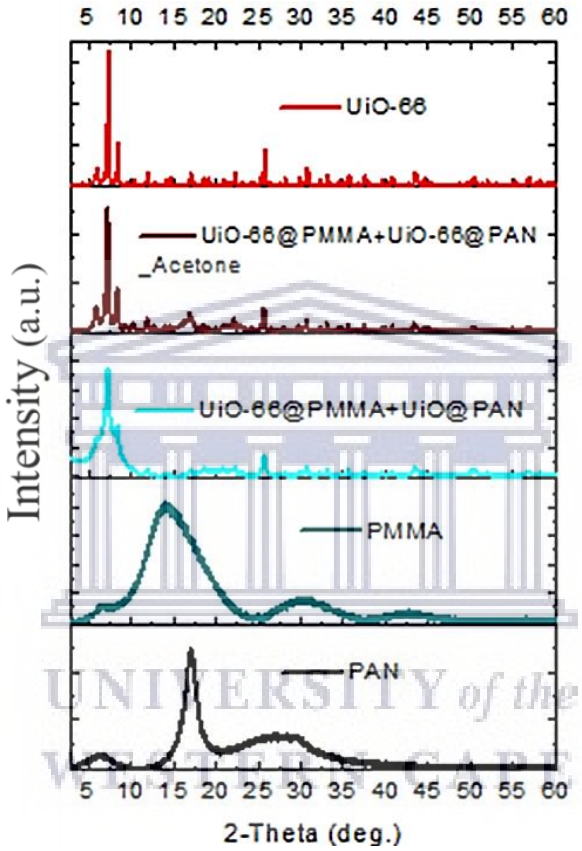

Figure 5.24: PXRD patterns for UiO-66/PMMA@UiO-66/PAN in comparison to pristine PAN, PMMA and UiO-66. The nanofibers were collected at 1.8 mL·h^{-1} flow rate, 11 kV voltage, and 15 cm needle-to-collector distance

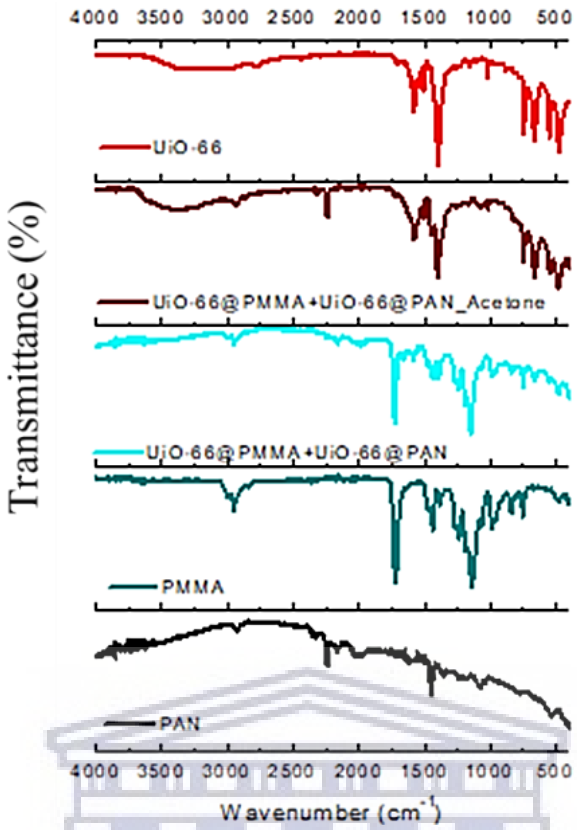

Figure 5.25: FTIR spectra for UiO-66/PMMA@UiO-66/PAN in comparison to pristine PAN, PMMA and UiO-66. The nanofibers were collected at 1.8 mL·h^{-1} flow rate, 11 kV voltage, and 15 cm needle-to-collector distance

5.3.2.3. Thermogravimetric analysis of core-shell UiO-66/PMMA@PAN nanofibers

In Fig. 5.26, the thermal behaviour of the UiO-66/PMMA@PAN and UiO-66/PMMA@UiO-66/PAN nanofibers were also found to be a combination of the behaviour of the component pristine materials as previously shown in section 5.3.1. After PMMA removal, the TGA profiles of the acetone-treated UiO-66/PMMA@UiO-66/PAN nanofibers were found to be consistent with that of pristine PAN, indicating the removal of PMMA from the nanofibers. This observation was not evident in the UiO-66/PMMA@PAN nanofibers which suggested that the removal of PMMA was not done to completion in the analysed sample. The incomplete removal of PMMA could be due to a non-uniform distribution of PMMA nanofibers throughout the length of the core-shell UiO-66/PMMA@PAN nanofibers.

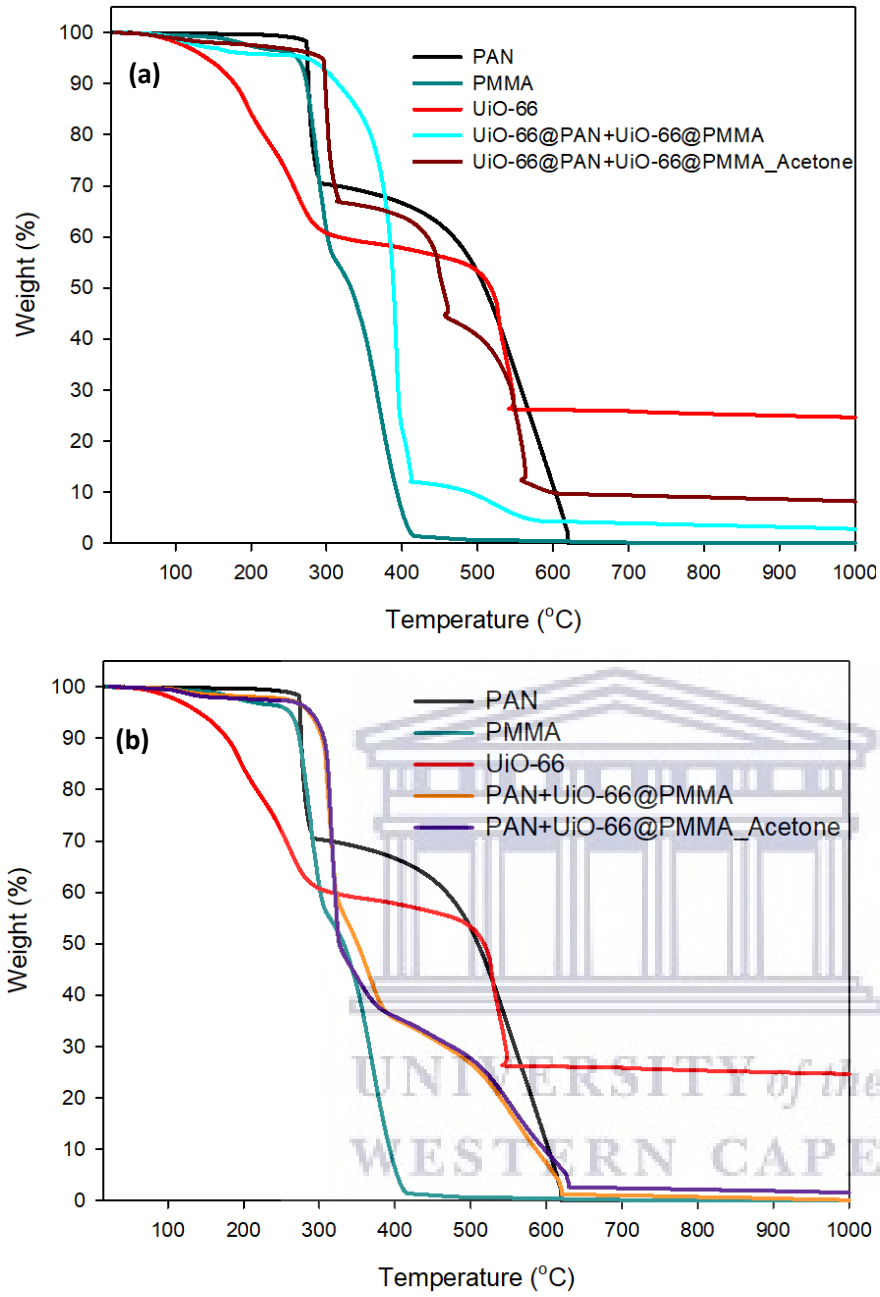

Figure 5.26: TGA profiles for core-shell nanofibers in comparison to pristine UiO-66, PMMA, and PAN: (a) UiO-66/PMMA@UiO-66/PAN, and (b) UiO-66/PMMA@PAN nanofibers. The nanofibers were collected at 1.8 mL·h^{-1} flow rate, 11 kV voltage, and 15 cm needle-to-collector distance

In section 5.3.3, the comparison of the textural properties of the core-shell nanofiber composites were used to confirm whether the removal of PMMA would result in an increase in the MOF loading.

5.3.3. Textural properties of core-shell UiO-66/PMMA@PAN and UiO-66/PMMA@UiO-66/PAN nanaofibers

The interaction of MOFs and the polymer nanofiber surface was observed to resemble a physical type of interaction with no apparent chemical bonding observed or suggested from FTIR and PXRD data. In this case, the adsorption properties of the core-shell MOF/polymer nanofibers were proposed to be governed by the law of mixtures. This meant that in order to improve the surface areas and pore volumes obtained in Table 5.1, the MOF loading had to be increased. Given that the statement is acceptable, it would mean that surface areas and pore volumes higher than those reported in Table 5.1 would be an indication of improved UiO-66 loadings in the core-shell nanofibers.

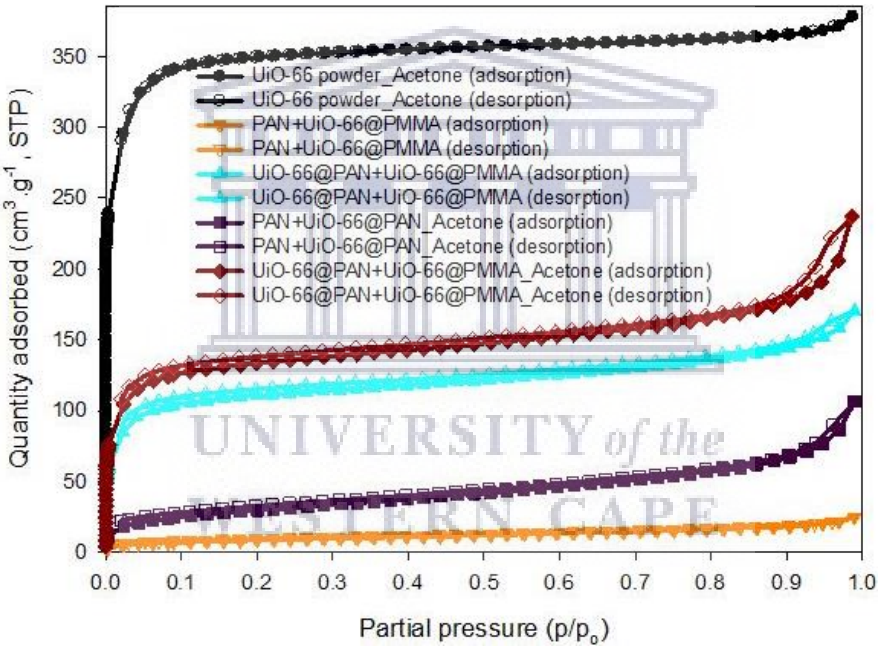

Figure 5.27: N_2 adsorption/desorption isotherms at 77 K obtained for core-shell UiO-66/PMMA@PAN and UiO-66/PMMA@UiO-66/PAN nanofiber composites. The open symbols represent the desorption curves. The nanofibers were collected at 1.8 mL·h^{-1} flow rate, 11 kV voltage, and 15 cm needle-to-collector distance.

In Fig. 5.27 the N_2 adsorption isotherm of UiO-66/PMMA@PAN was consistent with Type III adsorption, and no hysteresis was observed due to the high content of the non-porous polymers PAN and PMMA. The removal of PMMA resulted in Type II adsorption where there was a significant amount of N_2 adsorption at low pressure followed by a gradual increase up to p/p_o = 1. The increase in the low pressure adsorption could have indicated an increased UiO-66

loading due to the removal of PMMA since pristine UiO-66 typically shows Type I adsorption isotherms. The Type II isotherm observed for the remaining UiO-66/PAN (after PMMA removal) could be best described as a combination of Type I and Type III adsorption behaviour due to contributions of the highly microporous UiO-66 and the non-porous PAN. In the UiO-66/PMMA@UiO-66/PAN composite Type I adsorption was evident as shown by the high N_2 adsorption at low relative pressure (p/p_o). The observed adsorption behaviour of the UiO-66/PMMA@UiO-66/PAN could be attributed to the increased amount of UiO-66 present in the core *and* shell regions of the nanofibers, compared to UiO-66/PMMA@PAN nanofibers where the UiO-66 was present in the core region only. Upon removal of PMMA in UiO-66/PMMA@UiO-66/PAN, the isotherm remained Type I, however, the low pressure adsorption (i.e. monolayer capacity, Q_m) was improved and a Type H1 hysteresis loop was evident.

The result showed an improvement in the porosity of the nanofiber composite and in Fig. 5.28 the micropores at ~6 Å were also observable owing to the exposed UiO-66 crystals on the surface of the nanofibers, after PMMA removal (Fig. 5.23). In Table 5.2 it can be seen that the removal of PMMA from UiO-66/PMMA@PAN improved the surface area and pore volume by 70% and in UiO-66/PMMA@UiO-66/PAN nanofibers the surface area improved by 17% and pore volume by at least 30%. The highest surface area of 508 $m^2 \cdot g^{-1}$ obtained in the core-shell nanofibers was, however, only 36% of the surface area of pristine UiO-66 powder.

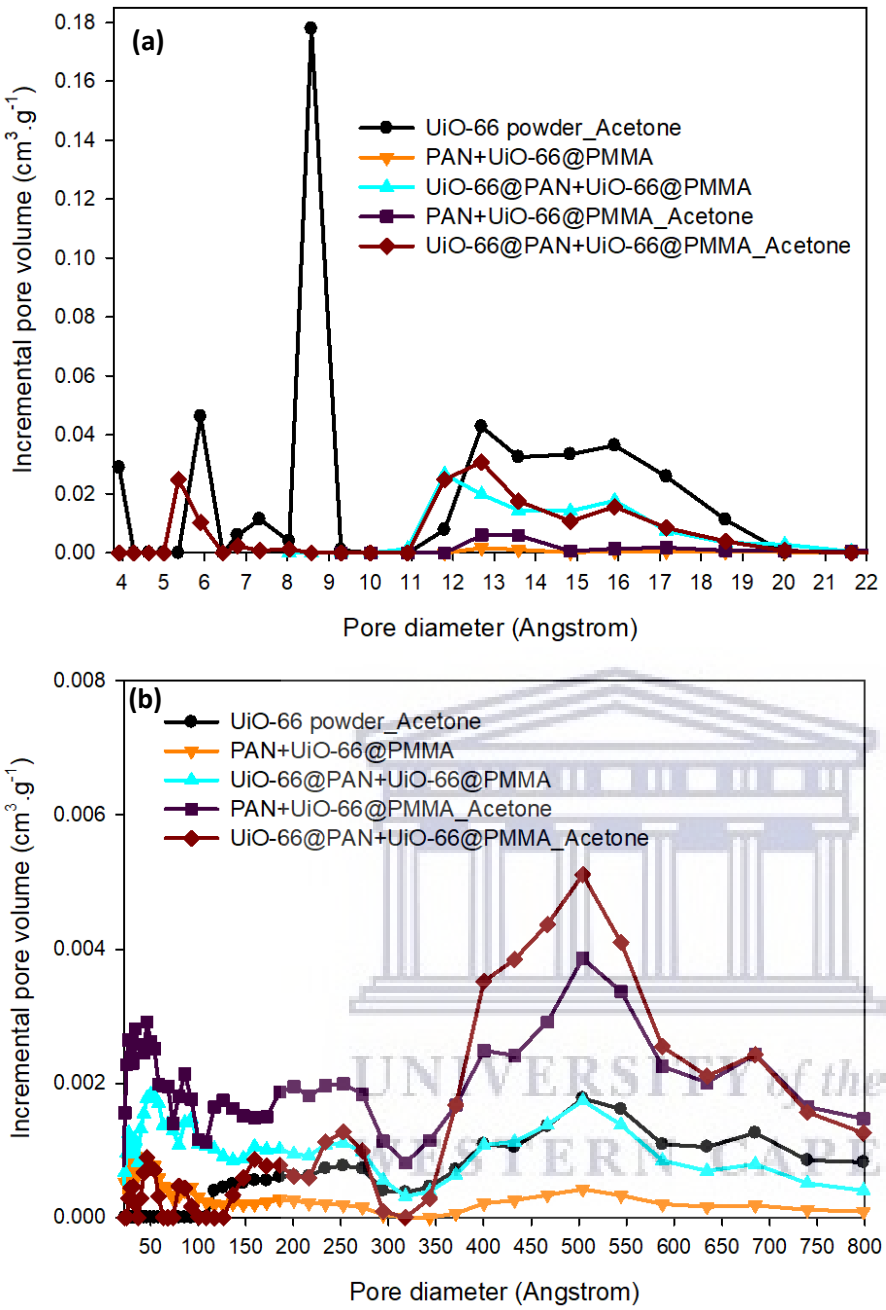

Figure 5.28: NLDFT pore size distribution curves for core-shell UiO-66/PMMA@PAN and UiO-66/PMMA@UiO-66/PAN nanofibers: (a) micropore region (pore size < 20 Å), and (b) mesopore and macropore region (pore size > 20 Å). The nanofibers were collected at 2 mL·h^{-1} flow rate, 11 kV voltage, and 15 cm needle-to-collector distance

Table 5.2: Summary of the BET report obtained for core-shell UiO-66/PMMA@PAN and UiO-66/PMMA@UiO-66/PAN nanofibers.

Isotherm property	**Nanofiber sample**			
	UiO-66/PMMA@PAN	**UiO-66/PMMA@UiO-66/PAN**	**UiO-66/PMMA@PAN_Acetone**	**UiO-66/PMMA@UiO-66/PAN_Acetone**
BET surface area ($m^2.g^{-1}$)[a]	31 (-)	421 (300)	106 (0.4)	508 (361)
NLDFT pore volume ($cm^3.g^{-1}$)[b]	0.038 (-0.0006)	0.26 (0.12)	0.17 (-0.0003)	0.37 (0.14)
Slope ($g.cm^{-3}$, STP)	0.1391	0.01031	0.004077	0.00855
Y-intercept ($g.cm^{-3}$, STP)	0.001827	0.000025	0.000427	0.000019
Q_m ($cm^3.g^{-1}$, STP)	7	97	24	117
Correlation coefficient	0.9997	0.9999	0.9998	0.9999

[a]values in parentheses are given for the t-plot micropore surface area; [b]values in parentheses are given for the t-plot micropore volume.

5.4. Coaxial electrospinning of MIL-101(Cr)-based nanofibers

The results in section 5.3 showed that the incorporation of UiO-66 into the core *and* the shell provided higher surface areas and pore volumes compared to the incorporation of UiO-66 in the core region only. Due to the limitation of synthesizing MIL-101(Cr) in small yields, as mentioned in chapter 2, it was decided that the MIL-101(Cr) powder would be incorporated in the core *and* shell via coaxial electrospinning and a comparison made of the surface areas of the nanofibers and pristine MIL-101(Cr) after its treatment with chloroform. The chloroform was used in small quantities in order to remove PS from co-electrospun MIL-101/PS@MIL-101@PAN nanofibers. In section 5.4.1, the study reports on the treatment of MIL-101(Cr) powder with chloroform and monitored possible changes to chemical composition and textural properties (surface area and pore volume).

5.4.1. Spectroscopy and textural properties of MIL-101(Cr) powder after treatment with chloroform

The results in Fig. 5.29, 5.30 and Table 5.3 showed that the treatment of MIL-101(Cr) with chloroform did not change its chemical composition and textural properties. After treatment with chloroform, the surface area and pore volume of MIL-101(Cr) was 92% and 109% respectively, compared to the untreated MIL-101(Cr) powder. The slight differences could be attributed to the appearance of the pore sizes around 34 Å after treatment of the MIL-101(Cr) powder with chloroform. The chloroform could replace solvent molecules (water) that were strongly adsorbed within the pores, which could have been difficult to remove with acetone treatment alone.

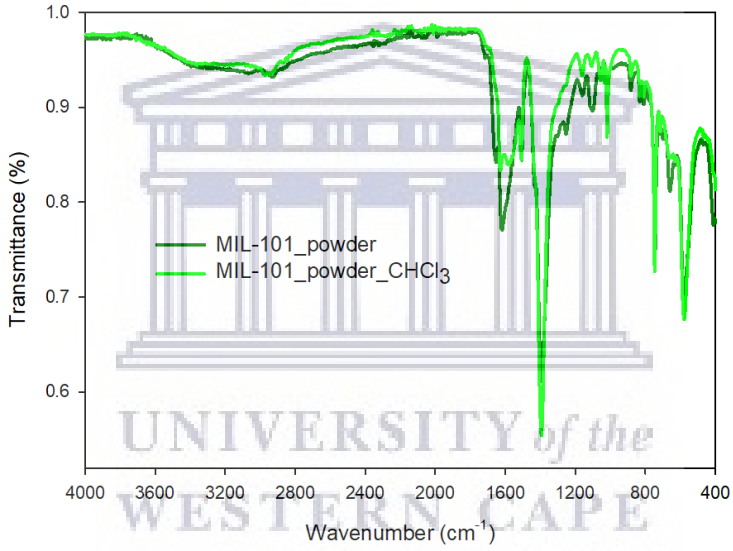

Figure 5.29: FTIR spectra of MIL-101(Cr) powder before and after treatment with chloroform.

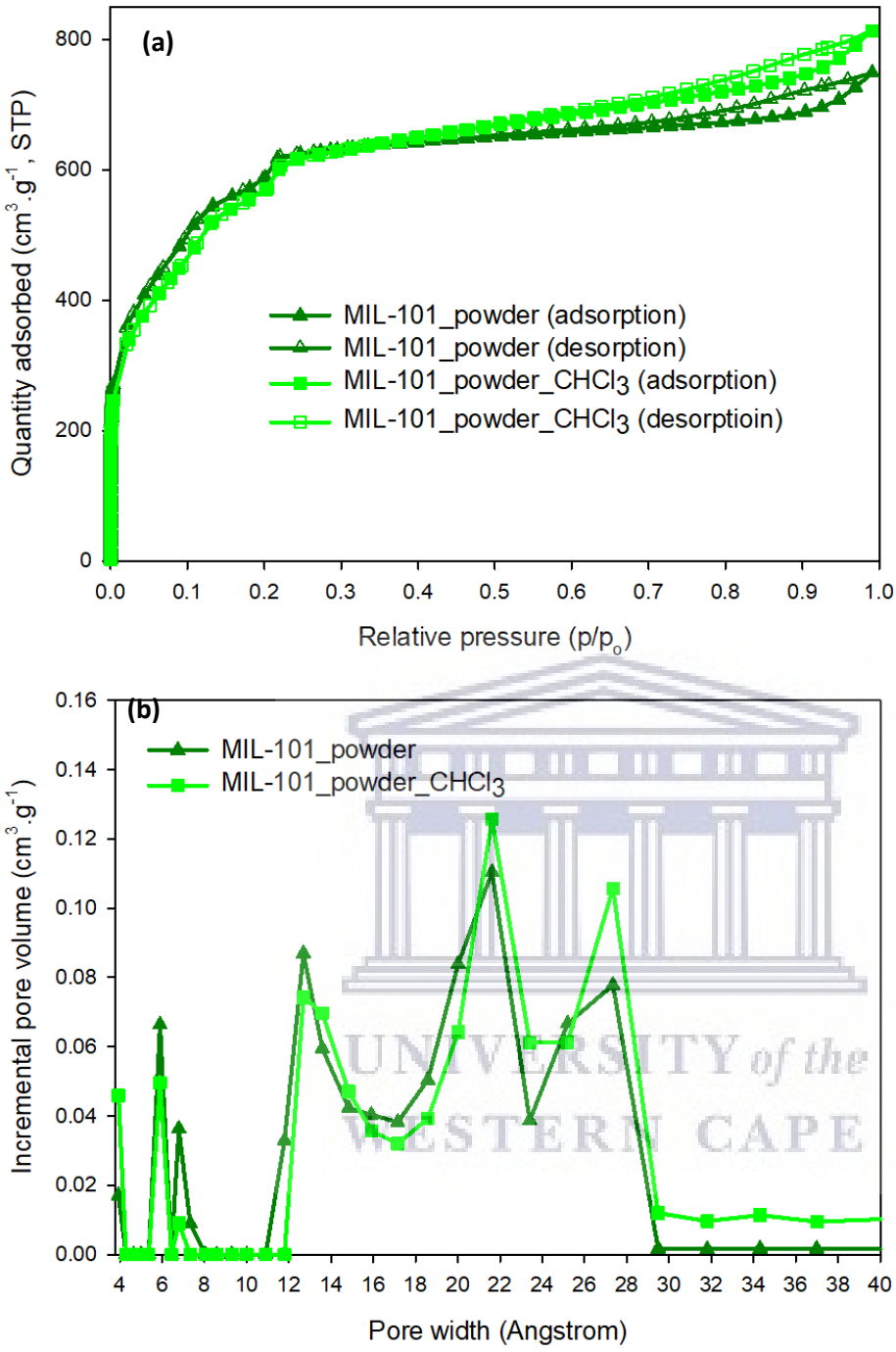

Figure 5.30: Textural properties of MIL-101(Cr) powder after treatment with chloroform in comparison to non-treated MIL-101(Cr) powder: (a) N_2 adsorption/desorption isotherms, and (b) NLDFT pore size distributions.

Table 5.3: Summary of the BET report obtained for pristine MIL-101(Cr) and MIL-101(Cr) treated with chloroform.

Isotherm property	**MIL-101(Cr) sample**	
	MIL-101 as-synthesized	**MIL-101(Cr) after $CHCl_3$ treatment**
BET surface area ($m^2.g^{-1}$)[a]	2151 (479)	1983 (430)
NLDFT pore volume ($cm^3.g^{-1}$)[b]	1.16 (0.18)	1.26 (0.13)
Slope ($g.cm^{-3}$, STP)	0.001998	0.002169
Y-intercept ($g.cm^{-3}$, STP)	0.000026	0.000026
Q_m ($cm^3.g^{-1}$, STP)	494	456
Correlation coefficient	0.9998	0.9997

[a]values in parentheses are given for the t-plot micropore surface area; [b]values in parentheses are given for the t-plot micropore volume.

The characterization of MIL-101/PS@MIL-101/PAN nanofibers (Fig. 5.31 to 5.35) was found to be consistent with the observations made on UiO-66/PMMA@UiO-66/PAN nanofibers. The incorporation of MIL-101 into the nanofibers and removal of PS were confirmed by PXRD and FTIR analysis as shown in Fig. 5.32 and Fig. 5.33 respectively. After the removal of the core polymer, PS, the resultant nanofibers were found to rupture, exposing MIL-101 crystals on the surface of the nanofibers (Fig. 31). After the removal of PS, meaning after treatment of the core-shell nanofibers with chloroform, the morphology of the remaining MIL-101/PAN nanofibers was vastly different to that observed for core-shell UiO-66/PAN nanofibers (Fig. 5.23). The rupturing observed after the removal of PS was more severe in the remaining PAN nanofibers, there was a high degree of MIL-101(Cr) crystals exposed on the surface of the PAN surface (Fig. 5.31). This could show that chloroform was more destructive in removing the core material in comparison to acetone.

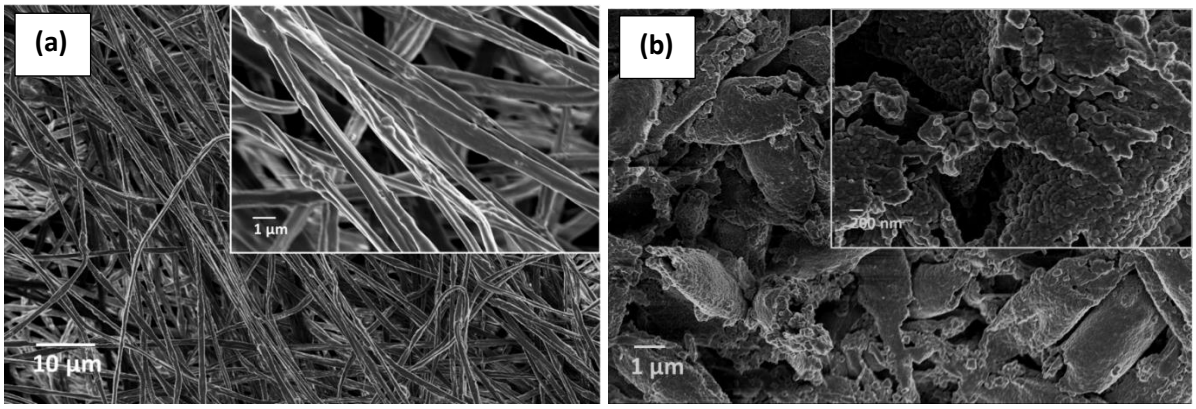

Figure 5.31: SEM images of MIL-101/PS@MIL-101/PAN nanofibers: (a) as-spun, and (b) after treatment with chloroform.

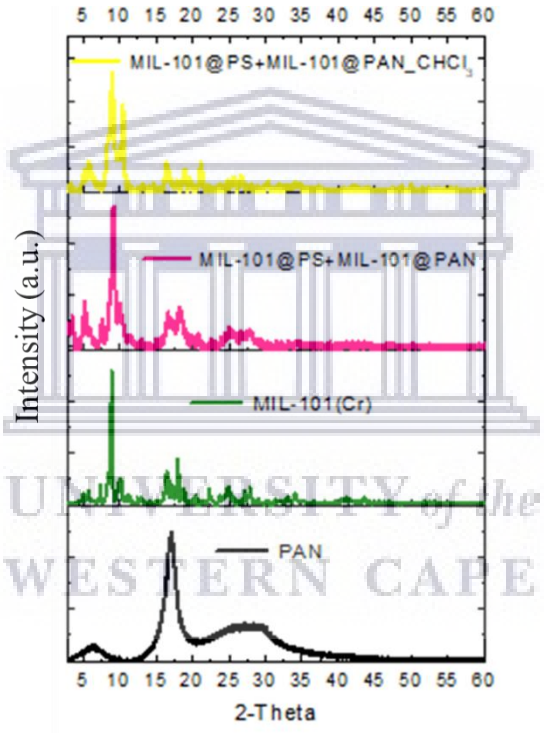

Figure 5.32: PXRD patterns for MIL-101/PS@MIL-101/PAN in comparison to pristine MIL-101(Cr) and PAN.

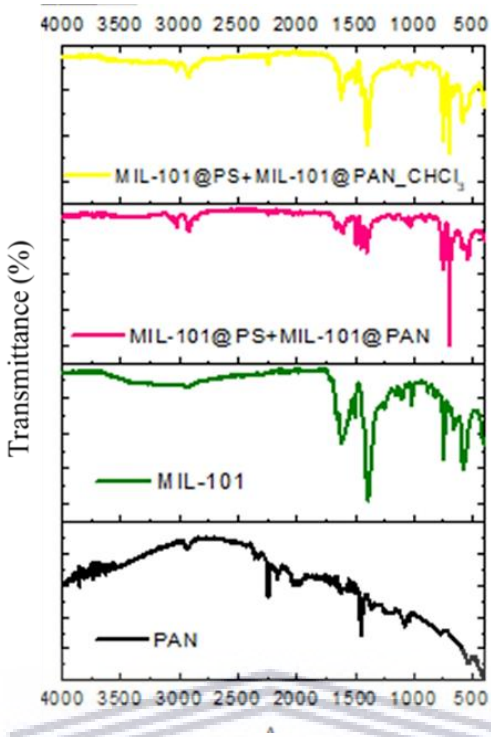

Figure 5.33: FTIR spectra for MIL-101/PS@MIL-101/PAN in comparison to pristine MIL-101(Cr) and PAN.

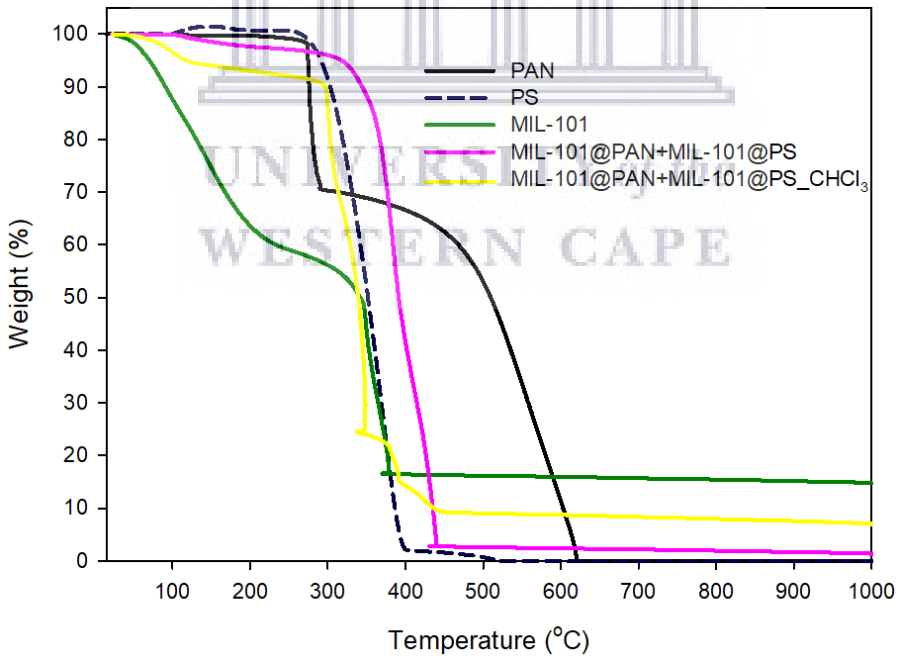

Figure 5.34: TGA of MIL-101/PS@MIL-101/PAN in comparison to pristine materials. The nanofibers were collected at 1.8 mL·h^{-1} flow rate, 11 kV voltage, and 15 cm needle-to-collector distance

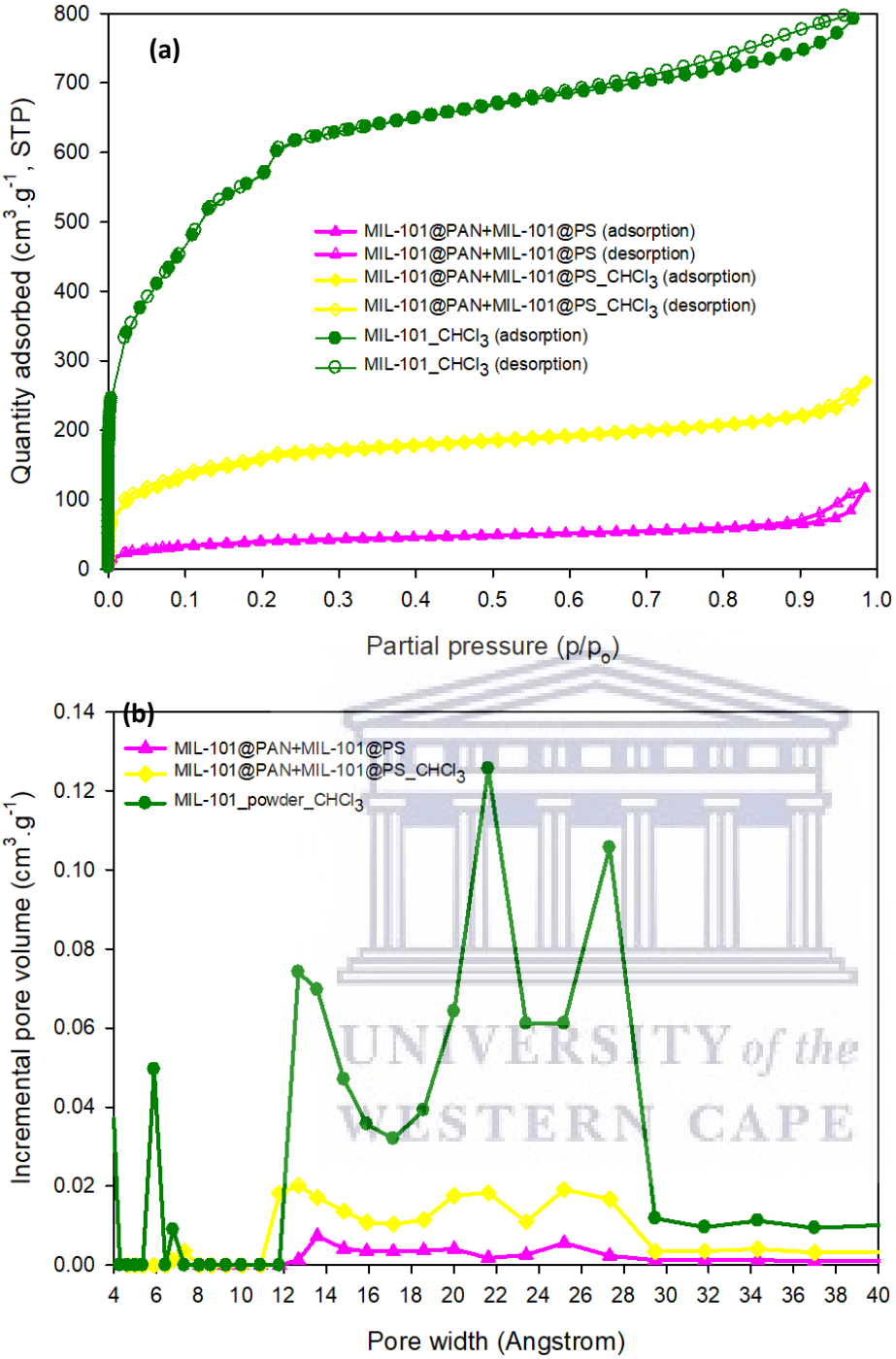

Figure 5.35: (a) N_2 adsorption/desorption isotherms and (b) NLDFT pore size distribution curves for MIL-101/PS@MIL-101/PAN in comparison to pristine MIL-101(Cr). The nanofibers were collected at 1.8 mL·h^{-1} flow rate, 11 kV voltage, and 15 cm needle-to-collector distance

The removal of PS from MIL-101/PS@MIL101@PAN was also observed to increase the low-pressure adsorption (monolayer capacity, Q_m) of the nanofiber composite. The surface area and pore volume were only 30% in comparison to that of pristine MIL-101(Cr), possibly due to the leaching of MIL-101 crystals after chloroform treatment.

Table 5.4: Summary of the BET report obtained for MOF@PAN nanofibers prepared via single-nozzle electrospinning in comparison to pristine UiO-66 and MIL-101 powders.

Isotherm property	**MIL-101(Cr) nanofiber sample**	
	MIL-101/PS@MIL-101/PAN	**MIL-101/PS@MIL-101/PAN_$CHCl_3$**
BET surface area ($m^2.g^{-1}$)[a]	148 (19)	570 (76)
NLDFT pore volume ($cm^3.g^{-1}$)[b]	0.18 (0.0036)	0.42 (0.024)
Slope ($g.cm^{-3}$, STP)	0.02903	0.00754
Y-intercept ($g.cm^{-3}$, STP)	0.000489	0.000093
Q_m ($cm^3.g^{-1}$, STP)	34	131
Correlation coefficient	0.9999	0.9998

[a]values in parentheses are given for the t-plot micropore surface area; [b]values in parentheses are given for the t-plot micropore volume.

Regardless of the low surface areas obtained in UiO-66- and MIL-101-based core-shell nanofiber composites, the results did show that the selective removal of core polymers using solvents was possible and could likely improve the MOF loading without affecting the adsorption properties of the MOF. The drawback, however, was the destructive nature of the solvent-based method as both UiO-66 and MIL-101 were observably leached out of the nanofibers when 20 wt% of the MOF was loaded into the core *and* shell regions of the nanofibers.

5.5. Hydrogen adsorption properties of electrospun MOF/PAN nanofibers

The nanofibers showing the highest surface areas and pore volumes were selected for H_2 adsorption studies at 77 K up to 100 bar. The selected fibers were the PIM-1, core-shell UiO-66/PMMA@UiO-66/PAN-Acetone and MIL-101/PS@MIL-101/PAN-$CHCl_3$ nanofiber composites.

The results in Fig. 5.36 and Table 5.5 showed that the total gravimetric H_2 capacity of PIM-1 nanofibers was 60% higher compared to the core-shell UiO-66-based nanofibers, and 37% higher compared to those based on MIL-101. The working capacity of 0.9 wt% obtained for core-shell MIL-101/PS@MIL-101/PAN was found to be highest of the three samples, with PIM-1 having a working capacity of 0.8 wt% and UiO-66/PMMA@UiO-66/PAN nanofibers only having 0.1 wt% working capacity. This could have been due to the fact that PIM-1 and the UiO-66-based nanofibers showed very high H_2 adsorption at low pressures, below 5 bar, and the increase in H_2 adsorption beyond 5 bar was found to reach saturation as it remained relatively constant, especially for the core-shell UiO-66-based nanofibers. This can be explained by the pore structure of PIM-1 and UiO-66 as they were shown to consist of a high degree of micropores (2 Å < pore size < 20 Å). Highly microporous materials tend to show a high degree of Type I gas adsorption isotherms where the highest rate of adsorption of gas molecules occurs at low pressures (~5 bar) compared to intermediate (~5 – 20 bar) to high pressures (> 20 bar) such as employed in this study [39]. Type H4 loop hysteresis observed on N_2 adsorption/desorption isotherm of PIM-1 (Fig. 5.4) was also observable on the H_2 isotherms of PIM-1 nanofibers, showing that the pore structure of PIM-1 could possibly influence condensation of H_2 within the micropores. Based on the IUPAC classification of isotherms [39], the appearance of a hysteresis loop generally describes condensation within narrow pores of the adsorbent, which may be also affected by the shape of pores. The large hysteresis loop characteristic of PIM-1 has been reported to result from possible adsorption-induced swelling of its pore walls, thereby promoting hysteresis behaviour unusual of many microporous materials [109,111,112,183,184,218,227,228]. The presence of the Type H4 hysteresis loop in the H_2 adsorption/desorption isotherm of PIM-1 was not expected since H_2 adsorption at 77 K was above the critical temperature of H_2 [39,118]. The narrow micropores (pore size < 10 Å) present in PIM-1 could promote strong bonding of H_2 within their pore walls and the swelling effects upon gas adsorption could change the diameter of the pores during adsorption and therefore could possibly promote hysteresis in H_2 adsorption/desorption at 77 K. For the MIL-

101-based nanofibers, the pore structure consists mainly of mesopores which may exhibit pore filling at intermediate to high pressures due to their wider pore widths [121]. As it can be seen in Fig. 5.36, the total H_2 adsorption isotherm for MIL-101-based nanofibers was found to steadily increase beyond 5 bar, showing little evidence of reaching saturation, meaning a higher total H_2 adsorption was possible at pressures greater than 100 bar.

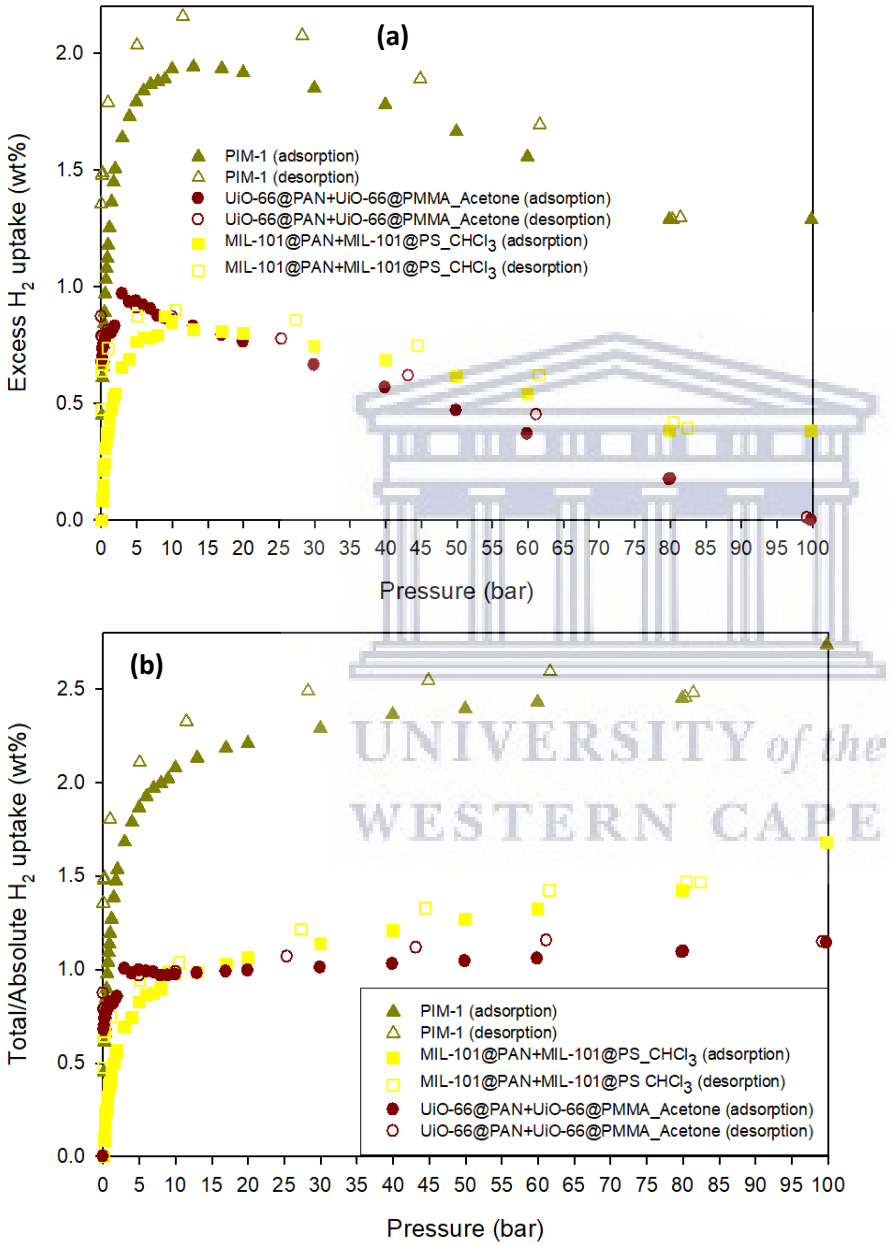

Figure 5.36: H_2 adsorption/desorption isotherms at 77 K for PIM-1, UiO-66/PMMA@UiO-66/PAN_Acetone, and MIL-101/PS@MIL-101/PAN_CHCl₃ (a) excess H_2 uptake for, and (b) total/absolute gravimetric H_2 uptake. The closed symbols represent the adsorption isotherms and open symbols represent the desorption isotherms.

Table 5.5: H_2 uptake at 77 K up to 100 bar obtained for PIM-1, UiO-66/PMMA@UiO-66/PAN-Acetone, and MIL-101/PS@MIL-101/PAN-$CHCl_3$ nanofibers.

Sample	Maximum excess Uptake (wt%)	Total/absolute gravimetric H_2 uptake (wt%)[a]		Working capacity (wt%)[b]
		5 bar	100 bar	
PIM-1	1.9	1.9	2.7	0.8
UiO-66/PMMA@UiO-66/PAN-Acetone	1.0	1.0	1.1	0.1
MIL-101/PS@MIL-101/PAN-$CHCl_3$	0.9	0.8	1.7	0.9

[a]Values calculated using eqn 3.3 in chapter 3 (section 3.4.5.2). [b]Values calculated from the difference between total H_2 uptake at 100 bar and 5 bar.

The preparation of core-shell MOF/X@PAN nanofibers followed by selective removal of the MOF was done to possibly increase the MOF loading onto electrospun MOF/PAN nanofibers. Initally it was observed that a MOF loading of 20 wt% was the limit, under the specified electospinning conditions, for nanofibers prepared via single-nozzle electrospinning. These nanofibers, prepared via single-nozzle electrospinning, were found to show significantly lower BET surface areas and pore volumes in comparison to the pristine MOF powders. Using the method of coaxial electrospinning and subsequent removal of the core polymer, it was found that BET surface areas could be improved from ~100 $m^2 \cdot g^{-1}$ to ~500 $m^2 \cdot g^{-1}$. The Chahine rule [209] states that the gravimetric H_2 capacity shows a direct relationship with the BET surface area and hence the improvements observed in the core-shell nanofibers could signify an improvement of their gravimetric H_2 capacities compared to MOF/PAN nanofibers prepared via single-nozzle electrospinning. The method of selectively removing the core polymer in core-shell nanofibers was, however, found to be destructive as it was clear from SEM images that both solvents used in this study (acetone and chloroform) resulted in ruptured MOF/PAN nanofibers. This could make the determination of the resultant MOF loading, after removal of the core material, difficult and unquantifiable. The incorporation of MOFs into non-porous polymers, and possible improvement of the MOF loading through coaxial electrospinning coupled with selective removal of the core polymer, could be crucial in addressing the challenges typically found in using polymer-based binders for the fabrication of MOF composites [116].

5.6. Chapter summary

This chapter reported on the fabrication of MOF/polymer nanofibers using the electrospinning technique. The polymers of choice were PAN, PIM-1, PS, and PMMA. Two types of electrospinning methods were employed, namely the single-nozzle electrospinning and the coaxial electrospinning methods. The single-nozzle method was used to optimize the electrospinning process parameters that would be suitable to incorporate MOFs into the nanofibers. Based on the optimized process parameters from the single-nozzle method, the coaxial method was then used to incorporate a higher loading of MOFs into the polymer nanofibers, through the addition of MOFs in both core and shell polymer solutions. The electrospinning process parameters were found to have a significant effect on the morphologies of the nanofibers, especially in the formation of beads on the nanofibers. In PAN electrospinning, the concentration of PAN in DMF and flow rate of the solution were found to be the main factors affecting fiber morphologies. In PIM-1 electrospinning, the solvent was found to have the most impact on the formation of nanofibers. Using pure TCE as a solvent led to the formation of a film instead of nanofibers. The addition of 30% v/v THF to TCE was, however, found to improve the electrospinnability of the PIM-1 solution and nanofibers of about 2 - 3 µm in diameter were obtainable. The preparation of MOF/nanofiber composites was found to have a limitation of 20 wt% MOF loading since a higher loading of 40 wt% was found to produce beaded nanofiber morphologies. The inclusion of 20 wt% loading of MOFs in core-shell nanofibers was found to be successful. In order to improve the MOF loading possibly beyond 20 wt%, the study proposed the selective removal of the core polymer material. In the core-shell nanofibers, the core polymer was PMMA in the case of the incorporation of UiO-66 and PS in the case of MIL-101. The method to remove PMMA and PS was through the immersion of the MOF/X@PAN (X = PMMA or PS) in acetone and chloroform, respectively. The removal of core polymers from X@PAN nanofibers using the aforementioned methods was proven successful, however collapsed the remaining PAN nanofibers as they were observed to be flattened. The collapse of the PAN nanofibers following affected both UiO-66/PMMA@UiO-66/PAN and MIL-101/PS@MIL-101/PAN nanofibers, as they ruptured after selective PMMA or PS removal and as a result the MOF loading after PMMA or PS removal could not be determined accurately. The H_2 uptake was therefore highest for PIM-1 nanofibers compared to core-shell UiO-66-based nanofibers and MIL-101-based nanofibers. The PIM-1 and UiO-66/PMMA@UiO-66/PAN nanofibers were used as binders for the pelletization of UiO-66.

Chapter 6

6. Co-pelletization of UiO-66 with electrospun nanofibers and fabrication of graphene foam/UiO-66 composite

This chapter presents the results on the pelletization of UiO-66 with the best performing MOF/polymer nanofibers as binders. The use of polymer-based binders has been proven successful in the shaping of MOFs, however, the main challenge exhibited in most studies was the compromise in the textural properties of the composite in comparison to that of the pristine MOF powder. In this study the aim, for the pelletization of UiO-66 with binders, electrospun MOF/PAN and PIM-1 nanofibers, was to exploit the porosity from the incorporated MOFs in the former and the permanent microporosity of PIM-1. The combination of MOFs, non-porous and porous electrospinnable polymers into nanofiber composites was postulated to result in polymer-based binders that could possibly retain a high degree of the textural properties of UiO-66 following its pelletization at ~700 MPa. In addition, the study also focused on the incorporation of a carbon material to potentially improve the thermal conductivity of a UiO-66-based composite in comparison to pristine UiO-66. The carbon material of choice was graphene foam (GF) prepared by chemical vapour deposition (CVD) using a nickel foam (NF) precursor or template. The first section (6.1) of this chapter discusses the preparation and properties of CVD-grown GF. Then section 6.2 discusses the addition of GF to monitor the thermal conductivities of pristine UiO-66 powder and pelletized UiO-66 in comparison to the GF/UiO-66 composite. Finally the chapter discusses the effect of adding polymer-based binders (from the best performing nanofibers in Chapter 5) on the textural properties of pelletized UiO-66, and the high-pressure H_2 adsorption of two of the co-pelletized UiO-66+binder composites are presented.

6.1. Preparation of GF and a GF/UiO-66 composite for hydrogen storage applications

In the preparation of GF from NF via the CVD procedure, there was a step involving the removal of the nickel (Ni) template by etching in a 3 M hydrochloric acid (HCl) solution in order to isolate GF. In this step, the Ni-C composite formed after deposition of carbon at 1000 ^{o}C, first had to be stabilized by adding a polymethylmethacrylate (PMMA) supporting film prior to the etching. After successfully removing most of the Ni template, the PMMA film was

removed using two methods, first by immersing in acetone to dissolve PMMA and secondly by thermal degradation of PMMA via pyrolysis under argon (Ar). In Fig. 6.1 it can be seen that the removal of PMMA by dissolving in acetone produced a high degree of contamination on the surface of the GF which could compromise the quality of the GF product. In Fig. 6.2, however, it was shown that the pyrolysis method was more effective in producing contaminant-free GF. Hydrocarbon materials have been reported to be a major contaminant in the preparation of graphene forms, including GF, and such contamination may compromise the intrinsic properties of graphene such as good electrical and thermal conductivity due to the creation of highly defective sites on the graphene surface [188][185].

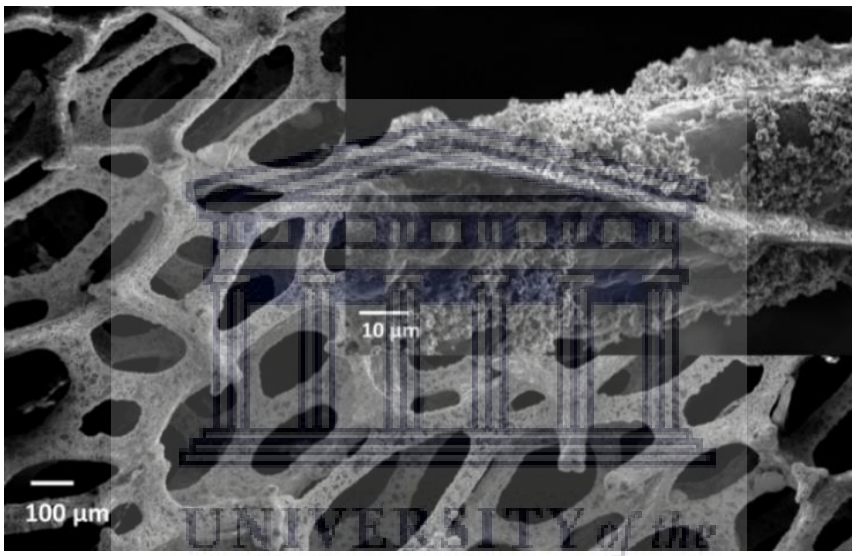

Figure 6.1: SEM image of the surface of the CVD-grown GF obtained after soaking the GF/PMMA composite in 20 mL acetone. Insert is a close up image (at 1 000 X magnification)

The confirmation of the preparation of GF from NF was monitored by, SEM-EDX, PXRD crystallography and Raman spectroscopy.

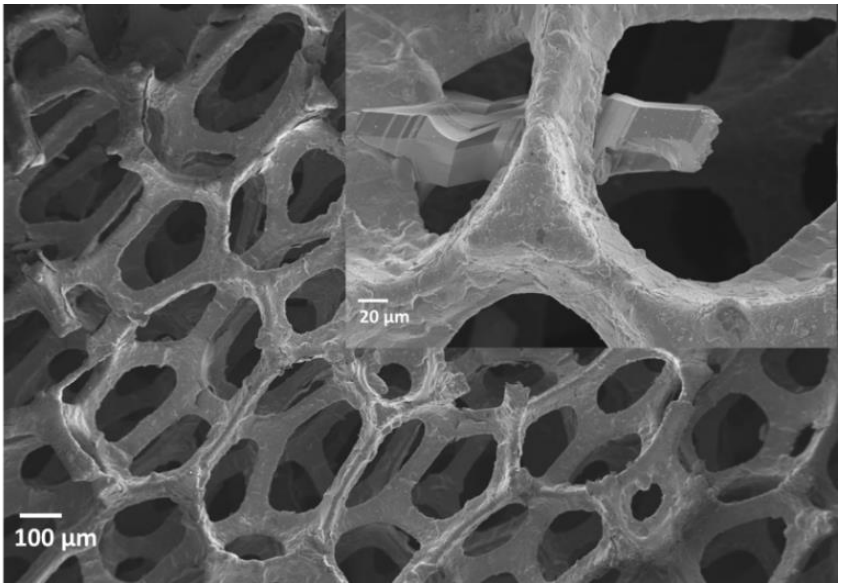

Figure 6.2: SEM image of the surface of GF obtained after pyrolysis of GF/PMMA composite at 800 ^{o}C under 0.025 $mL{\cdot}min^{-1}$ argon (Ar) flow. Insert is a close up image (at 300 X magnification).

The PXRD patterns presented in Fig. 6.3 showed the typical Ni peaks at $2\Theta \approx 45^{o}$, 53^{o}, and 76^{o} [157], however, after completion of the CVD process, a slightly broad peak at $2\Theta \approx 27^{o}$ was observable together with the characteristic Ni peaks. The appearance of the Ni peaks in the PXRD pattern and EDX mapping (Fig. 6.4) of the CVD-grown product was indicative of the incomplete etching of Ni from Ni-C composite. The presence of a small amount of Ni in the GF was not considered detrimental since some studies have reported Ni to have some H_2 storage capabilities [229]. Graphene forms (e.g. single-layer graphene and reduced graphene oxide) of carbon can be distinguishable from graphite forms (e.g. graphite and graphite oxide) by their characteristic (0 0 2) peak positions on a PXRD pattern. In graphene forms, the typical (0 0 2) crystalline phases occur as a flat and broad peak between $2\Theta \approx 20^{o}$ to 30^{o}, compared to the distinctly sharp peak around $2\Theta \approx 25^{o}$ normally observed in graphite forms [230]. In Fig. 6.3, the "new" peak was found to have a broad base spanning from $2\Theta \approx 20^{o}$ to 35^{o} and a very sharp portion at $2\Theta \approx 27^{o}$. The observation could have indicated that the CVD product consisted of a composite of graphenic and graphitic carbons. The characteristic difference between graphite and graphene is that graphite contains multiple layers of graphene in a three dimensional arrangement, whereas graphene consists of a single layer of sp^2-hybridized carbons. It would, therefore, be expected that in a three dimensional structure of CVD-grown carbon such as GF, there would be stacked graphene layers that could possibly resemble the

physical properties of graphite and also contain sp^2-hybridized carbons possibly on the outermost surface of the GF [75,187].

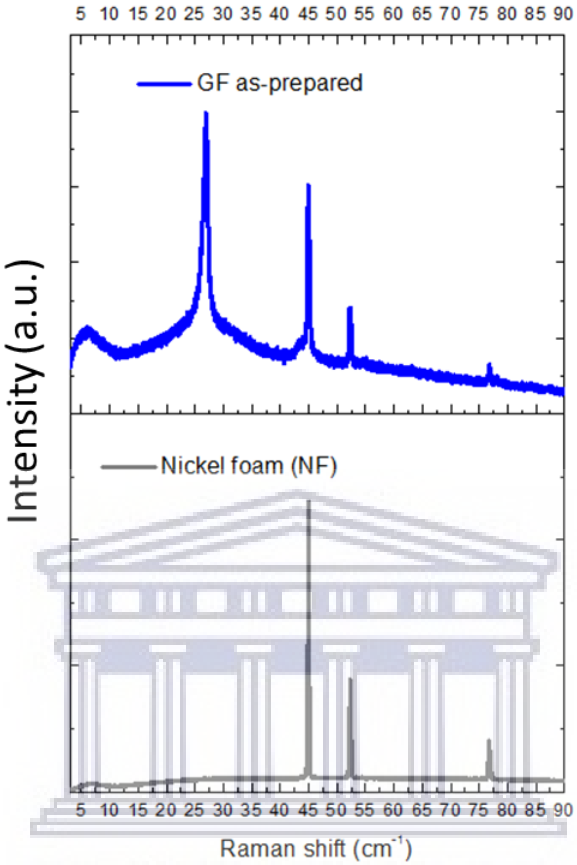

Figure 6.3: PXRD patterns of NF template in comparison to the CVD-grown GF product obtained under pyrolysis conditions under Ar flow.

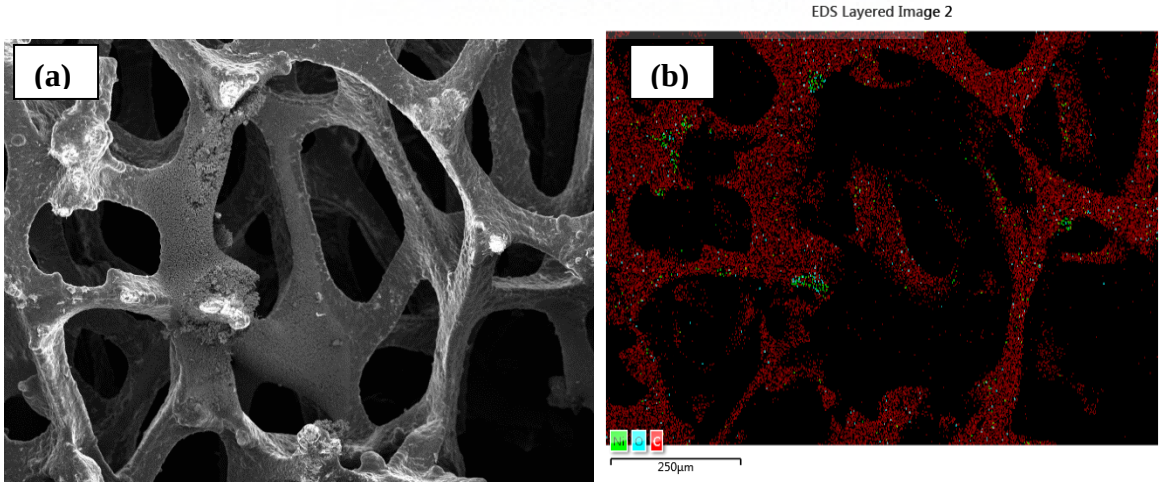

Figure 6.4: (a) SEM image showing the microstructure of CVD-grown GF, and (b) EDX image of GF showing the mapping of Nickel (Ni), Oxygen (O), and Carbon (C).

In Fig. 6.5, Raman spectroscopy was used to elucidate the composition and degree of layering in the CVD-grown product. The Raman analysis was initially done on intact GF, in order to analyse the outermost surface of GF, and then performed after grinding the GF into a powdery form, representing the bulk composition of the GF. In Fig. 6.5, the GF was observed to contain the characteristic graphene D, G, and 2D Raman shift bands around 1350 cm^{-1}, 1580 cm^{-1}, and 2700 cm^{-1}, respectively. Using the intensities of the bands could give information about the type of graphene that was obtained after the CVD process. The degree of defectiveness of the GF and number of graphene layers could be obtained by calculating the ratios I_D/I_G and I_{2D}/I_G, respectively [77,198]. The I_{2D}/I_D ratio was ~0.6 which indicated the GF consisted mainly of multi-layered graphene, and I_D/I_G of ~1.2 indicated that the GF was highly defective, i.e. contained less sp^2-hybridized carbons in comparison to an ideal single layer of graphene. In a three dimensional structure of graphene, both a high level of multi-layers and defects would be expected especially that the three dimensional structure of the Ni template was maintained in the product and hence forming the observed three dimensional network of carbon [75,201,230].

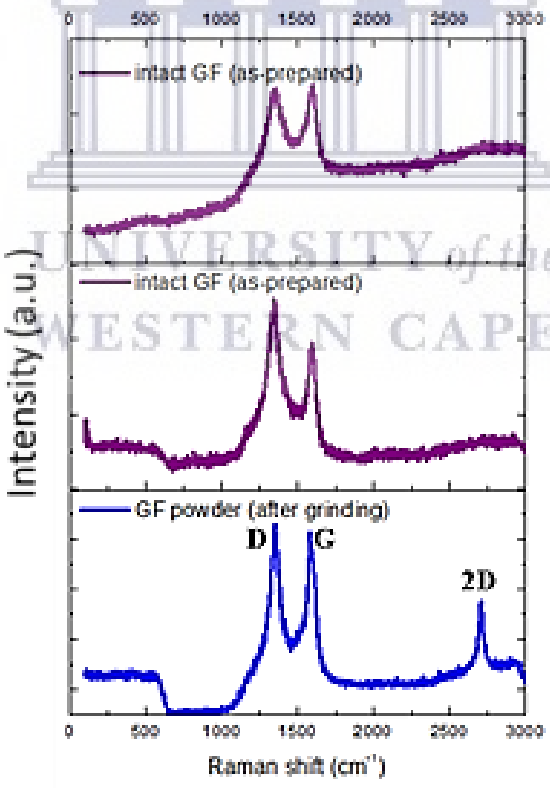

Figure 6.5: Raman spectra of intact CVD-grown GF, at two different positions on the GF surface (as-prepared) in comparison to the Raman spectrum of ground GF (powder).

After successful preparation and characterization of the GF, another sample of GF was prepared under the same conditions of the CVD procedure discussed in Chapter 3 (section 3.1). To this sample, UiO-66 crystals were grown on the surface of the GF via an in-situ synthesis method (Chapter 3, section 3.2.3). Due to the high degree of macroporosity (pores > 50 nm, as per IUPAC classification) observed on the GF network structure, the growth of UiO-66 was done using two methods, firstly a single-step crystal growth method where UiO-66 was grown directly onto GF. In the second method, UiO-66 was grown via a seed-mediated procedure where the single-step GF/UiO-66 product was re-immersed in a fresh solution of UiO-66 precursors so as to improve the amount of UiO-66 on the GF surface.

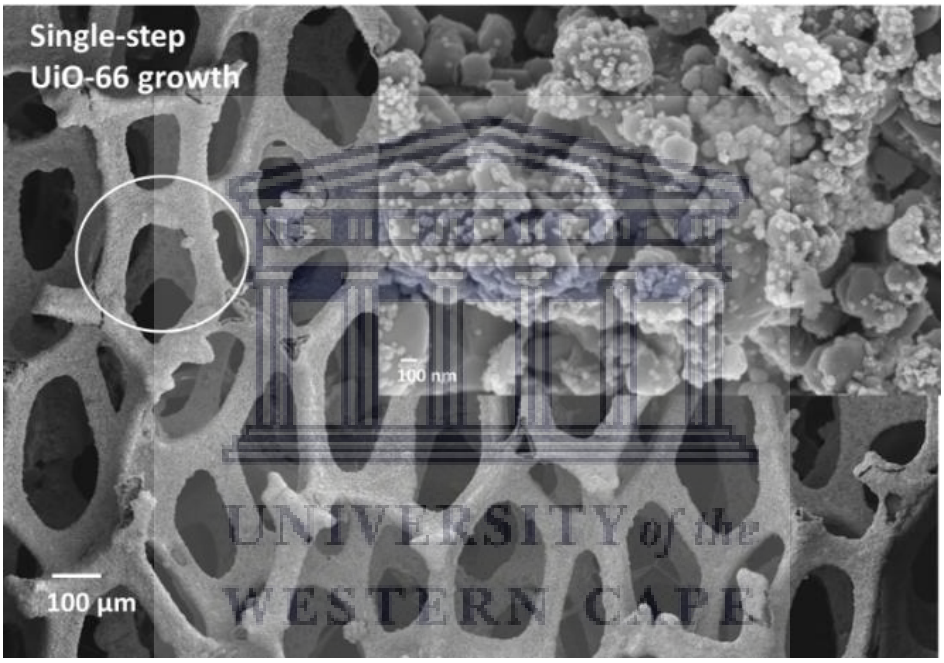

Figure 6.6: SEM image of GF/UiO-66 composite obtained after single-step growth of UiO-66 crystals. The circled area was analysed by EDX mapping (Fig. 6.7). Insert is a close up image (at 30 000 X magnification).

The images in Fig. 6.6 and 6.7 showed the distribution of crystals was mainly on the surface of the GF with little UiO-66 growth within the macropores of the GF network. The EDX maps in Fig. 6.7 showed the presence of Zr metal as the main metal on the GF surface, with no significant evidence of Cr or Ni on the GF surface. The Cr could have been a cross-contaminant arising from the glassware since washing of MIL-101(Cr) was also carried out on the same glassware. The presence of Ni was observed in both the PXRD and EDX maps of as-prepared GF but its presence in Fig. 6.7 was negligible, probably due to further etching of Ni under the

acidic conditions during UiO-66 synthesis. The crystals shown in Fig. 6.6 did not have well-defined octahedral shapes as generally observed for UiO-66. The bulk of the crystals were irregularly shaped, containing a high content of agglomerates and suggested the crystal growth was not provided enough time for UiO-66 crystals to assume their octahedral shapes.

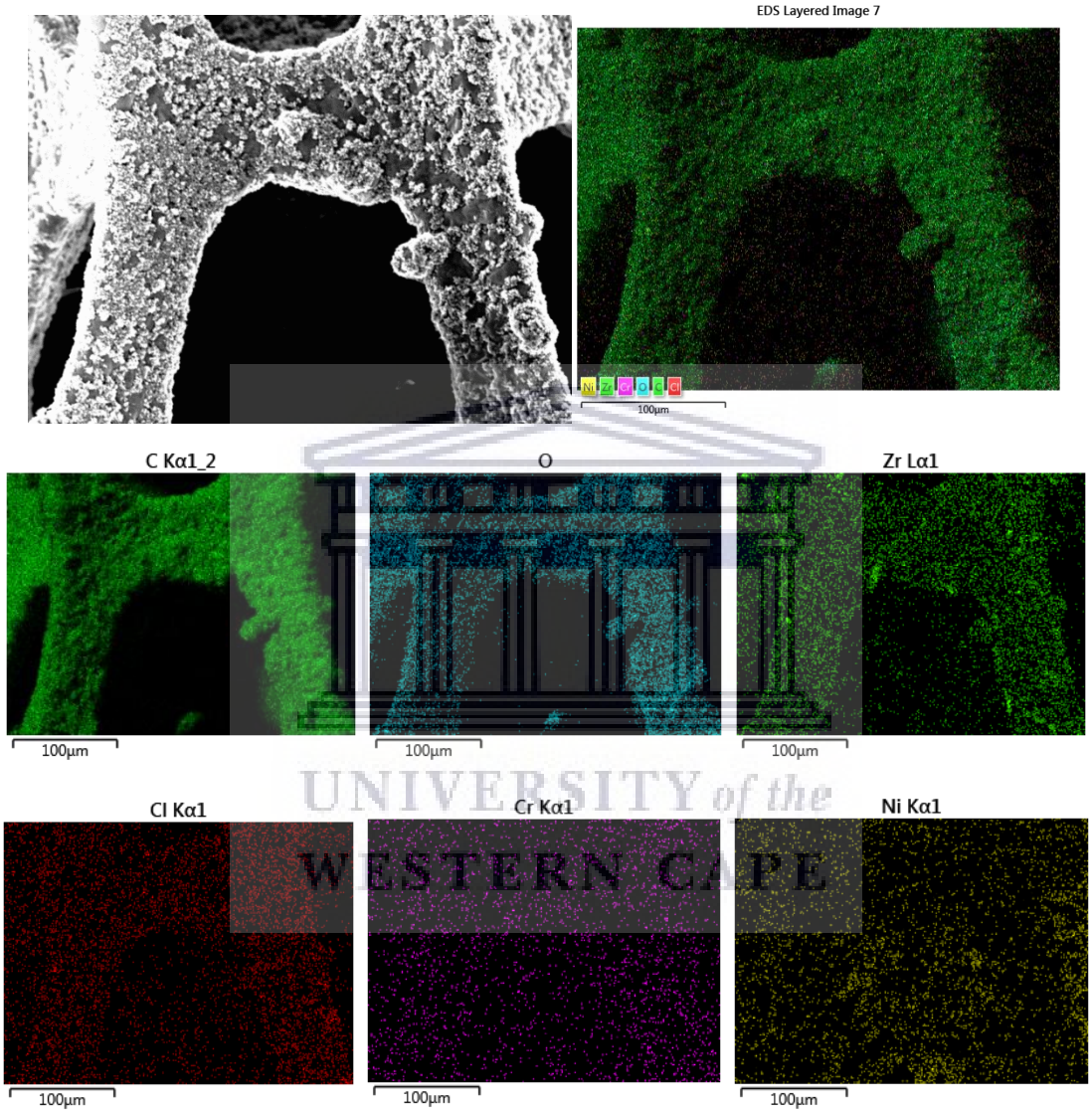

Figure 6.7: SEM and EDX mapping of GF/UiO-66 showing the distribution of C, Ni, O, Zirconium (Zr), Chromium (Cr), and Chlorine (Cl).

The reason could be described according to observations reported in the work of Petit et al. [146]. Their study showed irregularly shaped and agglomerated crystals of the copper paddle-wheel MOF, HKUST-1, grown by in-situ solvothermal synthesis onto the surface of graphite oxide. Their observations could suggested that defects on graphene and/or graphitic carbon

forms could possibly inhibit the growth of MOF crystals or result in distorted MOF structures that deviate from their pristine forms. In Fig. 6.8 and 6.9, the amount of UiO-66 crystals was observed to increase following the two-step growth method as their distribution was observed on the surface and within the macropores of the GF network. The graphene crystalline phase (0 0 2) was observed on the PXRD pattern of the GF/UiO-66 composite (Fig. 6.9) with little evidence of the Ni crystalline peaks at $2\theta \approx 45^{o}$, further demonstrating the etching of Ni under the UiO-66 synthesis conditions. In Fig. 6.8, the UiO-66 crystals were also observed to have relatively well-defined octahedral shapes with sizes around 100 nm. The observed results in Fig. 6.8 could suggest the two-step growth of UiO-66 onto GF could have facilitated a seed-mediated UiO-66 growth mechanism whereby the small UiO-66 crystals could have been nucleation sites that initiate crystal growth [231]. In that manner it would be possible that some crystals would grow bigger in size compared to crystals growing out of solution. The results in Fig. 6.8 indicated that seed-mediated growth onto defective graphene foam, achieved through the two-step UiO-66 growth method, could result not only in increasing the MOF content on GF, but also in improving the formation of crystals with well-defined shapes and sizes.

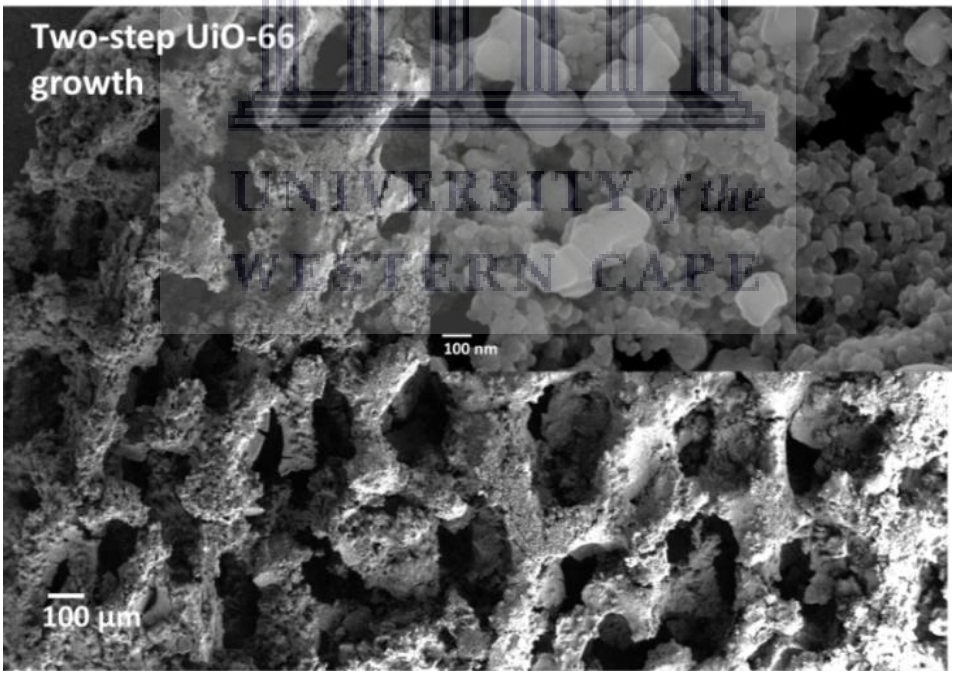

Figure 6.8: SEM images of GF/UiO-66 obtained for the two-step growth of UiO-66 crystals. Insert is a close up image (at 50 000 X magnification).

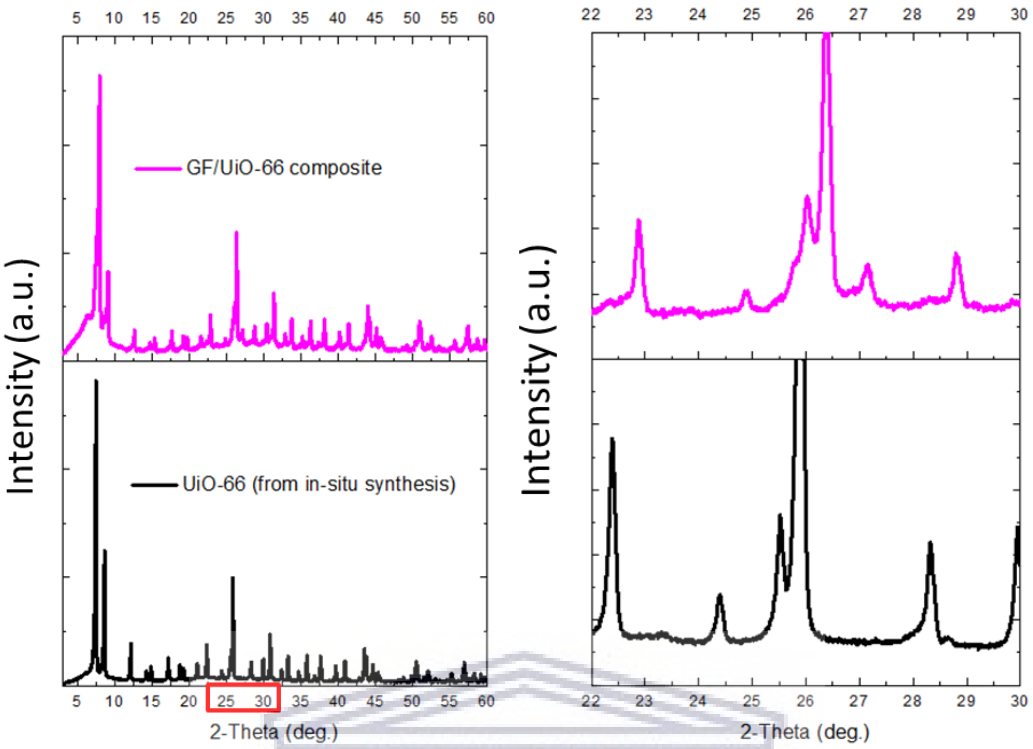

Figure 6.9: PXRD patterns for pristine UiO-66 and GF/UiO-66 obtained for the two-step growth method. The area marked red highlights the 2Θ range from 22° to 30°.

In Fig. 6.10, the N_2 adsorption isotherms for both GF/UiO-66 composites prepared by single-step and two-step growth showed Type I adsorption with little evidence of hysteresis observed. This demonstrated that the UiO-66 could be the main contributing component in the N_2 adsorption properties of GF/UiO-66 composites. In Table 6.1, the BET surface area of the GF/UiO-66 obtained via single-step growth was 48 % that of pristine UiO-66 powder, whilst the two-step grown GF/UiO-66 showed a 78 % BET surface area to that of pristine UiO-66. The results showed a 30 % increase in BET surface area owing to the two-step growth method of UiO-66 onto the surface of possibly defective graphene foam. On careful inspection of the two patterns, it can be seen that there is a shift towards higher Bragg peak positions in the UiO-66/GF composite. This may suggest that there is a chemical interaction between the GF and the UiO-66 crystals. It could be possible that during the single-step crystal growth, some of the UiO-66 were anchored and possibly nucleated from the GF defects.

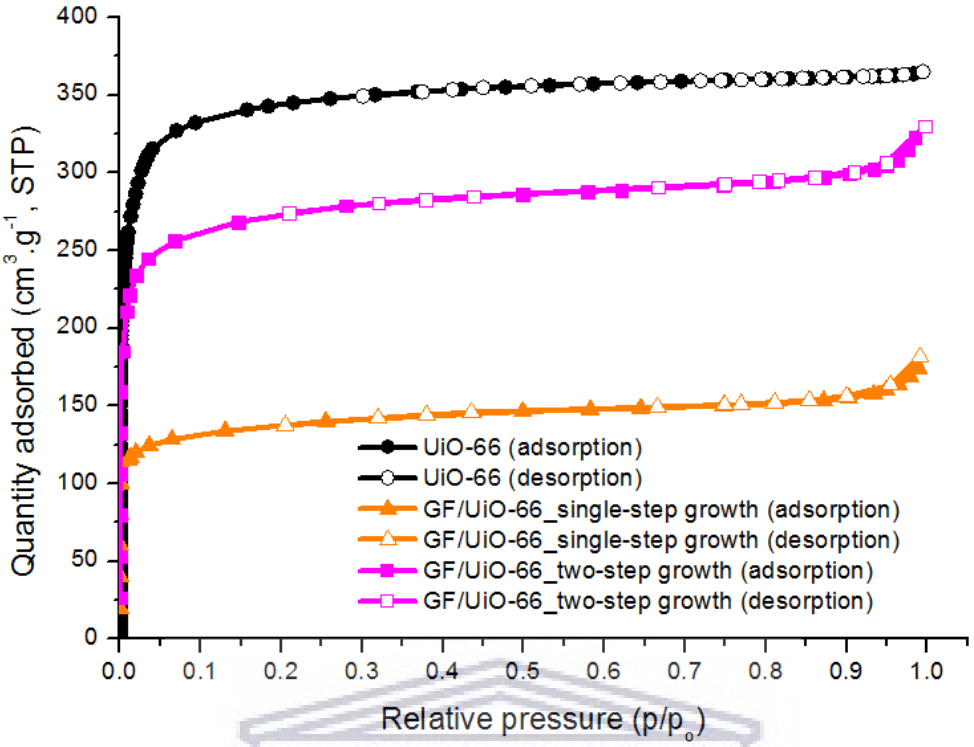

Figure 6.10: N_2 adsorption/desorption isotherms obtained for UiO-66 powder and GF/UiO-66 composites prepared via in-situ UiO-66 growth onto GF.

Table 6.1: Summary of the BET report obtained for GF/UiO-66 composites prepared via in-situ UiO-66 growth onto GF.

Isotherm property	**Sample**		
	UiO-66 powder[a]	**GF/UiO-66_single-step growth**	**GF/UiO-66_two-step growth**
BET surface area ($m^2.g^{-1}$)[b]	1376	665	1073
NLDFT pore volume ($cm^3.g^{-1}$)[b]	-	-	-
Slope ($g.cm^{-3}$, STP)	0.000456	0.00830	0.004175
Y-intercept ($g.cm^{-3}$, STP)	0.000001	0.000002	0.000002
Q_m ($cm^3.g^{-1}$, STP)	310	120	239
Correlation coefficient	0.9999	0.9999	0.9998

[a]Residual UiO-66 not incorporated onto the surface of GF during in-situ synthesis.

[b]Pore volume measurements were not obtained due to instrument limitations at the time of measurement.

The H_2 adsorption measurements for the GF/UiO-66 composites were obtained at 77 K and up to a pressure of 1.2 bar due to instrumental restrictions at the time of experimentation. Since

the density of H_2 is about 3.8 x 10^{-4} g·mL^{-1}, the excess H_2 uptake relatively equals the total/absolute H_2 uptake under these conditions. In Fig. 6.11 and Table 6.2, the H_2 uptake of single-step GF/UiO-66 was 60% that of pristine UiO-66 and the two-step GF/UiO-66 was 73% in comparison. The H_2 uptake results showed correlation to the observed BET surface areas as would be expected based on the Chahine rule [209]. The BET surface area and H_2 uptake observed for single-step GF/UiO-66 was surprisingly higher than suggested by the amount of UiO-66 observable on the GF surface in Fig. 6.6 and 6.7. This could suggest that the GF surface could have contributed to the adsorption of both N_2 and H_2. Indeed graphene sheets are well known for their extensive surface area with a theoretical BET surface area of about 2600 m^2·g^{-1}. Although single layered graphene does not contain a permanent porous structure in its pristine form, porosity can possibly be introduced into graphene sheets through methods involving removal of carbon rings from its structure and in most cases through compositing with other additives [75,188,230]. It is, therefore, possible that the compositing of GF with UiO-66 coupled to the potentially high surface area of GF could contribute to H_2 uptake values greater than 50% to that obtained onto UiO-66.

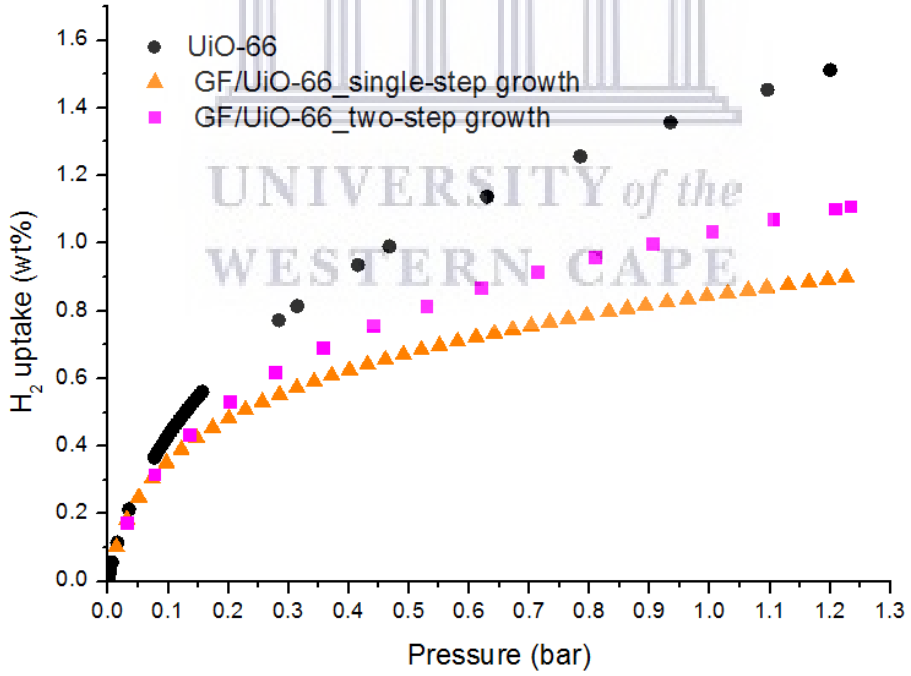

Figure 6.11: H_2 adsorption isotherms obtained for UiO-66 powder and GF/UiO-66 composites prepared via in-situ growth of UiO-66 onto GF.

Table 6.2: H_2 uptake at 77 K up to 1.2 bar obtained for UiO-66 powder and GF/UiO-66 composites prepared via in-situ UiO-66 growth using a single-step and two-step growth method.

Sample	**Maximum excess Uptake (wt%)**	**Total gravimetric uptake (wt%)**
UiO-66 powder	1.5	1.5
GF/UiO-66_single-step growth	0.9	0.9
GF/UiO-66_two-step growth	1.1	1.1

The main objective for the preparation of GF/UiO-66 composites was to possibly obtain an improved thermal conductivity in the GF/UiO-66 composite in comparison to pristine UiO-66 powder. In Table 6.3 and Fig. 6.12, the thermal conductivity of GF/UiO-66 was 8 % less than that of UiO-66 powder and an astounding 53 % less compared to that of UiO-66 pellet. Since graphene is known to exhibit one of the highest thermal conductivities recorded thus far, the significantly low experimental thermal conductivity could be explainable through consideration of the properties of the selected materials. As it was shown in Chapter 4, UiO-66 is a highly microporous MOF containing about 90 % micropores in its structure.

The GF, on the other hand, was shown to contain large macropores within which UiO-66 could be grown, however the connectivity of the GF network was observably disrupted due to breakages upon UiO-66 growth via the two-step method, as shown in Fig 6.8. The thermal conductivity is known to be lower in porous compared to non-porous solid-state materials, which was also observed in Table 6.3 as the Pyrex standard had more than 10 times the thermal conductivity of the UiO-66 pellet. In a porous powder material, there exists free-flow of air molecules within void spaces between powder particles and also through the internal pores, which greatly compromise the thermal conductivity of the material. The size of pores may also play a key factor as it has been shown that microporous solids tend to show higher thermal conductivities in comparison to meso- and macroporous materials [43,44,232]. The aforementioned observations made in literature may, therefore, provide justification to the observed experimental results since GF was found to contain a macroporous network structure compared to the highly microporous UiO-66.

The pelletization could also aid in reducing void spaces through densification of the UiO-66 crystals and hence improve the thermal conductivity of the material [52].

Table 6.3: Experimental values for thermal conductivities obtained for UiO-66 powder, pelletized UiO-66, and GF/UiO-66 composite. A Pyrex polymer block was used as a standard.

Measured thermal conductivity (W/mK)	**Sample**			
	Pyrex reference	**UiO-66 powder**	**GF/UiO-66**	**UiO-66 pellet**
1	1.175	0.0787	0.0709	0.1482
2	1.161	0.0771	0.0706	0.1478
3	1.151	0.0767	0.0710	0.1487
4	1.148	0.0767	0.0706	0.1489
5	1.153	0.0767	0.0703	0.1496
6	1.148	0.0766	0.0704	0.1492
7	1.149	0.0768	0.0705	0.1489
8	1.146	0.0763	0.0702	0.1488
9	1.146	0.0766	0.0707	0.1494
10	1.154	0.0762	0.0703	0.1492
Average	**1.153**	**0.0768**	**0.0705**	**0.1489**
Standard deviation (W/mK)	0.00895	0.000678	0.0002380	0.000559

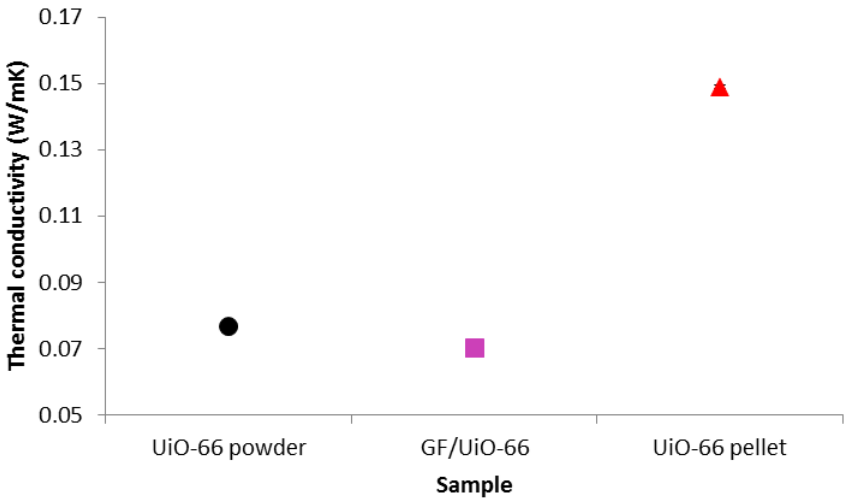

Figure 6.12: Comparison of the average thermal conductivities obtained for UiO-66 powder, UiO-66 pellet, and GF/UiO-66 composite (two-step growth).

6.2. Pelletization of UiO-66 with 5 wt% polymer binders

The pelletization of UiO-66 without binders was done to investigate the response of UiO-66 towards applied pressure up to ~700 MPa, which was unprecedented in MOFs (Chapter 4). This section reports on the co-pelletization of UiO-66 with 5 wt% binder at ~700 MPa. The addition of binders in the shaping of MOF powders has been a proven practice towards the improvement of their structural properties such as stability towards a "drop test", physical abrasion, or stability towards mechanical damage [46]. It is, however, important that the inclusion of binders contribute positively without significantly compromising the intrinsic properties of the MOF. In H_2 storage applications, MOFs are heavily dependent on their textural properties (surface area and porosity) as H_2 adsorption occurs in them via the physisorption mechanism and also the Chahine rule shows a strong correlation of the BET surface area of a MOF to its gravimetric H_2 capacity [209]. The shaping of MOFs with the inclusion of polymer-based binders has been shown to lead to significant reductions in the MOF textural properties. Some of the contributing factors include the non-porous nature of the binder, and pore blocking (seen as a reduced pore volume in MOF/binder composites compared to MOF) [34,80,114,116]. In H_2 storage applications, it is also important not to consider only the storage capacity of the material, but also the working/deliverable capacity is a key factor [36,151,197,233]. Given that non-porous polymers can be fabricated into fiber networks and composited with porous powder materials, e.g. via electrospinning, there exists an opportunity to develop MOF/polymer composites containing hierarchical pore structures. Materials with

hierarchical porosity have been shown to have better suitability towards H_2 storage in comparison to porous materials that exhibit Type I H_2 adsorption isotherms [15,39,63,125]. This is because hierarchical porosity in materials could have the potential to show low H_2 uptake at low pressure, i.e. $P \leq 5$ bar, and high adsorption at intermediate to high pressure, so as to obtain a large positive working/deliverable H_2 capacity. The problem in purely Type I materials is that the highest H_2 adsorption occurs at low pressure and little adsorption is observable at intermediate to high pressure and hence they tend to have low working/deliverable H_2 capacities [151]. This was also observed on the H_2 adsorption isotherms of UiO-66 powder in Chapter 4 of this study.

In this section the study proposed the co-pelletization of UiO-66 with nanofibers forming a layered pellet of alternating UiO-66 powder and polymer nanofibers (see Fig. 3.6). In Fig. 6.13 and 6.14 the structure of UiO-66 containing nanofiber binders clearly showed successful incorporation of nanofiber binders into UiO-66 through co-pelletization, and also the alternating structure was maintained even after breaking the pellet.

Figure 6.13: Photo images showing the cross-section of co-pelletized UiO-66 containing 5 wt% PIM-1 nanofibers.

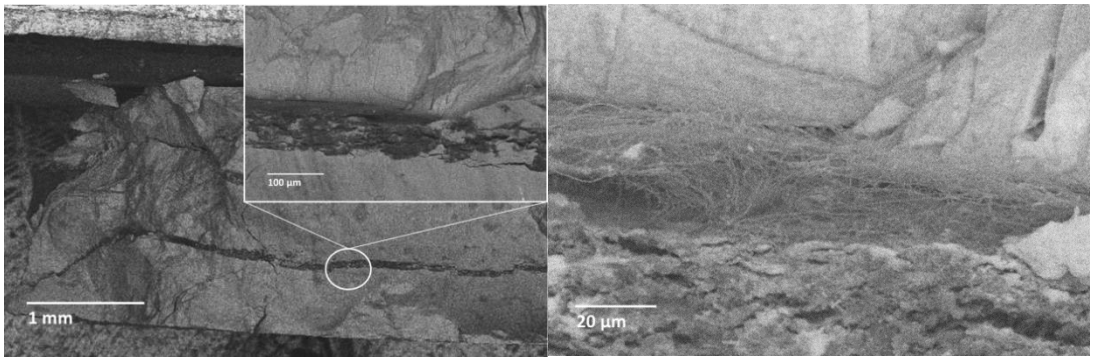

Figure 6.14: SEM images showing the cross-section of co-pelletized UiO-66 containing 5 wt% PIM-1 nanofibers.

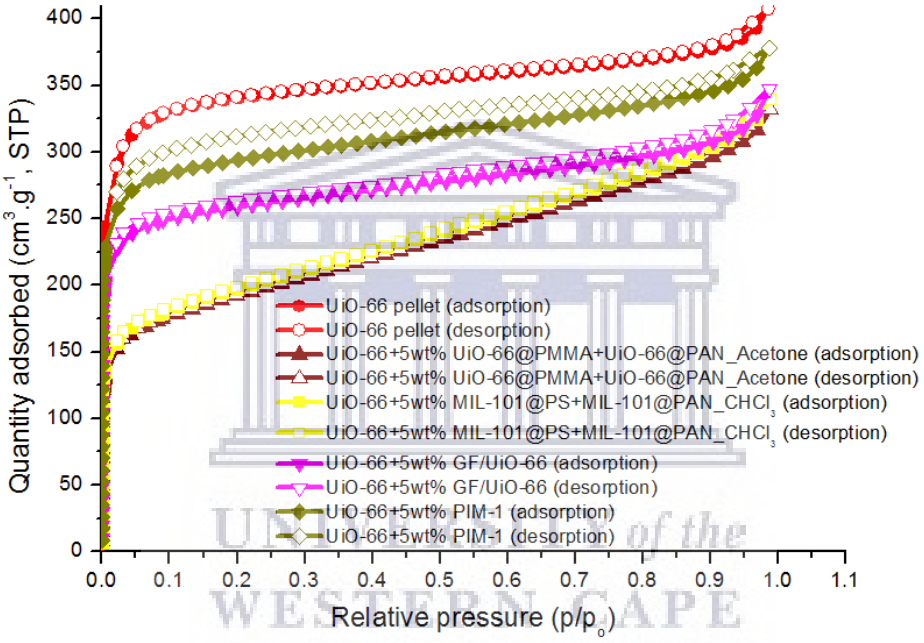

Figure 6.15: N_2 adsorption/desorption isotherms obtained for co-pelletized UiO-66 containing 5 wt% UiO-66/PMMA@UiO-66/PAN-Acetone and PIM-1 nanofibers as binders.

Since all the materials used in this section were fully characterized in Chapters 4 and 5, the main focus of this section was on the textural properties and H_2 adsorption behaviour of the UiO-66/binder composites. In Fig. 6.15 and 6.16, the isotherms for UiO-66 containing core-shell PAN nanofibers was found to be a combination of Type I and Type II isotherms. The Type I adsorption was observed due to the high adsorption at low relative pressure, with the Type II portion of the isotherm observable at increasing relative pressure towards $p/p_o = 1$. In the pore size distribution curves (Fig. 6.16)the UiO-66 pellets containing core-shell PAN nanofibers were found to consist of a high mesopore content, around 50 Å, which was not observable in the pore size distribution of the pristine UiO-66 pellet. The N_2 adsorption

properties of UiO-66 pellet containing GF/UiO-66 as a binder were found to closely resemble those of pristine UiO-66 pellet, as it was previously shown for their powdered counterparts (Fig. 6.10). The N_2 adsorption isotherm for the UiO-66 pellet containing PIM-1 nanofibers was found to show largely Type I adsorption. Also in the pore size distribution curves, the pore sizes around 6 and 7 Å were observed to increase in volume possibly due to the presence of PIM-1, which also was shown to have pores with 6 and 7 Å diameters (Fig. 5.5, Chapter 5). In Fig. 6.16, the UiO-66+PIM-1 pellet was also found to have a significant peak at a pore width of 50 Å, although to a lesser extent in comparison to the UiO-66+core-shell PAN composites. The proposed presence of mesopores indicated the possibility of introducing a hierarchical pore structure in a predominantly microporous material, such as to change its adsorption behaviour to resemble a combination of Type I and Type II adsorption instead of purely Type I adsorption. It was important to note that the mesopores around 50 Å were not observable on the as-spun or as-prepared nanofibers (Chapter 5, Fig. 5.5, 5.26, and 5.32). This suggested that the co-pelletization of the nanofibers with UiO-66 could have induced the formation of the mesopores.

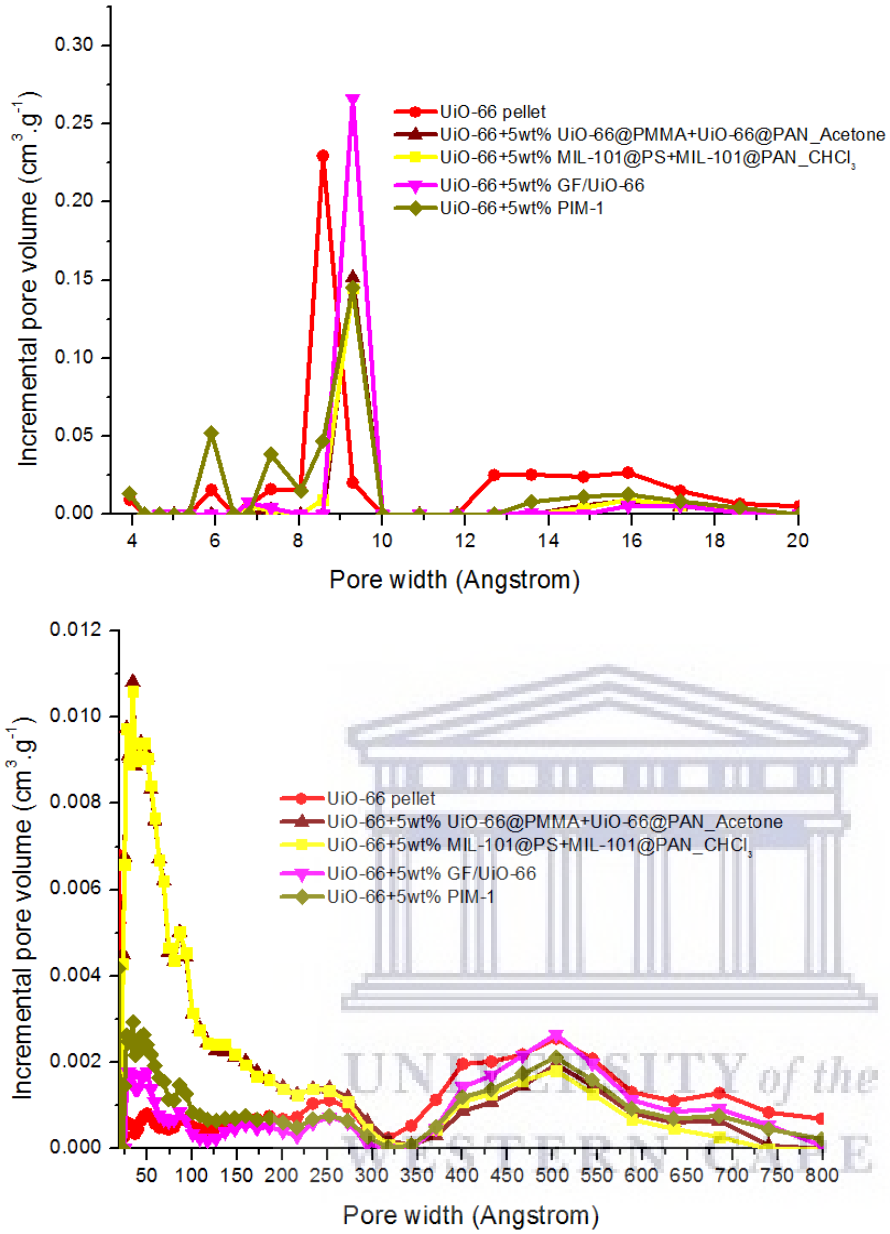

Figure 6.16: Pore size distribution curves obtained for co-pelletized UiO-66 containing 5 wt% UiO-66/PMMA@UiO-66/PAN-Acetone and PIM-1 nanofibers as binders.

In Table 6.4, the BET surface areas of the UiO-66 pellet containing MOF/PAN nanofibers was 46% less in comparison to the pristine UiO-66 pellet. The total pore volumes, however, were found to only be about 13% lower compared to that of the pristine UiO-66 pellet. The micropore surface area and micropore volumes were 68% lower compared to that of the pristine UiO-66 pellet. In addition, the micropore volumes of UiO-66 pellet containing core-shell MOF/PAN nanofibers were found to constitute about 27% of their total pore volumes and the micropore surface area contributing about 50% of their BET surface areas. The results, therefore, showed that about 70% of the total pore volume and 50% of BET surface area of the

UiO-66 pellets containing MOF/PAN nanofibers were not contributed by the micropores in the composites. In Fig. 6.16, it was observed that these pellets consisted of a significant amount of mesopores, possibly induced after the co-pelletization of UiO-66 with the MOF/PAN nanaofibers. The results suggested a possible micro-mesoporous hierarchical structure created upon co-pelletization at ~700MPa.

Table 6.4: Summary of the BET report obtained for pelletized UiO-66 containing 5 wt% binders.

Isotherm property	**Sample**				
	UiO-66 pellet	**UiO-66+PIM-1**	**UiO-66+ 5wt% [UiO-66/PMMA+UiO-66/PAN_Acetone]**	**UiO-66+ 5wt% [MIL-101/PS+MIL-101/PAN]**	**UiO-66+ 5wt% [GF/UiO-66]**
BET surface area ($m^2.g^{-1}$)[a]	1300 (1091)	1113 (902)	702 (350)	723 (370)	985 (788)
NLDFT pore volume ($cm^3.g^{-1}$)[b]	0.60 (0.44)	0.59 (0.36)	0.52 (0.14)	0.53 (0.15)	0.54 (0.32)
Slope ($g.cm^{-3}$, STP)	0.003347	0.003915	0.00619	0.00601	0.004459
Y-intercept ($g.cm^{-3}$, STP)	0.00001	0.0000003	0.00001	0.000009	-0.000004
Q_m ($cm^3.g^{-1}$, STP)	299	256	161	166	225
Correlation coefficient	0.99996	0.9999	0.9999	0.9999	0.9999

[a]values in parentheses are given for the t-plot micropore surface area; [b]values in parentheses are given for the t-plot micropore volume.

The results in Table 6.4 also showed that the UiO-66 pellet containing PIM-1 nanofibers retained in excess of 80% BET surface area, micropore surface area, and micropore volume in comparison to those originally obtained for the pristine UiO-66 pellet. The total pore volume was found to be 98% of the total pore volume of the pristine UiO-66 pellet. Within the UiO-66 pellet containing PIM-1 nanofibers, the micropore volume was 61% of the total pore volume, whereas in the pristine UiO-66 pellet the micropore volume was 73% of the total pore volume. The lower micropore contribution in UiO-66+PIM-1 could have been due to the presence of a small but significant amount of mesopores as shown in Fig. 6.16. The incorporation of GF/UiO-66 as a binder was found to follow a similar trend as the nanofibers, however, the micropore surface area of 80% relative to its BET surface area showed a resemblance of the UiO-66

component being the main contributing factor in the textural properties, as it was previously shown in section 6.1.

The implications of changing the adsorption properties of UiO-66 from Type I to potentially a combination of Type I and Type II could have had a direct effect on the H_2 adsorption behaviour. In this study, it was possible to only measure the high-pressure H_2 adsorption of two of the UiO-66+binder composites and hence the composites giving the highest and the lowest BET surface areas and pore volumes were selected for analysis, namely the pellets of UiO-66+ 5wt% PIM-1 and UiO-66+ 5wt%UiO-66/PMMA+UiO-66/PAN.

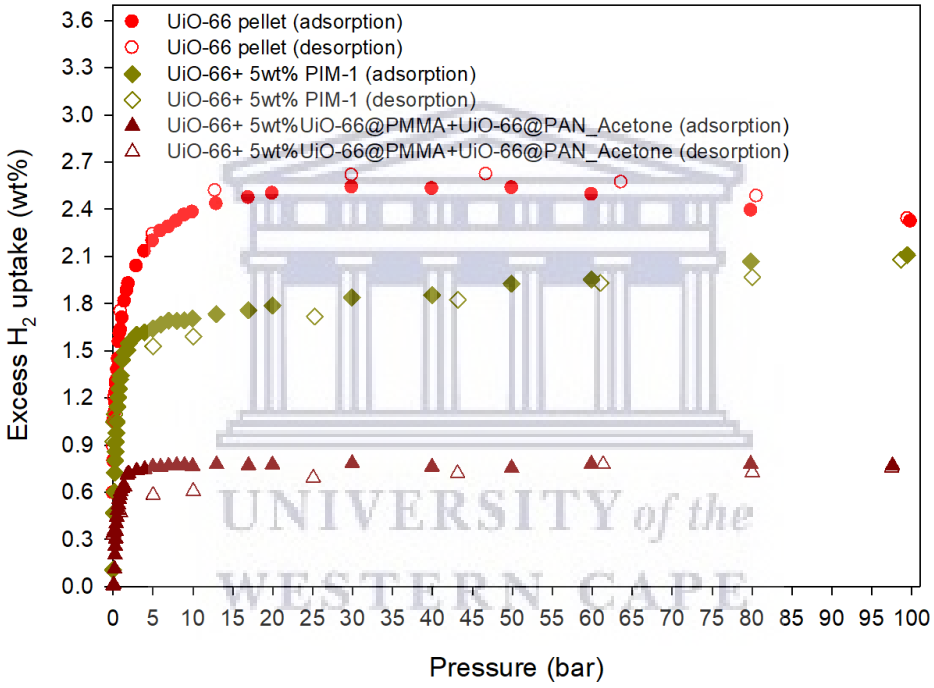

Figure 6.17: Excess H_2 uptake isotherms obtained for pristine UiO-66 pellet and UiO-66 pellets containing 5 wt% PIM-1 and 5 wt% UiO-66/PMMA@UiO-66/PAN-Acetone nanofibers.

The excess H_2 adsorption isotherms (Fig. 6.17) showed a similar trend as observed in Fig. 6.15 and Table 6.4, whereby excess H_2 uptake correlated to the BET surface areas of the materials, an expectation based on the Chahine rule [234]. The results in Fig. 6.18 showed that the observed trend in the excess H_2 uptake isotherms was also translated in the total/absolute H_2 uptake isotherms. Interestingly, it was observable that the low-pressure ($P \leq 5$ bar) H_2 uptake in UiO-66 pellets with binders (PIM-1 and core-shell UiO-66/PAN nanofibers) was significantly lower in comparison to that of the pristine UiO-66 pellet. At high pressures,

however, the H_2 uptake of the UiO-66+PIM-1 composite was about 93% to that of the pristine UiO-66 pellet at 100 bar. This showed that the working/deliverable H_2 capacity could be improved in UiO-66+PIM-1 beyond that of the pristine UiO-66 pellet. Indeed in Table 6.5, it can be seen that the calculated working/deliverable H_2 capacity for UiO-66+PIM-1 was 2.3 wt% in comparison to the 1.9 wt% obtained for the pristine UiO-66 pellet. The working/deliverable H_2 capacity of the UiO-66 pellet containing core-shell UiO-66/PAN nanofibers was only 16% less than that of the pristine UiO-66 pellet, even though the composite was shown to have a BET surface area that 46% lower. The observed results could be attributed to the extended pore structure that was demonstrated in the UiO-66 pellets containing the nanofibers as binders. The possible creation of micro-mesoporous hierarchical pore structure could be key in changing the H_2 adsorption behaviour of materials with typically Type I adsorption.

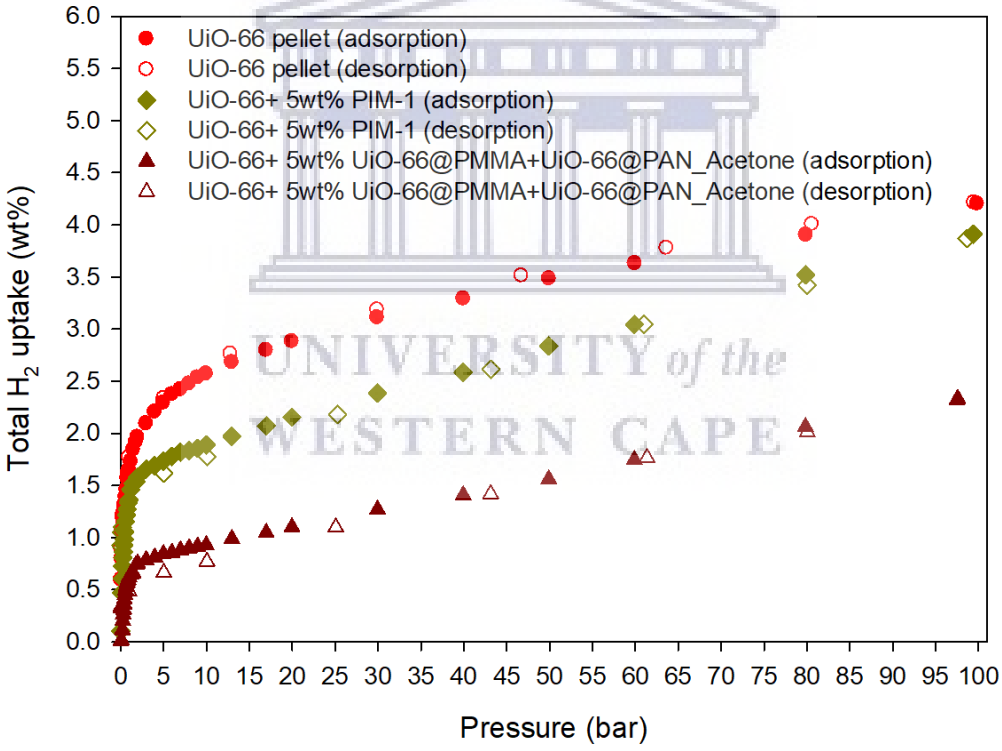

Figure 6.18: Total/absolute H_2 uptake isotherms obtained for pristine UiO-66 pellet, and UiO-66 pellets containing 5 wt% PIM-1 and 5 wt% UiO-66/PMMA@UiO-66PAN nanofibers.

Indeed it has been shown on MOF-derived carbons that the presence of a pore structure consisting of micropores, mesopores, and in some cases macropores, shows more suitability towards H_2 storage applications taking into account the importance of obtaining considerably high working/deliverable H_2 capacities.

Table 6.5: H_2 uptake at 77 K up to 100 bar obtained for PIM-1, UiO-66/PMMA@UiO-66/PAN-Acetone, and MIL-101/PS@MIL-101/PAN-$CHCl_3$ nanofibers.

Sample	Maximum excess Uptake (wt%)	Total/absolute gravimetric H_2 uptake (wt%)[a]		Working capacity (wt%)[b]
		5 bar	100 bar	
UiO-66 pellet	2.5	2.3	4.2	1.9
UiO-66+ 5wt% PIM-1	2.1	1.6	3.9	2.3
UiO-66+ 5wt% UiO-66/PMMA+UiO-66/PAN	0.8	0.7	2.3	1.6

[a]Values calculated using eqn 3.3 in chapter 3 (section 3.4.5.2). [b]Values calculated from the difference between total H_2 uptake at 100 bar (adsorption) and 5 bar (desorption).

6.3. Chapter summary

This chapter firstly reported on the preparation of a graphene foam (GF)/UiO-66 composite which was anticipated to possibly show improved thermal conductivities compared to pristine UiO-66 powder. The synthesis of GF was successfully achieved through the use of the carbon vapour deposition (CVD) method, using nickel foam (NF) as a template. Since H_2 adsorption/storage in porous materials is known to be sensitive to the material's textural properties, it was important to exploit the GF surface as a potential substrate to grow UiO-66 crystals via an in-situ synthesis process. This was done to obtain a GF/UiO-66 composite with surface areas and pore volumes close to those of pristine UiO-66 powder *and* with possibly improved thermal conductivity than pristine UiO-66. The two methods that were employed for the in-situ synthesis of UiO-66 included a single-step growth method which grew UiO-66 crystals directly onto the GF surface, and secondly a two-step growth method which made use of a seed-mediated approach. The two-step growth method not only improved the UiO-66 loading onto GF from about 50 wt% to 85 wt%, and improved the BET surface area by 38%, but also proved critical in growing UiO-66 crystals with well-defined shapes and sizes. However, the thermal conductivity of the GF/UiO-66 composite was compromised relative to UiO-66. The growth of MOF crystals was previously shown to be more inhibited onto graphene and graphite carbons due to the presence of defects on their surfaces. As a result, MOFs grown onto graphene/graphite surfaces were found to exhibit distorted crystal structures. This study

showed a two-step approach that could be used to grow UiO-66 crystals onto graphene with relatively pure phases.

The second part of this chapter reported on the incorporation of polymer nanofiber binders into UiO-66 via co-pelletization to form pellets consisting of layers of alternating UiO-66 and nanofiber binders. This approach of incorporating polymeric nanofiber binders through pelletization was found to possibly play a key role in introducing mesopores to the otherwise highly microporous UiO-66. The possible creation of mesopores could only be attributed to the layered pelletization strategy since no mesopores could be observed on the nanofibers in their as-prepared forms (i.e. prior to pelletization with UiO-66, see Chapter 5). The possible creation of hierarchical porosity in MOF-based composites, achieved through layering nanofibers into MOF pellets, is a new concept and could present new opportunities towards the development of MOF materials with high working/deliverable H_2 capacities.

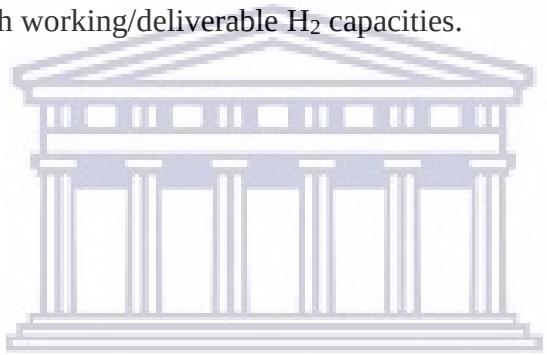

Chapter 7

7. Conclusions and recommendations

This chapter highlights the key conclusions and recommendations that were extracted based on the results obtained in this study. This chapter draws attention to the results obtained in this study which were comparable to those previously reported in similar studies pertaining to pelletization of MOFs, electrospinning of MOF/polymer nanofibers, and in the application of polymer-based materials as binders in MOF compaction. The main emphasis was on the gravimetric and volumetric H_2 capacities, thermal conductivity, and H_2 working/deliverable capacities of the materials.

7.1. Conclusions

The aim of the study was to fabricate MOF-based materials with application-specific properties tailored towards H_2 storage applications. The application of porous materials into H_2 storage systems is mostly envisaged on their use in combination with high-pressure cylinders [20,36,152]. Due to the poor packing of powdered materials in cylinders, it has become imperative that focus should be shifted towards investigating the properties of interest required in H_2 storage systems such as, thermal conductivity, gravimetric and volumetric H_2 capacities, and working/deliverable H_2 capacities, on shaped forms of the porous materials instead of their as-synthesized powder forms [15]. Shaping of powdered MOFs and porous carbons, through pelletization, has previously been shown to be successful in improving their packing densities, which in turn resulted in the improvement of their volumetric H_2 capacities. The main negative effect of pelletization was reported to be the compromise of the textural properties of MOFs mainly through pressure-induced structural changes that may include pore widening or structural collapse of the MOF framework. Since the gravimetric H_2 capacity is shown to be directly proportional to the BET surface area of the MOF, via the Chahine rule, any compromise to the textural properties could effectively lead to the compromise of the gravimetric H_2 capacity of the MOF material. This means that in most reported results for MOFs, the improvement of the volumetric H_2 capacity through pelletization has almost always been accompanied by significant reductions in the MOF's gravimetric H_2 capacity. Such

observations have been reported for a wide variety of MOF structures such as in MOF-5, MIL-101(Cr), MIL-101(Fe), and many more, but seldom have the applied pelletization pressures exceeded 500 MPa [34,45,57,116,154,156,205,226,235]. The pelletization of UiO-66 has also been reported where the packing density was improved with little compromise to its textural properties, however, the study was only done up to a pressure of 10 000 psi (equivalent to ~70 MPa) [65], a pressure 10 times less than reported in this study.

In this study, the effect of pelletization was investigated on two MOFs, UiO-66 and MIL-101(Cr), where the applied pressures were up to ~700 MPa. Prior to their pelletization, the textural properties of the MOFs (surface area and pore volume) were initially optimized in order to achieve the highest possible BET surface area and pore volumes under acid-modulated solvothermal synthesis conditions. In the synthesis of MIL-101(Cr) it was found that a BET surface area of about 3300 $m^2 \cdot g^{-1}$ and pore volume of 2.0 $cm^3 \cdot g^{-1}$ were achievable using a 1:1:100 molar equivalent $CrCl_3.6H_2O$:H_2BDC:CH_2O_2 (chromium chloride hexahydrate: terephthalic acid: formic acid) mixture dissolved in deionised water and synthesized under high pressure conditions at 210 °C for 8 hours. The MIL-101(Cr) was found to contain a high degree of mesopores, with only an 8% micropore content, and showed typical Type IV N_2 adsorption/desorption isotherms. Under the same conditions, however, lower values for BET surface area and pore volume could also be obtained owing to the possible co-crystallization of MIL-53(Cr) in subsequent batches. The presence of MIL-53(Cr) crystals was observed from SEM images which showed the appearance of elongated and multifaceted needle-like crystals which could not be removed through washing with dimethylformamide (DMF) and also through increased micropore content up to 23%, coupled to 40% reductions in the BET surface areas of subsequent batches. The main reason for the co-crystallization of MIL-53(Cr) could possibly have been the use of a multi-batch system for the synthesis of MIL-101(Cr) which could promote seed-mediated crystal growth of MIL-53(Cr) from MIL-101(Cr) seed crystals left over on the walls of the reactor/Teflon lining. In the pelletization of MIL-101(Cr) at ~700 MPa, it was observable through powder X-ray diffraction (PXRD) analysis that there were possible changes to its structure as there were observable strain/stress introduced within its crystal lattice, a phenomenon also reported in literature [104]. This study further showed that the strain/stress could have been more significant on the micropores of MIL-101(Cr) since the micropore volume was reduced from 8% of the total pore volume in MIL-101(Cr) powder (15% micropore surface area of the BET surface area) to 4% in MIL-101(Cr) pellet (8% micropore surface area of the BET surface area). The compromise to the textural properties of

MIL-101(Cr) were also found to be translatable to its gravimetric H_2 capacity and gravimetric H_2 working capacity as both were found to be reduced post-pelletization by ~30% and ~40%, respectively. The volumetric H_2 capacity of MIL-101(Cr) powder, at 77 K and 100 bar, was found to be 30% less in comparison to the theoretical volumetric H_2 density of a pressurized H_2 cylinder containing no adsorbent material. Upon pelletization, the packing density increased from 0.19 to 1.20 $g{\cdot}cm^{-3}$ translating to an increase in the volumetric H_2 capacity four times to that of the MIL-101(Cr) powder and three times the theoretical volumetric H_2 density in a pressurized H_2 cylinder at 77 K and 100 bar. After pelletization, the volumetric H_2 working capacity also improved from 15 $g{\cdot}L^{-1}$ to 57 $g{\cdot}L^{-1}$, which was 97 % higher in comparison to the volumetric H_2 working capacity of a pressurized H_2 cylinder. In this study, the pelletization of MIL-101(Cr) did show reduced textural properties and a reduced gravimetric H_2 capacity as previously shown in reported literature, but importantly, the results showed that MIL-101(Cr) could be pelletized at ~700 MPa without possibly collapsing its crystal structure. In addition, the achievable volumetric H_2 capacity, after pelletization, and its subsequent volumetric H_2 working capacity could be in excess of ~300% higher for MIL-101(Cr) pellets in comparison to powdered MIL-101(Cr). The pelletization of MIL-101(Cr) at ~700 MPa, without its amorphization, could possibly have positive implications for MOFs with high structural stabilities to attain even better results compared to MIL-101(Cr). One such robust MOF is the zirconium-based MOF, UiO-66, which has been reported to have a theoretical minimum shear modulus of at least 13.7 GPa [82]. In this study, the pelletization of UiO-66 was also investigated for H_2 storage applications under the same pelletization pressure applied to MIL-101(Cr).

The synthesis of UiO-66 did not require high-pressure conditions in order to grow well-defined UiO-66 crystal shapes and as a result it was found possible to synthesis batches of about 5 g using a reflux setup at 120 ^oC for 6 hours. The achievable BET surface areas were between 1400 to 1750 $m^2{\cdot}g^{-1}$ with total pore volumes of 0.60 to 0.96 $cm^3{\cdot}g^{-1}$. The values obtained in this study were amongst the highest experimentally determined BET surface areas and total pore volumes in comparison to previous studies [93,99,211,212]. This could be attributed to a variety of factors that were found to be key in the as-synthesized UiO-66 and after its post-synthesis treatment. Initially it was observed that using a solution containing 1:1:100 molar ratio of $ZrCl_4$:H_2BDC:CH_2O_2 (zicornium chloride: terephthalic acid: formic acid) at 120 ^oC and maintained for 6 hours, could have resulted in the synthesis of UiO-66 crystals with defects.

The use of monocarboxylic acids in UiO-66 synthesis has been shown to promote defect-formation through possible competing of the acid anions with the terephthalate linkers in solution. The defects can occur in different forms with missing linker defects being the most common to occur, however, missing nodes have also been reported as defects in UiO-66 [68,98,108,211,212,236,237]. A study by Shearer et al. [210] showed that the formation of defects in UiO-66 can result in additional crystal phases to be observed and using PXRD analysis showed that a symmetry forbidden crystal peak ($2\theta \sim 6^{o}$) could be the main sign of defect formation in UiO-66. Some studies made use of thermogravimetric analysis (TGA) to elucidate defect-formation in UiO-66 and showed that for an ideal UiO-66 crystal, a residue yield of 45 wt% could be expected for non-defective UiO-66 and any residue yield lower than 45 wt% would constitute at least one missing linker per cluster of UiO-66 [84,98].

The UiO-66 prepared in this study was confirmed to possibly have missing linkers through the observance of the symmetry forbidden crystalline peak at $2\theta \sim 6^{o}$ on all measured PXRD patterns for as-synthesized UiO-66. The TGA residue yields obtained after heating UiO-66 up to 1000 ^{o}C were all below 45 wt%, and in addition, on the pore size distribution curves of UiO-66 it was observed that there were pore sizes above 12 Å that would not be expected on a theoretically ideal crystal structure of UiO-66 [84,210]. It was also observed that the post-synthesis treatment of UiO-66 had major implications on the achievable BET surface areas and total pore volumes. The dehydroxylation of UiO-66, a process involving the removal of water molecules from $Zr_6O_4(OH)_4$ nodes to form Zr_6O_6 nodes [160,238], was confirmed to occur between 150 to 300 ^{o}C using thermogravimetric analysis coupled to mass spectroscopy data (TG-MS). Using Fourier transform infrared spectroscopy (FTIR) data, the possible removal of water molecules from zirconia nodes was also confirmed to occur up to 320 ^{o}C. This confirmed the previously reported existence of UiO-66 in two different forms, namely the hydroxylated and dehydroxylated forms. In this study, fully dehydroxylated UiO-66 could be obtained by heating UiO-66 under vacuum at 320 ^{o}C and partially dehydroxylated forms were obtainable between 150 to 290 ^{o}C. The textural properties of fully hydroxylated UiO-66 were measured on samples that were activated/degassed at 80 ^{o}C and compared to partially dehydroxylated forms after their activation at 200 and 290 ^{o}C and to the fully dehydroxylated form obtained after activation at 320 ^{o}C. The results showed that in the powdered form of UiO-66, hydroxylated UiO-66 obtained the highest BET surface areas and total pore volumes irrespective of the batches that were used in the measurements. Amongst the dehydroxylated

forms, at 200, 290, and 320 ºC, it was surprisingly found that the activation temperature did not show a direct relationship with the textural properties. The BET surface areas and pore volumes were found to follow a trend of UiO-66_{200} > UiO-66_{320} > UiO-66_{290}, meaning that the activation of UiO-66 at 290 ºC resulted in the lowest achievable textural properties. The result was unusual as it would be expected that removal of water molecules at 320 ºC to form fully dehydroxylated UiO-66 could possibly result in the lowest possible BET surface area and pore volume for UiO-66, as reported in other experimental studies of UiO-66 [107]. However, interestingly, the results corroborate the computational studies carried out by Vandichel et al. [72] and Rogge et. al [73] on the effect of the dehydroxylation process on the structure of UiO-66. It was reported in both studies that the UiO-66 framework could undergo structural rearrangements such that there could possibly exist two transition states at temperatures less than 300 ºC. It was further reported in both studies that the dehydroxylation process could possibly compromise the mechanical strength of UiO-66 such that partially dehydroxylated and fully dehydroxylated UiO-66 could show significantly reduced shear moduli in comparison to fully hydroxylated UiO-66.

In this study it was shown through PXRD analysis that the structure of UiO-66 indeed underwent changes upon its activation at 200, 290, and 320 ºC in comparison to the PXRD pattern obtained for hydroxylated UiO-66. Some of the diffraction peaks at 2θ ~ 6º, 10º, 11º and 12º were the most affected by the heat treatment. The diffraction peaks at 2θ ~ 6º, 10º, and 11º were not observable after activation at 290 ºC but could be observed after activation at 320 ºC. This observed difference in PXRD patterns could have been an indication of a possible rearrangement reaction as described in the work of Vandichel et al. [72]. Upon pelletization of hydroxylated and dehydroxylated UiO-66 forms at 700 MPa, it was found that the hydroxylated UiO-66 (activated at 80 ºC) retained at least 90% (up to 98%) of the BET surface area and at least 85% (up to 98%) of the pore volume obtained in its powder counterpart, irrespective of the batch that was measured. The pelletization of the dehydroxylated UiO-66 forms showed significantly compromised BET surface areas and pore volumes with the former not exceeding 300 $m^{2}{\cdot}g^{-1}$ (a reduction in excess of 50% in comparison to their powder counterparts). The pore volumes of the dehydroxylated forms followed the trend UiO-66_{200} > UiO-66_{320} > UiO-66_{290} indicated that the pore structure of UiO-66 after pelletization was also affected in a similar manner to that observed after heat treatment at increasing activation temperatures. The trends observed on the textural properties of hydroxylated and dehydroxylated UiO-66 were also

observed to be transferable to the H_2 adsorption behaviour of UiO-66. Hydroxylated UiO-66 obtained between 4.6 wt% to 5.0 wt%, which was the highest gravimetric H_2 capacity of the UiO-66 forms measured is this study at 77 K up to 100 bar. Remarkably, the gravimetric H_2 capacity for hydroxylated UiO-66 was not compromised upon pelletization at ~700 MPa, with the H_2 adsorption isotherms of both powdered and pelletized forms overlapping and showing virtually a total gravimetric H_2 capacity 100% retained at 100 bar. The volumetric H_2 capacity of hydroxylated UiO-66 powder was found to be 6% lower at 77 K and 100 bar in comparison to the theoretical volumetric H_2 density in a pressurized H_2 cylinder. The hydroxylated UiO-66 pellet showed a volumetric H_2 capacity about 155% higher in comparison to its powder counterpart *and* compared to the theoretical volumetric H_2 density in a pressurized H_2 cylinder. The volumetric H_2 working capacity was, however, found to be less in UiO-66 compared to a pressurized H_2 cylinder, possibly owing to the high microporosity of UiO-66 which typically affords it Type I adsorption isotherms that are characterized by high adsorption at low pressure ($P < 5$ bar) compared to relatively low adsorption at intermediate to high pressure ($P > 5$ bar). In this study, the improvement of the volumetric H_2 capacity without compromise in the gravimetric H_2 capacity was, for the first time, experimentally demonstrated in the pelletization of MOFs. Furthermore, such behaviour was reported in this study for the MOF pelletized at an unprecedented pressure of ~700 MPa.

Unlike the hydroxylated UiO-66, the pelletization of dehydroxylated UiO-66 forms showed gravimetric and volumetric H_2 capacities that were greatly compromised in comparison to their powder counterparts. Interestingly, it was found that the gravimetric and volumetric H_2 capacities of pelletized fully dehydroxylated UiO-66 (activated at 320 ^oC) was higher in comparison to the partially dehydroxylated forms pelletized after activation at 200 and 290 ^oC. The result suggested that the mechanical strength of the fully dehydroxylated UiO-66, although compromised compared to hydroxylated UiO-66, could have been restored to levels higher than the mechanical strengths of partially dehydroxylated UiO-66 forms. In the partially dehydroxylated UiO-66 forms it was also noticeable that the working H_2 capacities were zero, a sign of lower H_2 adsorption at high pressure in comparison to adsorption at low pressure. These observations could show that the partially dehydroxylated forms could have reached levels of saturation whereby the rate of H_2 desorption at high pressure far exceeded the H_2 adsorption rate. These results could be the first experimental demonstration for the possible existence of stable intermediate structures or transition states during the dehydroxylation of

UiO-66. The results on UiO-66 showed remarkable proof on the possibility of the dynamic temperature-dependent behaviour of UiO-66, however, the observed working H_2 capacities needed further optimization. Therefore, in this study, it was proposed that the incorporation of polymer-based binders could possibly create MOF/polymer composites with hierarchical pore structures which could likely show improved working H_2 capacities.

The preparation of polymer binders was based on the concept of electrospinning in order to obtain the polymers in their nanof iber forms. The polymers of interest were polyacrylonitrile (PAN) and the polymer of intri nsic microporosity-1 (PIM-1), with two complementary polymers, polystyrene (PS) and polymethylmethacrylate (PMMA). In previous studies, MOF/polymer nanofibers were successfully electrospun by single-nozzle electrospinning and shown to give higher BET surface areas in comparison to the pristine polymer nanofibers without MOFs. The textural properties of the MOF/polymer nanofibers showed significantly lower values compared to the pristine MOF powders [57,59,80,219,226]. Since MOFs are generally incorporated in nanofibers by physical attachment to the nanofiber surface, the MOF loading (amount/quantity of MOF in the composite with respect to the polymer) could possibly be increased by adding higher amounts of MOF powder into the polymer solution. In this study, however, it was shown that a MOF loading as low as 40 wt% was observed to compromise the morphology of the nanofibers showing severe formation of beads on the nanofiber surface. A 20 wt% MOF loading was found to be the highest possible to produce MOF@PAN nanofibers with negligible bead formation. In order to improve the MOF loading, this study proposed the use of a coaxial electrospinning method where two different polymer/MOF solutions could be electrospun silmutaneously to produce core-shell MOF/X@PAN (X = PS or PMMA) nanofibers. After the electrospinning, the core-shell nanofibers were treated in a solvent (acetone or chloroform) which would selectively remove "X", the polymer constituent in the core region of the nanofibers, without affecting the shell polymer and the MOF crystals. The results in this study showed through microstructural imaging (SEM and TEM), FTIR, and TGA data that the core region could be completely removed from core-shell X@PAN nanofibers using acetone or chloroform to remove PMMA or PS respectively. The resultant PAN nanofibers were, however, found to undergo significant shrinkage after the removal of the core polymer. Upon incorporation of MOFs to form MOF/X@PAN nanofibers, it was found that following the removal of "X", the remaining MOF/PAN nanofibers were ruptured along the length of the nanofibers such that the MOF crystals were exposed on the surface of the

nanofibers. It was, therefore, difficult to determine the MOF loading of the remaining MOF/PAN nanofibers. Regardless of the destructiveness of the removal technique, the textural properties of the core-shell MOF/PAN nanofibers were found to be higher in comparison to MOF/PAN nanofibers prepared by single-nozzle electrospinning and containing 20 wt% MOF loading. The core-shell UiO-66/PMMA@UiO-66/PAN and MIL-101/PS@MIL-101/PAN nanofibers were found to have total gravimetric H_2 capacities of 1.1 wt% and 1.7 wt%, respectively, at 77 K and 100 bar. The total gravimetric H_2 capacity of electrospun PIM-1 nanofibers was 2.7 wt% under the same conditions. Interestingly, the H_2 working capacity obtained in core-shell MIL-101/PS@MIL-101/PAN nanofibers was 0.9 wt% in comparison to the respective 0.1 wt% and 0.8 wt% obtained for UiO-66/PMMA@UiO-66/PAN and PIM-1 nanofibers. This was due to the highly microporous nature of UiO-66 and PIM-1 which were found to show more Type I adsorption isotherms. The possibility to change the adsorption behaviour of MOF-based materials from Type I to other adsorption types that show higher gas adsorption rates at pressures greater than 5 bar could possibly improve the working/deliverable H_2 capacity. In order to impart optimum application-specific properties onto UiO-66-based composite materials, the study proposed the incorporation of graphene foam (GF) as a carbon source that could impart an improved the thermal conductivity in comparison to that of pristine UiO-66.

The preparation of GF was done through chemical vapour deposition (CVD) using a nickel foam (NF) as a template. The GF was successfully synthesized using acetylene deposition gas at 1000 ^{o}C under an inert argon (Ar) atmosphere. The GF was found to retain the structure of the NF showing large macropores and synthesis of GF with a high degree of defects due to the presence of multilayers of graphene in the bulk composition of the GF. In previous studies, the growth of MOFs on the surface of defective graphite/graphene forms was observed to hinder the growth of well-defined MOF crystals and was shown to possibly lead to MOF crystals with distorted structures [146]. In this study, UiO-66 crystals were successfully grown on the surface of the GF product and using a two-step crystal growth method it was found that well-defined UiO-66 crystals were obtainable in comparison to growing UiO-66 directly on the surface of GF (via a single-step growth method). The use of a two-step crystal growth method was also found to improve the UiO-66 loading up to ~80 wt% with respect to the weight of GF in the GF/UiO-66 composite. The thermal conductivity was, however, found to be greatly influenced by the porosity of the materials compared to its chemical composition. The GF/UiO-66 composite was found to have the lowest thermal conductivity, 8% less in comparison to UiO-

66 powder and 53% less than pelletized UiO-66. The highly microporous structure of UiO-66 and extensive connectivity in its nodes could greatly contribute to a relatively moderate thermal conductivity in comparison to the more macroporous GF/UiO-66 composite.

The final part of the study was focused on incorporating polymer-based binders through co-pelletization with UiO-66 powder. The binders of choice were the PIM-1 nanofibers and core-shell MOF/X@PAN nanofibers. The adsorption behaviour of pristine UiO-66 pellet was the typical Type I adsorption isotherms for both N_2 adsorption/desorption and H_2 adsorption/desorption at 77 K. The incorporation of 5 wt% of the nanofibers was found to change the adsorption behaviour of the UiO-66 to a combination of Type I and Type II isotherms. This was attributed to the production of mesopores in co-pelletized UiO-66+ 5wt% nanofiber composites which was previously not observable in the pristine UiO-66 and MOF/PAN nanofibers prior to co-pelletization. The conversion to Type I/Type II adsorption behaviour meant that the co-pelletized UiO-66+nanofiber composites could obtain low H_2 adsorption at low pressure ($P < 5$ bar) and increased adsorption at higher pressures in comparison to the pristine UiO-66 pellet. As a result the total gravimetric H_2 capacity of pelletized UiO-66+PIM-1 composite was 3.9 wt% in comparison to 4.2 wt% obtained for pristine UiO-66 pellet, however, the gravimetric H_2 working capacity was 2.3 wt% and 1.9 wt%, respectively. Ultimately the pelletization of UiO-66 could possibly ensure the improvement of the volumetric H_2 capacity without greatly compromising its gravimetric H_2 capacity. In addition, the incorporation of electrospun nanofibers via co-pelletization with UiO-66 could form UiO-66/nanofiber composites with a hierarchical pore structure that could possibly improve the gravimetric H_2 working capacity of pelletized UiO-66.

This study was focused on the development of a UiO-66-based composite with application-specific properties for H_2 storage and it was evident from the results that the volumetric H_2 capacity of UiO-66 could be improved without compromise of its gravimetric H_2 capacity, a very rare case in MOFs pelletized at applied pressure above 500 MPa. In addition, the gravimetric H_2 working capacity was improved through the incorporation of nanofibers as binders through the creation of a hierarchical pore structure resulting from the co-pelletization method. The study showed that the porosity of a carbon-based material was a key factor that affected the thermal conductivity more than the chemical composition of the carbon. Lastly,

this study showed the possibility to introduce a hierarchical pore structure via a co-pelletization method of UiO-66 powder with 5 wt% electrospun nanofibers based on PIM-1 and PAN. The hierarchical pore structure was shown to be a key factor in changing the adsorption behaviour of a 95 wt% UiO-66 composite from Type I to a combination of Type I and Type II adsorption. This was found to ensure that the gravimetric H_2 working capacity would be further improved owing to the reduced H_2 uptake at pressures around 5 bar and below, without greatly reducing the H_2 uptake at 100 bar.

7.2. Recommendations

This study was successful in demonstrating the high mechanical stability of UiO-66 and how it could be exploited to improve the volumetric H_2 capacity, H_2 working capacity, and thermal conductivity of UiO-66 without compromising its gravimetric H_2 capacity. Some of the recommendations and future work that could be gained from this study are included in the following list:

i. Preparation of MIL-101@UiO-66 core-shell MOF composites. These have been shown to have higher gravimetric H_2 capacities in comparison to the individual MOFs (Ren *et al.*, 2014). Using the information from this study MIL-101@UiO-66 composites could possibly show improved volumetric H_2 capacity and H_2 working capacity in their pelletized forms, without any compromise to their original gravimetric H_2 capacity obtained in their powder counterparts.
ii. The post-synthesis heat treatment of UiO-66 should ideally involve a solvent exchange step prior to low-temperature activation/degassing (80 to 150 ^{o}C) in order to maintain UiO-66 in its mechanically robust hydroxylated form.
iii. Preparation of electrospun MOF/PIM-1 nanofibers that could possibly show higher BET surface areas and pore volumes in comparison to PIM-1 nanofibers. The co-pelletization of MOF/PIM-1 nanofibers with MOF powders could produce MOF/nanofiber pellets with hierarchical pore structures with even higher gravimetric H_2 capacities and H_2 working capacities compared to the pristine MOF pellet.
iv. The use of a two-step or multi-step crystal growth method onto graphene foam could be employed for any MOF types, with the focus directed at reducing the macroporosity of the graphene foam substrate so as to improve its thermal conductivity.

v. The use of coaxial electrospinning of PMMA@PAN and PS@PAN nanofibers was successfully employed to facilitate the selective removal of the core polymer (PMMA or PS) without affecting the PAN shell. The use of solvents was however found to be a destructive method. The use of irradiation to selectively remove PMMA and/or PS from core-shell PMMA@PAN and/or PS@PAN nanofibers could be an alternative method.

References

[1] H. Ritchie, M. Roser, Fossil fuels, Cited from: https://ourworldindata.org/fossil-fuels.

[2] A. Ahmed, Y. Liu, J. Purewal, L.D. Tran, A.G. Wong-Foy, M. Veenstra, A.J. Matzger, D.J. Siegel, Balancing gravimetric and volumetric hydrogen density in MOFs, *Energy Environ. Sci*. 10 (2017) 2459–2471. doi:10.1039/c7ee02477k.

[3] N.P. Brandon, Z. Kurban, Clean energy and the hydrogen economy, *Phil. Trans. R. Soc. A* 375: 20160400. http://dx.doi.org/10.1098/rsta.2016.0400 (2017).

[4] U. Bossel, B. Eliasson, G. Taylor, The Future of the Hydrogen Economy : Bright or Bleak ?, *Cogeneration & Distributed Generation Journal*, 18 (3), (2003). https://doi.org/10.1080/15453660309509023

[5] M. Carmo, D. L. Fritz, J. Mergel .D. Stolten, A comprehensive review on PEM water electrolysis, *Int. J. Hydrogen Energy.* 38 (2013) 4901–4934. doi:http://doi.org/10.1016/j.ijhydene.2013.01.151.

[6] G.A. Olah, A. Goeppert, G.K.S. Prakash, Chemical Recycling of Carbon Dioxide to Methanol and Dimethyl Ether : From Greenhouse Gas to Renewable , Environmentally Carbon Neutral Fuels and Synthetic Hydrocarbons, *J. Org. Chem.* 74 (2) (2009) 487–498. doi:10.1021/jo801260f.

[7] N. Meiri, R. Radus, M. Herskowitz, Simulation of novel process of CO_2 conversion to liquid fuels, *Biochem. Pharmacol.* 17 (2017) 284–289. doi:10.1016/j.jcou.2016.12.008.

[8] A. Ra, M. Panahi, K. Rajab, CO_2 utilization through integration of post-combustion carbon capture process with Fischer-Tropsch gas-to-liquid (GTL) processes, *Journal of CO2 utilization*, 18 (2017) 98–106. doi:10.1016/j.jcou.2017.01.016.

[9] J.O. Abe, A.P.I. Popoola, E. Ajenifuja, O.M. Popoola, ScienceDirect Hydrogen energy , economy and storage : Review and recommendation, *Int. J. Hydrogen Energy.* 44 (2019) 15072–15086. doi:10.1016/j.ijhydene.2019.04.068.

[10] M.P. Suh, H.J. Park, T.K. Prasad, D. Lim, Hydrogen Storage in Metal-Organic Frameworks, *Chem. Rev.* 112 (2), (2017) 782–835. doi:10.1021/cr200274s.

[11] P.A. Parilla, K. Gross, K. Hurst, T. Gennett, Recommended volumetric capacity definitions and protocols for accurate, standardized and unambiguous metrics for hydrogen storage materials, *Appl. Phys. A Mater. Sci. Process.* 122 (2016) 1–18. doi:10.1007/s00339-016-9654-1.

[12] United States Department of Energy (US DOE), Target Explanation Document : Onboard Hydrogen Storage for Light-Duty Fuel Cell Vehicles, (2017). Cited from: https://www.energy.gov/sites/prod/files/2017/05/f34/fcto_targets_onboard_hydro_storage_explanation.pdf.

[13] L. Zhou, Progress and problems in hydrogen storage methods, *Renew. Sustain. Energy Rev. 9* (2005) 395–408. doi:10.1016/j.rser.2004.05.005.

[14] Physical properties of fluid systems, Cited from: https://webbook.nist.gov/chemistry/fluid/.

[15] D.P. Broom, C.J. Webb, G.S. Fanourgakis, G.E. Froudakis, P.N. Trikalitis, M. Hirscher, ScienceDirect Concepts for improving hydrogen storage in nanoporous materials, *Int. J. Hydrogen Energy.* 44 (2019) 7768–7779. doi:10.1016/j.ijhydene.2019.01.224.

[16] K.M. Thomas, Hydrogen adsorption and storage on porous materials, *Catalysis Today* 120 (3 - 4) (2007) 389 - 398. doi:10.1016/j.cattod.2006.09.015.

[17] F. Schüth, B. Bogdanović, M. Felderhoff, Light metal hydrides and complex hydrides for hydrogen storage, *Chem. Commun.* (2004) 2249–2258. doi:10.1039/B406522K.

[18] A. Zaluska, L. Zaluski, Structure , catalysis and atomic reactions on the nano-scale : a systematic approach to metal hydrides for hydrogen storage, *Applied Physics A* 72 (2001) 157–165. https://doi.org/10.1007/s003390100783

[19] M.B. Ley, L.H. Jepsen, Y. Lee, Y.W. Cho, M.B. Von Colbe, M. Dornheim, M. Rokni, J.O. Jensen, M. Sloth, Y. Filinchuk, J.E. Jørgensen, F. Besenbacher, T.R. Jensen, Complex hydrides for hydrogen storage – new perspectives, *Materials Today* 17 (3) (2014) 122 - 128. doi:10.1016/j.mattod.2014.02.013.

[20] L. Schlapbach, A. Züttel, Hydrogen-storage materials for mobile applications, *Nature* 414 (2001) 353–358. https://doi.org/10.1038/35104634

[21] M. V Lototskyy, V.A. Yartys, B.G. Pollet, R.C. Bowman Jr, Metal hydride hydrogen

compressors : A review, *Int. J. Hydrogen Energy*. 39 (2013) 5818–5851. doi:10.1016/j.ijhydene.2014.01.158.

[22] S. Tedds, A. Walton, D.P. Broom, D. Book, Characterisation of porous hydrogen storage materials: carbons, zeolites, MOFs and PIMs, *Faraday Discuss.* 151 (2011) 75–94. doi:10.1039/C0FD00022A.

[23] J. Germain, J.M.J. Fréchet, F. Svec, Hypercrosslinked polyanilines with nanoporous structure and high surface area: potential adsorbents for hydrogen storage, *J. Mater. Chem.* 17 (2007) 4989–4997. doi:10.1039/B711509A.

[24] O.K. Farha, I. Eryazici, N.C. Jeong, B.G. Hauser, C.E. Wilmer, A.A. Sarjeant, R.Q. Snurr, S.T. Nguyen, A. O, J.T. Hupp, Metal − Organic Framework Materials with Ultrahigh Surface Areas: Is the Sky the Limit?, *J. Am. Chem. Soc.* 134 (36) (2012) 15016 - 15021. doi:10.1021/ja3055639.

[25] E. Klontzas, A. Mavrandonakis, G.E. Froudakis, Y. Carissan, W. Klopper, Molecular Hydrogen Interaction with IRMOF-1 : A Multiscale Theoretical Study, *J. Phys. Chem. C* 111 (36) (2007) 13635–13640. doi:10.1021/jp075420q.

[26] C. Buda, B.D. Dunietz, Hydrogen Physisorption on the Organic Linker in Metal Organic Frameworks : Ab Initio Computational Study, *J. Phys. Chem. B* 110 (21) (2006) 10479–10484. doi:10.1021/jp061249r.

[27] K.V. Kumar, A. Salih, L. Lu, E.A. Müller, Molecular Simulation of Hydrogen Physisorption and Chemisorption in Nanoporous Carbon Structures, *Adsorption Science & Technology* 29 (8) (2011) 799–817. doi:10.1260/0263-6174.29.8.799.

[28] R. Zacharia, S. Rather, Review of Solid State Hydrogen Storage Methods Adopting Different Kinds of Novel Materials, *Journal of Nanomaterials* 2015 (2015) 1-18. https://doi.org/10.1155/2015/914845

[29] M. Murialdo, N.J. Weadock, Y. Liu, C.C. Ahn, S.E. Baker, K. Landskron, B. Fultz, High-Pressure Hydrogen Adsorption on a Porous Electron-Rich Covalent Organonitridic Framework, *ACS Omega* 4 (1) (2019) 444-448. doi:10.1021/acsomega.8b03206.

[30] A.M. Kriesten, J.V. Schmitz, J. Siegel, C.E. Smith, M. Kaspereit, M. Hartmann, Shaping

of Flexible Metal-Organic Frameworks: Combining Macroscopic Stability and Framework Flexibility, *Eur. J. Inorg. Chem* (2019) 4700-4709. doi:10.1002/ejic.201901100.

[31] A.D. Wiersum, J. Chang, C. Serre, P.L. Llewellyn, An Adsorbent Performance Indicator as a First Step Evaluation of Novel Sorbents for Gas Separations: Application to Metal − Organic Frameworks, *Langmuir* 29 (10) (2013) 3301-3309. doi:10.1021/la3044329.

[32] A.J. Howarth, A.W. Peters, N.A. Vermeulen, T.C. Wang, J.T. Hupp, O.K. Farha, Best Practices for the Synthesis, Activation, and Characterization of Metal − Organic Frameworks, *Chem. Mater.* 29 (1) (2017) 26-39. doi:10.1021/acs.chemmater.6b02626.

[33] J.D. Tarver, H.Z.H. Jiang, M.T. Kapelewski, K.E. Hurst, P.A. Parilla, A. Ayala, T. Gennett, S.A. Fitzgerald, C.M. Brown, R. Long, Record High Hydrogen Storage Capacity in the Metal − Organic Framework Ni2 (m - dobdc) at Near-Ambient Temperatures, *Chem. Mater* 30 (22) (2018) 8179-8189. doi:10.1021/acs.chemmater.8b03276.

[34] N. Chanut, A.D. Wiersum, U.H. Lee, Y.K. Hwang, F. Ragon, H. Chevreau, S. Bourrelly, B. Kuchta, J.S. Chang, C. Serre, P.L. Llewellyn, Observing the Effects of Shaping on Gas Adsorption in Metal-Organic Frameworks, *Eur. J. Inorg. Chem.* 2016 (2016) 4416–4423. doi:10.1002/ejic.201600410.

[35] H. Li, K. Wang, Y. Sun, C.T. Lollar, J. Li, H. Zhou, Recent advances in gas storage and separation using metal – organic frameworks, *Mater. Today.* 21 (2018) 108–121. doi:10.1016/j.mattod.2017.07.006.

[36] J. Purewal, M. Veenstra, D. Tamburello, A. Ahmed, A.J. Matzger, A.G. Wong-foy, S. Seth, Y. Liu, D.J. Siegel, Estimation of system-level hydrogen storage for metal-organic frameworks with high volumetric storage density, *Int. J. Hydrogen Energy.* 44 (2019) 15135–15145. doi:10.1016/j.ijhydene.2019.04.082.

[37] D.A. Gómez-Gualdrón, T.C. Wang, P. García-Holley, R.M. Sawelewa, E. Argueta, R.Q. Snurr, J.T. Hupp, T. Yildirim, O.K. Farha, Understanding volumetric and gravimetric hydrogen adsorption trade-off in metal-organic frameworks, *ACS Appl. Mater. Interfaces.* 9 (2017) 33419–33428. doi:10.1021/acsami.7b01190.

[38] O. Ardelean, G. Blanita, G. Borodi, M.D. Lazar, I. Misan, I. Coldea, D. Lupu,

Volumetric hydrogen adsorption capacity of densified MIL-101 monoliths, *Int. J. Hydrogen Energy*. 38 (2013) 7046–7055. doi:10.1016/j.ijhydene.2013.03.161.

[39] M. Thommes, K. Kaneko, A. V. Neimark, J.P. Olivier, F. Rodriguez-Reinoso, J. Rouquerol, K.S.W. Sing, Physisorption of gases, with special reference to the evaluation of surface area and pore size distribution (IUPAC Technical Report), *Pure Appl. Chem.* 87 (2015) 1051–1069. doi:10.1515/pac-2014-1117.

[40] T.K.A. Hoang, D.M. Antonelli, Exploiting the kubas interaction in the design of hydrogen storage materials, *Adv. Mater.* 21 (2009) 1787–1800. doi:10.1002/adma.200802832.

[41] Y.B. Zudin, Non-equlibrium evaporation and condensation processes, *Mathematical Engineering* (2019) 321–349. doi:10.1007/978-3-030-13815-8.

[42] M. Oschwald, A. Schik, Supercritical nitrogen free jet investigated by spontaneous Raman scattering, *Experiments in Fluids* 27 (1999) 497-506. https://doi.org/10.1007/s003480050374

[43] J. Vu, Modelling of Convective Heat Transfer in Porous Media, Electronic Thesis and Dissertation Repository (2017). 4852. https://ir.lib.uwo.ca/etd/4852

[44] C. Zlotea, M. Latroche, Role of nanoconfinement on hydrogen sorption properties of metal nanoparticles hybrids, *Colloids Surfaces A Physicochem. Eng. Asp.* 439 (2013) 117–130. doi:10.1016/j.colsurfa.2012.11.043.

[45] B. Van De Voorde, I. Stassen, B. Bueken, F. Vermoortele, D. De Vos, Improving the mechanical stability of zirconium-based metal – organic frameworks by incorporation of acidic modulators, *J. Mater. Chem. A* 3 (2015) 1737-1742. doi:10.1039/c4ta06396a.

[46] N.M. Musyoka, M.K. Mathe, J. Ren, N.M. Musyoka, H.W. Langmi, A. Swartbooi, B.C. North, M. Mathe, A more efficient way to shape metal-organic framework (MOF) powder materials for hydrogen storage applications, *Int. J. Hydrog. Energy* 40 (13) (2016) 4617-4622. doi:10.1016/j.ijhydene.2015.02.011.

[47] M. Rubio-martinez, C. Avci-camur, D. Maspoch, M.R. Hill, A.W. Thornton, I. Imaz, M. Rubio-martinez, New synthetic routes towards MOF production at scale, *Chem. Soc. Rev.* (2017) 3453–3480. doi:10.1039/c7cs00109f.

[48] R. Zacharia, D. Cossement, L. Lafi, R. Chahine, Volumetric hydrogen sorption capacity of monoliths prepared by mechanical densification of MOF-177, *J. Mater. Chem.* 20 (2010) 2145–2151. doi:10.1039/b922991d.

[49] L.T. Holy, T.J. Mays, C.R. Bowen, A.D. Burrows, Hydrogen storage in polymer-based processable microporous composites, *J. Mater. Chem. A* 5 (2017) 18752-18761. doi:10.1039/c7ta05232d.

[50] R. Balderas-Xicohténcatl, M. Schlichtenmayer, M. Hirscher, Volumetric Hydrogen Storage Capacity in Metal-Organic Frameworks, *Energy Technol.* (2017) 578–582. doi:10.1002/ente.201700636.

[51] C. Xu, J. Yang, M. Veenstra, A. Sudik, J.J. Purewal, Y. Ming, B.J. Hardy, J. Warner, S. Maurer, U. Mu, D.J. Siegel, Hydrogen permeation and diffusion in densified MOF-5 pellets, *Int. J. Hydrogen Energy* 38 (2013) 3268–3274. https://doi.org/10.1016/j.ijhydene.2012.12.096

[52] J.J. Purewal, D. Liu, J. Yang, A. Sudik, D.J. Siegel, S. Maurer, U. Müller, Increased volumetric hydrogen uptake of MOF-5 by powder densification, *Int. J. Hydrogen Energy*. 37 (2012) 2723–2727. doi:10.1016/j.ijhydene.2011.03.002.

[53] M.R. Lohe, M. Rose, S. Kaskel, Metal–organic framework (MOF) aerogels with high micro- and macroporosity, *Chem. Commun.* (2009) 6056–6058. doi:10.1039/B910175F.

[54] K. Sumida, K. Liang, J. Reboul, I.A. Ibarra, S. Furukawa, P. Falcaro, Sol − Gel Processing of Metal − Organic Frameworks, *Chem. Mater.* 29 (7) (2017) 2626-2645. doi:10.1021/acs.chemmater.6b03934.

[55] S.K. Bhardwaj, N. Bhardwaj, R. Kaur, J. Mehta, A.L. Sharma, K. Kim, A. Deep, conductivity in metal – organic frameworks and miscellaneous applications thereof, *J. Mater. Chem. A* 6 (2018) 14992-15009. doi:10.1039/c8ta04220a.

[56] S. Edubilli, S. Gumma, Separation and Puri fi cation Technology A systematic evaluation of UiO-66 metal organic framework for CO2 / N2 separation, *Sep. Purif. Technol.* 224 (2019) 85–94. doi:10.1016/j.seppur.2019.04.081.

[57] P. Annamalai, N.M. Musyoka, J. Ren, H.W. Langmi, M. Mathe, D. Bessarabov, Electrospun zeolite-templated carbon composite fibres for hydrogen storage

applications, *Res. Chem. Intermed.* 43 (2017) 4095–4102. doi:10.1007/s11164-017-2867-x.

[58] L. Yu, P. Cebe, Crystal polymorphism in electrospun composite nanofibers of poly (vinylidene fluoride) with nanoclay of poly (vinylidene fluoride) with nanoclay, *Polymer* 50 (9) (2009) 2133-2141. doi:10.1016/j.polymer.2009.03.003.

[59] H. Liu, Electrospun fibrous mats as skeletons to produce free-standing MOF membranes Electrospun fibrous mats as skeletons to produce free-standing MOF, *J. Mater. Chem.* 22 (2012) 16971-16978. doi:10.1039/C2JM32570E.

[60] B.M. Connolly, N.A. Danaf, D.C. Lamb, J.P. Mehta, D. Vulpe, S. Wuttke, P.Z. Moghadam, A.E.H. Wheatley, Tuning porosity in macroscopic monolithic metal-organic frameworks for exceptional natural gas storage, *Nat. Commun.* (2019) 1–11. doi:10.1038/s41467-019-10185-1.

[61] G. Blanita, I. Coldea, I. Misan, D. Lupu, Hydrogen cryo-adsorption by hexagonal prism monoliths of MIL-101, *Int. J. Hydrogen Energy*. 39 (2014) 17040–17046. doi:10.1016/j.ijhydene.2014.08.038.

[62] M. Kriesten, V. Schmitz, J. Siegel, C.E. Smith, M. Kaspereit, M. Hartmann, Shaping of Flexible Metal-Organic Frameworks : Combining Macroscopic Stability and Framework Flexibility, *Eur. J. Inorg. Chem.* (2019) 4700–4709. doi:10.1002/ejic.201901100.

[63] W.J. Roth, B. Gil, W. Makowski, B. Marszalek, P. Eliášová, Layer like porous materials with hierarchical structure, *Chem. Soc. Rev.* 45 (2016) 3400–3438. doi:10.1039/C5CS00508F.

[64] M. Rubio-martinez, C. Avci-camur, D. Maspoch, M.R. Hill, A.W. Thornton, I. Imaz, M. Rubio-martinez, New synthetic routes towards MOF production at scale, *Chem. Soc. Rev.* 46 (2017) 3453-3480. doi:10.1039/C7CS00109F.

[65] G.W. Peterson, J.B. Decoste, T.G. Glover, Y. Huang, H. Jasuja, K.S. Walton, Effects of pelletization pressure on the physical and chemical properties of the metal-organic frameworks Cu3(BTC)2 and UiO-66, *Microporous Mesoporous Mater.* 179 (2013) 48–53. doi:10.1016/j.micromeso.2013.02.025.

[66] J. Landers, G.Y. Gor, A. V. Neimark, Density functional theory methods for characterization of porous materials, *Colloids Surfaces A Physicochem. Eng. Asp.* 437 (2013) 3–32. doi:10.1016/j.colsurfa.2013.01.007.

[67] J. Hajek, C. Caratelli, R. Demuynck, L. Vanduyfhuys, M. Waroquier, V. Van Speybroeck, Chemical Science metal – organic framework, *Chem. Sci.* 9 (2018) 2723–2732. doi:10.1039/C7SC04947A.

[68] F. Firth, M. Cliffe, D. Vulpe, P. Moghadam, D. Fairen-jimenez, C. Firth, E. New, D. Phases, F.M. Frameworks, Engineering New Defective Phases of UiO Family Metal-Organic Frameworks with Water, *ChemRxiv*, Preprint (2018). doi:10.26434/chemrxiv.7301951.v1.

[69] G. Thiele, J. Kim, Excavating hidden adsorption sites in metal-organic frameworks using rational defect engineering, *Nat. Commun.* 8 (2017) 1539 doi:10.1038/s41467-017-01478-4.

[70] H. Wu, T. Yildirim, W. Zhou, Exceptional Mechanical Stability of Highly Porous Zirconium Metal − Organic Framework UiO-66 and Its Important Implications, *The Journal of Physical Chemistry Letters* 4(6) (2013) 925-930. doi:10.1021/jz4002345.

[71] F.X. Coudert, Responsive metal-organic frameworks and framework materials: Under pressure, taking the heat, in the spotlight, with friends, *Chem. Mater.* 27 (2015) 1905–1916. doi:10.1021/acs.chemmater.5b00046.

[72] M. Vandichel, J. Hajek, A. Ghysels, A. De Vos, M. Waroquier, V. Van Speybroeck, Water coordination and dehydration processes in defective UiO-66 type metal organic frameworks, *Cryst. Eng. Comm.* 18 (2016) 7056-7069. doi:10.1039/c6ce01027j.

[73] S.M.J. Rogge, J. Wieme, L. Vanduyfhuys, S. Vandenbrande, G. Maurin, T. Verstraelen, M. Waroquier, V. Van Speybroeck, Thermodynamic Insight in the High-Pressure Behavior of UiO-66 : Effect of Linker Defects and Linker Expansion, *Chem. Mater.* 28 (16) (2016) 5721-5732. doi:10.1021/acs.chemmater.6b01956.

[74] J. Ren, N.M. Musyoka, H.W. Langmi, B.C. North, M. Mathe, X. Kang, Fabrication of core – shell MIL-101 (Cr)@ UiO- 66 (Zr) nanocrystals for hydrogen storage, *Int. J. Hydrogen Energy* 39 (27) (2014) 14912-14917. doi:10.1016/j.ijhydene.2014.07.056.

[75] Z. Chen, W. Ren, L. Gao, B. Liu, S. Pei, H. Cheng, Three-dimensional flexible and conductive interconnected graphene networks grown by chemical vapour deposition, *Nat. Mater.* 10 (2011) 424–428. doi:10.1038/nmat3001.

[76] D.W. Boukhvalov, M.I. Katsnelson, A.I. Lichtenstein, Hydrogen on graphene: Electronic structure, total energy, structural distortions, and magnetism from first-principles calculations, *Phys. Rev. B* 77, (2008) 035427. https://doi.org/10.1103/PhysRevB.77.035427

[77] A.C. Ferrari, Raman spectroscopy of graphene and graphite : Disorder , electron – phonon coupling, doping and nonadiabatic effects, *Solid state Communications* 143 (1-2) (2007) 47–57. doi:10.1016/j.ssc.2007.03.052.

[78] S. Lin, Q. Cai, J. Ji, G. Sui, Y. Yu, X. Yang, Q. Ma, Y. Wei, X. Deng, Electrospun nanofiber reinforced and toughened composites through in situ nano-interface formation, *Compos. Sci. Technol.* 68 (2008) 3322–3329. doi:10.1016/j.compscitech.2008.08.033.

[79] A.D. Burrows, Gas sensing using porous materials for automotive applications, *Chem. Soc. Rev.* 44 (2015) 4290-4321. doi:10.1039/c5cs00040h.

[80] R. Ostermann, J. Cravillon, C. Weidmann, M. Wiebcke, B.M. Smarsly, Metal–organic framework nanofibers viaelectrospinning, *Chem. Commun.* 47 (2011) 442–444. doi:10.1039/C0CC02271C.

[81] Q. Zhao, W. Yuan, J. Liang, J. Li, Synthesis and hydrogen storage studies of metal L organic framework UiO-66, *Int. J. Hydrogen Energy.* 38 (2013) 13104–13109. doi:10.1016/j.ijhydene.2013.01.163.

[82] H. Wu, T. Yildirim, W. Zhou, Exceptional Mechanical Stability of Highly Porous Zirconium Metal–Organic Framework UiO-66 and Its Important Implications, *J. Phys. Chem. Lett.* 4 (2013) 925–930. doi:10.1021/jz4002345.

[83] D.A. Links, Advanced fabrication of metal – organic frameworks : template-directed formation of polystyrene @ ZIF-8 core – shell and hollow ZIF-8 microspheres, *Chem. Comm* 48 (2012) 221–223. doi:10.1039/c1cc16213f.

[84] L. Valenzano, B. Civalleri, S. Chavan, S. Bordiga, M.H. Nilsen, S. Jakobsen, K.P.

Lillerud, C. Lamberti, Disclosing the complex structure of UiO-66 metal organic framework: A synergic combination of experiment and theory, *Chem. Mater.* 23 (2011) 1700–1718. doi:10.1021/cm1022882.

[85] S. Bhattacharjee, C. Chen, W.-S. Ahn, Chromium terephthalate metal–organic framework MIL-101: synthesis, functionalization and applications for adsorption and catalysis, *RSC Adv.* 4 (2014) 52500–52525. doi:10.1039/C4RA11259H.

[86] L. Paseta, G. Potier, S. Sorribas, J. Coronas, Solventless synthesis of MOFs at high pressure, *ACS Sustain. Chem. Eng.* 4 (2016) 3780–3785. doi:10.1021/acssuschemeng.6b00473.

[87] X. Dyosiba, J. Ren, N.M. Musyoka, H.W. Langmi, M.K. Mathe, M. Onyango, Feasibility of varied polyethylene terephthalate (PET) wastes as linker source in MOF UiO-66 (Zr) synthesis, *Ind. Eng. Chem. Res.* 58 (36) (2019) 17010-17016. doi:10.1021/acs.iecr.9b02205.

[88] J. Ren, X. Dyosiba, N.M. Musyoka, H.W. Langmi, B.C. North, M. Mathe, M.S. Onyango, Green synthesis of chromium-based metal-organic framework (Cr-MOF) from waste polyethylene terephthalate (PET) bottles for hydrogen storage applications, *Int. J. Hydrogen Energy.* 41 (2016) 1841–1846. https://doi.org/10.1016/j.ijhydene.2016.08.040

[89] W.P.R. Deleu, I. Stassen, D. Jonckheere, R. Ameloot, D.E. De Vos, Waste PET (bottles) as a resource or substrate for MOF synthesis, *J. Mater. Chem. A.* 4 (2016) 9519–9525. doi:10.1039/C6TA02381A.

[90] J. Ren, N.M. Musyoka, H.W. Langmi, T. Segakweng, B.C. North, M. Mathe, X. Kang, Modulated synthesis of chromium-based metal-organic framework (MIL-101) with enhanced hydrogen uptake, *Int. J. Hydrogen Energy.* 39 (2014) 12018–12023. doi:10.1016/j.ijhydene.2014.06.019.

[91] G. Kaur, S. Øien-ødegaard, A. Lazzarini, S.M. Chavan, S. Bordiga, K.P. Lillerud, U. Olsbye, Controlling the Synthesis of Metal–Organic Framework UiO-67 by Tuning Its Kinetic Driving Force, *Cryst. Growth Des.* 19 (2019) 4246–4251. doi:10.1021/acs.cgd.9b00916.

[92] I. Pakamore, An ambient-temperature aqueous synthesis of zirconium-based metal-

organic frameworks, *Green Chem.* 20 (2018) 5292-5298. doi:10.1039/C8GC02312C.

[93] M.J. Katz, Z.J. Brown, Y.J. Colón, P.W. Siu, K.A. Scheidt, R.Q. Snurr, J.T. Hupp, O.K. Farha, A facile synthesis of UiO-66, UiO-67 and their derivatives, *Chem. Commun.* 49 (2013) 9449. doi:10.1039/c3cc46105j.

[94] A.J. Howarth, A.W. Peters, N.A. Vermeulen, T.C. Wang, J.T. Hupp, O.K. Farha, Best Practices for the Synthesis, Activation, and Characterization of Metal − Organic Frameworks, *Chem. Mater.* 29 (1) (2017) 26-39. doi:10.1021/acs.chemmater.6b02626.

[95] Y. Zhao, Q. Zhang, Y. Li, R. Zhang, G. Lu, Large-Scale Synthesis of Monodisperse UiO-66 Crystals with Tunable Sizes and Missing Linker Defects via Acid/Base Co-Modulation, *ACS Appl Mater Interfaces* 9 (17) (2017) 15079-15085. doi:10.1021/acsami.7b02887.

[96] C.H. Lau, T.C. Scientific, R. Babarao, T.C. Scientific, A route to drastic increase of CO2 uptake in Zr metal organic framework UiO-66, *Chem. Commun.* 49 (2013) 3634-3636 doi:10.1039/c3cc40470f.

[97] G.C. Shearer, S. Chavan, S. Bordiga, S. Svelle, U. Olsbye, K.P. Lillerud, Defect Engineering: Tuning the Porosity and Composition of the Metal-Organic Framework UiO-66 via Modulated Synthesis, *Chem. Mater.* 28 (2016) 3749–3761. doi:10.1021/acs.chemmater.6b00602.

[98] G.C. Shearer, S. Chavan, S. Bordiga, S. Svelle, U. Olsbye, K.P. Lillerud, Defect Engineering: Tuning the Porosity and Composition of the Metal − Organic Framework UiO-66 via Modulated Synthesis, *Chem. Mater.* 28 (11) (2016) 3749-3761. doi:10.1021/acs.chemmater.6b00602.

[99] J. Ren, H.W. Langmi, B.C. North, M. Mathe, D. Bessarabov, Modulated synthesis of zirconium-metal organic framework (Zr-MOF) for hydrogen storage applications, *Int. J. Hydrogen Energy.* 39 (2014) 890–895. doi:10.1016/j.ijhydene.2013.10.087.

[100] J. Goldsmith, A.G. Wong-Foy, M.J. Cafarella, D.J. Siegel, Theoretical limits of hydrogen storage in metal-organic frameworks: Opportunities and trade-offs, *Chem. Mater*. 25 (2013) 3373–3382. doi:10.1021/cm401978e.

[101] M.- Al, P.G. Yot, Z. Boudene, J. Macia, D. Granier, L. Vanduyfhuys, T. Verstraelen, V.

Van Speybroeck, N. Stock, G. Maurin, Metal – organic frameworks as potential shock absorbers : the case of the highly flexible, *Chem. Commun.* 50 (2014) 9462-9464. doi:10.1039/c4cc03853c.

[102] A. Clearfield, Flexible MOFs under stress : pressure and temperature, *Dalton Trans.* 45 (2016) 4100-4112. doi:10.1039/c5dt03228h.

[103] S. Dissegna, P. Vervoorts, C.L. Hobday, T. Du, D. Daisenberger, A.J. Smith, R.A. Fischer, G. Kieslich, Tuning the Mechanical Response of Metal − Organic Frameworks by Defect Engineering, *J. Am. Chem. Soc.* 140 (37) (2018) 11581-11584. doi:10.1021/jacs.8b07098.

[104] T. Ung, Microstructural parameters from X-ray diffraction peak broadening, *Scripta Materialia*, 51(8 SPEC. ISS.) (2004) 777–781. doi:10.1016/j.scriptamat.2004.05.007.

[105] K. Chapman, G. Halder, P. Chupas, Induced Amorphization and Porosity Modification in a Metal− Organic Framework, *J. Am. Chem. Soc.* 131 (2009) 17546–17547. http://pubs.acs.org/doi/abs/10.1021/ja908415z.

[106] S. Chavan, J.G. Vitillo, D. Gianolio, O. Zavorotynska, B. Civalleri, S. Jakobsen, M.H. Nilsen, L. Valenzano, *Phys. Chem. Chem. Phys.* 14 (2012) 1614-1626. doi:10.1039/c1cp23434j.

[107] H. Wu, Y. Shen Chua, V. Krungleviciute, M. Tyagi, P. Chen, T. Yildirim, W. Zhou, Unusual and Highly Tunable Missing-Linker Defects in Zirconium Metal−Organic Framework UiO-66 and Their Important Effects on Gas Adsorption, *J. Am. Chem. Soc.* 135 (28) (2013) 10525-10532. doi:10.1021/ja404514r.

[108] M. Vandichel, J. Hajek, F. Vermoortele, M. Waroquier, D.E. De Vos, V. Van Speybroeck, Active site engineering in UiO-66 type metal–organic frameworks by intentional creation of defects: a theoretical rationalization, *Cryst. Eng. Comm.* 17 (2015) 395–406. doi:10.1039/C4CE01672F.

[109] B.S. Ghanem, M. Hashem, K.D.M. Harris, K.J. Msayib, M. Xu, P.M. Budd, N. Chaukura, D. Book, S. Tedds, A. Walton, N.B. Mckeown, Triptycene-Based Polymers of Intrinsic Microporosity : Organic Materials That Can Be Tailored for Gas Adsorption, *Macromolecules* 43 (12) (2010) 5287-5294. doi:10.1021/ma100640m.

[110] N. Du, G.P. Robertson, J. Song, I. Pinnau, S. Thomas, M.D. Guiver, Phenylsulfone Groups as Materials for Membrane Gas Separation, *Macromolecules* 41 (24) (2008) 9656-9662. https://doi.org/10.1021/ma801858d

[111] Q. Song, S. Cao, R.H. Pritchard, B. Ghalei, S.A. Al-muhtaseb, E.M. Terentjev, A.K. Cheetham, E. Sivaniah, polymers of intrinsic microporosity towards tunable molecular sieve membranes, *Nat. Commun.* (2014). doi:10.1038/ncomms5813.

[112] T.O. Mcdonald, R. Akhtar, C.H. Lau, T. Ratvijitvech, G. Cheng, R. Clowes, D.J. Adams, T. Hasell, A.I. Cooper, Using intermolecular interactions to crosslink PIM-1 and modify its gas sorption properties, *J. Mater. Chem. A* 3 (2015) 4855–4864. doi:10.1039/c4ta06070a.

[113] J.S. Bonso, G.D. Kalaw, J.P. Ferraris, High surface area carbon nanofibers derived from electrospun PIM-1 for energy storage applications, *J. Mater. Chem. A* 2 (2014) 418-424. doi:10.1039/c3ta13779a.

[114] S. Li, F. Huo, Metal–organic framework composites: from fundamentals to applications, *Nanoscale* 7 (2015) 7482–7501. doi:10.1039/c5nr00518c.

[115] K.M. Thomas, Hydrogen adsorption and storage on porous materials, *Catal. Today.* 120 (2007) 389–398. doi:10.1016/j.cattod.2006.09.015.

[116] D. Bazer-Bachi, L. Assié, V. Lecocq, B. Harbuzaru, V. Falk, Towards industrial use of metal-organic framework: Impact of shaping on the MOF properties, *Powder Technol.* 255 (2014) 52–59. doi:10.1016/j.powtec.2013.09.013.

[117] M. Mohan, V. Kumar, Hydrogen storage in carbon materials — A review, *Energy Storage* (2019) 1–26. doi:10.1002/est2.35.

[118] K.S.W. Sing, R.T. Williams, Physisorption Hysteresis Loops and the Characterization of Nanoporous Materials, *Adsorption Science & Technology* 22 (10) (2004) 773–782. doi:10.1260/0263617053499032.

[119] M.T. J. Moellmera, E.B. Celerc, R. Luebkeb, A.J. Cairnsb, R. Staudta, M. Eddaoudib, Insights on Adsorption Characterization of Metal-Organic Frameworks: A Benchmark Study on the Novel soc-MOF, *Microporous Mesoporous Mater.* 129 (2010) 345–353. doi:https://doi.org/10.1016/j.micromeso.2009.06.014.

[120] J.A. Mason, M. Veenstra, J.R. Long, Evaluating metal–organic frameworks for natural gas storage, *Chem. Sci.* 5 (2014) 32–51. doi:10.1039/C3SC52633J.

[121] J.C. Groen, L.A.A. Peffer, J. Pèrez-Ramirez, Pore size determination in modified micro- and mesoporous materials. Pitfalls and limitations in gas adsorption data analysis, *Microporous Mesoporous Mater.* 60 (2003) 1–17. doi:10.1016/S1387-1811(03)00339-1.

[122] J. Jeromenok, J. Weber, Restricted Access: On the Nature of Adsorption/Desorption Hysteresis in Amorphous, Microporous Polymeric Materials, *Langmuir* 29 (42) (2013) 12982-12989. doi:10.1021/la402630s.

[123] Y. Gogotsi, A. Nikitin, H. Ye, W. Zhou, J.E. Fischer, B. Yi, Nanoporous carbide-derived carbon with tunable pore size, *Nat. Mater.* 2 (2003) 591–594. https://doi.org/10.1038/nmat957

[124] M.R. Andalibi, A. Qajar, H.C. Foley, Evidence of Nanoconfinement Effects in the Adsorption of Hydrogen on Coinage Metal Complexes Dispersed within Porous Carbon, *J. Phys. Chem. C.* 119 (2015) 21314–21322. doi:10.1021/acs.jpcc.5b05173.

[125] K. Xia, Q. Gao, J. Jiang, J. Hu, Hierarchical porous carbons with controlled micropores and mesopores for supercapacitor electrode materials, *Carbon N. Y.* 46 (2008) 1718–1726. doi:10.1016/j.carbon.2008.07.018.

[126] T.R. Cook, Y-R. Zheng, P.J. Steng, Metal–Organic Frameworks and Self-Assembled Supramolecular Coordination Complexes: Comparing and Contrasting the Design, Synthesis, and Functionality of Metal–Organic Materials, *Chem. Rev.* 113 (1) (2013) 734-777. doi:10.1021/cr3002824.Metal-Organic.

[127] T.E. Mallouk, Crowns get organized, *Nature* 387 (1997) 350–351. https://doi.org/10.1038/387350a0

[128] B. Yukio, The Crystal Structure of Bis (adiponitrilo) copper (I), *BCSJ* 32 (11) (1959) 1221-1226. https://doi.org/10.1246/bcsj.32.1221

[129] P. Linked, B.F. Abrahams, B.F. Hoskins, R. Robson, A New Type of Infinite 3D Polymeric Network, *J. Am. Chem. Soc.* 113 (9) (1991) 3606-3607. doi:10.1021/ja00009a065.

[130] B. Spasm, Cooperative bonding affords a holesome story, *Nature* 386 (1997) 220–221. https://doi.org/10.1038/386220a0

[131] H. Li, M. Eddaoudi, M. O'Keeffe, O.M. Yhagi, Design and synthesis of an exceptionally stable and highly stable metal-organic framework, *Nature* 402 (1999) 276–279. https://doi.org/10.1038/46248

[132] Y. Bai, Y. Dou, L. Xie, W. Rutledge, J. Li, H. Zhou, *Chem Soc Rev*, (2016) 2327–2367. doi:10.1039/c5cs00837a.

[133] F. Xi, Y. Yang, H. Liu, H. Yao, E. Gao, Different acidity and additive effects of zirconium metal–organic frameworks as catalysts for cyanosilylation, *RSC Adv.* 5 (2015) 79216–79223. doi:10.1039/c5ra13149a.

[134] S.A. Moggach, T.D. Bennett, A.K. Cheetham, The effect of pressure on ZIF-8: Increasing pore size with pressure and the formation of a high-pressure phase at 1.47 GPa, *Angew. Chemie - Int. Ed.* 48 (2009) 7087–7089. doi:10.1002/anie.200902643.

[135] M.C. Raj, S. Senthilkumar, R.S. Somani, H.C. Bajaj, Preparation, characterization and hydrogen sorption study of MIL-101(Cr) pellets, *Int. J. Environ. Stud.* 73 (2016) 357–368. doi:10.1080/00207233.2016.1165477.

[136] B. Bueken, I. Stassen, R. Ameloot, D.A. Keen, G. V Baron, J.F.M. Denayer, Gel-based morphological design of zirconium metal–organic frameworks, *Chem. Sci.* 8 (2017) 3939–3948. doi:10.1039/c6sc05602d.

[137] P.M. Suh, P.H. Jeong, T.K. Prasad, D.-W. Lim, Hydrogen Storage in Metal–Organic Frameworks, *Chem. Rev.* 112 (2012) 782–835. https://doi.org/10.1021/cr200274s

[138] A. Dhakshinamoorthy, Z. Li, H. Garcia, Catalysis and photocatalysis by metal organic frameworks, *Chem. Soc. Rev.* 47 (2018) 8134-8172. doi:10.1039/c8cs00256h.

[139] J. Klinowski, F.A. Almeida Paz, P. Silva, J. Rocha, Microwave-Assisted Synthesis of Metal–Organic Frameworks, *Dalt. Trans.* 40 (2011) 321–330. doi:10.1039/C0DT00708K.

[140] J. Ren, T. Segakweng, H.W. Langmi, N.M. Musyoka, B.C. North, M. Mathe, D. Bessarabov, Microwave-assisted modulated synthesis of zirconium-based metal-organic framework (Zr-MOF) for hydrogen storage applications, *Int. J. Mater. Res.* 105 (2014)

516–519. doi:10.3139/146.111047.

[141] J-L. Do, T. Friščić, Mechanochemistry: A Force of Synthesis, *ACS Cent. Sci.* 3 (1) (2017) 13-19. doi:10.1021/acscentsci.6b00277.

[142] X. Dyosiba, J. Ren, N.M. Musyoka, H.W. Langmi, M. Mathe, M.S. Onyango, Preparation of value-added metal-organic frameworks (MOFs) using waste PET bottles as source of acid linker, *Sustain. Mater. Technol.* 10 (2016) 10-13. doi:10.1016/j.susmat.2016.10.001.

[143] H. Furukawa, H. Furukawa, K.E. Cordova, M.O. Keeffe, O.M. Yaghi, The Chemistry and Applications of Metal-Organic Frameworks, *Science* 341 (2013). doi:10.1126/science.1230444.

[144] H. Jasuja, K.S. Walton, Experimental Study of CO 2 , CH 4 , and Water Vapor Adsorption on a Dimethyl-Functionalized UiO-66 Framework, *J. Phys. Chem. C* 117 (14) (2013) 7062-7068. doi:10.1021/jp311857e.

[145] S. Chavan, J.G. Vitillo, D. Gianolio, O. Zavorotynska, B. Civalleri, S. Jakobsen, M.H. Nilsen, L. Valenzano, C. Lamberti, K.P. Lillerud, S. Bordiga, H2storage in isostructural UiO-67 and UiO-66 MOFs, Phys. *Chem. Chem. Phys.* 14 (2012) 1614–1626. doi:10.1039/c1cp23434j.

[146] C. Petit, J. Burress, T.J. Bandosz, The synthesis and characterization of copper-based metal – organic framework / graphite oxide composites, *Carbon N. Y.* 49 (2010) 563–572. doi:10.1016/j.carbon.2010.09.059.

[147] S.X. Xin Lia, Jin Zhangab, Wanling Shena, Rapid synthesis of metal-organic frameworks MIL-53(Cr), *Mater. Lett.* 255 (2019) 126519. doi:https://doi.org/10.1016/j.matlet.2019.126519.

[148] R.A. Dodson, A.G. Wong-foy, A.J. Matzger, The Metal–Organic Framework Collapse Continuum: Insights from Two-Dimensional Powder X-ray Diffraction, *Chem. Mater.* 30 (2018) 6559–6565. doi:10.1021/acs.chemmater.8b03378.

[149] A.P. Nelson, O.K. Farha, K.L. Mulfort, J.T. Hupp, Supercritical Processing as a Route to High Internal Surface Areas and Permanent Microporosity in Metal - Organic Framework Materials, *J. Am. Chem. Soc.* 131 (2) (2009) 458-460.

doi:10.1021/ja808853q.

[150] D. Britt, D. Tranchemontagne, O.M. Yaghi, Metal-organic frameworks with high capacity and selectivity for harmful gases, *PNAS* 105 (33) (2008) 11623-11627. https://doi.org/10.1073/pnas.0804900105

[151] M. Schlichtenmayer, M. Hirscher, The usable capacity of porous materials for hydrogen storage, *Appl. Phys.* A. 122 (2016) 1–11. doi:10.1007/s00339-016-9864-6.

[152] J. Yang, A. Sudik, C. Wolverton, D.J. Siegel, High capacity hydrogenstorage materials: attributes for automotive applications and techniques for materials discovery, *Chem. Soc. Rev.* 39 (2010) 656–675. doi:10.1039/B802882F.

[153] B. Ugale, S.S. Dhankhar, C.M. Nagaraja, Interpenetrated Metal − Organic Frameworks of Cobalt (II): Structural Diversity , Selective Capture , and Conversion of CO2, *Cryst. Growth Des.* 17 (6) (2017) 3295-3305. doi:10.1021/acs.cgd.7b00274.

[154] A.H. Valekar, K. Cho, U. Lee, S. Lee, W. Yoon, Y.K. Hwang, G. Lee, J. Cho, J. Chang, Shaping of porous metal–organic framework granules using mesoporous ρ-alumina as a binder, *RSC Adv.* 7 (2017) 55767–55777. doi:10.1039/c7ra11764g.

[155] M.A. Moreira, C. Santos, A.F.P. Ferreira, J.M. Loureiro, F. Ragon, P. Horcajada, K. Shim, Y. Hwang, U. Lee, J. Chang, C. Serre, E. Rodrigues, Reverse Shape Selectivity in the Liquid-Phase Adsorption of Xylene Isomers in Zirconium Terephthalate MOF UiO-66, *Langmuir* 28 (13) (2012) 5715-5723. doi:10.1021/la3004118.

[156] L. Pinto, S. Dias, Composite MOF Foams : The Example of UiO-66 / Polyurethane, *ACS Appl. Mater. Interfaces* 5 (7) (2013) 2360-2363. doi:10.1021/am303089g.

[157] J. Ren, T. Segakweng, H.W. Langmi, B.C. North, M. Mathe, Ni foam-immobilized MIL-101 (Cr) nanocrystals toward system integration for hydrogen storage, *J. Alloys Compd.* 645 (2015) S170–S173. doi:10.1016/j.jallcom.2015.01.083.

[158] G.J.H. Lim, Y. Wu, B.B. Shah, J.J. Koh, C.K. Liu, D. Zhao, A.K. Cheetham, J. Wang, J. Ding, 3D-Printing of Pure Metal–Organic Framework Monoliths, *ACS Mater. Lett.* 1 (2019) 147–153. doi:10.1021/acsmaterialslett.9b00069.

[159] J. Dhainaut, J. Troyano, A. Legrand, J. Canivet, I. Imaz, D. Maspoch, H. Reinsch, D. Farrusseng, densification into tablets on textural and mechanical properties,

Cryst. Eng. Comm. 19 (2017) 4211-4218. doi:10.1039/c7ce00338b.

[160] J.H. Cavka, S. Jakobsen, U. Olsbye, N. Guillou, C. Lamberti, S. Bordiga, K.P. Lillerud, A new zirconium inorganic building brick forming metal organic frameworks with exceptional stability, *J. Am. Chem. Soc.* 130 (2008) 13850–13851. doi:10.1021/ja8057953.

[161] S.M.J. Rogge, M. Waroquier, V. Van Speybroeck, Reliably Modeling the Mechanical Stability of Rigid and Flexible Metal − Organic Frameworks, *Acc. Chem. Res.* 51 (1) (2018) 138-148. doi:10.1021/acs.accounts.7b00404.

[162] L.R. Redfern, L. Robison, M.C. Wasson, S. Goswami, J. Lyu, T. Islamoglu, K.W. Chapman, O.K. Farha, Porosity Dependence of Compression and Lattice Rigidity in Metal–Organic Framework Series, *J. Am. Chem. Soc.* 141 (2019) 4365–4371. doi:10.1021/jacs.8b13009.

[163] A.U. Ortiz, A. Boutin, A.H. Fuchs, F. Coudert, Anisotropic Elastic Properties of Flexible Metal – Organic Frameworks : How Soft are Soft Porous Crystals ?, *Phys. Rev. Lett.* 109 (19) (2014). https://doi.org/10.1103/PhysRevLett.109.195502

[164] A.E. Platero-prats, A. Mavrandonakis, L.C. Gallington, Y. Liu, J.T. Hupp, O.K. Farha, C.J. Cramer, K.W. Chapman, Structural Transitions of the Metal-Oxide Nodes within Metal − Organic Frameworks: On the Local Structures of NU-1000 and UiO-66, *J. Am. Chem. Soc.* 138 (12) (2016) 4178-4185. doi:10.1021/jacs.6b00069.

[165] J.R. Long, L.J. Murray, M. Dinca, Hydrogen storage in metal – organic frameworks, *Chem. Soc. Rev.* 38 (2009) 1294-1314. doi:10.1039/b802256a.

[166] B. Panella, M. Hirscher, S. Roth, Hydrogen adsorption in different carbon nanostructures, *Carbon* 43 (10) (2005) 2209–2214. doi:10.1016/j.carbon.2005.03.037.

[167] W.E. Teo, S. Ramakrishna, A review on electrospinning design and nanofibre assemblies, *Nanotechnology* 17 (2006) R89–R106. doi:10.1088/0957-4484/17/14/R01.

[168] I.M. Alarifi, A.R. Alharbi, M.N. Khan, W.S. Khan, A. Usta, R. Asmatulu, Journal of Material Science and Research Water Treatment using Electrospun PVC / PVP Nanofibers as Filter Medium, *Int. J. Mater. Sci. Res.* 2 (1) (2018) 43-49. doi:10.18689/ijmsr-1000107.

[169] D.H. Reneker, A.L. Yarin, Electrospinning jets and polymer nanofibers, *Polym. with Aligned Carbon Nanotub. Act. Compos. Mater.* 49 (2008) 2387–2425. doi:10.1016/j.polymer.2008.02.002.

[170] A. Baji, Y-W. Mai, S-C. Wong, M. Abtahi, P. Chen, Electrospinning of polymer nanofibers : effects on oriented morphology , structures and tensile properties. *Compos. Sci. Technol.* 70 (5) (2010) 703-718. doi:10.1016/j.compscitech.2010.01.010.

[171] R. Jalili, M. Morshed, S. Abdolkarim, H. Ravandi, Fundamental Parameters Affecting Electrospinning of PAN Nanofibers as Uniaxially Aligned Fibers, *Journal of Applied Polymer Science* 101 (2006) 4350 – 4357. doi:10.1002/app.24290.

[172] A. Frenot, I.S. Chronakis, Polymer nanofibers assembled by electrospinning, *Current Opinion in Colloid and Interface Science* 8 (2003) 64–75. https://doi.org/10.1016/S1359-0294(03)00004-9.

[173] A.L. Yarin, Coaxial electrospinning and emulsion electrospinning of core – shell fibers, *Polymers for Advanced Technologies* 22 (3) (2011) 310-317. doi:10.1002/pat.1781.

[174] N.N. Yarns, B.F. Ko, Y. Gogotsi, A. Ali, N. Naguib, H. Ye, G. Yang, C. Li, P. Willis, Electrospinning of Continuous Carbon Nanotube-Filled Nanofiber Yarns, *Advanced Materials* 15 (14) (2003) 1161–1165. doi:10.1002/adma.200304955.

[175] D.H. Reneker, I. Chun, Nanometre diameter fibres of polymer , produced by electrospinning, *Nanotechnology* 7 (3) (1996) 216–223. https://doi.org/10.1088/0957-4484/7/3/009

[176] S.Y. Gu, J. Ren, G.J. Vancso, Process optimization and empirical modeling for electrospun polyacrylonitrile (PAN) nanofiber precursor of carbon nanofibers, *Eur. Polym. J.* 41 (2005) 2559–2568. doi:10.1016/j.eurpolymj.2005.05.008.

[177] R. J. Doshi, D.H, Electrospinning process and applications of electrospun fibers, *J. Electrostat.* 35 (1995) 151–160. doi:https://doi.org/10.1016/0304-3886(95)00041-8.

[178] J. Choi, K.M. Lee, R. Wycisk, P.N. Pintauro, P.T. Mather, Nanofiber network ion-exchange membranes, *Macromolecules* 41 (2008) 4569–4572. doi:10.1021/ma800551w.

[179] H. Chen, N. Wang, J. Di, Y. Zhao, Y. Song, L. Jiang, Nanowire-in-microtube structured

core/shell fibers via multifluidic coaxial electrospinning, *Langmuir* 26 (2010) 11291–11296. doi:10.1021/la100611f.

[180] C. Wang, J. Wang, L. Zeng, Z. Qiao, X. Liu, H. Liu, Fabrication of Electrospun Polymer Nanofibers with Diverse Morphologies, *Molecules* 24 (5) (2019) 834. doi:10.3390/molecules24050834.

[181] D. Li, Y. Wang, Y. Xia, V. Uni, Electrospinning of Polymeric and Ceramic Nanofibers as Uniaxially Aligned Arrays, *Nano Letters* 3 (8) (2003) 1167-1171. https://doi.org/10.1021/nl0344256

[182] H. Fong, I. Chun, D.H. Reneker, Beaded nanofibers formed during electrospinning, *Polymer* 40 (16) (1999) 4585–4592. https://doi.org/10.1016/S0032-3861(99)00068-3

[183] P.M. Budd, K.J. Msayib, C.E. Tattershall, B.S. Ghanem, K.J. Reynolds, N.B. Mckeown, D. Fritsch, Gas separation membranes from polymers of intrinsic microporosity, *Journal of Membrane Science* 251 (1-2) (2005) 263–269. doi:10.1016/j.memsci.2005.01.009.

[184] J. Weber, Q. Su, M. Antonietti, A. Thomas, Exploring Polymers of Intrinsic Microporosity – Microporous , Soluble Polyamide and Polyimide, *Macromolecular Rapid Communications* 28 (18-19) (2007) 1871–1876. doi:10.1002/marc.200700346.

[185] P. Science, T. Kuila, C. Mechanical, E. Resea, S. Bhadra, S. Engineering, P. Limited, Recent Advances in Graphene Based Polymer Composites, *Progress in Polymer Science* 35 (11) (2016) 1350-1375. doi:10.1016/j.progpolymsci.2010.07.005.

[186] V. Georgakilas, M. Otyepka, A.B. Bourlinos, V. Chandra, N. Kim, K.C. Kemp, P. Hobza, R. Zboril, K.S. Kim, Functionalization of Graphene : Covalent and Non-Covalent Approaches , Derivatives and Applications, *Chem. Rev.* 112 (11) (2012) 6156-6214. https://doi.org/10.1021/cr3000412

[187] A.A. Ali, R. Luoh, F. Ko, B.J.J. Mack, L.M. Viculis, A. Ali, R. Luoh, G. Yang, H.T. Hahn, F.K. Ko, R.B. Kaner, Graphite Nanoplatelet Reinforcement of Electrospun Polyacrylonitrile Nanofibers, (2005) 13–17. *Advanced Materials* 17 (1) (2005) 77-80. doi:10.1002/adma.200400133.

[188] P. Chen, 3D Graphene Foam as a Monolithic and Macroporous Carbon Electrode for Electrochemical Sensing, *ACS Appl. Mater. Interfaces* 4 (6) (2012) 3129-3133.

https://doi.org/10.1021/am300459m

[189] C. Wang, X. Liu, J.P. Chen, K. Li, Superior removal of arsenic from water with zirconium metal-organic framework UiO-66, *Sci. Rep.* 5 (2015) 16613. doi:10.1038/srep16613.

[190] J. Canivet, M. Vandichel, D. Farrusseng, Origin of highly active metal – organic framework catalysts : defects ? Defects !, *Dalton Trans.* 45 (2016) 4090-4099. doi:10.1039/c5dt03522h.

[191] B. Liu, A.E. Baumann, V.S. Thoi, Modulating charge transport in MOFs with zirconium oxide nodes and redox-active linkers for lithium sulfur batteries, *Polyhedron* 170 (2019) 788–795. doi:10.1016/j.poly.2019.06.044.

[192] J.H. He, Y.Q. Wan, J.Y. Yu, Effect of concentration on electrospun polyacrylonitrile (PAN) nanofibers, *Fibers Polym.* 9 (2008) 140–142. doi:10.1007/s12221-008-0023-3.

[193] L. Wannatong, A. Sirivat, P. Supaphol, Effect of Solvents on Electrospun Polymeric Fibers : Preliminary Study on Polystyrene, *Polymer International* 53 (11) (2016) 1851-1859. doi:10.1002/pi.1599.

[194] M. Ding, R.W. Flaig, H. Jiang, Carbon capture and conversion using metal – organic frameworks and MOF-based materials, *Chem. Soc. Rev.* 48 (10) (2019) 2783–2828. doi:10.1039/c8cs00829a.

[195] S. Sanda, S. Parshamoni, S. Konar, Third-generation breathing metal-organic framework with selective, stepwise, reversible, and hysteretic adsorption properties, *Inorg. Chem.* 52 (2013) 12866–12868. doi:10.1021/ic402095u.

[196] J. Huang, T. Cavanaugh, B. Nur, An Introduction to SEM Operational Principles and Geologic Applications for Shale Hydrocarbon Reservoirs, *American Association of Petroleum Geologists* 102 (2013) 1–6. doi:10.1306/13391699M1023580.

[197] K.J. Gross, H. Technology, C. Llc, K.R. Carrington, C. Berkeley, Recommended Best Practices for the Characterization of Storage Properties of Hydrogen Storage Materials, (2008) 1–124.

[198] D. Graf, F. Molitor, K. Ensslin, C. Stampfer, A. Jungen, C. Hierold, L. Wirtz, Raman imaging of graphene, *Solid State Communications* 143 (1-2) (2007) 44–46.

doi:10.1016/j.ssc.2007.01.050.

[199] L.M. Malard, M.A. Pimenta, G. Dresselhaus, M.S. Dresselhaus, Raman spectroscopy in graphene, *Phys. Rep.* 473 (2009) 51–87. doi:10.1016/j.physrep.2009.02.003.

[200] N.E. Zander, K.E. Strawhecker, J.A. Orlicki, A.M. Rawlett, T.P. Beebe, Coaxial Electrospun Poly (methyl methacrylate)-Polyacrylonitrile Nanofibers : Atomic Force Microscopy and Compositional Characterization, *J. Phys. Chem. B* 115 (43) (2011) 12441–12447. doi:10.1021/jp205577r.

[201] M.S. Dresselhaus, G. Dresselhaus, R. Saito, A. Jorio, Raman spectroscopy of carbon nanotubes, *Physics Reports* 409 (2) (2005) 47–99. doi:10.1016/j.physrep.2004.10.006.

[202] Y. Inokuma, S. Yoshioka, J. Ariyoshi, T. Arai, Y. Hitora, K. Takada, S. Matsunaga, X-ray analysis on the nanogram to microgram scale using porous complexes, *Nature* 495 (2013) 461–466. doi:10.1038/nature11990.

[203] P. Study, P. Rev, Role of Disorder and Anharmonicity in the Thermal Conductivity of Silicon-Germanium Alloys : A First- Principles Study, *Phys. Rev. Lett.* 106 (2017) 045901. doi:10.1103/PhysRevLett.106.045901.

[204] S. V Kolotilov, V. V Pavlishchuk, Effect of structural and thermodynamic factors on the sorption of hydrogen by metal–organic framework compounds, *Theoretical and Experimental Chemistry* 45 (2009) 67–87. https://doi.org/10.1007/s11237-009-9068-7

[205] P. Iacomi, U. Lee, A.H. Valekar, J. Chang, P.L. Llewellyn, Investigating the e ff ect of alumina shaping on the sorption properties of promising metal – organic frameworks, *RSC Adv.* 9 (2019) 7128-7135. doi:10.1039/c9ra00534j.

[206] A.M. Ploskonka, S.E. Marzen, J.B. Decoste, Facile Synthesis and Direct Activation of Zirconium Based Metal − Organic Frameworks from Acetone, *Ind. Eng. Chem. Res.* 56 (6) (2017) 1478-1484. doi:10.1021/acs.iecr.6b04361.

[207] L. Bromberg, C.Z. Ag, S. Speakman, B. V Panalytical, Chromium(III) Terephthalate Metal Organic Framework (MIL-101): HF-Free Synthesis, Structure, Polyoxometalate Composites, and Catalytic Properties, *Chem. Mater.* 24 (9) (2012) 1664-1675. doi:10.1021/cm2034382.

[208] T. Zhao, M. Dong, L. Yang, Y. Liu, Synthesis of Stable Hierarchical MIL-101 (Cr)

with Enhanced Catalytic Activity in the Oxidation of Indene, *Catalysts* 8 (9) (2018) 394. doi:10.3390/catal8090394.

[209] E. Masika, R. Mokaya, Progress in Natural Science : Materials International Preparation of ultrahigh surface area porous carbons templated using zeolite 13X for enhanced hydrogen storage, *Prog. Nat. Sci. Mater. Int.* 23 (2013) 308–316. doi:10.1016/j.pnsc.2013.04.007.

[210] G.C. Shearer, S. Chavan, J. Ethiraj, J.G. Vitillo, S. Svelle, U. Olsbye, C. Lamberti, S. Bordiga, K.P. Lillerud, Tuned to perfection: Ironing out the defects in metal-organic framework UiO-66, *Chem. Mater.* 26 (2014) 4068–4071. doi:10.1021/cm501859p.

[211] K. Wang, C. Li, Y. Liang, T. Han, H. Huang, Q. Yang, D. Liu, C. Zhong, Rational construction of defects in a metal-organic framework for highly efficient adsorption and separation of dyes, *Chem. Eng. J.* 289 (2016) 486–493. doi:10.1016/j.cej.2016.01.019.

[212] T. Devic, G. Clet, Acid-functionalized UiO-66(Zr) MOFs and their evolution after intra-framework cross-linking: structural features and sorption properties, *J. Mater. Chem. A* 3 (2015) 3294-3309. doi:10.1039/c4ta03992k.

[213] H. Furukawa, M.A. Miller, O.M. Yaghi, Independent verification of the saturation hydrogen uptake in MOF-177 and establishment of a benchmark for hydrogen adsorption in metal-organic frameworks, *J. Mater. Chem.* 17 (2007) 3197–3204. doi:10.1039/b703608f.

[214] Micromeritics characterization guide, Cited from: micromeritics.com.

[215] A. Dailly, E. Poirier, Evaluation of an industrial pilot scale densified MOF-177 adsorbent as an on-board hydrogen storage medium, *Energy Environ. Sci.* 4 (2011) 3527–3534. doi:10.1039/C1EE01426A.

[216] G. Eda, S. Shivkumar, Bead structure variations during electrospinning of polystyrene, *Journal of Materials Science* 41 (2006) 5704–5708. doi:10.1007/s10853-006-0069-9.

[217] S. Ramakrishna, K. Fujihara, W. Teo, T. Yong, Z. Ma, R. Ramaseshan, Electrospun na nofibers, *Mater. Today* 9 (2006) 40–50. doi:10.1016/S1369-7021(06)71389-X.

[218] N.B. Mckeown, Polymers of Intrinsic Microporosity, I*SRN Materials Science* 2012 (2012) 513986. doi:10.5402/2012/513986.

[219] H. Amid, B. Maze, M.C. Flickinger, B. Pourdeyhimi, Hybrid adsorbent nonwoven structures: a review of current technologies, *J. Mater. Sci.* 51 (2016) 4173–4200. doi:10.1007/s10853-016-9741-x.

[220] E. Lasseuguette, M. Ferrari, Development of microporous electrospun PIM-1 fibres, *Materials Letters* 177 (2016) 116–119. doi:10.1016/j.matlet.2016.04.181.

[221] M. Chen, B. Coasne, R. Guyer, D. Derome, J. Carmeliet, polymers, *Nat. Commun.* 9 (2018) 3507. doi:10.1038/s41467-018-05897-9.

[222] E. Zussman, J.P. Quintana, R.S. Ruoff, Mechanical and structural characterization of electrospun PAN-derived carbon nanofibers, *Carbon* 43 (10) (2005) 2175–2185. doi:10.1016/j.carbon.2005.03.031.

[223] X.J. Id, L. Li, R.X. Id, Q. Liu, L. Ding, Y. Pan, Effects of Thermal Cross-Linking on the Structure and Property of Asymmetric Membrane Prepared from the Polyacrylonitrile, *Polymers* 10 (5) (2018) 539. doi:10.3390/polym10050539.

[224] N. Yusof, A.F. Ismail, Post spinning and pyrolysis processes of polyacrylonitrile (PAN)-based carbon fiber and activated carbon fiber: A review, *J. Anal. Appl. Pyrolysis.* 93 (2012) 1–13. doi:10.1016/j.jaap.2011.10.001.

[225] M.S.A. Rahaman, A.F. Ismail, A. Mustafa, A review of heat treatment on polyacrylonitrile fiber, *Polym. Degrad. Stab.* 92 (2007) 1421–1432. doi:10.1016/j.polymdegradstab.2007.03.023.

[226] J. Ren, N.M. Musyoka, P. Annamalai, H.W. Langmi, B.C. North, M. Mathe, Electrospun MOF nanofibers as hydrogen storage media, *Int. J. Hydrogen Energy* 40 (30) (2015) 9382-9387. https://doi.org/10.1016/j.ijhydene.2015.05.088

[227] M. Heuchel, D. Fritsch, P.M. Budd, N.B. Mckeown, D. Hofmann, Atomistic packing model and free volume distribution of a polymer with intrinsic microporosity (PIM-1), *J. Membr. Sci.* 318 (2008) 84–99. doi:10.1016/j.memsci.2008.02.038.

[228] P.M. Budd, N.B. Mckeown, B.S. Ghanem, K.J. Msayib, D. Fritsch, L. Starannikova, N. Belov, O. Sanfirova, Y. Yampolskii, V. Shantarovich, Gas permeation parameters and other physicochemical properties of a polymer of intrinsic microporosity : Polybenzodioxane PIM-1, *Journal of Membrane Science* 325 (2) (2008) 851–860.

doi:10.1016/j.memsci.2008.09.010.

[229] B.A. Stein, Z. Wang, M.A. Fierke, Functionalization of Porous Carbon Materials with Designed Pore Architecture, *Advanced Materials* 21 (3) (2009) 265–293. doi:10.1002/adma.200801492.

[230] F.T. Johra, J. Lee, W. Jung, Facile and safe graphene preparation on solution based platform Journal of Industrial and Engineering Chemistry Facile and safe graphene preparation on solution based platform, *J. Ind. Eng. Chem.* 20 (2014) 2883–2887. doi:10.1016/j.jiec.2013.11.022.

[231] Y. Gu, Y. Wu, L. Li, W. Chen, F. Li, S. Kitagawa, Controllable Modular Growth of Hierarchical MOF-on-MOF Architectures, *Angewadte Chemie Int. Ed.* 56 (49) (2017) 15658–15662. doi:10.1002/anie.201709738.

[232] I. Sumirat, Y.A.S. Shimamura, Theoretical consideration of the effect of porosity on thermal conductivity of porous materials, *Journal of Porous Materials* 13 (2006) 439–443. doi:10.1007/s10934-006-8043-0.

[233] C. Chung, J. Ihm, H. Lee, Recent progress on Kubas-type hydrogen-storage nanomaterials: from theories to experiments, *J. Korean Phys. Soc.* 66 (2015) 1649–1655. doi:10.3938/jkps.66.1649.

[234] E. Masika, R. Mokaya, Exceptional gravimetric and volumetric hydrogen storage for densified zeolite templated carbons with high mechanical stability, *Energy Environ. Sci.* 7 (2014) 427–434. doi:10.1039/c3ee42239a.

[235] J. Ren, N.M. Musyoka, H.W. Langmi, A. Swartbooi, B.C. North, M. Mathe, A more efficient way to shape metal-organic framework (MOF) powder materials for hydrogen storage applications, *Int. J. Hydrogen Energy.* 40 (13) (2015) 4617-4622. doi:10.1016/j.ijhydene.2015.02.011.

[236] S. Øien, D. Wragg, H. Reinsch, S. Svelle, S. Bordiga, C. Lamberti, K.P. Lillerud, Detailed structure analysis of atomic positions and defects in zirconium metal-organic frameworks, *Cryst. Growth Des.* 14 (2014) 5370–5372. doi:10.1021/cg501386j.

[237] D. Yang, M.A. Ortun, V. Bernales, C.J. Cramer, L. Gagliardi, B.C. Gates, Structure and Dynamics of Zr_6O_8 Metal − Organic Framework Node Surfaces Probed with Ethanol

Dehydration as a Catalytic Test Reaction, *J. Am. Chem. Soc.* 140 (10) (2018) 3751-3759 .doi:10.1021/jacs.7b13330.

[238] D.M. Driscoll, A.J. Morris, D. Troya, P.M. Usov, A.J. Maynes, J.R. Morris, Geometry and energetics of CO adsorption on hydroxylated UiO-66, *Phys. Chem. Chem. Phys*. 21 (2019) 5078–5085. doi:10.1039/c8cp07778a.